Reconfigurable Intelligent Surface-Centric Communication Networks: A Comprehensive Exploration of Channel Modeling and Coverage Extension

by

İbrahim Yıldırım

A Dissertation Submitted to the
Graduate School of Sciences and Engineering
in Partial Fulfillment of the Requirements for
the Degree of

Doctor of Philosophy

in

Electrical and Electronics Engineering

KOÇ ÜNİVERSİTESİ

March, 2024

Reconfigurable Intelligent Surface-Centric Communication Networks: A Comprehensive Exploration of Channel Modeling and Coverage Extension

Koç University
Graduate School of Sciences and Engineering

This is to certify that I have examined this copy of a doctoral dissertation by

İbrahim Yıldırım

and have found that it is complete and satisfactory in all respects,
and that any and all revisions required by the final
examining committee have been made.

Committee Members:

Assoc. Prof. Dr. Ertuğrul Başar (Advisor)

Prof. Dr. Hüseyin Arslan

Prof. Dr. Sinem Çöleri

Asst. Prof. Dr. Murat Kuşcu

Dr. İbrahim Hökelek

Date: ______________________

To my beloved family, whose unwavering support and encouragement have been my anchor throughout this academic journey.

ABSTRACT

Reconfigurable Intelligent Surface-Centric Communication Networks: A Comprehensive Exploration of Channel Modeling and Coverage Extension

İbrahim Yıldırım

Doctor of Philosophy in Electrical and Electronics Engineering

March, 2024

Reconfigurable intelligent surface (RIS)-empowered communication has received growing interest from the wireless research community due to its undeniable potential in extending the coverage, enhancing the link capacity, mitigating interference, deep fading, and Doppler effects, and increasing the physical layer security. RISs enable the control of wireless propagation through their unique electromagnetic functionalities and provide a new degree of freedom in the system design. Delving into the potential of RISs, this thesis unfolds across four detailed chapters, each contributing distinct insights into the deployment and application of RIS in enhancing wireless communication systems. Each chapter is crafted to provide a different perspective on RIS deployment and explain how this technology can be innovatively applied to support various aspects of wireless communication networks. This thesis takes a journey from the theoretical foundations of RIS to its envisioned practical applications and provides insights into how RIS can reshape wireless communication infrastructures to meet the demanding requirements of 6G networks. In the scope of this thesis, the RIS is introduced as a groundbreaking technology, reshaping the future of wireless communications by offering enhanced network capabilities, crucial for meeting the advanced requirements of next-generation applications. First, a comprehensive discussion of the intricacies of RISs in channel modeling is embarked on, which is a cornerstone for the effective deployment of sixth-generation (6G) wireless networks. In this regard, the physical channel modeling methodologies are provided for emerging RIS-empowered networks and aimed to fill an important gap in the open literature by providing a open-source and widely applicable physical channel model for mmWaves. Morevover, the open-source *SimRIS Channel Simu-*

lator MATLAB package is introduced, which can be used in channel modeling and computer simulations of RIS-based communication systems with tunable operating frequency, terminal and RIS locations, number of RIS elements, and environments. The upcoming parts go beyond merely introducing the technology, delving into how RIS can be strategically employed to address some of the most challenging aspects of modern wireless communication, such as coverage extension, signal quality improvement, and network throughput enhancement. The following chapters build upon this foundation, each focusing on specific applications and implications of RIS in the realm of wireless communications. From intricate channel modeling to practical deployment strategies for coverage extension and advanced beamforming designs, the study offers a comprehensive and nuanced understanding of the multifaceted role of RIS in future wireless networks. This work stands as a testament to the transformative impact of RIS technology within the 6G landscape, offering an extensive exploration of its applications in channel modeling, coverage extension, and more. By weaving RIS into the fabric of various network design aspects, from sophisticated beamforming to coverage optimization, the study sets a robust framework for the advancement of future wireless communications, paving the way for the realization of the 6G vision.

ÖZETÇE

Yeniden Yapılandırılabilir Akıllı Yüzey Odaklı İletişim Ağları: Kanal Modellemesi ve Kapsama Alanı Genişletmesine Kapsamlı Bir Bakış
İbrahim Yıldırım
Elektrik ve Elektronik Mühendisliği, Doktora
Mart 2024

Yeniden yapılandırılabilir akıllı yüzey (reconfigurable intelligent surface, RIS) destekli iletişim, kapsama alanını genişletme, bağlantı kapasitesini artırma, girişim, derin sönümleme ve Doppler gibi kanal etkilerini azaltma ve fiziksel katman güvenliğini artırma konusundaki yadsınamaz potansiyeli nedeniyle araştırmacılardan kayda değer bir ilgi görmüştür. RIS benzersiz elektromanyetik işlevsellikleri sayesinde kablosuz yayılımın dinamik kontrolünü mümkün kılmakta ve sistem tasarımında yeni bir serbestlik derecesi sağlamaktadır. RIS'lerin potansiyelini inceleyen bu tez, her biri kablosuz iletişim sistemlerinin geliştirilmesinde RIS'in konuşlandırılması ve uygulanmasına farklı anlayışlar katan dört ayrıntılı bölümden oluşmaktadır. Her bir bölüm, RIS'in konuşlandırılmasına farklı bir bakış açısı sağlamak ve bu teknolojinin kablosuz iletişim ağlarının çeşitli yönlerini desteklemek için nasıl yenilikçi bir şekilde uygulanabileceğini açıklamak üzere titizlikle hazırlanmıştır. Bu tez, RIS'in teorik temellerinden öngörülen pratik uygulamalarına doğru bir yolculuk yapmakta ve RIS'in 6G ağlarının zorlu gereksinimlerini karşılamak için kablosuz iletişim altyapılarını nasıl yeniden şekillendirebileceğine dair içgörüler sunmaktadır. Bu tez kapsamında RIS, yeni nesil uygulamaların gelişmiş gereksinimlerini karşılamak için çok önemli olan gelişmiş ağ yetenekleri sunarak kablosuz iletişimin geleceğini yeniden şekillendiren çığır açan bir teknoloji olarak tanıtılmaktadır. İlk olarak, altıncı nesil (6G) kablosuz ağların etkili bir şekilde konuşlandırılması için bir mihenk taşı olan kanal modellemesinde RIS'lerin etkileri kapsamlı bir şekilde tartışılmaktadır. Bu bağlamda, gelişmekte olan RIS destekli ağlar için fiziksel kanal modelleme yöntemleri sunulmakta ve milimetre dalgalar için açık kaynaklı ve yaygın olarak uygulanabilir bir fiziksel kanal modeli sağlayarak açık literatürdeki önemli bir boşluğu doldurmayı amaçlamaktadır. Ayrıca, kullanıcı tarafından ayarlanabilir çalışma frekansı, termi-

nal ve RIS konumları, RIS elemanlarının sayısı ve ortamları ile RIS tabanlı iletişim sistemlerinin kanal modellemesi ve bilgisayar benzetimlerinde kullanılabilen açık kaynaklı *SimRIS Kanal Simülatörü* tüm detaylarıyla tanıtılmıştır. İlerleyen bölümler bu teknolojiyi tanıtmanın ötesine geçerek, kapsama alanının genişletilmesi, sinyal kalitesinin iyileştirilmesi ve ağ veriminin artırılması gibi modern kablosuz iletişimin en zorlu yönlerinden bazılarını ele almak için RIS'in stratejik olarak nasıl kullanılabileceğini araştırmaktadır. Takip eden bölümler bu temel üzerine inşa edilmiş olup, her biri RIS'in kablosuz iletişim alanındaki belirli uygulamalarına ve özgün kullanım senaryolarına odaklanmaktadır. Detaylı kanal modellemesinden, kapsama alanının genişletilmesi ve gelişmiş hüzmeleme tasarımları için pratik system tasarım stratejilerine kadar, bu çalışma, RIS'in gelecekteki kablosuz iletişim ağlarındaki çok yönlü rolüne dair kapsamlı bir anlayış ve çözüm sunmaktadır. Özetle, bu çalışma, RIS teknolojisinin 6G perspektifine paradigma değiştirici katkısını destekleyici bir sonuçlar içermesinin yanı sıra kanal modelleme, kapsama alanı genişletme ve daha pek çok alandaki uygulamalarının kapsamlı bir incelemesini sunmaktadır. RIS'i sofistike hüzmelemeden kapsama alanı optimizasyonuna kadar çeşitli ağ tasarım yöntemlerinin dokusuna işleyerek, gelecekteki kablosuz iletişim ağlarının gelişmesi için sağlam bir çerçeve oluşturmakta ve 6G vizyonunun gerçekleştirilmesinin önünü açmaktadır.

ACKNOWLEDGMENTS

Sanman taleb-i devlet ü câh etmeye geldik
Biz âleme bir yâr için âh etmeye geldik.
Yenişehirli Avnî

Deem not that we have come to covet worldly power or indulge in folly
We have arrived to lament for a beloved
Yenişehirli Avnî

This thesis marks the inception of a journey into the vast sea of knowledge. It is not an expression of seeking worldly power or indulging in folly; rather, it signifies delving into the depths of the universe, an ode to a beloved, an expression of our passion and love for knowledge.

In the genesis of this thesis and throughout my academic trajectory, paramount gratitude is extended to my esteemed advisor, Dr. Ertuğrul Başar, whose unwavering support transcended the conventional advisor role. I sincerely convey my heartfelt thanks to him for the sincerity he maintained and the steadfast support he consistently provided, surpassing the mere duties of an advisor.

Expressions of gratitude are also extended to Mr. Sefa Çetinkaya, whose enduring camaraderie and sagacious guidance proved invaluable whenever I found myself in need. Furthermore, my heartfelt appreciation is directed towards Mr. Taha Kılınç, whose exemplary work discipline and resolute dedication to his craft have served as a beacon of inspiration for me. The steadfast commitment and focused efforts of both Mr. Taha and Sefa, in their discipline, have been instrumental in fortifying my resolve during challenging moments.

My gratitude extends to the Scientific and Technological Research Council of

Turkey (TÜBİTAK) for its financial support not only in fostering my doctoral endeavors under the BİDEB 2211-E program but also in facilitating my overseas research under the BİDEB 2214-A program.

I also extend profound appreciation to Prof. Dr. Tho Le-Ngoc at McGill University's Broadband Communications Research Lab for his warm welcome and insightful guidance throughout my year-long tenure as a visiting researcher. His wealth of wisdom has been an invaluable source, and I sincerely appreciate the consistent support and openness he generously shared with me.

I extend my gratitude to Prof. Dr. Sinem Çöleri and Prof. Dr. Hüseyin Arslan, members of my thesis committee, for their encouragement and valuable insights.

In addition to supporting my academic endeavors, my deepest appreciation goes to my mother Nevin, father Ruhi, and siblings Suğra and Mustafa Erdem for their unwavering devotion and encouragement throughout my life. Their unconditional support has not only been a pillar for my personal growth but has also shaped me into a person who values and prioritizes contributing to our nation, community, and ummah. It is through their teachings and exemplary guidance that I have imbibed the principles of serving the homeland, nation, and the larger community. Their efforts in instilling a sense of responsibility, compassion, and dedication to a greater cause have been instrumental in my journey, making every success a collective achievement.

An exceptional recognition is dedicated to my treasured life companion, Semanur. Her enduring moral support and resilience amidst the challenges of my doctoral journey not only rendered this demanding process bearable but also became the cornerstone of my strength and perseverance. Her immeasurable contributions and understanding transformed the arduous path into a shared adventure, making every hurdle surmountable and every achievement more meaningful. Semanur's presence has been an unwritten chapter in the narrative of my success, and I express my deepest gratitude for her indelible imprint to this significant chapter of my academic odyssey.

TABLE OF CONTENTS

LIST OF TABLES

LIST OF FIGURES

ABBREVIATIONS

AB-HBF	Angular-Based Hybrid Beamforming
AoA	Angle-of-Arrival
AoD	Angle-of-Departure
AWGN	Additive White Gaussian Noise
BB	Baseband
BER	Bit Error Rate
CSI	Channel State Information
HBF	Hybrid Beamforming
IoT	Internet-of-Things
LoS	Line-Of-Sight
MGF	Moment Generating Function
MIMO	Multiple-Input Multiple-Output
OFDM	Orthogonal Frequency-Division Multiplexing
PHY	Physical
PLE	Path Loss Exponent
PSK	Phase Shift Keying
PSO	Particle Swarm Optimization
RF	Radio Frequency
QAM	Quadrature Amplitude Modulation
RIS	Reconfigurable Intelligent Surface
SNR	Signal-to-Noise Ratio
SVD	Singular Value Decomposition
UAV	Unmanned Aerial Vehicle
ULA	Uniform Linear Array
UPA	Uniform Planar Array

Chapter 1

INTRODUCTION

In an era where the telecommunications landscape is rapidly evolving towards sixth-generation (6G) wireless systems, the integration of advanced technologies is imperative to meet the burgeoning demands for enhanced connectivity and network capabilities [1]. These next-generation applications include revolutionary concepts beyond the internet-of-things (IoT), such as holographic telepresence, large-scale digital twinning, industrial robots, and autonomous vehicles. This evolution is characterized by a concerted push towards delivering not just broader bandwidths but also more dynamic and versatile transmission strategies. In this context, a major paradigm shift from "connected things" to "connected intelligence" is expected, signaling a fundamental shift in the understanding of wireless communications [2].

With this transformation comes the need for extremely high data transmission rates and ultra-high energy efficiency. In particular, data transmission speeds are expected to reach unprecedented levels of 1 Tb/s. Such a speed has the potential to radically expand not only the capacity but also the functionality and use cases of wireless networks. Another critical need emphasized by 6G is extremely low latency and ultra-high reliability [3,4]. In particular, a latency of less than 1 ms is targeted, which is vital for real-time applications and critical communication requirements [2]. These attractive features can be supported by utilizing effective physical layer tools such as ultra massive multiple-input multiple-output (MIMO) systems, millimeter wave (mmWave) and terahertz (THz) communications, and reconfigurable intelligent surfaces (RISs). RIS-empowered communication has received growing interest from the wireless research community due to its undeniable potential in extending the coverage, enhancing the link capacity, mitigating interference, deep fading, and Doppler effects, and increasing the physical layer security. RISs enable the control of wireless propagation through their unique electromagnetic functionalities and provide a new degree of freedom in the system design [5–9].

Delving into the potential of RISs, this thesis unfolds across three detailed chapters, each contributing distinct insights into the deployment and application of RIS in enhancing wireless communication systems. Each chapter is crafted to provide a different perspective on RIS deployment and explain how this technology can be innovatively applied to support various aspects of wireless communication networks. This thesis takes a journey from the theoretical foundations of RIS to its envisioned practical applications and provides insights into how RIS can reshape wireless communication infrastructures to meet the demanding requirements of 6G networks. In the scope of this thesis, the RIS is introduced as a groundbreaking technology, reshaping the future of wireless communications by offering enhanced network capabilities, crucial for meeting the advanced requirements of next-generation applications.

This thesis lays the foundational understanding of RIS, elucidating its role in augmenting network capabilities to meet the advanced demands of future wireless applications. The upcoming parts go beyond merely introducing the technology, delving into how RIS can be strategically employed to address some of the most challenging aspects of modern wireless communication, such as coverage extension, signal quality improvement, and network throughput enhancement.

1.1 Thesis Motivations and Contributions

First, a comprehensive discussion of the intricacies of RISs in channel modeling is embarked on, which is a cornerstone for the effective deployment of 6G wireless networks. In this regard, the physical channel modeling methodologies are provided for emerging RIS-empowered networks and aimed to fill an important gap in the open literature by providing an open-source and widely applicable physical channel model for mmWaves. Moreover, the open-source *SimRIS Channel Simulator* MATLAB package is introduced, which can be used in channel modeling and computer simulations of RIS-based communication systems with tunable operating frequency, terminal and RIS locations, number of RIS elements, and environments. Using SimRIS Channel Simulator, we provide preliminary computer simulation results and reveal the practical use cases of RISs for indoors and outdoors. The given comprehensive channel modeling efforts that include 3D channel models for 5G networks and physical RIS characteristics, and computer simulations reveal that *RISs* will work! by carefully adjusting their size, position, and functionality. In other words, using a physical channel modeling methodology that is unique to RIS-empowered systems, we prove that the received signal quality, in return the achievable rate, can be significantly boosted for both indoor and outdoor environments at certain locations. The following chapters build upon this foundation, each focusing on specific applications and implications of RIS in the realm of wireless communications. From intricate channel modeling to practical deployment strategies for coverage extension and advanced beamforming designs, the study offers a comprehensive and nuanced understanding of the multifaceted role of RIS in future wireless networks.

Second, it is focused on how RIS technology can cost-efficiently improve coverage in wireless networks. This chapter details the potential of RIS in wireless communications by covering two key studies. The first study examines how RIS can be effectively deployed in indoor and outdoor wireless applications. This analysis shows how RIS technology can enhance wireless communications even in the presence of obstacles or when direct connections between terminals are not available. This highlights the potential of RIS to extend the coverage of wireless networks in single and multiple-use scenarios, especially in challenging communication environments. The second work given in this chapter considers the combination of RIS-assisted reflection and relaying techniques. This approach explores the synergy of RIS technology and relaying strategies and how it can improve the coverage and transmission quality of wireless networks. Particularly in challenging communication environments, this section demonstrates how the combined use of RIS and relaying can optimize network performance, effectively broadening the coverage area.

Then, the integration of RIS technology into massive MIMO systems operating in mmWave and THz frequency bands are investigated and its innovative applications in this field are elaborated. Within this goal, the ways to reduce CSI overhead in high frequency bands by examining angular-based hybrid beamforming (AB-HBF) methods specifically designed for single- and multi-RIS-enabled THz massive MIMO systems. The design of the RIS phase shift matrix using particle swarm optimization (PSO) is highlighted and it is shown how this design can maximize the achievable rate of massive MIMO systems. A dynamic RIS implementation specifically called ”Spider RIS” is also introduced within this part of the thesis. This novel approach aims to increase spatial multiplexing and network efficiency by providing mobility. This part of the thesis meticulously presents innovative methodologies that integrate RIS technology into wireless communication systems, shaping the future of wireless networks in terms of capacity, coverage, and reliability.

The findings of this thesis have been disseminated through various academic channels, resulting in significant publications and submissions. Specifically, the outputs of this research are completely or partially included in 1 book chapter, 6 journal articles, and 5 conference proceedings, as detailed in the list below.

1. I. Yildirim, A. Uyrus, E. Basar, ”Modeling and Analysis of Reconfigurable Intelligent Surfaces for Indoor and Outdoor Applications in Future Wireless Systems”, *IEEE Transactions on Communications*, vol. 69, no. 2, pp. 1290-1301, Feb. 2021, doi: 10.1109/TCOMM.2020.3035391.

2. I. Yildirim, F. Kilinc, E. Basar and G. C. Alexandropoulos, ”Hybrid RIS-Empowered Reflection and Decode-and-Forward Relaying for Coverage Extension”, *IEEE Communications Letters*, vol. 25, no. 5, pp. 1692-1696, May 2021, doi: 10.1109/LCOMM.2021.3054819.

3. I. Yildirim and E. Basar, ”Channel Modeling in RIS-Empowered Wireless Communications”, Chapter in *Intelligent Reconfigurable Surfaces (IRS) for Prospective 6G Wireless Networks*, John Wiley & Sons, Inc., 2023.

4. E. Basar, I. Yildirim and F. Kilinc, ”Indoor and Outdoor Physical Channel

Modeling and Efficient Positioning for Reconfigurable Intelligent Surfaces in mmWave Bands", *IEEE Transactions on Communications*, vol. 69, no. 12, pp. 8600-8611, Dec. 2021, doi: 10.1109/TCOMM.2021.3113954

5. E. Basar and I. Yildirim, "Reconfigurable Intelligent Surfaces for Future Wireless Networks: A Channel Modeling Perspective", *IEEE Wireless Communications*, vol. 28, no. 3, pp. 108-114, June 2021. doi: 10.1109/MWC.001.2000338.

6. S Kayraklık, I Yildirim, Y Gevez, E Basar and A Gorcin, "Indoor Coverage Enhancement for RIS-Assisted Communication Systems: Practical Measurements and Efficient Grouping",*IEEE International Conference on Communications*, Rome, Italy, 2023, pp. 485-490, doi: 10.1109/ICC45041.2023.10278759.

7. I. Yildirim, A. Koc, E. Basar and T. Le-Ngoc, "RIS-Aided Angular-Based Hybrid Beamforming Design in mmWave Massive MIMO Systems", *IEEE Global Communications Conference (GLOBECOM) 2022*, Rio de Janeiro, Brazil, 2022, pp. 5267-5272, doi: 10.1109/GLOBECOM48099.2022.10001250.

8. F. Kilinc, I. Yildirim and E. Basar, "Physical Channel Modeling for RIS-Empowered Wireless Networks in Sub-6 GHz Bands", *in Proc. 55th Asilomar Conference on Signals, Systems, and Computers*, Nov. 2021, Pacific Grove, CA, USA, doi: 10.1109/IEEECONF53345.2021.9723295

9. E. Basar and I. Yildirim, "SimRIS Channel Simulator for Reconfigurable Intelligent Surface-Empowered Communication Systems", *in Proc. IEEE Latin-American Conference on Communications (LATINCOM 2020)*, Virtual Conference, Nov. 2020, doi: 10.1109/LATINCOM50620.2020.9282349. **Best Paper Award**

10. I. Yildirim, M. Mahmoud, E. Basar, T. Le-Ngoc, "Spider RIS: Mobilizing Intelligent Surfaces for Enhanced Wireless Communication ", *Submitted to 2024 IEEE International Conference on Communications*, Nov., 2023.

11. I. Yildirim, A. Koc, E. Basar, T. Le-Ngoc, "Multi-RIS Assisted Hybrid Beamforming Design for Terahertz Massive MIMO Systems ", *Submitted to IEEE Open Journal of the Communications Society*, Nov., 2023.

12. S. Kayraklik, I. Yildirim, I. Hokelek, Y. Gevez, E. Basar, A. Gorcin, "Indoor Measurements for RIS-Aided Communication: Practical Phase Shift Optimization, Coverage Enhancement, and Physical Layer Security", *Submitted to IEEE Open Journal of the Communications Society*, Oct., 2023.

Additionally, collaborations undertaken during the course of this thesis have culminated in the production of 8 additional works, which are also listed below. These collaborative efforts have further extended the impact and reach of the research conducted in this thesis.

1. M. Raeisi, A. Koc, I. Yildirim, E. Basar, T. Le-Ngoc, "Cluster Index Modulation for Reconfigurable Intelligent Surface-Assisted mmWave Massive MIMO", *IEEE Transactions on Wireless Communications (Early Access)*, doi: 10.1109/TWC.2023.3290618.

2. E. Arslan, I. Yildirim, F. Kilinc and E. Basar, "Over-the-Air Equalization with Reconfigurable Intelligent Surfaces", *IET Commun.*, vol. 16, pp. 1486–1497, June 2022, doi: 10.1049/cmu2.12425

3. M. Raeisi, A. Koc, I. Yildirim, E. Basar, T. Le-Ngoc, "Antenna Array Structures for Enhanced Cluster Index Modulation", 2023 Joint European Conference on Networks and Communications & 6G Summit (EuCNC/6G Summit), Gothenburg, Sweden, 2023, pp. 102-107. doi: 10.1109/EuCNC/6GSummit58263.2023.10188340

4. B. Ozpoyraz, I. Yildirim and E. Basar, "Index Modulation Based Coordinate Interleaved Orthogonal Design for Secure Communications", *IEEE Transactions on Vehicular Technology*, vol. 70, no. 5, pp. 5155-5159, May 2021. doi: 10.1109/TVT.2021.3076688.

5. M. Raeisi, I. Yildirim, M. C. Ilter, M. Gerami, E. Basar, "Plug-In RIS: A Novel Approach to Fully Passive Reconfigurable Intelligent Surfaces", *Submitted to IEEE Transactions on Wireless Communications*, Nov. 2023.

6. S. Kayraklik, I. Yildirim, E. Basar, I. Hokelek, A. Gorcin, "Practical Implementation of RIS-Aided Spectrum Sensing: A Deep Learning-Based Solution", *Submitted to IEEE Transactions on Wireless Communications*, Nov. 2023.

7. E. Koktas, R. A. Tasci, I. Yildirim, E. Basar, "Unleashing the Potential of Reconfigurable Intelligent Surfaces in Martian Communication", *Submitted to IEEE Vehicular Technology Magazine*, Dec. 2023.

8. I. Yildirim, E. Basar and I. Altunbas, "Coordinate Interleaved Orthogonal Design with Media-Based Modulation", *IEEE Transactions on Vehicular Technology*, vol. 70, no. 3, pp. 2867-2871, Mar. 2021,
doi: 10.1109/TVT.2021.3059325.

1.2 Organization of the Thesis

The rest of the thesis is organized as follows. Chapter 2 presents developing channel Models in RIS-Enabled Wireless environments and open source SimRIS Channel Simulator. This chapter also provides an overview of RIS channel modeling, as well as discusses indoor and outdoor physical channel modeling and effective positioning for RIS in mmWave bands. Chapter 3 focuses on modeling and analysis of RIS in indoor and outdoor applications for future wireless networks, and enhanced coverage through combined RIS-aided reflecting and decode-and-forward relaying techniques. Chapter 4 provides RIS-enhanced hybrid beamforming solutions for massive MIMO systems by including RIS-enabled angular-based hybrid beamforming design in mmWave massive MIMO systems, multiple RIS-enabled THz communications, and an innovative system called “Spider RIS”. Finally, Chapter 5 concludes the thesis.

Chapter 2

CHANNEL MODELING AND OPEN-SOURCE CHANNEL SIMULATOR DESIGN FOR IN RIS-AIDED WIRELESS ENVIRONMENTS

Despite the vast drastic expectations, fifth-generation (5G) wireless communication networks can be considered as an evolution of fourth-generation (4G) wireless networks by providing a more adaptive and flexible structure in terms of adapted physical layer technologies. In sixth-generation (6G) wireless networks, which are expected to be rolled out in 2030s, it is an undeniable fact that there should be paradigm-shifting developments, especially in the physical layer, in order to meet the increasing massive demand in data consumption [10]. Within this context, millimeter wave (mmWave) and Terahertz (THz) communications, massive multiple-input multiple-output systems (MIMO), cell-free networks, high-altitude platform stations, integrated space and terrestrial networks, and reconfigurable intelligent surfaces (RISs) can be considered as promising candidate technologies for 6G systems in order to satisfy broadband connectivity by keeping new use-cases with very high mobility and extreme capacity requirements [11].

RIS-empowered communication can be regarded as a paradigm-shifting revolution that provides operators with software-based and dynamic control capability over the wireless propagation channel [12]. An RIS, which consists of a large number of nearly passive reflecting elements, can intelligently direct the beams to the desired users and ensure reliable communication by creating virtual line-of-sight (LoS) links even when the direct link between terminals is blocked. Due to these unprecedented contributions of RISs, researchers have shown remarkable interest in RIS-empowered communication systems, and plentiful applications that are candidates for use in next-generation communication systems have been explored [5, 13–16]. The various use-cases of RISs, including multi-user systems, physical (PHY) layer security, indoor-coverage extension, Doppler mitigation, vehicular and non-terrestrial networks, localization and sensing, and non-orthogonal multiple access (NOMA), have recently attracted significant attention from the research community. Despite these rich RIS use-cases, there is no strong consensus to identify the killer applications that effectively exploit the potential of RISs to control the transmission medium with intelligent reflections for enhanced end-to-end system performance [17]. The first step in clearing this ambiguity is to form a unified and physical RIS-assisted channel model that can be adapted to different use-cases and operating frequencies, taking into account the physical characteristics of RISs. Since intelligent reflection is the art of manipulating the channel characteristics in a brilliant and dynamic way, modeling the RIS-assisted transmission link is essential to provide detailed insights into the practical use-cases. This chapter mainly aims to present a vision on channel modeling strategies for the RIS-empowered communications systems considering the state-of-the-art channel and propagation modeling efforts in the literature. Another objective of the chapter is to draw attention to open-source and standard-compliant physical channel modeling efforts to provide comprehensive insights regarding the practical use-cases of RISs in future wireless networks.

The rest of the chapter is organized as follows: Section 2.1 presents a general framework on channel modeling strategies for RIS-empowered communications systems considering the state-of-the-art channel modeling efforts in the literature. Section 2.2 provides a framework for the cluster-based statistical channel model for mmWave bands. Section 2.3 introduces the various applications including RIS integration and the open-source *SimRIS Channel Simulator* package that considers a proposed narrowband channel model for RIS-empowered communication systems. The numerical results throughout this chapter are obtained by using *SimRIS Channel Simulator* designed within the framework of this thesis.

2.1 A General Perspective on RIS Channel Modeling

One of the most important aspects of enabling next-generation wireless technologies is the development of an accurate and consistent channel model to be validated effectively with the help of real-world measurements. From this point of view, remarkable research has recently been conducted to model propagation channels involving the modification of the wireless propagation environment through the inclusion of RISs. While many studies in the literature have modeled the path loss for RIS-assisted communication systems, modeling the end-to-end channel has also recently attracted significant attention. The near-field and far-field effects of RISs should also be considered when modeling the total path loss of RIS-empowered systems. Another critical point is the methodology followed when modeling the end-to-end channel. From this perspective, while many researchers follow physics-based channel modeling strategies by examining the physical properties of reflection and scattering effects, statistical channel modeling strategies have also been followed by considering the statistical properties of scatterers and clusters in the environment. Further, electromagnetic (EM) compatible channel models have also been proposed that take into account EM properties, such as mutual coupling among the sub-wavelength unit cells of the RIS. By considering the existing RIS-assisted channel modeling studies, the channel and propagation modeling approaches can be mainly classified as in Fig. 2.1. Since there is no obvious distinction between certain approaches in this classification, channel modeling studies in which more than one approach is used can provide a broader perspective.

Initial studies on RIS propagation modeling have predominantly focused on the path-loss and scattered power characterization by an RIS in RIS-assisted communication systems [18–24]. In [18], the authors characterize the path-loss in near-field and far-field of RISs by using the general scalar theory of diffraction and the Huygens-Fresnel principle. Moreover, the power reflected from an RIS is obtained as a function of the distance between the transmitter (Tx)/receiver (Rx) and the RIS, the size of the RIS, and the phase shifts induced by the RIS. By modeling

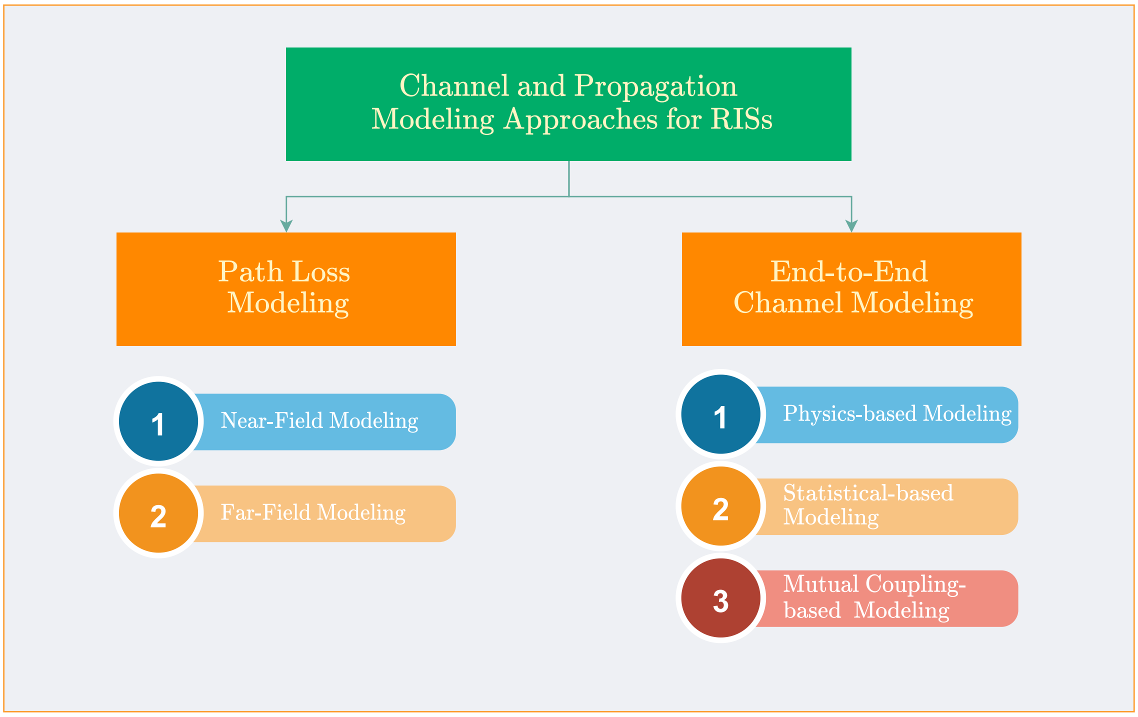

Figure 2.1: Classification of the channel and propagation modeling approaches based on the existing RIS literature.

RISs as a sheet of EM material of negligible thickness, the conditions under which an RIS acts as an anomalous mirror are identified. In [19], the authors characterize the path-loss using physics-based approaches and exploited the antenna theory on the calculation of the electric field both in the far-field and near-field of a finite-size RIS. While it is shown that an RIS can act as an anomalous mirror in the near field of the array, the received power expression is not formulated analytically for varying distances. The author in [20] calculates the path-loss as a function of RIS size, link geometry and practical gain of RIS elements by considering a passive reflectarray-type RIS design under the far-field and near-field cases. The practical power scaling laws are introduced in [21] for the far-field region of array using the physical optic techniques. The authors also clarify why the surface comprises a large number of reflecting elements that individually act as diffuse scatterers but can jointly beamform the signal in the desired direction with a specific beamwidth. In [22], the free-space path-loss models for RIS-enabled communication systems are characterized with physics and EM-based approaches by considering the distances from the Tx/Rx to the RIS, the size of the RIS, the near-field/far-field effects of the RIS, and the radiation patterns of antennas and unit cells. The proposed models are validated through extensive computer simulation results and experimental measurements using a specifically manufactured RIS. In [23], the authors leverage the vector generalization of Green's theorem and characterize the free space path-loss of the RIS-assisted communications by using physical optic methods in order to overcome the limitation of geometric optics. The analyses are conducted for two-dimensional (2D) homogenized metasurfaces that can operate in reflection or refraction mode under both far-field and near-field cases. Furthermore, the power scaling laws for asymptotically large RISs are studied in [24] using a deterministic propagation model and observed that the asymptotic limit could only be achieved in the near-field case.

While aforementioned studies characterize the path loss by using physics and EM-based approaches, in [25], a physics-based end-to-end channel model for RIS-empowered communication systems is introduced and a scalable optimization framework for large RISs is presented. This model includes the impact of all RIS tiles, the transmission modes of all tiles, and the incident, reflection, and polarization angles. Furthermore, each tile is modeled as an anomalous reflector, and physical optics-based analyses are conducted by adopting the concepts from the radar literature under the far-field conditions.

In [26], the authors propose a physics and EM-compliant end-to-end channel model for the RIS-assisted communication systems by considering the mutual coupling among the sub-wavelength unit cells of the RIS. This mutual coupling and unit cell aware model can be applied to an RIS consisting of closely-spaced scattering elements controlled by tunable impedances. Inspiring from the impedance-based channel model in [26], an analytical framework and a iterative algorithm are presented to obtain the end-to-end received power in [27]. In [28], a multi-user multiple-input multiple-output (MIMO) interference network is investigated in the presence of multiple RISs by using a circuit-based model for the transmitters, receivers, and RISs. The mutual coupling between impedance-controlled thin dipoles and the impact of the tuning elements are also investigated. Additionally, a provably convergent optimization algorithm is proposed to maximize the sum-rate of RIS-assisted MIMO interference channels by assessing the mutual coupling among closely-spaced scattering elements.

Recently, there have been a rapid and growing interest on stochastic non-stationary channel modeling activities for RIS-empowered wireless systems [29–33]. Within this context, in [29], a three-dimensional (3D) geometry-based stochastic channel model (GBSM) is introduced for a massive MIMO communication system in the presence of an RIS. The authors split the end-to-end channel into the sub-channels and characterize the large and small scale fading, respectively. In [30], practical phase shifts are considered and the reflection phases of the RIS are represented using two-bit quantization set in addition to the work in [29]. However, these two studies do not consider the practical deployment and physical properties of RISs. The study in [31] proposes a geometric RIS-assisted MIMO channel model for fixed-to-mobile communications based on a 3D cylinder model. While this study examines the non-stationary channels in which the receiver moves, the characteristic features of the scatterers in the environment are ignored, and analyses are merely conducted under sub-6 GHz frequency bands. Recently, the authors in [32] propose a general wideband non-stationary channel model for RIS-empowered communication systems operating at sub-6 GHz bands. By splitting the RIS-assisted MIMO channel model into subchannels, equivalent end-to-end channel models based on these subchannels are characterized under time-varying characteristics of MIMO systems in the presence of an RIS. Although the authors consider the physical characteristics of the wideband subchannel model between the mobile Tx and RIS, and RIS and mobile Rx for different propagation delays, LoS links between the Tx and Rx are ignored, and frequency bands above 6 GHz are not considered. More recently, a non-stationary 3D wideband GBSM for RIS-empowered MIMO communication systems are introduced in [33] by including propagation characteristics of RISs, such as unit number and size, relative terminal locations and RIS configuration. Nevertheless, this study does not consider a direct link between the Tx and the mobile Rx due to the blockage, and the applicability of this model is limited to sub-6 GHz frequency bands in an outdoor environment.

Against this background, due to the spectrum shortage of sub-6 GHz frequency bands, it is unavoidable to migrate to the mmWave and THz bands in future wireless networks. Since transmission at higher frequencies makes the signals more vulnerable to blockage and interference, the signal attenuation and blockage prevent mmWaves from reaching long distances. Especially in mmWave frequencies, using an RIS in the transmission can enable additional transmission paths when the direct link between the Tx and Rx is blocked or not sufficiently robust. Therefore, modeling a physical open-source, and widely applicable mmWave channel for the RIS-assisted systems in indoor and outdoor environments is of great importance to shed light on realistic use-cases of RISs in future wireless networks. From this point of view, a unified narrowband channel model for RIS-assisted systems both in indoor and outdoor environments is introduced in [7, 17, 34] by incorporating the 5G mmWave channel model under a random number of clusters, scatterers and the properties of the RIS. Moreover, a physical channel model for RIS-assisted systems is proposed in [35] by following the present technical specifications of sub-6 GHz bands.

An overview of the aforementioned channel modeling studies and brief explanations of their main contributions and characteristics can be seen in Table 2.1 [7, 17–34].

2.2 Indoor and Outdoor Physical Channel Modeling and Efficient Positioning for Reconfigurable Intelligent Surfaces in mmWave Bands

2.2.1 Introduction

6G wireless systems are expected to provide broadband connectivity by supporting new use-cases including extreme capacity and very high mobility, integrated with satellite networks and autonomous systems [11]. However, these attractive features might only be possible with effective tools such as ultra massive multiple-input multiple-output (MIMO) systems, millimeter wave (mmWave) and TeraHertz (THz) communications, reconfigurable intelligent surfaces (RISs), cell-free networks, and integrated space and terrestrial networks. While 5G wireless networks are being introduced in various countries worldwide, wireless experts have already set their sights on 6G networking by starting active research on these interesting technologies [36].

RIS-empowered communication has received tremendous interest from the wireless research community due to its undeniable potential in extending the coverage, enhancing the link capacity, mitigating interference, deep fading, and Doppler effects, and increasing the physical layer (PHY) security [12, 37–39]. This can be accomplished by controlling the wireless propagation through unique electromagnetic (EM) functionalities provided by RISs. Numerous studies from the past two years have demonstrated that RISs, which are artificial, electronically controlled, 2D surfaces of EM material, can be effectively used to boost the performance of existing communication systems by exploiting the inherent randomness of wireless propagation [40, 41]. Notable use-cases of RISs include energy efficient single/multi-

Table 2.1: An overview of RIS channel modeling studies and their contributions.

Work	Contributions
[18]	• Path-loss in near-field and far-field of RISs is characterized by using Huygens-Fresnel principle and physical optics-based methods • RISs are modeled as a sheet of EM material of negligible thickness
[19]	• Path-loss is characterized with physics-based approach • Electric field of a finite-size RIS is computed both in its far-field and near-field
[20]	• Path-loss is calculated for a passive reflectarray-type RIS • The path-loss is characterized as a function of RIS size, link geometry, and gain of RIS elements
[21]	• Power scaling laws are introduced for the far-field region using the physical optic principles
[22]	• Free-space path-loss with physic and EM-based approaches is characterized by considering the near-field/far-field effects of the RIS • It is validated through experimental measurements using manufactured RIS
[23]	• Path-loss is characterized as a function of the transmission distance and the RIS size by using physical optic methods and Huygens-Fresnel principle • 2D homogenized metasurfaces that can operate in reflection or refraction mode are considered under both far-field and near-field case
[24]	• Power scaling laws for asymptotically large RISs are analysed using a deterministic propagation model • It is shown that the asymptotic limit can only be achieved in the near-field
[25]	• Physical optics-based analysis are conducted by adopting the concepts from the radar literature • Each tile is modeled as an anomalous reflector
[26–28]	• EM-compliant model is characterized by considering mutual coupling among the RIS elements • The mutual coupling between impedance-controlled thin dipoles and the impact of the tuning elements are investigated
[29–33]	• A statistical geometry-based non-stationary models are derived for the RIS-aided MIMO systems • The various physical properties of RIS are considered, such as unit number and size, relative locations among Tx, RIS, and Rx
[7, 17, 34, 35]	• Comprehensive channel modeling efforts are introduced by considering 3D channel models for practical deployments and physical RIS characteristics • Open-source and widely applicable *SimRIS Channel Simulator* is introduced • Technical specifications on sub-6 GHz and mmWave bands are considered

user MIMO system designs with joint beamforming, PHY security systems, non-orthogonal multiple access schemes, index modulation systems, mmWave systems, vehicular/aerial networks, cognitive radio networks, wireless power transfer systems, posture recognition, and radio localization, and so on.

There has been a recent interest on practical aspects and modeling of RIS-assisted communication systems due to their rich use-cases and applications. While the initial studies of [12] and [42] and provide useful insights regarding the performance limits of RIS-assisted systems, they do not include path loss effects and consider relatively large RISs with specular reflection only. The subsequent studies of [21] and [19] discuss the scattering nature of RIS elements and introduce practical power scaling laws using the principles of physical optics and scattered fields for array near/far-field regions. However, a unified view is presented in [20] by considering plate scattering and radar range paradigms along with the physical area and practical gain of RIS elements. This study also verifies the fundamental findings of [43], which presents experimental results on the received signal power involving RISs. Nevertheless, the studies above consider pure line-of-sight (LOS) links between communication terminals and the RIS, limiting their validity in real-world systems.

More recently, the researchers put forward RIS-assisted mmWave communication systems within the perspective of future networks and reported promising results [44–48]. Nevertheless, although including physical mmWave channel models and massive MIMO architectures, [44] does not consider the effect of the RIS on the mmWave channel and models the RIS as an access point with a feed antenna. Similarly, [45] assumes an RIS in the form of a uniform linear array (ULA), which might be difficult to implement in practice. Moreover, the authors deals with point-to-point mmWave links only with ULA-type RISs in [46]. In [47], a scalable optimization framework is presented by considering a large RIS based on a physics-based model. Finally, the optimal placement for the RIS-assisted transmission is discussed in mmWave point-to-point link in [48].

Against this background, we observe that there is an urgent need for a physical, open-source, and widely applicable mmWave channel model to be used in various

RIS-assisted systems in indoor and outdoor environments. Considering that RIS channel modeling is the first step towards standardized RIS-empowered networks, this work aims to create a new line of research by integrating RISs into state-of-the-art 5G physical channel models and provide a solid baseline for practical implementation campaigns with sophisticated RIS designs under the far-field assumption. This work also paves the way for more sophisticated MIMO and time-varying models. Within this context, our major contributions are summarized below:

- By using power scaling laws and the far-field assumption, a fundamental channel model is provided for RIS-empowered systems including multiple scatterers and a baseline cascaded physical channel model.

- Considering the channel modeling strategies of 5G mmWave band transmission with a random number of clusters/scatterers and the characteristics of the RIS, we provide a unified narrowband channel model for RIS-assisted systems in indoor and outdoor environments for the first time. This model includes many physical characteristics such as LoS probability, shadowing effects, and shared clusters. More importantly, our model considers realistic gains and array responses for RIS elements in addition to the existing channel models.

- Using our comprehensive channel model, we demonstrate the potential use-cases and promising gains of RIS-assisted communication in certain setups and provide useful guidelines towards the effective use of RISs.

- We introduce the open-source *SimRIS Channel Simulator* MATLAB package, which can be used in channel modeling of RIS-based systems with tunable operating frequency, terminal locations, number of RIS elements, and environments.

2.2.2 RIS-Assisted Communications: System Model

In this section, we present a simplified and deterministic system model by considering the link power equation and the channel model of an RIS-assisted system with

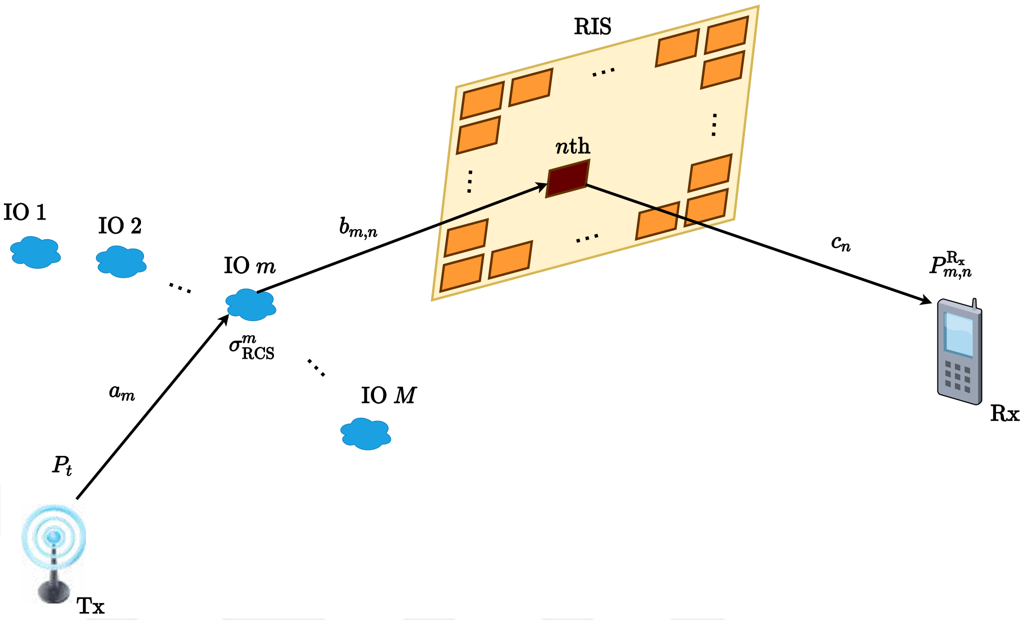

Figure 2.2: RIS-assisted communication with M IOs between Tx-RIS.

obstacles or reflecting/scattering elements (interacting objects, IOs) between the terminals and the RIS. It is assumed that there are M IOs (scatterers) between the transmitter (Tx) and the RIS as shown in Fig. 2.2, while assuming a pure LoS link between the RIS and the receiver (Rx). We also assume unit transmit power and antenna gains for clarity of presentation. Here, a_m, $b_{m,n}$, and c_n respectively stand for the distances between Tx and the mth IO, the mth IO and the nth RIS element, and the nth RIS element and Rx. Furthermore, radar cross section (RCS, in m^2) of the mth IO is shown by σ^m_{RCS}, and the gain of the corresponding RIS element is assumed to be G_e, while a generalized element radiation pattern is considered in the sequel.

Considering the scattering concept for an RIS with N elements and the direct signal component between Tx and Rx (with or without IOs), the received discrete-time baseband (noise-free) signal can be expressed in vector form as

$$y = \left(\mathbf{g}^{\mathrm{T}}\boldsymbol{\Theta}\mathbf{h} + h_{\mathrm{SISO}}\right) x \tag{2.1}$$

where $\mathbf{g} = \left[\sqrt{L_1^{\mathrm{LOS}}}e^{-jkc_1} \ \cdots \ \sqrt{L_N^{\mathrm{LOS}}}e^{-jkc_N}\right]^{\mathrm{T}}$ is the vector of LoS channel coefficients between the RIS and the Rx, $\mathbf{\Theta} = \mathrm{diag}(\begin{bmatrix}\alpha_1 e^{j\phi_1} & \cdots & \alpha_N e^{j\phi_N}\end{bmatrix})$ is the matrix of RIS element responses, $\mathbf{h} = \begin{bmatrix}\sum_{m=1}^{M}\sqrt{L_{m,1}^{\mathrm{RIS}}}e^{-jk(a_m+b_{m,1})} & \cdots & \sum_{m=1}^{M}\sqrt{L_{m,N}^{\mathrm{RIS}}}e^{-jk(a_m+b_{m,N})}\end{bmatrix}$ is the vector of channel coefficients for the Tx-RIS link composed of M scatterers, h_{SISO} characterizes the direct link (narrowband) channel between Tx and Rx, which is equal to $h_{\mathrm{SISO}} = \sqrt{P_{\text{T-R}}}e^{-jkd_{\text{T-R}}}$ for a LoS dominated link, and x is the transmitted signal. Here, $k = 2\pi/\lambda$ is the wave number with λ being wavelength, α_n and ϕ_n respectively represent controllable magnitude and phase response of the nth RIS element, and $L_n^{\mathrm{LOS}} = G_e\lambda^2/(4\pi c_n)^2$ and $L_{m,n}^{\mathrm{RIS}} = G_e\lambda^2\sigma_{\mathrm{RCS}}^m/((4\pi)^3 a_m^2 b_{m,n}^2)$ respectively stand for the path gains of the LoS (RIS-Rx) path and the Tx-IOs-RIS path according to the radar range equation [49]. $P_{\text{T-R}} = \lambda^2/(4\pi d_{\text{T-R}})^2$ stands for the received LoS power with $d_{\text{T-R}}$ being the Tx-Rx distance in the presence of a direct link between Tx and Rx. Therefore, the received power via nth RIS element at the receiver can be obtained as $P_{m,n}^{\mathrm{Rx}} = L_n^{\mathrm{LOS}}L_{m,n}^{\mathrm{RIS}}$. It is worth noting that when the RIS is far from the Tx and the Rx, $b_{m,n}$ and c_n may be assumed to be independent of the RIS element n from the perspective of channel gains, but not from the phases. We also note that the overall path gain (attenuation) is obtained as the product of the path gains of individual paths, which are related by $1/a_m^2$, $1/b_{m,n}^2$, and $1/c_n^2$, respectively.

The signal model of (2.1) can be used to assess the power budget of an RIS-assisted system operating in a more realistic environment with multiple IOs compared to the initial LOS-dominated model of [20]. However, this model again does not capture the variations of the environmental objects and transmit/receiver movements, i.e., based on a static setup.

2.2.3 Physical Channel Modeling: Indoors

In this section, we will build on the signal model developed in the previous section and provide a unified signal/channel model for RIS-assisted 6G communication systems operating under mmWave frequencies. Our model is generic and can be applied to different environments (indoor/outdoor) and operating frequencies. Here, we focus on indoor channel modeling while the outdoor case is covered in the next section.

It is obvious that the deterministic signal model of (2.1) might be useful for a static environment, i.e., when all IOs as well as the Tx and the Rx are stationary. On the other hand, for a dynamic environment, we need to resort to statistical channel models. For instance, for large number of randomly distributed IOs, the summations in the entries of the RIS-assisted channel vector go to complex Gaussian distribution, yielding a Rayleigh-type amplitude distribution for the received signal, even with fixed terminals. However, the RIS-based channel model involves more sophisticated fading phenomena (double Rayleigh) when both terminals are moving.

The important question is how the channel amplitudes and phases can be modeled in a real-world setup involving an RIS with adjustable phase shifts. To answer this question, there is a need for the development of a unified statistical channel model to be used in RIS-assisted communications. For this purpose, we revisit and apply the well-known statistical channel models to our general signal model of (2.1).

Considering the promising potential of RIS-assisted systems for mmWave communications, we build our framework on the clustered statistical MIMO model, which is widely used in 3GPP standardization [50], while a generalization is possible. In the following three subsections, we present our solutions to generate Tx-RIS, RIS-Rx and Tx-Rx subchannels.

2.2.3.1 Tx-RIS Channel (h)

It is assumed that M number of IOs exist in the environment and are grouped to form C independent clusters each of which has S_c number of sub-rays ($c = 1, \ldots, C,$) by satisfying $M = \sum_{c=1}^{C} S_c$ A group of sub-rays that show the same spatial and/or temporal characteristics can be defined as a cluster [51]. Under the clustered model assumption by including path attenuation and array responses, we rewrite the channel between the Tx and RIS ($\mathbf{h} \in \mathbb{C}^{N\times 1}$) as

$$\mathbf{h} = \gamma \sum_{c=1}^{C} \sum_{s=1}^{S_c} \beta_{c,s} \sqrt{G_e(\theta_{c,s}^{\mathrm{RIS}}) L_{\text{T-RIS}}}\ \mathbf{a}(\phi_{c,s}^{\mathrm{RIS}}, \theta_{c,s}^{\mathrm{RIS}}) + \mathbf{h}_{\mathrm{LOS}} \tag{2.2}$$

where $\gamma = \sqrt{\frac{1}{\sum_{c=1}^{C} S_c}}$ stands for a normalization term [50], $\mathbf{h}_{\text{LOS}}$ represents the LoS component, $L_{\text{T-RIS}}$ denote attenuation of the Tx-RIS path, $\beta_{c,s} \sim \mathcal{CN}(0,1)$ represents the complex Gaussian distributed path gain and $G_e(\theta_{c,s}^{\text{RIS}})$ denotes the radiation pattern of RIS element towards the (c,s)th scatterer [52]. Moreover, the array response vector[1] of the RIS for the considered azimuth and elevation arrival angles (with respect to the RIS broadside) is represented by $\mathbf{a}(\phi_{c,s}^{\text{RIS}}, \theta_{c,s}^{\text{RIS}}) \in \mathbb{C}^{N\times 1}$ and expressed as below under uniformly distributed RIS elements with a spacing of d [53]:

$$\mathbf{a}(\phi_{c,s}^{\text{RIS}}, \theta_{c,s}^{\text{RIS}}) = \begin{bmatrix} 1 & \cdots & e^{jkd((\sqrt{N}-1)\sin\theta_{c,s}^{\text{RIS}} + (\sqrt{N}-1)\sin\phi_{c,s}^{\text{RIS}}\cos\theta_{c,s}^{\text{RIS}})} \end{bmatrix}^{\text{T}} \tag{2.3}$$

by satisfying $0 \le x \le \sqrt{N}-1$ and $0 \le y \le \sqrt{N}-1$. In order to calculate the array response vector, the 3D RIS geometry in Fig. 2.3 is used. Here, we count the RIS elements from bottom to up and from right to left, and the RIS element at the origin is considered as the reference. This origin is the first entry of the array response vector given in (2.3).

To model the RIS element radiation $G_e(\theta_{c,s}^{\text{RIS}})$, we consider the $\cos^q$ pattern, which is widely used for reflectarrays as well as feed patterns [52]. In light of this, we consider

$$G_e(\theta_{c,s}^{\text{RIS}}) = 2(2q+1)\cos^{2q}(\theta_{c,s}^{\text{RIS}}), \quad -\pi/2 < \theta_{c,s}^{\text{RIS}} < \pi/2 \tag{2.4}$$

where $2(2q+1)$ is a normalization term used for energy conservation, i.e., the integral of $G_e(\theta_{c,s}^{\text{RIS}})$ over a surface enclosing the element is 4π steradian:

$$\int_{\phi=0}^{2\pi}\int_{\theta=0}^{\pi/2} G_e(\theta)\sin\theta d\theta d\phi = 4\pi \tag{2.5}$$

Although being idealistic, this pattern not only is easy to work with but also presents the major part of the main lobe of many realistic antennas [53]. Following the

[1]The same array response is valid when the RIS is placed either on the xz or yz planes since elevation and azimuth angles are defined with respect to the array broadside not to the axes. However, this array response should be modified if the RIS lies on the xy plane or on another surface that is tilted with respect to the global coordinate system.

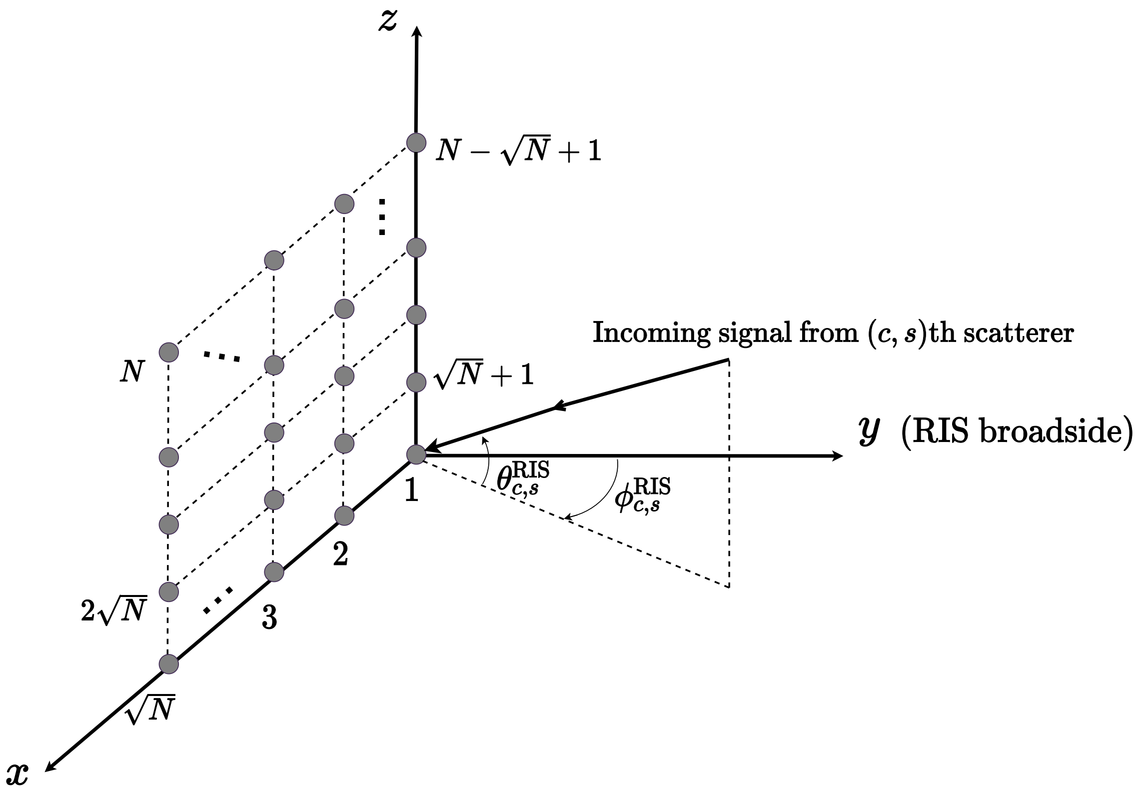

Figure 2.3: The considered array response geometry of the RIS consists of N reflecting elements.

steps of [20], we consider $q = 0.25G_e(0) - 0.5$, where $G_e(0)$ is calculated from $G_e(0) = 4\pi A_e(0)/\lambda^2$. Considering the physical area of an RIS element given by $A_e(0) = (\lambda/2)^2$, we obtain $q = 0.285$, which corresponds to an element gain of $G_e(0) = \pi$ (5 dBi). It is worth noting that although this gain value is consistent with the ones used for patch antennas in practice, the parameter q can be tuned as well by increasing the physical area of RIS elements. We also note that all elements have the same radiation pattern, which is also a reasonable assumption for electrically-large RISs [20].

In our model, the number of clusters (C), number of sub-rays per cluster ($S_c, c = 1, \ldots, C$), and the locations of the clusters can be determined according to the given model and wireless application. As suggested by [51] and the references there-in, the number of clusters in mmWaves is typically modeled by Poisson distribution

$C \sim \mathcal{P}(\lambda_p)$, whose variance λ_p is determined according to a given scenario and operating frequency[2]. As noted in [51, 54], $\lambda_p = 1.8$ can be considered for the 28 GHz band, while $\lambda_p = 1.9$ is a suggested value for 73 GHz. Following [55], we assume that the number of sub-rays for the cth cluster in an integer uniformly distributed between 1 and 30, i.e., $S_c \sim \mathcal{U}[1, 30]$, which is a reasonable assumption for both 28 and 73 GHz bands. For a given reference cluster c, the azimuth departure angles ($\phi_{c,s}^{\mathrm{Tx}}, s = 1, \ldots, S_c$) of the available sub-rays are assumed to be conditionally Laplacian distributed with a mean value ϕ_c^{Tx} following $\mathcal{U}[-\pi/2, \pi/2]$ distribution [54]. Similarly, the elevation departure angles ($\theta_{c,s}^{\mathrm{Tx}}, s = 1, \ldots, S_c$) are conditionally Laplacian with a mean value $\theta_c^{\mathrm{Tx}} \sim \mathcal{U}[-\pi/4, \pi/4]$[3]. The standard deviation (angular spread) of their Laplacian distribution is set to $\sigma_\theta = \sigma_\phi = 5^o$ [56]. Consequently, we have $\phi_{c,s}^{\mathrm{Tx}} \sim \mathcal{L}(\phi_c^{\mathrm{Tx}}, 5)$ and $\theta_{c,s}^{\mathrm{Tx}} \sim \mathcal{L}(\theta_c^{\mathrm{Tx}}, 5)$. All these departure angles are given with respect to the Tx broadside. It is worth noting that our model is generic and all these small-scale fading parameters can be adjusted according to the given environment.

The fundamental difficulty in modeling of a wireless channel involving an RIS arises from the fact that once C clusters, as well as their sub-rays, are randomly generated, the azimuth and elevation arrival angles for an RIS cannot be modeled random as in 3GPP LTE and 5G spatial channel models due to random orientation of mobile receivers. This can be explained by the fact that the orientation of an RIS, which might typically hang on a wall in indoors or facade of a building in outdoors, is deterministic. Furthermore, unless mounted on a car or UAV, an RIS can be also considered a stationary system entity. As a result, the corresponding departure angles -to be used in the calculation of the RIS array response vector in (2.3)- should be calculated considering the random positions of the clusters in channel modeling. This necessities a new approach in mmWave channel modeling for RISs, which will

[2] To ensure that at least one cluster exists in the environment, we consider $C = \max\{1, \mathcal{P}(\lambda_p)\}$.

[3] This modification has been made in the interval of the target uniform distribution to have more evenly distributed clusters, particularly for indoor environments. However, more sophisticated distributions can be considered in our model for azimuth/elevation angles of departure.

be discussed in the sequel.

For simplicity in calculation of link path losses and arrival angles for the RIS, it is assumed that all scatterers in a given cluster c are at the same distance from the Tx, shown by a_c for $c = 1, 2, \ldots, C$. Denoting the length of the Tx-RIS LoS link[4] by $d_{\text{T-RIS}}$, we assume that $a_c \sim \mathcal{U}[1, d_{\text{T-RIS}}]$, however, for clusters whose angle of departure points toward the ground/ceiling or that fall beyond the side walls (in indoor environments), a_c is reduced. Furthermore, the scatterers that fall outside the walls for indoors or underground for outdoors are ignored. The distances[5] between the scatterers and the RIS are shown by $b_{c,s}$ for $c = 1, 2, \ldots, C$ and $s = 1, 2, \ldots, S_c$. For given Tx and RIS coordinates $(x^{\text{Tx}}, y^{\text{Tx}}, z^{\text{Tx}})$ and $(x^{\text{RIS}}, y^{\text{RIS}}, z^{\text{RIS}})$, we have $d_{\text{T-RIS}} = ((x^{\text{RIS}} - x^{\text{Tx}})^2 + (y^{\text{RIS}} - y^{\text{Tx}})^2 + (z^{\text{RIS}} - z^{\text{Tx}})^2)^{1/2}$. Particularly, let us consider that the Tx lies on the yz plane, while the RIS lies either on the xz plane (Scenario 1 - side wall) or yz plane (Scenario 2 - opposite wall). The coordinates of the sth scatterer in cth cluster are calculated by $x^{c,s} = x^{\text{Tx}} + a_c \cos\theta_{c,s}^{\text{Tx}} \cos\phi_{c,s}^{\text{Tx}}$, $y^{c,s} = y^{\text{Tx}} - a_c \cos\theta_{c,s}^{\text{Tx}} \sin\phi_{c,s}^{\text{Tx}}$, and $z^{c,s} = z^{\text{Tx}} + a_c \sin\theta_{c,s}^{\text{Tx}}$ for $c = 1, \ldots, C$ and $s = 1, \ldots, S_c$. From the given coordinates of the scatterers, the distance between each scatterer and the RIS can be easily obtained by $b_{c,s} = ((x^{\text{RIS}} - x^{\text{c,s}})^2 + (y^{\text{RIS}} - y^{\text{c,s}})^2 + (z^{\text{RIS}} - z^{\text{c,s}})^2)^{1/2}$, while the corresponding RIS arrival angles are obtained by $\phi_{c,s}^{\text{RIS}} = I_\phi \tan^{-1} \frac{|x^{\text{RIS}} - x^{c,s}|}{|y^{\text{RIS}} - y^{c,s}|}$ and $\theta_{c,s}^{\text{RIS}} = I_\theta \sin^{-1} \frac{|z^{\text{RIS}} - z^{c,s}|}{b_{c,s}}$, where $I_\phi = \text{sgn}(x^{\text{RIS}} - x^{c,s})$ and $I_\theta = \text{sgn}(z^{c,s} - z^{\text{RIS}})$ for Scenario 1. For Scenario 2, we have $\phi_{c,s}^{\text{RIS}} = I_\phi \tan^{-1} \frac{|y^{\text{RIS}} - y^{c,s}|}{|x^{\text{RIS}} - x^{c,s}|}$ with $I_\phi = \text{sgn}(y^{c,s} - y^{\text{RIS}})$, while the same $\theta_{c,s}^{\text{RIS}}$ of Scenario 1 is valid. Finally, the obtained azimuth and elevation arrival angles ($\phi_{c,s}^{\text{RIS}}$ and $\theta_{c,s}^{\text{RIS}}$) are used in the calculation of the array response vector of (2.3). The considered 3D geometry is given in Fig. 2.4 as a reference for Scenario 1.

For the attenuation of the corresponding path, we adopt the 5G path loss model

---

[4] This does not necessarily mean that there exists a LoS transmission path between the Tx and the RIS.

[5] Without loss of generality, the first RIS element can be taken as a reference under the far case, i.e., $d_{\text{T-RIS}} > N\lambda/2$ for a square RIS. It is worth noting that the RIS is assumed to be lying in the far field of both Tx and Rx terminals.

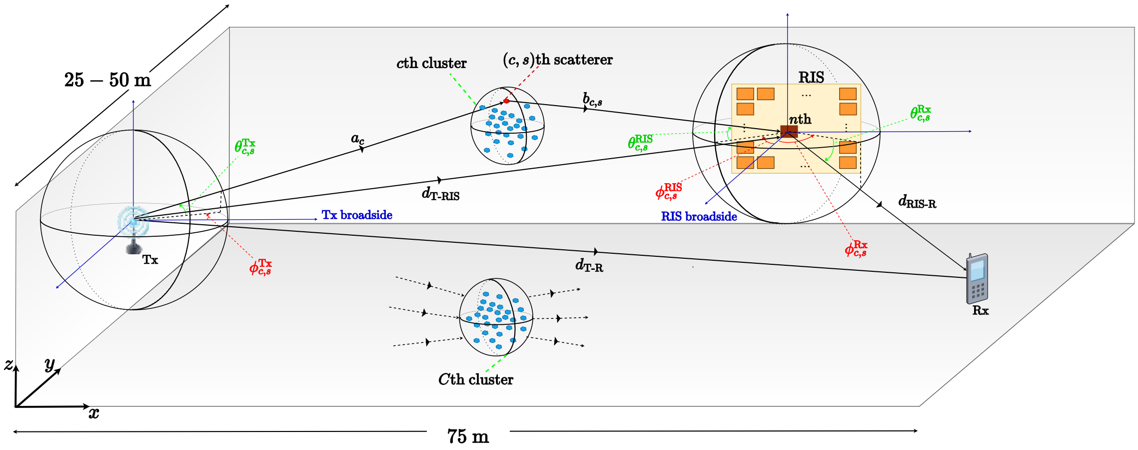

Figure 2.4: Generic InH Indoor Office environment with C clusters between Tx-RIS and an RIS mounted in the xz plane (side wall).

(the close-in free space reference distance model with frequency-dependent path loss exponent, in dB), which is applicable to various environments including Urban Microcellular (UMi) and Indoor Hotspot (InH) as given in [57]:

$$L_{\text{T-RIS}} = -20\log_{10}\left(\frac{4\pi}{\lambda}\right) - 10n\left(1 + b\left(\frac{f - f_0}{f_0}\right)\right)\log_{10}(d_{\text{T-RIS}}) - X_\sigma. \quad (2.6)$$

Here, $d_{\text{T-RIS}}$ is the distance between the Tx and the RIS, n is the path loss exponent, b is a system parameter, and f_0 is a fixed reference frequency (the centroid of all frequencies represented by the path loss model), and $X_\sigma \sim \mathcal{N}(0, \sigma^2)$ is the shadow fading term (also known as the shadow factor [58]) in logarithmic units. We consider the channel parameters reported in [57] for InH Office-NLoS/LoS and UMi Street Canyon-NLOS/LOS, which are summarized in Table 2.2.

Finally, the obtained array response vector and link attenuation for each sub-ray is substituted in (2.2) to generate NLoS components of $\mathbf{h}$. On the other hand, its LoS component is calculated by

$$\mathbf{h}_{\text{LOS}} = I_{\mathbf{h}}(d_{\text{T-RIS}})\sqrt{G_e(\theta^{\text{RIS}}_{\text{LOS}})L_{\text{T-RIS}}}e^{j\eta}\mathbf{a}(\phi^{\text{RIS}}_{\text{LOS}}, \theta^{\text{RIS}}_{\text{LOS}}) \quad (2.7)$$

where $G_e(\theta^{\text{RIS}}_{\text{LOS}})$ is the RIS element gain in the LoS direction, $\mathbf{a}(\phi^{\text{RIS}}_{\text{LOS}}, \theta^{\text{RIS}}_{\text{LOS}})$ is the array response of the RIS in the direction of the Tx, and $\eta \sim \mathcal{U}[0, 2\pi]$ is the random

Table 2.2: Path Loss Parameters

Scenario	*Parameters*
InH Indoor Office (NLOS)	$n = 3.19$, $\sigma = 8.29$ dB, $b = 0.06$, $f_0 = 24.2$ GHz
InH Indoor Office (LOS)	$n = 1.73$, $\sigma = 3.02$ dB, $b = 0$
UMi Street Canyon (NLOS)	$n = 3.19$, $\sigma = 8.2$ dB, $b = 0$
UMi Street Canyon (LOS)	$n = 1.98$, $\sigma = 3.1$ dB, $b = 0$

phase term. Here $I_{\mathbf{h}}(d_{\text{T-RIS}})$ is a Bernoulli random variable taking values from the set $\{0, 1\}$, characterizes the existence of a LoS link for a Tx-RIS separation of $d_{\text{T-RIS}}$. Denoting the frequency independent LoS probability by p, i.e., $P(I_{\mathbf{h}} = 1) = p$, we can resort to the 5G channel model [57] to obtain

$$p = \begin{cases} 1 & d_{\text{T-RIS}} \leq 1.2 \\ e^{-\left(\frac{d_{\text{T-RIS}}-1.2}{4.7}\right)} & 1.2 < d_{\text{T-RIS}} \leq 6.5 \\ 0.32e^{-\left(\frac{d_{\text{T-RIS}}-6.5}{32.6}\right)} & d_{\text{T-RIS}} > 6.5. \end{cases} \tag{2.8}$$

It is worth noting that the LoS probabilities of (2.8) are reported based on intensive measurements in various indoor office environments, most probably, for Rxs at a height of 1-1.5 m and decays very fast with increasing distance. Consequently, for the link between the Tx and the RIS, we resort to (2.8) if the RIS is located below the level of Tx ($z^{\text{RIS}} < z^{\text{Tx}}$), while we assume $p = 1$ for $z^{\text{RIS}} \geq z^{\text{Tx}}$ regardless of $d_{\text{T-RIS}}$. In other words, if the height of the RIS is not smaller than that of the Tx, we assume a clear LoS path between them, which is a reasonable assumption for any choice of $d_{\text{T-RIS}}$.

2.2.3.2 RIS-Rx Channel ($\mathbf{g}$)

In our indoor communications model, to simply our initial analyses, we assume that the RIS and the Rx are sufficiently close together to have a clear LoS link without noticeable NLOS components in between. According to (2.8), a LOS probability of greater than 50% is achieved when the inter-terminal distance is less 4.5 m. We later relax the LoS dominated channel conditions between the RIS and the Rx for outdoor setups.

For the calculation of LOS-dominated RIS-Rx channel $\mathbf{g}$, we re-calculate the RIS array response from (2.3) in the direction of the Rx by calculating azimuth and elevation departure angles $\phi_{\text{Rx}}^{\text{RIS}}$ and $\theta_{\text{Rx}}^{\text{RIS}}$ for the RIS from the coordinates of the RIS and the Rx[6]. The attenuation of these N LoS paths ($L_{\text{RIS-R}}$) is calculated from (2.6) by replacing $d_{\text{T-RIS}}$ with $d_{\text{RIS-R}}$ along with other channel related parameters. The gain of RIS elements is again reflected to $\mathbf{g}$ by considering departure elevation angle $\theta_{\text{Rx}}^{\text{RIS}}$ in (2.4). Finally, with $\eta \sim \mathcal{U}[0, 2\pi]$, the vector of LoS channel coefficients can be generated as

$$\mathbf{g} = \sqrt{G_e(\theta_{\text{Rx}}^{\text{RIS}}) L_{\text{RIS-R}}} e^{j\eta} \mathbf{a}(\phi_{\text{Rx}}^{\text{RIS}}, \theta_{\text{Rx}}^{\text{RIS}}). \tag{2.9}$$

2.2.3.3 Tx-Rx Channel (h_{SISO})

The RIS-assisted channel has a double-scattering nature, as a result, the single-scattering link between the Tx and Rx has to be taken into account in our channel model. As will be discussed later, even if the RIS is placed near the Rx, the Tx-Rx channel is relatively stronger than the RIS-assisted path, and cannot be ignored in the channel model.

Since we assume that the RIS and the Rx are relatively closer with a clear LoS path, we may assume that they experience the same clusters. In other words,

[6] For given RIS and Rx coordinates $(x^{\text{RIS}}, y^{\text{RIS}}, z^{\text{RIS}})$ and $(x^{\text{Rx}}, y^{\text{Rx}}, z^{\text{Rx}})$, we have $d_{\text{RIS-R}} = ((x^{\text{Rx}} - x^{\text{RIS}})^2 + (y^{\text{Rx}} - y^{\text{RIS}})^2 + (z^{\text{Rx}} - z^{\text{RIS}})^2)^{1/2}$. For both scenarios, we obtain $\theta_{\text{Rx}}^{\text{RIS}} = I_\theta \sin^{-1} \frac{|z^{\text{Rx}} - z^{\text{RIS}}|}{d_{\text{RIS-R}}}$ for $I_\theta = \text{sgn}(z^{\text{Rx}} - z^{\text{RIS}})$. However, for Scenario 1, we have $\phi_{\text{Rx}}^{\text{RIS}} = I_\phi \tan^{-1} \frac{|x^{\text{Rx}} - x^{\text{RIS}}|}{|y^{\text{Rx}} - y^{\text{RIS}}|}$ for $I_\phi = \text{sgn}(x^{\text{RIS}} - x^{\text{Rx}})$, and for Scenario 2, we have $\phi_{\text{Rx}}^{\text{RIS}} = I_\phi \tan^{-1} \frac{|y^{\text{Rx}} - y^{\text{RIS}}|}{|x^{\text{Rx}} - x^{\text{RIS}}|}$ for $I_\phi = \text{sgn}(y^{\text{Rx}} - y^{\text{RIS}})$.

it is assumed that the distance between the RX and the RIS is smaller than the correlation distance (stationarity interval [57]) in indoor environments so that they have common clusters. This also allows us to model the potential correlation between the channels of RIS and the Rx through shared clusters [59].

Using SISO mmWave channel modeling, the channel between these two terminals can be easily obtained (by ignoring arrival and departure angles) as

$$h_{\text{SISO}} = \gamma \sum_{c=1}^{C} \sum_{s=1}^{S_c} \beta_{c,s} e^{j\eta_e} \sqrt{L_{\text{SISO}}} + h_{\text{LOS}} \tag{2.10}$$

where γ, C, S_c, and $\beta_{c,s}$ are as defined in (2.2) and remain the same for the Tx-Rx channel under the assumption of shared clusters with the Tx-RIS channel, while h_{LOS} is the LoS component. Here, L_{SISO} stands for the path attenuation for the Tx-Rx link and η_e is the excess phase caused by different travel distances of Tx-RIS and Tx-Rx links over the same scatterers[7]. L_{SISO} is calculated from (2.6) by considering the same shadow factors. Similarly, h_{LOS} is generated considering the link attenuation for $d_{\text{T-R}}$ if a LoS exists between Tx and the RIS, i.e., we assume that due to relatively close separation of the RIS and the Rx, they simultaneously experience LoS signals with a probability of p (2.8). However, if the RIS is positioned at a higher height to have a LoS link with the Tx, we calculate p independently for h_{SISO}.

2.2.4 Physical Channel Modeling: Outdoors

The comprehensive mmWave channel modeling method of the previous section can be easily extended to outdoor environments by modifying certain system parameters. Differences in the positions of the RIS and terminals in an outdoor environment will cause changes in channel parameters, while following the same channel modeling strategy. Particularly, path loss exponent n and shadow fading parameter σ in (2.6) can be adjusted according to the given outdoor propagation environment. In terms of small-scale fading, only for the clusters whose angle of departure points toward the

[7]Denoting the distances from the RIS and the Rx to the (c, s)th scatterer by $b_{c,s}$ and $\tilde{b}_{c,s}$, respectively, we have $\eta_e = k(b_{c,s} - \tilde{b}_{c,s})$.

ground, we may reduce the maximum distance by considering terminal distances in the outdoor environment. It is worth noting that our model assumes the placement of the RIS on xz and yz planes, while certain modifications can be made in the array responses and azimuth/elevation angle calculations for the placement of the RIS on the xy plane (on the ground or the roof) or for other tilted/rotated RIS orientations. Following the same steps of Section III.A, $\mathbf{h}$ can be easily generated.

The major change in contrast to our indoor channel model will be in the channel between the RIS and the Rx, which might be subject to small-scale fading as well in outdoor environments with a random number of unique clusters. The LOS-dominated channel of (2.9) may be still useful when the distance between the RIS and the Rx is relatively short with a high LoS probability. However, for the general case, we have

$$\mathbf{g} = \bar{\gamma} \sum_{c=1}^{\bar{C}} \sum_{s=1}^{\bar{S}_c} \bar{\beta}_{c,s} \sqrt{G_e(\theta_{c,s}^{\mathrm{Rx}}) L_{\text{RIS-R}}}\, \mathbf{a}(\phi_{c,s}^{\mathrm{Rx}}, \theta_{c,s}^{\mathrm{Rx}}) + \mathbf{g}_{\mathrm{LOS}} \tag{2.11}$$

where, similar to (2.2), $\bar{\gamma}$ is a normalization term, $\bar{C}$ and $\bar{S}_c$ stand for number of clusters and sub-rays per cluster for the RIS-Rx link, $\bar{\beta}_{c,s}$ is the complex path gain, $L_{\text{RIS-R}}$ is the path attenuation, $G_e(\theta_{c,s}^{\mathrm{Rx}})$ is the RIS element radiation pattern in the direction of the (c, s)th scatterer, $\mathbf{a}(\phi_{c,s}^{\mathrm{Rx}}, \theta_{c,s}^{\mathrm{Rx}})$ is the array response vector of the RIS for the given azimuth and elevation angles, and $\mathbf{g}_{\mathrm{LOS}}$ is the LoS component. Similar steps of the previous section can be followed to generate $\mathbf{g}$ in fading environments[8]. Different from indoor scenarios, the LoS probability is also modified as [57]

$$p = \min(20/d, 1)(1 - e^{-d/39}) + e^{-d/39} \tag{2.12}$$

where $d \in \{d_{\text{T-RIS}}, d_{\text{RIS-R}}, d_{\text{T-R}}\}$. This model is adopted from 3GPP/ITU standards and does not include the receiver height as other urban macrocellular models [60]. Furthermore, this model considers ground-level Rxs, which might not completely hold for RIS-assisted links. Nevertheless, since the Tx-RIS and RIS-Rx link lengths

[8]We assume a reduced interval ($[\pi/4, \pi, 4]$) for the uniform distribution of the mean angle of departure (in azimuth) to ensure that all scatters are within the field of view of the RIS, i.e., not to have scatterers at the back of the RIS.

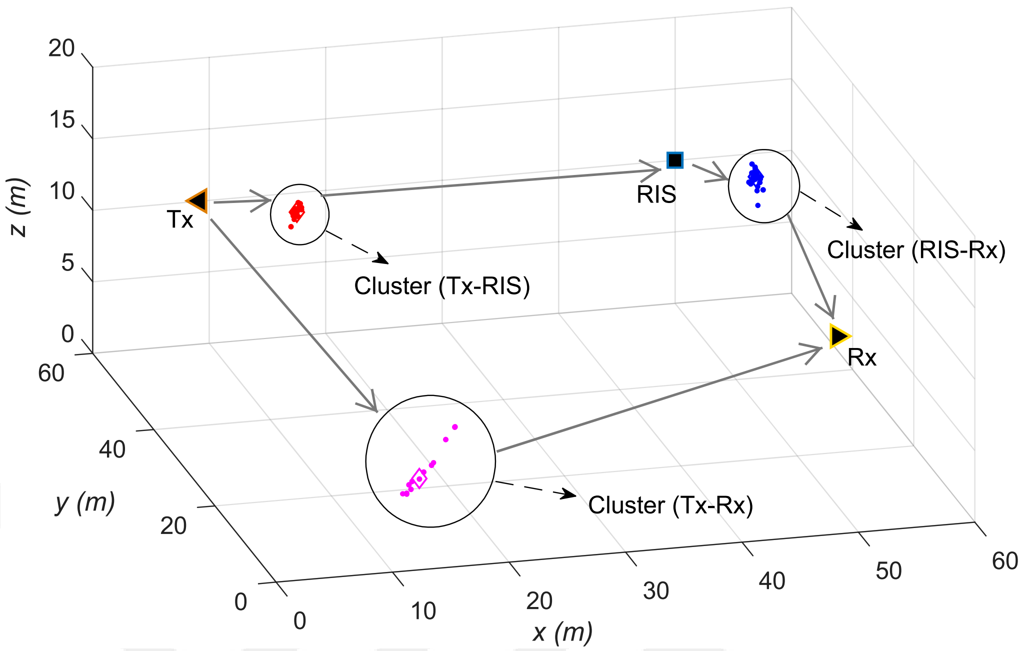

Figure 2.5: The considered UMi Street Canyon outdoor environment with random number of clusters/scatterers and an RIS on the xz plane.

are typically larger compared to indoor environments, it is taken as a reference to model the worst-case scenario, while a higher LoS probability is expected for Tx-RIS and RIS-Rx links.

For outdoor environments, we assume that the RIS and the Rx are not too close to ensure that they have independent clusters (small scale parameters) as in the 3GPP 3D channel model [50]. In other words, the distance between the Rx and the RIS is not smaller than the correlation distance so that they do not have common clusters. Using SISO mmWave channel modeling, the Tx-Rx channel can be easily obtained (by ignoring arrival and departure angles once more) as

$$h_{\text{SISO}} = \tilde{\gamma} \sum_{c=1}^{\tilde{C}} \sum_{s=1}^{\tilde{S}_c} \tilde{\beta}_{c,s} \sqrt{L_{\text{SISO}}} + h_{\text{LOS}} \tag{2.13}$$

An example realization of the considered 3D geometry for UMi Street Canyon outdoor environment is given in Fig. 2.5 for Scenario 1, where the Tx is mounted at a height of 20 m, while the Rx is a ground-level user. In this specific 3D geometry, each path has a single cluster with a different number of scatterers, while the number of clusters for each path varies randomly in general.

2.2.5 On RIS-Assisted Channel Modeling with SimRIS

In this section, we first summarize the major steps of RIS-assisted channel modeling for indoor and outdoor environments of the previous two sections and then introduce the open-source *SimRIS Channel Simulator*.

The steps of RIS-assisted channel modeling can be summarized as below. Here, steps 1-5 focus on the generation of $\mathbf{h}$, while Steps 6-7 and Step 8 respectively deal with $\mathbf{g}$ and h_{SISO}:

1. Give the coordinates of the Tx/Rx and the RIS. Then calculate the direct link distance $d_{\text{T-RIS}}$ between the Tx and the RIS. Calculate the LoS probability for this link and generate the LoS component of $\mathbf{h}$ accordingly using $\phi_{\text{LOS}}^{\text{Tx}}$ and $\theta_{\text{LOS}}^{\text{Tx}}$.

2. Determine the number of clusters C and sub-rays S_c for $c = 1, \dots, C$. Generate azimuth and elevation departure angles $\phi_{c,s}^{\text{Tx}}$ and $\theta_{c,s}^{\text{Tx}}$, and the distances between the Tx and the clusters.

3. Calculate the distances between scatterers and the RIS $b_{c,s}$. Calculate the angles of arrival $\phi_{c,s}^{\text{RIS}}$ and $\theta_{c,s}^{\text{RIS}}$ for the RIS with respect to the RIS broadside.

4. Calculate the array response vector $\mathbf{a}(\phi_{c,s}^{\text{RIS}}, \theta_{c,s}^{\text{RIS}})$ for all c and s.

5. Calculate the link attenuation $L_{\text{T-RIS}}$ for given system parameters and complex path gains $\beta_{c,s}$. Generate the vector of channel coefficients $\mathbf{h}$ for the Tx-RIS link.

6. Calculate the LoS distance $d_{\text{RIS-R}}$ as well as LoS azimuth and elevation departure angles $\phi_{\text{Rx}}^{\text{RIS}}$ and $\theta_{\text{Rx}}^{\text{RIS}}$ for the RIS.

7. For indoor environments, re-calculate the array response vector by $\phi_{\text{Rx}}^{\text{RIS}}$ and $\theta_{\text{Rx}}^{\text{RIS}}$, and generate the vector of LoS channel coefficients $\mathbf{g}$ between the RIS

and the Rx. For outdoor environments, determine the number of clusters $\bar{C}$ and sub-rays $\bar{S}_c$ and repeat corresponding procedures under Steps 2-5 (without calculating arrival angles and array response (Step 4) at the Rx due to its single antenna) for the RIS-Rx channel by also considering its LoS component.

8. Generate the direct link channel coefficient h_{SISO} by considering the same clusters with the Tx-RIS link for indoors and independent clusters for outdoors. For indoors, calculate the excess phase η_e and link distances only to obtain h_{SISO}. For outdoors, determine the number of clusters $\tilde{C}$ and sub-rays $\tilde{S}_c$ and generate h_{SISO}. Consider its LoS component for all cases.

9. Considering the matrix of RIS responses $\mathbf{\Theta}$ (to be discussed in Section VI), generate the overall channel coefficient $h = \mathbf{g}^{\text{T}}\mathbf{\Theta}\mathbf{h} + h_{\text{SISO}}$.

Following the main steps given above, for InH Indoor Office and UMi Street Canyon environments, $\mathbf{h}$, $\mathbf{g}$ and h_{SISO} channels can be produced by performing Monte Carlo simulations at 28 and 73 GHz frequencies in *SimRIS Channel Simulator* [34]. Number of RIS elements (N) and number of channel realizations can be defined as user-selectable parameters as well as the Tx, Rx and RIS locations by considering our 3D geometry. Furthermore, the RIS position can be selected for xz plane (side wall) or yz plane (opposite wall) for both environments. *SimRIS Channel Simulator* MATLAB package is provided as a companion of this work, and interested readers are referred to [34] for the details of channel generation and the use of this simulator.

2.2.6 Numerical Results

In this section, we provide comprehensive numerical results to test our new channel model for RIS-empowered communication using the open-source SimRIS Channel Simulator MATLAB package [34]. We consider the operating frequencies of 28 and 73 GHz, since considered system parameters are valid both these bands. The noise power is assumed to be -100 dBm.

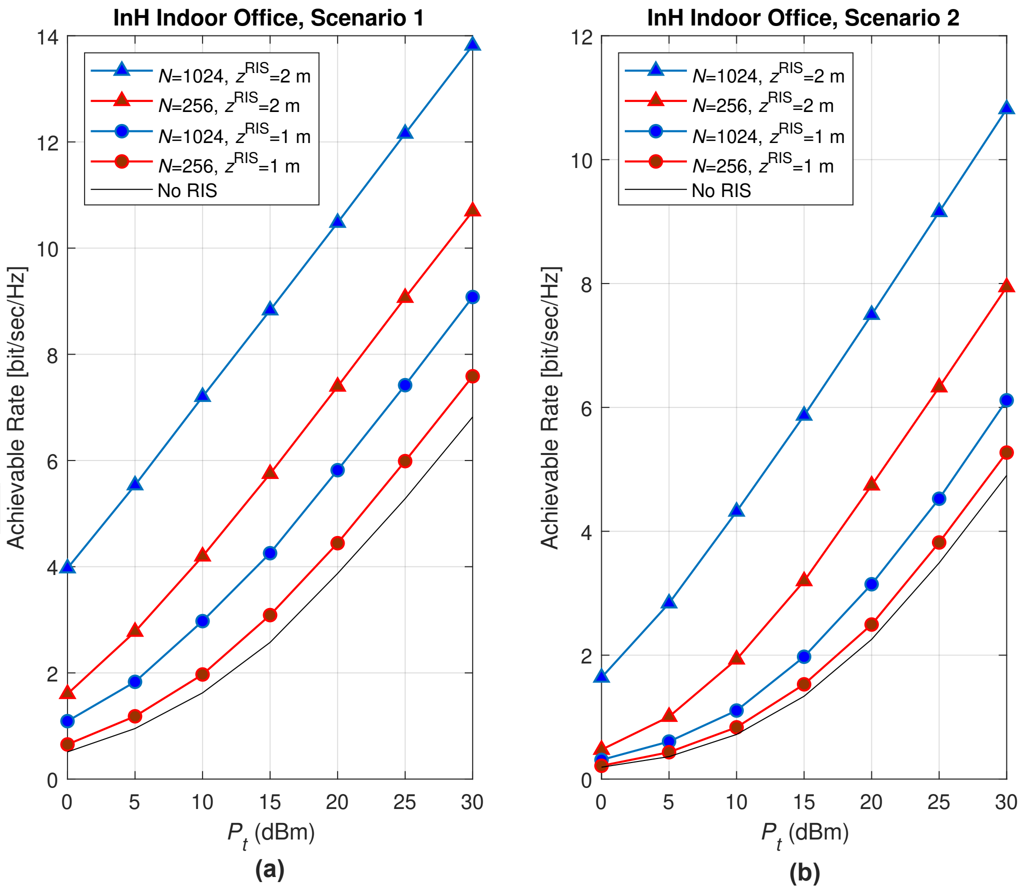

Figure 2.6: Achievable rates of RIS-assisted systems for indoors under (a) Scenario 1 and (b) Scenario 2.

In Figs. 2.6(a) and (b), we evaluate the (ergodic) achievable rate (R) of a communication system with and without an RIS operating in indoor environments for $N = 256$ and 1024 at 28 GHz under the far-field conditions. Here R is defined as $R = \mathrm{E}\{\log_2(1+\rho)\}$ [bits/s/Hz], where $\mathrm{E}\{.\}$ is the expectation. In Fig. 2.6(a), we consider Scenario 1 where the RIS is mounted on the side wall and the coordinates of the Tx, the Rx, and the RIS are respectively given as $(0, 25, 2)$, $(38, 48, 1)$, $(40, 50, z^{\mathrm{RIS}})$. Similarly, in Fig. 2.6(b), we consider Scenario 2 with the Tx, the Rx, and the RIS coordinates given by $(0, 25, 2)$, $(65, 35, 1)$, and $(70, 30, z^{\mathrm{RIS}})$, respectively. Here, we consider two different RIS placements: RIS mounted at a moderate height of $z^{\mathrm{RIS}} = 1$ m and at a higher height of $z^{\mathrm{RIS}} = 2$ m. For these given parameters, we have $d_{\text{RIS-R}} \in \{2.82, 3\}$ m and $d_{\text{RIS-R}} \in \{7.07, 7.14\}$ m for Scenarios 1 and 2, respectively, which are valid assumptions to have a pure LoS link between the RIS and the Rx. As seen from Figs. 2.6(a) and (b), for the case of $z^{\text{RIS}} = 1$ m, since the LoS probability is relatively low for the Tx-RIS link, which has a LoS distance of 47.1 m, the RIS provides only a minor improvement in the received SNR. The reason of this behavior can be explained by the relatively higher attenuation of the RIS-assisted channel compared to the channel between Tx-Rx. However, a major improvement is observed for the case of $z^{\text{RIS}} = 2$ m, which assumes a LOS-dominated Tx-RIS link as discussed after (2.8). Finally, a noticeable degradation is observed in Fig. 2.6(b) due to larger Tx-Rx/RIS separations, which further degrades the benefits of the RIS for $z^{\text{RIS}} = 1$ m. From the given results of Fig. 2.6, we conclude that the RIS can be used as an effective tool to boost the achievable rate in indoor environments when both the Tx-RIS and RIS-Rx links are LoS dominated.

In Figs. 2.7(a) and (b), we investigate the effect of phase imperfections on the achievable rates of an RIS-assisted system in InH Indoor Office environment at 73 GHz under the far-field assumption. Considering Scenario 1, the Tx and the Rx are located as in Fig. 2.6(a) while the coordinates of RIS are given by $(40, 50, 2)$. In Fig. 2.7(a), under $N = 64$ and 256, we compare the achievable rates of RIS-assisted systems for discrete phase shifts with 1 and 2 controlling bits and, ideal-continuous phase shifts over $[-\pi, \pi]$. As clearly seen, the quantization level affects the achievable rate of the system, and for increased N values, the effect of quantization errors becomes more visible. In addition, the disruptive effect of imperfect phase knowledge on the system performance is observed in Fig. 2.7(b) for $N = 256$. Here, the concentration parameter κ is inversely proportional to estimation accuracy. Although the phase estimation and quantization errors cause degradation in achievable rate performance, the constructive effect of the RIS-controlled channel on the system remains favorable.

In Fig. 2.8, we investigate the system achievable rate for 10 test points within a 10 m azimuth distance of the RIS for Scenario 2, where $N = 256$ and $P_t = 30$ dBm are considered. Here we assume that our LoS dominated RIS-Rx channel of (2.9)

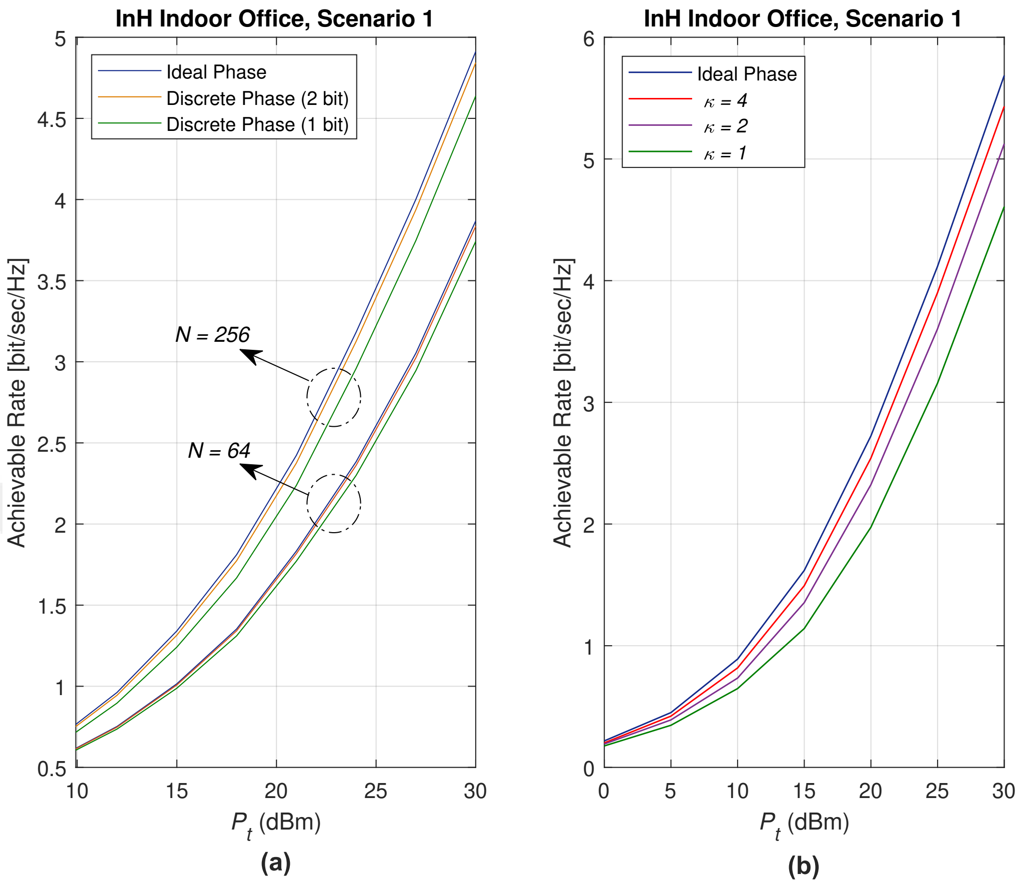

Figure 2.7: Achievable rates of RIS-assisted systems with (a) discrete phase shifts and (b) imperfect phase knowledge for InH Indoor Office environment.

is still valid in the considered environment, which might be in the form of a open office. $(x^{\text{Rx}}, y^{\text{Rx}})$ coordinates of the test points are marked on Fig. 2.8, while z^{Rx} is fixed to 1 m for all points. The coordinates of the Tx and the RIS (Scenario 2) are given respectively as $(0, 25, 2)$ and $(75, 25, 2)$, where the distances between the RIS and test points vary between $\sqrt{13.5}$ and $\sqrt{101}$ m. In this setup, the RIS has a clear LoS path with the Tx, and reflects the incoming signals in an effective way to boost the rate. As seen from Fig. 2.8, a significant improvement is obtained in R with an RIS, particularly for the test points closer to the RIS. We observe that even at a 10 m azimuth distance from the RIS, around 1.6 bits/s/Hz improvement can be provided by an RIS. We further observe that R is quite sensitive to the length of

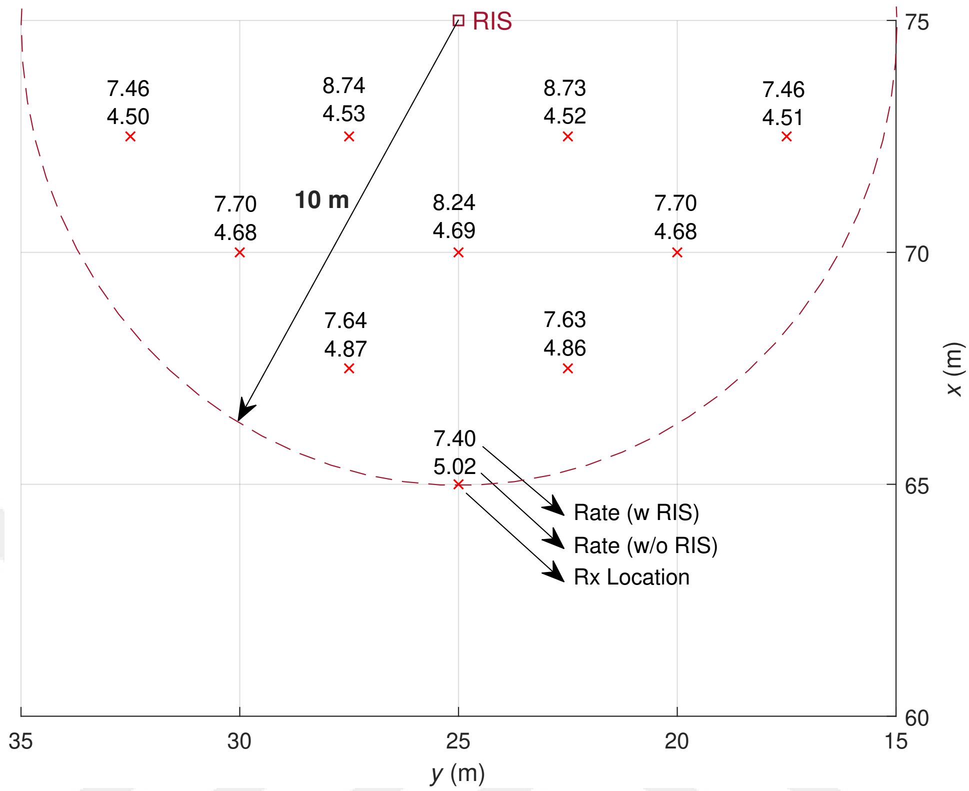

Figure 2.8: Top view of the considered test scenario with 10 reference points along with achievable rate values.

the RIS-Rx link by varying up to 1.35 bits/s/Hz and might be identical for certain points due to our symmetrical setup (aligned Tx-RIS link).

In Figs. 2.9(a) and 2.9(b), the effect of varying Rx positions on the achievable rate of an RIS-assisted system at 28 GHz is examined for a UMi Street Canyon outdoor environment. Here, we consider Scenario 1 where the RIS is mounted on the side wall and the coordinates of the Tx, the Rx, and the RIS are respectively given as $(0, 25, 20)$, $(x^{\mathrm{Rx}}, y^{\mathrm{Rx}}, 1)$, $(70, 85, 10)$. In Fig. 2.9(a), the direct link between the Tx-Rx is available as well as the RIS-assisted link for transmission, while it is assumed that the direct link between Tx-Rx is blocked in Fig. 2.9(b). In Fig. 2.9(a), we observe that the highest achievable rate is obtained where the Rx is close to the Tx, since the channel between Tx-Rx is more dominant than the RIS-assisted link in terms of achievable rate. Furthermore, if the Rx moves to an area far from the RIS on x and y-axes, the effect of the RIS will drastically diminish as shown in Fig.

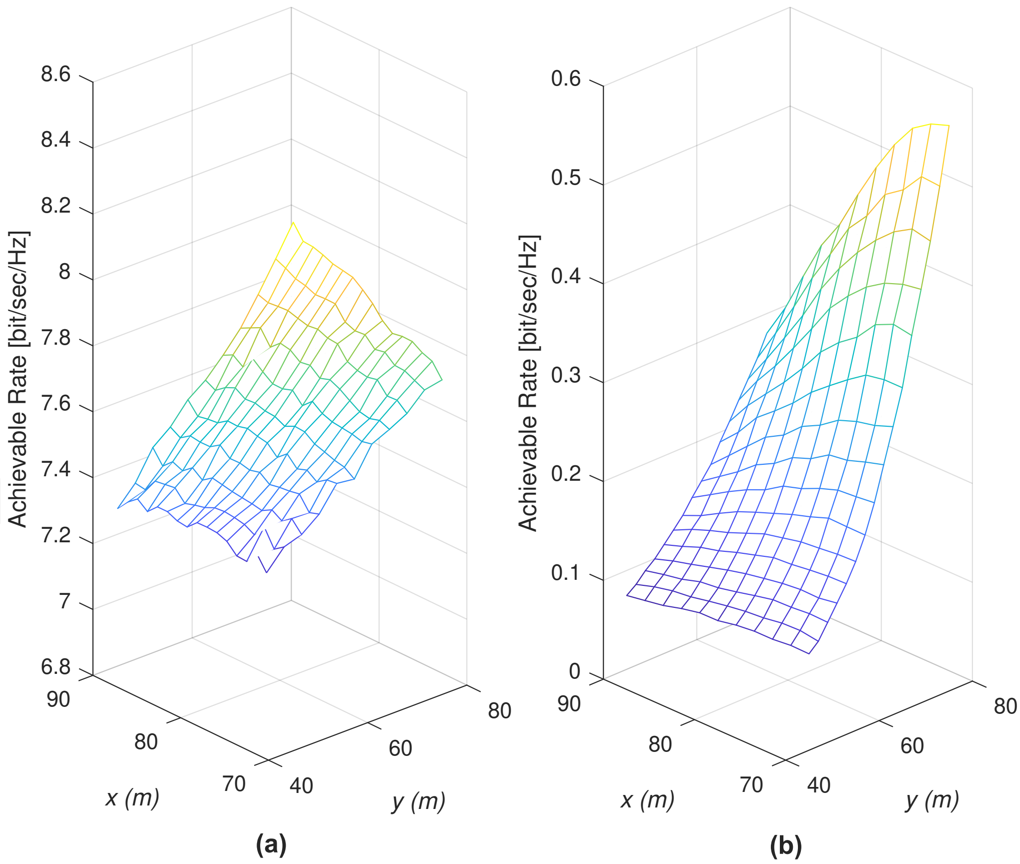

Figure 2.9: Achievable rates of the an RIS-assisted system under varying Rx positions in an outdoor environment in the presence (a) and absence (b) of the direct link between the Tx-Rx.

2.9(b). We also observe that the most critical system parameter is the separation between RIS-Rx when the direct link between Tx-Rx is blocked.

In Fig. 2.10, the effect of the RIS position on the achievable rate is examined in the absence of a direct path between Tx-Rx in an outdoor environment for $N =$ 64, 256 and 1024. Considering Scenario 1 and UMi Street Canyon model at 28 GHz, the coordinates of the Tx, the Rx, and the RIS are respectively given as $(0, 25, 20)$, $(50, 50, 1)$, $(x^{\mathrm{RIS}}, 60, 10)$. As clearly seen in Fig. 2.10, a noticeable increase in achievable rate is obtained at regions where the RIS is closely aligned with the Rx on the x-axis. Moreover, when the RIS moves away from the Rx and the Tx, a substantial decrease in achievable rate is observed and reliable transmission cannot

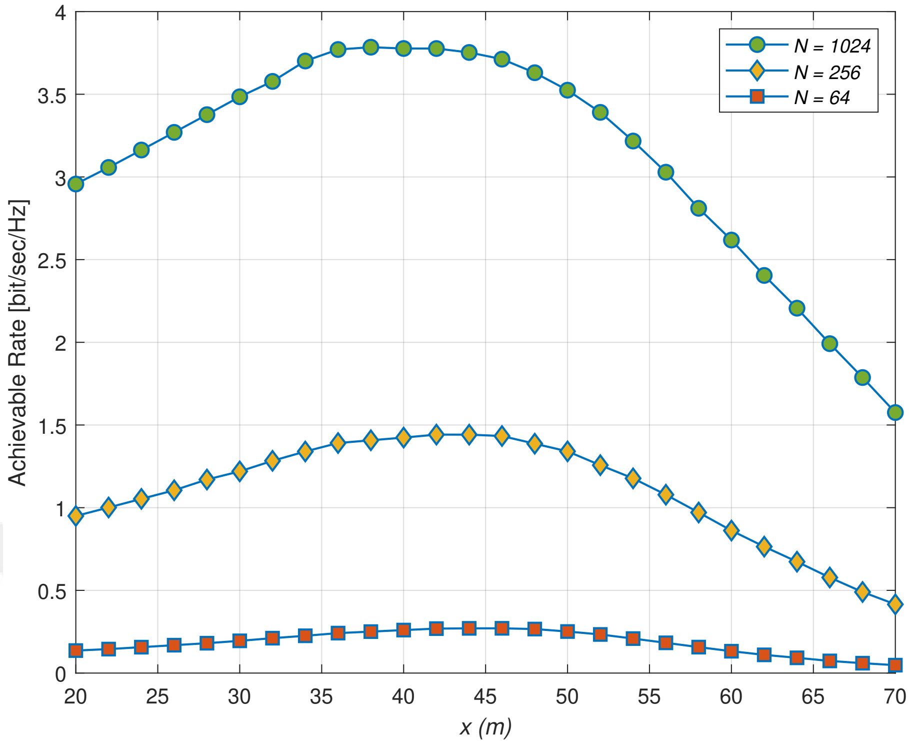

Figure 2.10: Achievable rate of the an RIS-assisted system under varying RIS positions in an outdoor environment.

be guaranteed. We conclude that in outdoors, the most effective scenario is obtained when $d_{\text{RIS-R}}$ is kept less than 15 m.

Another important scenario that should be considered when designing an RIS-assisted system is the placement of the RIS in the near-field of the Rx. If N increases considerably, the far-field assumption is no longer valid and near-field conditions should be considered to investigate the performance. Placing the RIS in the near-field of the Rx will lead to a pure LoS link between the RIS and Rx. In Fig. 2.11, we evaluate the achievable rate of an RIS-assisted communication system operating in indoor environments for varying N values at 28 GHz under near-field conditions. Here, the channel gain for the RIS-Rx link is approximated as in [61]. Moreover, we consider Scenario 1 where the RIS is mounted on the side wall, and the coordinates of the Tx, the Rx, and the RIS are respectively given as $(0, 25, 2)$, $(55, 35, 1)$, $(50, 30, 2)$. As clearly seen, increasing N values provide a significant improvement

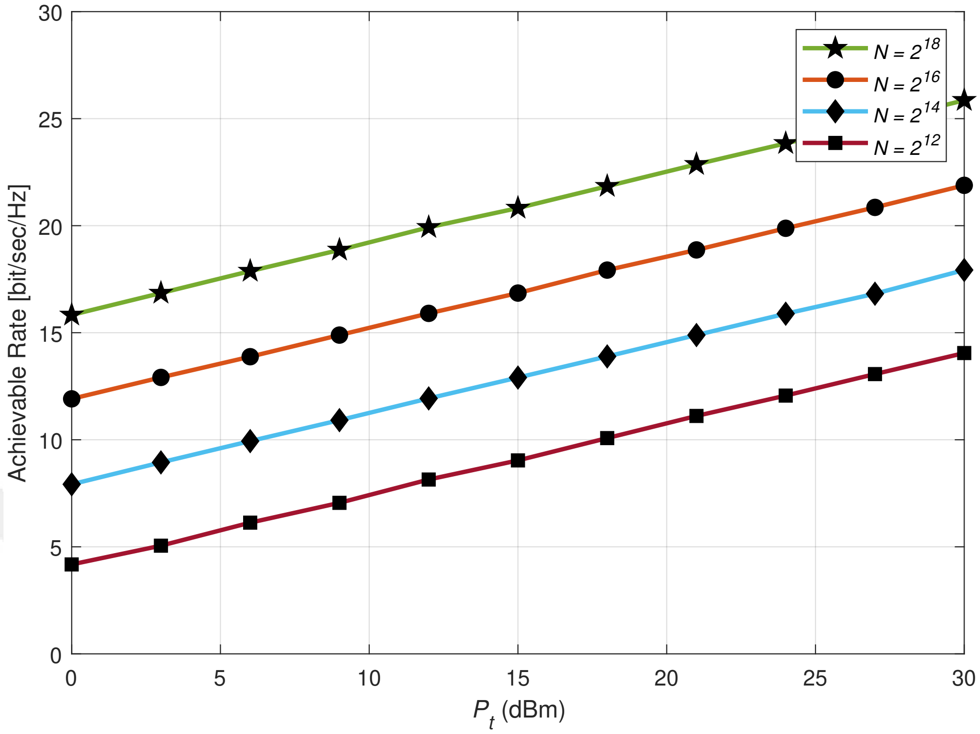

Figure 2.11: Achievable rate of the an RIS-assisted system under the near-field assumption in an indoor environment.

in the achievable rate even in the near-field conditions. As seen from Fig. 2.11, a decrease of approximately 10 dB is obtained in P_t when the N value is quadrupled, while a decrease of approximately 15 dB is obtained in the far-field case as seen from Fig. 2.6(a). From the given results, we conclude that the effect of increasing N value in the far-field conditions is more dominant than the near-field conditions, and the provision of far-field conditions will be beneficial when designing the RIS-assisted communication system at mmWave frequencies.

2.2.7 Conclusions

This study has been a first step towards physical channel modeling with RIS-empowered networks and aimed to create a new line of research for wireless researchers. Our SimRIS Channel Simulator package can be used effectively in Monte Carlo simulations to assess the capacity, SNR gain, secrecy, outage and error performance of RIS-assisted systems by providing cascaded channel coefficients separately. We also note that our channel modeling methodology can be easily extended for multi-carrier cases by considering time delays of each particular path. Our future research questions are summarized below: *i)* What about the delay spread? Can an RIS reduce the delay spread in wideband channel models? *ii)* What is the statistical distribution of the composite channel (h)? While we expect it to follow Gaussian distribution due to the Central Limit Theorem, what is the influence of an RIS? *iii)* How fast h changes and what effect will this have on correlation? Can the RIS slow down (or speed up) the rate of change of h? *v)* How realistic? Extensive measurements are required to obtain more realistic system parameters for RIS-assisted links.

2.3 Reconfigurable Intelligent Surfaces for Future Wireless Networks: A Channel Modeling Perspective

2.3.1 Introduction

The wireless community is witnessing very exciting period in which the standardization and commercialization of 5G has been completed, and academia and industry have set their sights on 6G wireless technologies of 2030 and beyond by starting active research campaigns. According to July 2020 white work of Samsung Research [10], three key services will dominate 6G: truly immersive extended reality (XR), high-fidelity mobile hologram, and digital replica. These interesting and advanced multimedia services will require a peak data rate of 1,000 Gbps and a user experienced data rate of 1 Gbps with an air latency less than 0.1 ms. These highly challenging performance requirements of 6G urged the researchers to investigate alternative solutions in the physical layer (PHY) of future wireless networks. Within this context, promising solutions such as energy harvesting, optical wireless communications, communications with intelligent surfaces, aerial communications, cell-free massive multiple-input multiple-output (MIMO) systems, full-duplex communications, and Terahertz communications have been put forward in recent years [11].

At this point, the concept of communications with *reconfigurable intelligent surfaces (RISs)* stands out as a strong candidate due to its undeniable potential in realizing truly pervasive networks by re-engineering and recycling the electromagnetic (EM) waves.

It is an undeniable fact that a level of saturation has been reached in current wireless systems despite the use of sophisticated PHY techniques such as adaptive modulation and coding, multi-carrier signaling, large-scale MIMO systems, relaying, beamforming, reconfigurable antennas and so on. As a result, next-generation wireless systems require a radical transformation to satisfy the unprecedented demands of 6G networking by enabling software control, not only in the network layer as in 5G but also at various layers of the communications stack. Within this context, RIS-assisted communication challenges the current status quo in legacy wireless systems by providing means to manipulate the wireless signals over the air [12, 62]. This is accomplished by RISs, which are man-made and two-dimensional meta (*beyond* in ancient Greek)-surfaces equipped with integrated electronics to enable reconfigurable EM properties.

RIS-empowered communication systems have received tremendous interest from academia and industry in recent times and have been explored in numerous applications, including but limited to multi-user systems, PHY security, low-cost transmitter implementation, vehicular and non-terrestrial networks, non-orthogonal multiple access, device-to-device communication, Internet-of-things (IoT), Doppler and multi-path mitigation, localization and sensing, and so on [13]. Despite their rich use-cases shown in Fig. 2.12, in which the intelligent scattering feature of RISs is exploited to improve the end-to-end system performance, potential killer applications of RISs have not been well understood in the open literature. This can be mainly attributed to the lack of practical and physical RIS-assisted channel models for different operating frequencies and bands, which considers physical characteristics of RISs.

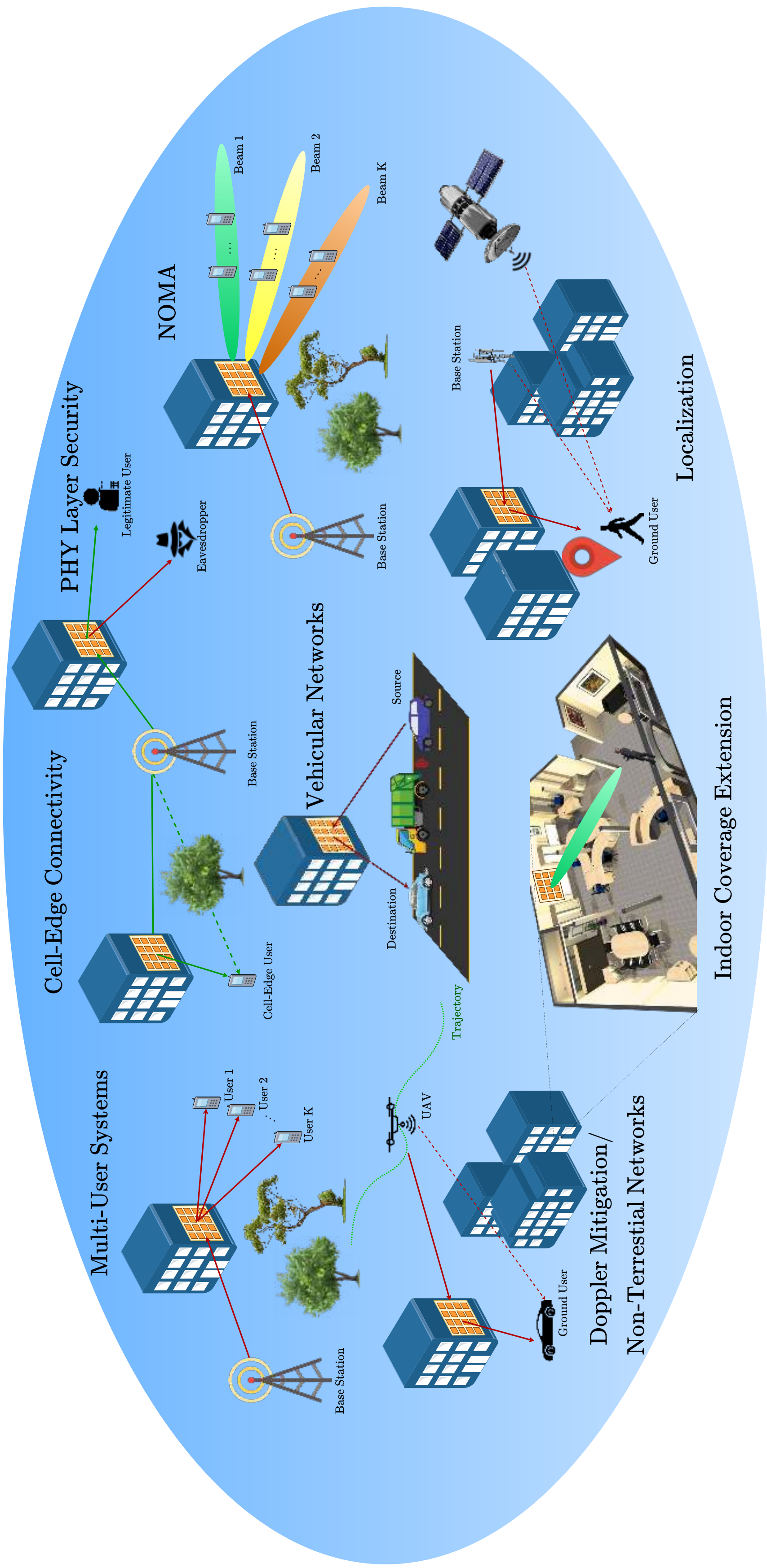

Figure 2.12: Emerging applications and use-cases of RIS-assisted communication systems in future wireless networks.

Against this background, this article takes a step back and approaches RIS-empowered communication systems from the perspective of physical channel modeling to shed light into their practical use-cases in future networks. Building on our previous channel modeling campaign presented in [63] and [34], in this article, we also propose *SimRIS Channel Simulator v2.0* by incorporating MIMO-aided transmit and receive terminals into its earlier version. Our comprehensive channel modeling efforts that include 3D channel models for 5G networks and physical RIS characteristics, and computer simulations reveal that *RISs will work!* by carefully adjusting their size, position, and functionality. In other words, using a physical channel modeling methodology that is unique to RIS-empowered systems, we prove that the received signal quality, in return the achievable rate, can be significantly boosted for both indoor and outdoor environments at certain locations.

It will still take a village to find energy- and cost-efficient ways to reconfigure practical RISs in real time with fully passive elements, however, this article may help to validate the potential applications of emerging RISs in 6G and beyond wireless networks. We hope that this article, which follows a novel channel modeling perspective, might be a useful source for future practical implementation campaigns with sophisticated RISs and can be supported with real data in the future. The open-source nature of the SimRIS Channel Simulator might also be very helpful for interested researchers and engineers, and the outcomes (generated channels) of our simulator can be easily used for the evaluation (capacity, secrecy, error/outage performance etc.) of existing RIS-assisted systems. This article also reviews the state-of-the-art use-cases and potential future directions of RIS-empowered networks and might be a useful source for interested readers.

2.3.2 Reconfigurable Intelligent Surfaces: How Do They Work?

RISs are man-made surfaces of EM material that are electronically controlled with integrated electronics, and have unnatural and unique wireless communication capabilities. The core functionality of RISs relies on a basic physics principle, which states that EM emissions from a surface are defined by the distribution of electrical currents over it. The surface currents are caused by the impinging EM waves and RISs aim to control and modify the current distribution over them in a deliberate manner to enable exotic EM functionalities, including wave absorption, anomalous reflection, and reflection phase modification. This control is accomplished by ultra-fast switching elements such as varactors, PIN diodes, or micro-electro-mechanical systems (MEMS) switches to manipulate the available RIS elements. In different terms, software-defined RISs that are placed in propagation environments, enable wireless network designers to control the scattering, reflection, and refraction characteristics of radio waves, by overcoming the negative effects of natural wireless propagation.

A typical RIS consists of three main layers. The outermost layer consists of a large number of small and metallic (copper etc.) patch elements printed on a dielectric material and interacts directly with the incoming signals. The second layer is a conducting back-plane that prevents the energy leakage to the back of the RIS. Finally, the third layer contains control circuits connected to a micro-controller, which distinguishes an RIS from a passive reflect-array. The micro-controller might be equipped with an IoT gateway to receive commands from a central controller or the base station to reconfigure the RIS. Alternatively, it might run artificial intelligence (AI) algorithms in a stand-alone mode to determine the states of the RIS. Although the operation of the RIS itself is passive, that is, without requiring a power source for signal reflection, the RIS needs a power source for its micro-controller and switch elements.

To illustrate the concept of communications over an RIS with N tiny (sub-wavelength) reflecting elements, let us consider the basic use-case of cell-edge connectivity in Fig. 2.12, where the direct path between the transmitter (Tx) and the receiver (Rx) is blocked by obstacles. Denoting the distances between the Tx and the RIS and the RIS and the Rx by d_1 and d_2 respectively, according to the free-space propagation and plate scattering theory, the received (maximized) signal power P_r follows

$$P_r \propto P_t \frac{N^2\lambda^4}{(4\pi)^2 d_1^2 d_2^2}. \tag{2.14}$$

Here, P_t is the transmit power, λ is the wavelength, and the gains of antennas and RIS elements are ignored for brevity. We further assume that the variation of d_1 and d_2 is negligible across the RIS, which is a valid assumption in the far-field. We further note that P_r is always less than P_t due to the conservation of power and we have different power scaling laws for the near-field as recently reported with practical measurements in [22].

Considering the above equation, our observations are as follows: First, scattering is not merciful as received signal power decays with $d_1^2 d_2^2$, which requires very careful planning and positioning for the RIS. In other words, the Rx might not even notice the existence of an RIS that is relatively far away from either the Tx or the Rx. Accordingly, the received signal can only be boosted significantly when the LoS path is not strong enough or fully blocked. Second, thanks to phase coherent combining of all scattered signals from the RIS, which is possible by careful adjustment of phase responses (time delays or impedances) of RIS elements, we have the term of N^2 in the received signal power. This requires a careful planning on the overall size, total cost, and physical structure of the RIS. Although increasing N is a great booster to the overall system performance, it also increases the cost, complexity, and training overhead of RISs in return. At this point, we might use AI-aided tools or sophisticated optimization methods to reach a compromise.

Finally, it is worth noting that communication through intelligent surfaces is different compared with other related technologies currently employed in wireless networks, such as relaying, MIMO beamforming, passive reflect-arrays, and backscatter communications. This can be attributed to the unique features of RISs such as their nearly passive structure without requiring any RF signal processing, up/down-conversion, power amplification or filtering, inherently full-duplex nature, low cost, and more importantly, real-time reconfigurability.

These distinctive characteristics make RIS-assisted communication a unique technology and introduce important design challenges that need to be tackled under the rich applications and use-cases in Fig. 2.12. Our channel modeling campaign and SimRIS Channel Simulator consider physical millimeter-wave (mmWave) channels and RIS characteristics to provide useful insights to system designers.

2.3.3 Channel Modeling for RIS-Empowered Systems

Despite their rich applications and potential use-cases in future wireless networks, there is still an urgent need for physical, open-source, and widely applicable channel models involving RISs to be used in various systems in indoor and outdoor environments at different operating frequencies. Considering that RIS channel modeling is the first step towards future RIS-empowered networks, the importance of accurate and physical RIS-assisted channel models even increases. This article aims to shed light on this fundamental issue by laying the foundations for physical channel modeling of RIS-empowered communications.

The scattering nature of RISs in the far-field, their reconfigurable amplitude and phase responses, and fixed orientation render channel modeling for RIS-based systems an interesting problem. Due to the scattering nature of RISs, each RIS element behaves as a new signal source by capturing the transmitted signals [63]. Let us consider a MIMO system with N_t transmit and N_r receive antennas operating in the presence of an RIS with N reflecting elements. Consequently, the end-to-end channel matrix $\mathbf{C} \in \mathbb{C}^{N_r \times N_t}$ of an RIS-assisted MIMO system can be given as follows

$$\mathbf{C} = \mathbf{G}\mathbf{\Phi}\mathbf{H} + \mathbf{D}. \tag{2.15}$$

Here, $\mathbf{H} \in \mathbb{C}^{N \times N_t}$ is the matrix of channel coefficients between the Tx and the RIS, $\mathbf{G} \in \mathbb{C}^{N_r \times N}$ is the matrix of channel coefficients between the RIS and the Rx, and $\mathbf{D} \in \mathbb{C}^{N_r \times N_t}$ stands for the direct channel (not necessarily a line-of-sight (LOS)-dominated one and is likely to be blocked for mmWave bands due to obstacles in the environment) between the Tx and the Rx. The beauty of the RIS-assisted model lies in the middle of the composite channel: $\mathbf{\Phi}$, which is a diagonal matrix capturing the (complex) reconfigurable responses of the RIS elements. The researchers have been working on the optimization of $\mathbf{\Phi}$ since the early works of [64] and [65] under different constraints and objectives: maximizing the signal-to-noise ratio (SNR),

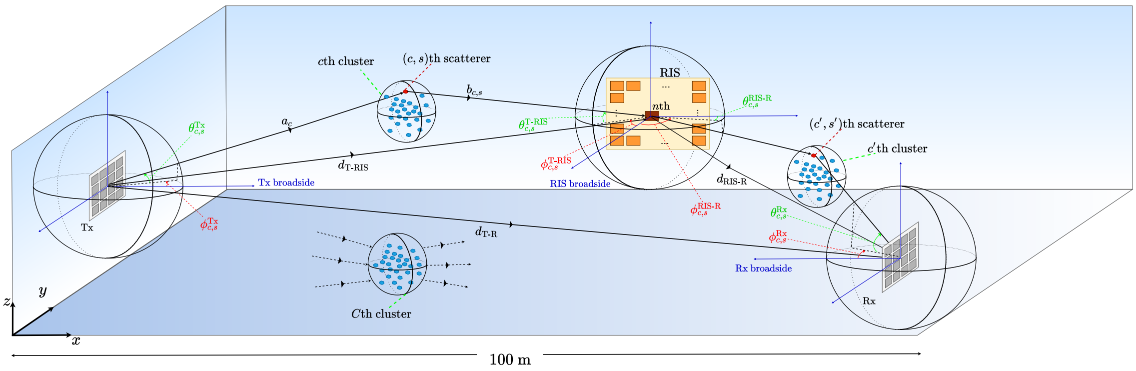

Figure 2.13: Generic 3D communication environment with random clusters/scatterers and an RIS mounted on the xz-plane.

capacity, sum-rate, or secrecy and reducing the interference. In a physical channel model for RIS-assisted systems, the LoS probability between terminals as well as the gain and array response of RIS elements should be carefully reflected to channel matrices of $\mathbf{H}$ and $\mathbf{G}$. Furthermore, the close proximity of the RIS to the terminals, its limited field of view and 2D architecture as well as fixed orientation complicates RIS channel modeling compared to simplified cascaded channel models and brings new technical challenges. As we will discuss next, SimRIS Channel Simulator aims to open a new line of research by taking into account all these effects in channel modeling.

2.3.4 SimRIS Channel Simulator

In this section, the open-source, user-friendly, and widely applicable *SimRIS Channel Simulator v2.0* is presented. Our SimRIS Channel Simulator opens a new line of research for physical channel modeling of RIS-empowered networks by taking into account the LoS probabilities between terminals, array responses of RISs and Tx/Rx units, RIS element gains, realistic path loss and shadowing models, and environmental characteristics in different propagating environments and operating frequencies. More specifically, it considers Indoor Hotspot (InH) - Indoor Office and

Urban Microcellar (UMi) - Street Canyon environments for popular mmWave operating frequencies of 28 GHz and 73 GHz from the 5G channel model [50]. Compared to its earlier version with only single-input single-output (SISO) Tx/Rx terminals, its v2.0 considers MIMO terminals with different types of arrays. We support terminals in the far-field of the RIS only, which is a reasonable assumption for mmWaves with shorter wavelengths and smaller RIS sizes, while the integration of near-field RIS models will be evaluated in its future releases.

The considered generic 3D geometry is given in Fig. 2.13 for the representation of physical channel characteristics. In this setup, the RIS is mounted on the xz-plane while a generalization is possible in the simulator. Our model considers various indoor and outdoor wireless propagation environments in terms of physical aspects of mmWave frequencies while numerous practical 5G channel model issues are adopted to our channel model [50]. For a considered operating frequency and environment, the number of clusters (C), number of sub-rays (scatterers) per cluster (S_c), and the positions of the clusters can be determined by following the detailed steps and procedures in [63]. More specifically, according to the 5G channel model, the number of clusters and scatterers are determined using the Poisson and uniform distributions with certain parameters, respectively. Although the clusters between Tx-RIS and Tx-Rx can be modeled independently, it can be assumed that the Rx and the RIS might share the same clusters when the Rx is located relatively closer to the RIS. Due to the fixed orientation of the Tx and the RIS, the array response vectors of the Tx and the RIS are easily calculated for given azimuth and elevation departure/arrival angles. However, it is worth noting that if azimuth and elevation angles are generated randomly for the Tx, due to fixed orientation of the RIS, they will not be random anymore at the RIS and should be calculated from the 3D geometry using trigonometric identities. Nevertheless, the array response vector of the Rx can be calculated with randomly distributed azimuth and elevation angles of arrival due to the random orientation.

Using the SimRIS Channel Simulator, the wireless channels of RIS-aided communication systems can be generated with tunable operating frequencies, number of RIS elements, number of transmit/receive antennas, Tx/Rx array types, terminal locations, and environments. As discussed earlier, in SimRIS Channel Simulator v2.0, MIMO-aided Tx and Rx terminals are incorporated into its earlier version, and the array response vectors and receiver orientation are reconstructed by considering this MIMO system model. This new version also offers two different types of antenna array configurations: Uniform linear array (ULA) and uniform planar array (UPA), and the corresponding array response vectors are calculated according to the selected antenna array type. The graphical user interface (GUI) of our SimRIS Channel Simulator v2.0 is given in Fig. 2.14. In this GUI, the selected scenario specifies the RIS position for both indoor and outdoor environments as xz-plane (Scenario 1) and yz-plane (Scenario 2). Considering the 3D geometry illustrated in Fig. 2.13, Tx, Rx, and RIS positions can be manually entered into the SimRIS Channel Simulator. Furthermore, N_t (the number of Tx antennas), N_r (the number of Rx antennas), N (the number of RIS elements), and the number of channel realizations are also user-selectable input parameters and these options offer a flexible and versatile channel modeling opportunity to the users. Considering these input parameters, our simulator produces $\mathbf{H}$, $\mathbf{G}$, and $\mathbf{D}$ channel matrices in (2.15) by conducting Monte Carlo simulations for the specified number of realizations under 28 and 73 GHz mmWave frequencies. The general expressions of these channel matrices are given in Table 2.3 for the interested readers. Here, the double summation terms stem from the random number of clusters and scatterers and the LoS components might be equal to zero with a certain probability for increasing distances.

In a nutshell, our open-source SimRIS Channel Simulator package considers a narrowband channel model for RIS-empowered communication systems for both indoor and outdoor environments and it includes various physical characteristics of the wireless propagation environment. The open-source nature of our simulator, which is written in the MATLAB programming environment, encourages all researchers to use and contribute to the development of its future versions by reaching a wider audience. We aim a Web-based simulator application and more sophisticated propagation scenarios (wideband and time-varying channels) in its future versions.

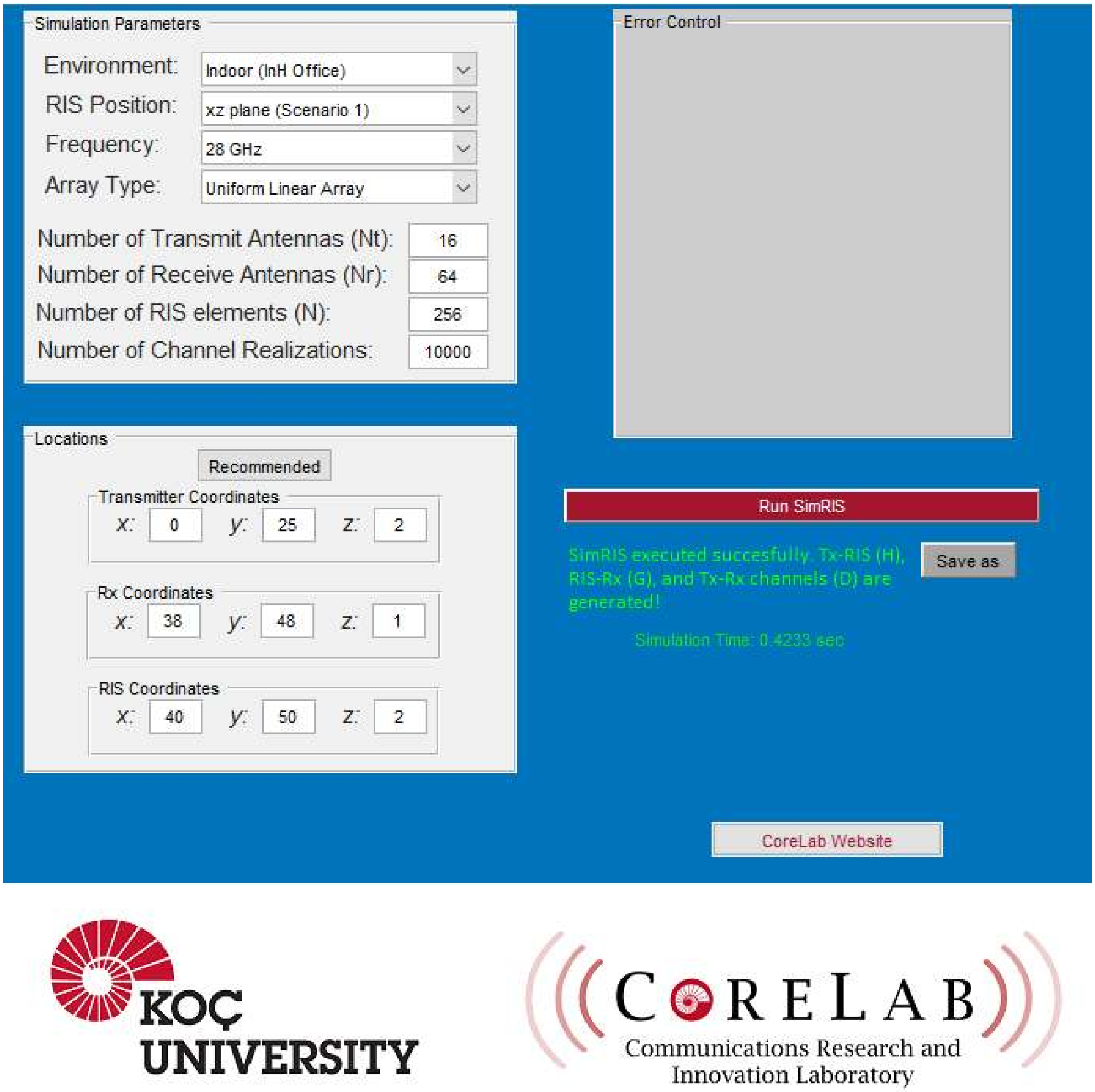

Figure 2.14: Graphical user interface (GUI) of the SimRIS Channel Simulator v2.0.

Table 2.3: System Configurations and Simulation Parameters For SimRIS Channel Simulator

Channel Matrices*:	$\mathbf{H} = \gamma \sum_{c=1}^{C} \sum_{s=1}^{S_c} \beta_{c,s} \sqrt{G_e(\theta_{c,s}^{\text{T-RIS}}) L_{c,s}^{\text{T-RIS}}}\ \mathbf{a}(\phi_{c,s}^{\text{T-RIS}}, \theta_{c,s}^{\text{T-RIS}}) \mathbf{a}^T(\phi_{c,s}^{\text{Tx}}, \theta_{c,s}^{\text{Tx}}) + \mathbf{H}_{\text{LOS}}$
	$\mathbf{G} = \bar{\gamma} \sum_{c=1}^{\bar{C}} \sum_{s=1}^{\bar{S}_c} \bar{\beta}_{c,s} \sqrt{G_e(\theta_{c,s}^{\text{RIS-R}}) L_{c,s}^{\text{RIS-R}}}\ \mathbf{a}(\phi_{c,s}^{\text{Rx}}, \theta_{c,s}^{\text{Rx}}) \mathbf{a}^T(\phi_{c,s}^{\text{RIS-R}}, \theta_{c,s}^{\text{RIS-R}}) + \mathbf{G}_{\text{LOS}}$
	$\mathbf{D} = \tilde{\gamma} \sum_{c=1}^{\tilde{C}} \sum_{s=1}^{\tilde{S}_c} \tilde{\beta}_{c,s} \sqrt{L_{c,s}^{\text{T-R}}} \mathbf{a}(\phi_{c,s}^{\text{Rx'}}, \theta_{c,s}^{\text{Rx'}}) \mathbf{a}^T(\phi_{c,s}^{\text{Tx'}}, \theta_{c,s}^{\text{Tx'}}) + \mathbf{D}_{\text{LOS}}$
Environments:	Indoor: InH Indoor Office
	Outdoor: UMi Street Canyon
Tx, Rx and RIS Positions:	Indoor: (0,25,2), (45,45,1), (40,50,2)
	Outdoor: (0,25,20), (50,50,1), (40,60,10)
Operating Frequency:	28 GHz
Antenna Array Type:	Uniform linear array (ULA) and uniform planar array (UPA)
Algorithm for Phase Shifts:	Pseudoinverse (pinv)-based algorithm [66]

* $\gamma/\bar{\gamma}/\tilde{\gamma}$: normalization factor [34], $\beta_{c,s}/\bar{\beta}_{c,s}/\tilde{\beta}_{c,s}$: complex Gaussian distributed gain of the (c,s)th propagation path, $G_e(.)$: RIS element gain, $L_{c,s}^{i}$: attenuation of the (c,s)th propagation path [50], $\mathbf{a}\left(\phi_{c,s}^{i}, \theta_{c,s}^{i}\right)$: array response vectors for the considered azimuth $(\phi_{c,s}^{i})$ and elevation angles $(\theta_{c,s}^{i})$, $\mathbf{H}_{\text{LOS}}$/ $\mathbf{G}_{\text{LOS}}$/ $\mathbf{D}_{\text{LOS}}$: LoS component of sub-channels (i: indicator for the corresponding path/terminal as $i \in \{\text{T-RIS}, \text{RIS-R}, \text{T-R}, \text{Tx}, \text{Rx}\}$).

2.3.5 Simulation of Indoor/Outdoor Scenarios Using SimRIS Channel Simulator

The goal of the section is to pave the way for the detailed elaboration of how RISs can be effectively used in future networks to enhance the existing transmission systems. In next-generation wireless networks, it is inevitable to use a high number of antennas at Rx and Tx units. Many transmission scenarios involving massive MIMO systems offer significant increases in achievable rates. However, when high frequencies are considered, especially using a large number of antennas in mobile users will increase the cost of signal processing and required hardware. By using RISs in transmission, it will be still possible to obtain high achievable rates, while alleviating the cost of physical implementation and signal processing. The summary of the considered system configurations, generated channel matrices, and computer simulation parameters are given in Table 2.3, which will be used for the numerical results in this section. Here, all computer simulations are conducted at an operating frequency of 28 GHz and pseudoinverse (pinv)-based algorithm [66] is used for adapting the phase shifts of an RIS-assisted MIMO transmission system. Here, the selection of the pinv-based algorithm can be explained by its relatively easy to implement architecture without any iterative operations, compared to non-convex optimization algorithms. The ergodic achievable rate for the MIMO systems is given by

$$R = \log_2 \det \left(\mathbf{I}_{N_r} + \frac{P_t}{\sigma^2} \mathbf{C}^H \mathbf{C} \right) \text{ bit/sec/Hz} \tag{2.16}$$

where $\mathbf{I}_{N_r}$ and σ^2 denote $N_r \times N_r$ identity matrix and the average noise power, respectively. The noise power is assumed to be -100 dBm for all simulations in this section. As stated above, the pinv algorithm can be effectively used to maximize R, without resorting to more complicated convex optimization problems due to non-concavity of the MIMO channel capacity [13]. Finally, the determination and execution of optimal RIS adaptation algorithms are beyond the scope of the SimRIS Channel Simulator, at least in this version, while interested readers can easily use our generated channels in their own optimization models.

In Fig. 2.15(a) the effect of varying numbers of transmit and receive antennas on

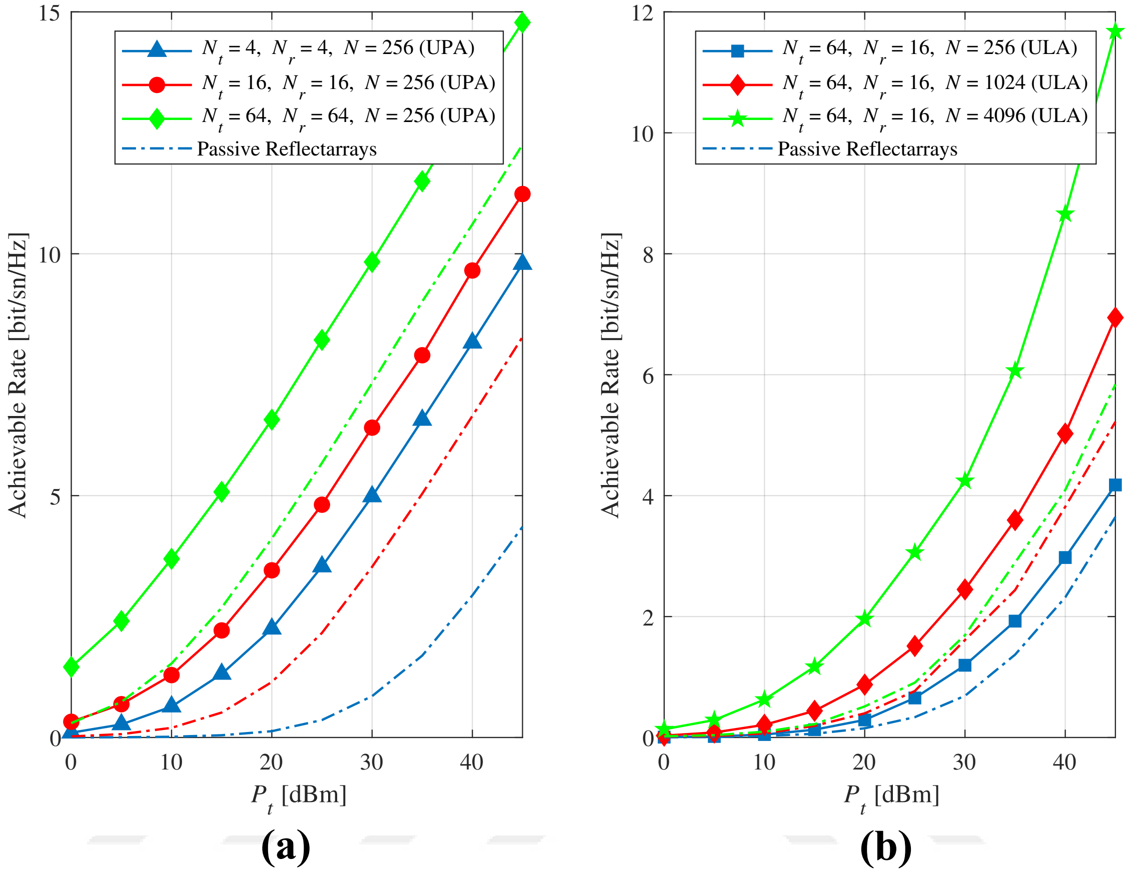

Figure 2.15: Achievable rates of RIS-assisted systems (a) in an indoor environment under different N_t and N_r with fixed N, and (b) in an outdoor environment under different N with fixed N_t and N_r.

the achievable rate is examined, considering the indoor environment parameters in Table 2.3. Using UPAs both in transmitter and receiver, increasing N_t and N_r values have been observed to enable a significant increase in achievable rates for $N = 64$ under increasing P_t. As clearly seen from Fig. 2.15(a), compared to the passive reflectarrays, which simply reflect the incident waves without any phase adjustment, RISs can provide a remarkable improvement in the achievable rate for the same N value. In Fig. 2.15(b), the achievable rate is investigated by keeping the number of antennas constant and increasing N considering the outdoor environment parameters in Table 2.3. As seen from Fig. 2.15(b), a substantial increase in achievable

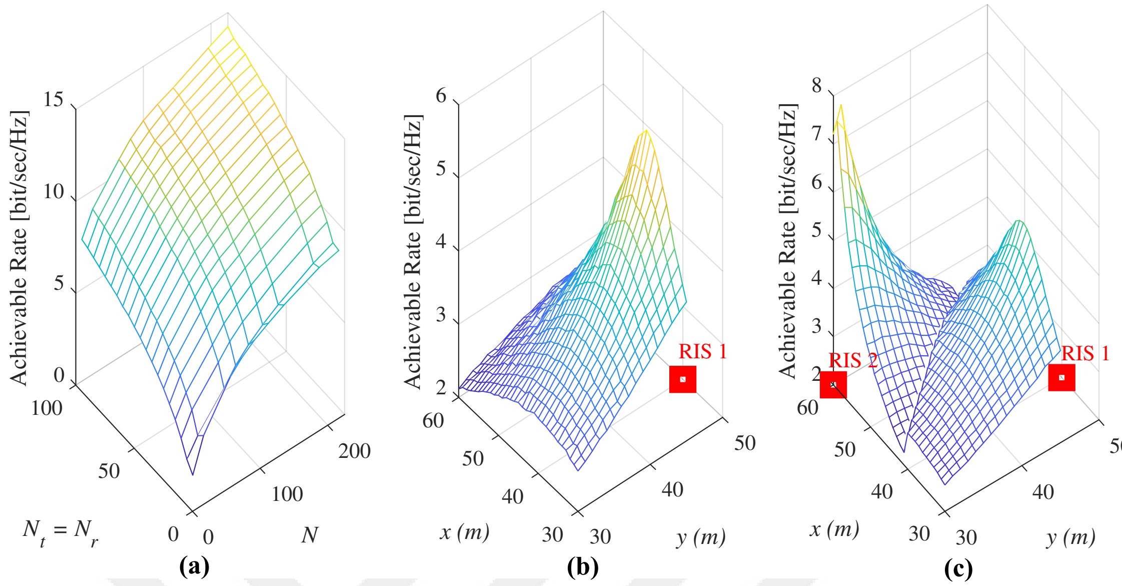

Figure 2.16: Achievable rate analysis using SimRIS Channel Simulator: (a) For varying N_t/N_r and N, (b) For a single RIS with varying Rx positions, (c) For two RISs with varying Rx positions. Here, the red squares indicate the positions of the RISs on the x and y-axes.

rate is also obtained by increasing N with fixed N_t and N_r when ULA type antennas are used. Moreover, the RIS-assisted system also reaches a considerably better achievable rate performance than the reference passive reflectarray-based system for the outdoor environment. Here, the RIS is positioned to have a LoS transmission link with the Tx and the Rx, as well as to have a closer RIS-Rx distance for both indoor and outdoor environments when the Tx-Rx path is blocked by obstacles. Figs. 2.15(a) and 2.15(b) show that increasing numbers of antennas and reflecting elements have a similarly favorable effect on the achievable rate, while the overall cost of the latter might be much lower due to its passive nature. We also note that the differences in Figs. 2.15(a) and (b) can be mainly attributed to the longer range transmission in the outdoor environment. Finally, it is worth noting that our channel simulator can be used for the calculation of system throughput by effective signal-to-noise ratio mapping tables.

In order to get a more accurate understanding of the effects of the number of Tx/Rx antennas and reflecting elements, we also observe the joint effect of these two parameters on the achievable rate in Fig. 2.16. The joint effect of the number of antennas and reflecting elements on the achievable rate is demonstrated in Fig. 2.16(a) for an indoor environment when $N_t = N_r$ and $P_t = 40$ dBm. As seen from Fig. 2.16(a), if the number of antennas is doubled under a fixed N, an increase of approximately 2 bit/sec/Hz is achieved in the achievable rate. Similarly, if N_t and N_r are kept constant, when N is doubled, a gain of about 2 bit/sec/Hz is also obtained. Since doubling the number of reflectors is much less costly than doubling the number of Tx/Rx antennas, the demand for ultra-reliable and high-speed transmission that will emerge in the next-generation wireless networks can be met effectively by increasing the N.

Fig. 2.16(b) explores the use of an RIS for indoor coverage extension. When the direct path between the Tx and the Rx is lost due to surrounding objects and obstacles, reliable transmission conditions are guaranteed by placing an RIS near to the Rx. Here, we consider the indoor parameters in Table 2.3 and the effect of the movement of the Rx on the xy-plane to its achievable rate is examined. It is observed that the highest rates are achieved in particular regions, where the distance between the Rx and the RIS is 10 meters or less and this reveals the promising role of an RIS in future wireless networks while providing a general perspective for the effective positioning of RISs. Under the LOS-dominated Tx-RIS-Rx channels, the use of an RIS in transmission improves signal quality even in dead zones or cell-edges by providing low-cost and energy-efficient solutions with low complexity.

If we want to go one step further to provide a wider coverage extension, the idea of using more than one RISs in transmission might be considered in the system design. The variation of the achievable rate of the Rx for its different locations is observed in Fig. 2.16(c) when a second RIS with coordinates $(60, 30, 2)$ is placed in the system in addition to the first RIS at $(40, 50, 2)$. Here, we aim to increase the quality of the received signal by adjusting the reflecting element phases of the RIS, which is closer to the Rx. In other words, our two RISs create a handover opportunity for the Rx to boost its signal strength. As seen from Fig. 2.16(c), when the Rx is located in areas close to one of the RISs, one can observe a significant increase in its achievable rate. Furthermore, in locations, where the Rx is far from both RISs, rapid decreases are observed in the achievable rate. From the given results, we observe that RISs can be considered as powerful and energy-efficient tools to boost the achievable rate as well as for the coverage extension, and alleviates the large number of antenna requirements in next-generation wireless networks.

In light of our extensive computer simulations using the SimRIS Channel Simulator, we can certainly state that RISs might have a huge potential under certain conditions such as LOS-dominated Tx-RIS-Rx channels and shorter RIS-Rx distances. Another important point here is that an RIS provides the maximum benefit when the direct path is lost due to surrounding objects and obstacles since the presence of a LOS-dominated and a strong Tx-Rx path will guarantee a reliable communication eliminating the need for an RIS. Our findings are also consistent with one of the most recent practical applications of RISs, scatterMIMO [67], which considers careful RIS size adjustment and positioning to achieve a strong Tx-RIS-Rx composite channel.

2.3.6 Future Directions

Despite their huge potential and rich applications for future wireless networks, we believe that there is still a long way to go for the standardization of this promising technology. More importantly, we need to bridge the gap between theoretical analysis and real-world deployments for RIS-empowered systems. For instance, the received signal power given in (2.14), as well as the achievable rate results obtained by the SimRIS Channel Simulator, can be considered as benchmarks for practical systems due to hardware imperfections, estimation/feedback errors, and the limited phase resolution of practical RIS elements. Furthermore, we do not have clear answers to the total energy consumption and cost of RISs in realistic systems.

Open research issues towards 6G wireless networks are summarized as follows:

- Practical path-loss/channel modeling and real-time testing of large-scale RISs in different propagating environments

- Determination of convincing use-cases in which the RISs might have a huge potential to boost the communication quality-of-service
- Assessment of practical protocols for reconfigurability of RISs
- Determination of fundamental performance limits of RIS-assisted networks
- Robust optimization and resource allocation issues in space, time, and frequency domains
- Optimal positioning of multiple RISs and optimization/coordination of the overall network
- Development of EM-based RIS models and exploration of hardware imperfections/effects
- Exploration of effective mmWave and Terahertz communication systems with RISs
- Exploration of the potential of RISs for beyond communication (sensing, radar, localization etc.)
- AI-driven tools for designing/optimizing/reconfiguring surfaces
- Exploration of futuristic scenarios such as very high number of devices, combination of enhanced mobile broadband and ultra-reliable and low latency communications, and very high mobility
- Standardization and integration into existing wireless communication networks (5G, 6G, IoT, IEEE 802.11x), which requires a joint effort from academia and industry.

2.3.7 Conclusion

It is inevitable that 6G networking will necessitate radically new concepts for the PHY design of next-generation radios. Within this context, this article has discussed the potential of intelligent surfaces-empowered communication by following a bottom-up approach from its main methodology and use-cases to its open problems and potential future directions. Special emphasis has been given to the open-source and widely acceptable SimRIS Channel Simulator, which considers a novel physical channel modeling methodology for RIS-empowered systems operating in different environments and frequencies. Based on our initial findings and numerical results using this simulator, from a communication theoretical perspective, we can certainly state that RISs might be game changers after careful assessment and planning for certain use-cases and environments. We have also discussed the future challenges to bridge the gap between theory and practice for RIS-empowered systems. The future of wireless communications looks very exciting and stay tuned into this promising technology!

Chapter 3

BROADENING NETWORK HORIZONS: THE ROLE OF RIS IN COVERAGE EXTENSION

This chapter focuses on how RIS technology can improve coverage in wireless networks. This chapter also details the potential of RIS in wireless communications by covering two key studies. The first study of this chapter examines efficient use-cases of the RISs in indoor and outdoor applications. The potential of RIS to extend the coverage of wireless networks in single and multiple-use scenarios is investigated, especially in challenging communication environments.

The second work of this chapter considers the combination of RIS-assisted reflection and decode-and-forward transmission techniques. This approach explores the synergy of RIS technology and relaying strategies and how it can improve the coverage and transmission quality of wireless networks. Furthermore, this study elaborates on how the efficient integration of RIS and relaying can optimize network performance and extend coverage, especially in challenging communications environments.

The findings presented by these two studies highlight the critical role that RIS technology can play in extending the coverage of next-generation wireless networks. It demonstrates that RIS technology can become a key component in the design and implementation of future wireless networks and play a vital role in realizing the 6G vision. This chapter provides a valuable guide on how RIS technology can be used strategically to overcome current challenges in wireless communications and make future wireless networks more efficient and inclusive.

3.1 Modeling and Analysis of Reconfigurable Intelligent Surfaces for Indoor and Outdoor Applications in Future Wireless Networks

3.1.1 Introduction

One of the areas that has made the most progress as a result of the digitalization experienced by human life in recent decades is wireless communications [4]. Due to the enormous increase in data traffic, existing communication systems have faced challenges in providing high-quality of service. Both academia and industry have carried out intensive research activities in order to overcome the deficiencies of legacy transmission concepts. All these efforts and targets have attracted the attention of the wireless community in recent times, most notably within the context of fifth-generation (5G) wireless networks. 3rd Generation Partnership Project (3GPP) Release 15, which is the first full set of 5G standard, has been completed in 2018. This initial 5G standard enables high data rate, ultra-reliability and low latency using novel technologies, such as scalable orthogonal frequency-division multiplexing (OFDM) numerologies, millimeter-wave (mmWave) wireless communications and massive multiple-input multiple-output (MIMO) systems [68]. Massive machine type communications, enhanced mobile broadband, and ultra-reliable and low latency communications are defined as three use-cases with diverse requirements and applications in 5G wireless networks. Beyond all these approaches, more radical physical layer concepts are needed to comprehend the potential requirements of future networks due to sophisticated applications with extremely high quality-of-service (QoS) requirements, such as augmented reality, massive Internet-of-everything, and autonomous vehicles. Despite the high expectations, 5G has not brought these sophisticated applications into reality to date [69]. This has pushed researchers to look new paradigms beyond 5G and start to conceptualize 6G wireless networks. Within the frame of 6G studies, it is aimed to design systems that are expected to have substantial differences from previous generations by achieving a radical transformation in wireless networks.

In light of the above, it is also essential to develop flexible, versatile, and inclusive physical layer solutions in order to support potential requirements of 6G wireless networks. Although researchers have put forward promising solutions for beyond 5G, including index modulation schemes [70], non-orthogonal multiple access [71], and alternative waveforms [72], the overall progress has been still relatively slow in terms of QoS, reliability and security.

In radio communication environments, one of the most deteriorating characteristics of the channel is its random and dynamic nature. However, when the spectrum shortage below 6 GHz frequency bands has taken into account, it is inevitable to migrate to the mmWave (30-100 GHz) and THz (above 100 GHz) bands. In above 6 GHz, the signal will be more susceptible to blockage and interference, since collecting high energy in the receiver will be difficult because of small antenna sizes. Therefore, the severe signal attenuation and blockage prevent mmWaves to reach long distances. In order to ensure reliable wireless transmission and to alleviate these disruptive effects at high frequencies, we need to overcome the negative and uncontrollable effects of the wireless channel.

Most of the promising methods for next-generation wireless networks are mainly based on the intelligence or reconfigurability of the building blocks of communication systems. Recently, reconfigurable intelligent surfaces (RISs) have been put forward by researchers to enable the control of wireless environments via their unique and effective functionalities, such as wave absorption, anomalous reflection, polarized reflection, wave splitting, wave focusing, and phase modification [73–75]. Recent results have revealed that these attractive electromagnetic functionalities are possible without complex operations such as decoding, encoding, and radio frequency (RF) processing and the communication system performance can be enhanced by exploiting the implicit randomness of wireless propagation [12, 65, 76, 77].

The use of RISs is particularly useful when the line-of-sight (LOS) link is blocked or not strong enough since it is possible to provide additional transmission paths by utilizing the reflecting elements of an RIS. Although it is possible to alleviate the negative effects of the channel using relays, the hardware cost, power consumption and latency increase considerably as the signal has been actively processed at each relay [78]. In addition, real-time controlled phase shifts of each RIS element allow the optimization of certain system performance metrics, such as transmit power, achievable rate, energy efficiency, and received signal-to-noise ratio (SNR) [79–81]. On the other hand, various secrecy enhancing schemes have been proposed by optimizing the transmit beamformer and RIS phase shifts jointly in [82–84]. In [42], the communication through RISs has been investigated in terms of error performance and the symbol error probability (SEP) is derived for a scenario without a direct path between the transmitter and the receiver. However, to the best of our knowledge, a general analysis that elaborates the performance of single and multiple RIS-assisted systems in indoor and outdoor scenarios as well as under different conditions is missing in the literature.

In this work, we investigate the performance of single and multiple RIS-assisted systems without a direct path between the transmitter and the receiver in indoor and outdoor propagation environments. First, in Section II, we show that the employment of an RIS is a dominant factor in the received signal power even in the absence of a direct communication link. By deriving mathematical expressions for the error performance under both large-scale and small-scale fading effects, we show that the RIS-assisted link acts as a superior LoS path by suppressing the the disruptive effects of the propagation environment. Furthermore, we investigate the effects of RISs on the path loss exponent (PLE) for the log-distance path loss model [85], and determine the achievable data rate of an RIS-assisted system under emprical path loss models for below and above 6 GHz operating frequencies. In Section III, we investigate the wireless communications in the presence of multiple RISs under two envisioned scenarios: simultaneous transmission over two RISs in indoor environment and the double-RIS reflected transmission in outdoor environment. We introduce a mathematical framework on the error performance for these two scenarios and demonstrate that the use of multiple RISs can be a remedy for the blockage problem in 6G and beyond systems. We also introduce RIS selection strategies for systems equipped with multiple RISs. Finally, we study the RIS imperfections, such as practical phase shifts and phase estimation errors, and demonstrate the robust-

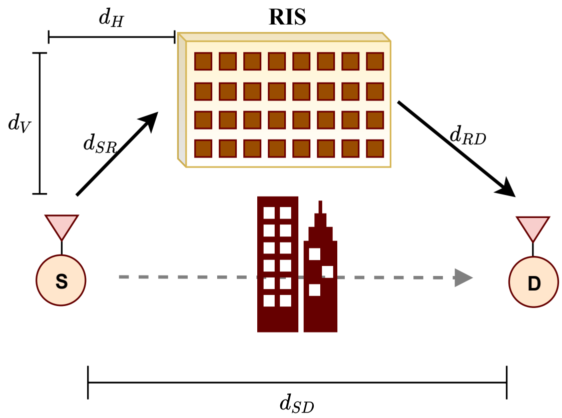

Figure 3.1: An RIS-assisted SISO system consisting of a direct path and an RIS with N reflecting elements.

ness of RIS-assisted systems. Our comprehensive theoretical and numerical results in Section IV show that the transmission through RISs appear as an attractive candidate for indoor/outdoor communication systems at various operating frequencies by suppressing the destructive effects of wireless propagation.

3.1.2 Communications Through a Single RIS

In this section, we consider the wireless communication system shown in Fig. 3.1 with a transmitter/receiver pair and a single RIS. Here, we provide first time a unified error performance analysis that is applicable to various path loss models in indoor and outdoor communication scenarios. Furthermore, the effect of an RIS on the overall path loss is examined in frequency bands below and above 6 GHz.

3.1.2.1 The General Model and Performance Analysis

As illustrated in Fig. 3.1, a generic RIS-assisted communication scenario is considered, where the transmission is carried out via an RIS under the blocked direct link between the source (S) and the destination (D). We assume that the real-time controlled RIS is equipped with N reconfigurable reflect elements that can be adjusted according to channel phases. In Fig. 3.1 and the remainder of the work we use the notations d_{SD}, d_{SR} and d_{RD} to represent the distances from source-to-destination (S-

D), source-to-RIS (S-R), and RIS-to-destination (R-D), respectively. In this setup, d_V and d_H respectively denote the vertical and horizontal distance between S and RIS. Under the Rician fading assumption, the channel fading coefficients of S-R and R-D links for ith reflecting element ($i = 1, \dots, N$) are respectively represented by

$$\begin{aligned} h_i^{SR} =& \sqrt{\frac{K_1}{1+K_1}}\bar{h}_i^{SR} + \sqrt{\frac{1}{1+K_1}}\tilde{h}_i^{SR}, \\ h_i^{RD} =& \sqrt{\frac{K_2}{1+K_2}}\bar{h}_i^{RD} + \sqrt{\frac{1}{1+K_2}}\tilde{h}_i^{RD} \end{aligned} \tag{3.1}$$

where K_1 and K_2 are the Rician factors of these two links, $\bar{h}_i^{SR}$ and $\bar{h}_i^{RD}$ stand for the LoS components, and $\tilde{h}_i^{SR}$ and $\tilde{h}_i^{RD}$ represent the NLoS components for $i = 1, \dots, N$. Here, $\tilde{h}_i^{SR}$ and $\tilde{h}_i^{RD}$ follow $\mathcal{CN}(0, 1)$ distribution.

Under the condition of slow and flat fading channels, the baseband received signal at D can be expressed as

$$r = \sqrt{p_t}\left[\sqrt{P_L^R}\left(\sum\nolimits_{i=1}^{N} h_i^{SR} e^{j\phi_i} h_i^{RD}\right)\right] x + w \tag{3.2}$$

where p_t is the total transmitted power, ϕ_i stands for the controllable phase shift prompted by the ith RIS element under the assumption of unit-gain reflection coefficients, x is the data symbol selected from M-ary phase shift keying/quadrature amplitude modulation (PSK/QAM) constellations with unit power, and $w \sim \mathcal{CN}(0, N_0)$ represents the additive white Gaussian noise (AWGN) sample, where N_0 is the total noise power. Additionally, P_L^R stands for the path loss of the RIS-assisted path. Under the specular reflection in the near-field case [86], P_L^R will be proportional to total length of the RIS-assisted path $(d_{SR} + d_{RD})^2$, while P_L^R will be a proportional with $d_{SR}^2 d_{RD}^2$ under plate scattering paradigm in far-field case [20]. All analyses and derivations in this work are performed by considering reflect-array type RISs in which the RIS elements are separated with half-wavelength under the far-field case. Using well known radar range equation, the path loss P_L^R can be expressed as

$$P_L^R = \left(\left(\frac{\lambda}{4\pi}\right)^4 \frac{G_e^i G_e^r}{d_{SR}^2 d_{RD}^2}\epsilon_p\right)^{-1} \tag{3.3}$$

where λ is the wavelength, G_e^i is the gain of the RIS in the direction of incoming wave, G_e^r is the gain of RIS in the direction of received wave and ϵ_p is the efficiency of RIS, which is described as ratio of power transmit signal power by RIS to received signal power by RIS. In this work, it is assumed that that RIS consist of passive elements and $\epsilon_p = 1$.

Expressing the channel fading coefficients as $h_i^{SR} = \alpha_i e^{-j\theta_i}$ and $h_i^{RD} = \beta_i e^{-j\varphi_i}$, where α_i and β_i stand for channel amplitudes while θ_i and φ_i denote channel phases, the received signal can be rewritten as

$$r = \sqrt{p_t}\left[\sqrt{P_L^R}\left(\sum\nolimits_{i=1}^{N} \alpha_i \beta_i e^{j\Delta\Phi_i}\right)\right]x + w \tag{3.4}$$

where $\Delta\Phi_i = \phi_i - \theta_i - \varphi_i$ is the phase difference term for $i = 1, ..., N$. Therefore, the instantaneous SNR at D is given by

$$\gamma = \frac{\left|\sqrt{P_L^R}\left(\sum_{i=1}^{N} \alpha_i \beta_i e^{j\Delta\Phi_i}\right)\right|^2 p_t}{N_0}. \tag{3.5}$$

Here, the SNR can be maximized by aligning the phases of the reflected signals from the RIS to the phase of the direct path, that is, $\Delta\Phi_i = 0$ for $i = 1, 2, ..., N$ considering trigonometric identities [42]. Under this intelligent reflection model with manipulated reflection phases, the maximized instantaneous SNR at D is obtained as

$$\gamma_{\max} = \frac{\left(\sqrt{P_L^R}\left(\sum_{i=1}^{N} \alpha_i \beta_i\right)\right)^2 p_t}{N_0} = \frac{A^2 p_t}{N_0} \tag{3.6}$$

where α_i and β_i follow Rician distribution. Using the central limit theorem (CLT), it can be shown that A, which is the sum of N independently identical distributed (iid) random variables, follows the Gaussian distribution for $N \gg 1$ with the following mean and variance:

$$\begin{aligned} \mathrm{E}[A] =& N\frac{\sqrt{P_L^R}\pi}{4(K+1)}\left(L_{1/2}\left(-\frac{K^2}{(K+1)}\right)\right)^2, \\ \mathrm{VAR}[A] =& NP_L^R - N\frac{P_L^R\pi^2}{16(K+1)^2}\left(L_{1/2}\left(-\frac{K^2}{(K+1)}\right)\right)^4 \end{aligned} \tag{3.7}$$

where $L_{1/2}(x)$ is the Laguerre polynomials of degree $1/2$. Since γ follows non-central chi-square distribution with one degree of freedom, its moment generating function

(MGF) [87] is obtained as

$$M_{\gamma_{\max}}(s)=\frac{\exp\left(\frac{\frac{sN^2P_L^R\pi^2L_{1/2}^4\left(-K^2/(K+1)\right)p_t}{16(K+1)^2N_0}}{1-\frac{sNP_L^R\left[16(K+1)^2-\pi^2L_{1/2}^4(-K^2/(K+1))\right]p_t}{8(K+1)^2N_0}}\right)}{\sqrt{1-\frac{sNP_L^R\left[16(K+1)^2-\pi^2L_{1/2}^4(-K^2/(K+1))\right]p_t}{8(K+1)^2N_0}}}. \tag{3.8}$$

Considering the generic SEP expression of [88] for M-PSK signaling, we obtain

$$P_e=\frac{1}{\pi}\int_0^{(M-1)\pi/M}M_{\gamma_{\max}}\left(-\frac{\sin(\pi/M)}{\sin^2\eta}\right)d\eta. \tag{3.9}$$

When binary PSK (BPSK) signaling is used, the average SEP can be simplified as

$$P_e=\frac{1}{\pi}\int_0^{\pi/2}\frac{1}{\sqrt{1+\frac{NP_L^R\left[16(K+1)^2-\pi^2L_{1/2}^4(-K^2/(K+1))\right]p_t}{8(K+1)^2N_0\sin^2\eta}}}$$
$$\times\exp\left(-\frac{\frac{N^2P_L^R\pi^2L_{1/2}^4\left(-K^2/(K+1)\right)p_t}{16(K+1)^2N_0\sin^2\eta}}{1+\frac{NP_L^R\left[16(K+1)^2-\pi^2L_{1/2}^4(-K^2/(K+1))\right]p_t}{8(K+1)^2N_0\sin^2\eta}}\right)d\eta. \tag{3.10}$$

Here, the average SEP in (3.10) can be further upper bounded by letting $\eta=\pi/2$.

As will be shown in Section IV, the average SEP decreases with N^2 for the low p_t/N_0 region. Furthermore, we observe from (3.10) that for sufficiently large N, the effect of the blocked direct path becomes less significant since the signals reflected from the RIS compensate deficiencies in the received SNR. Using the similar methods in [77] and [12], the average SEP is derived under the Rician fading channel and the path loss is also taken into account in (3.10). Finally, we note that (3.10) can be used under different path loss models and generalizes the SEP derivations of [12].

3.1.2.2 Performance under Empirical Path Loss Models for Outdoor Applications: Below and Above 6 GHz

In this subsection, we examine the effect of an RIS on the overall path loss between S and D in frequency bands below and above 6 GHz for the scenario of Fig. 3.1. Empirical path loss models for outdoor communication scenarios have been taken into account to assess the potential of RIS-assisted systems. Then, the impact of an RIS on the PLE and achievable data rate is observed under the empirical transmission scenarios.

3.1.2.2.1 Urban Micro (UMi) Path Loss Models with a Single RIS

In order to assess the potential of an RIS over an empirical transmission environment, we consider the 3GPP UMi [89] and 5G UMi-Street Canyon [90] path loss models. As a reference, a point-to-point LoS and NLoS transmission scenarios with a single transmitter/receiver path are considered. At the 2-6 GHz frequency band and S-D distance ranging from 10 m to 2000 m, 3GPP UMi path loss models are respectively expressed for LoS and non-LoS (NLOS) transmission as [89]

$$\begin{aligned} P_L(d)\,[\text{dB}] &= 22\log_{10}(d) + 28 + 20\log_{10}(f_c), \\ P_{NL}(d)\,[\text{dB}] &= 36.7\log_{10}(d) + 22.7 + 26\log_{10}(f_c). \end{aligned} \tag{3.11}$$

At frequency bands from 6 GHz to 100 GHz, the UMi-Street Canyon path loss models both LoS and NLoS cases are respectively given by [90]

$$\begin{aligned} P_L(d)\,[\text{dB}] &= 21\log_{10}(d) + 32.4 + 20\log_{10}(f_c), \\ P_{NL}(d)\,[\text{dB}] &= 31.7\log_{10}(d) + 32.4 + 20\log_{10}(f_c). \end{aligned} \tag{3.12}$$

The received signals at D for RIS-assisted scenarios with N reflecting elements is obtained as in (3.2) under plate scattering paradigm with $P_L^R \propto P_L(d_{SR})P_L(d_{RD})$, that is, assuming LoS links for RISs. By considering the same analysis in (3.5), the achievable data rate expressions for a single RIS-assisted system is given by

$$R_{RIS} = \log_2\left(1 + \gamma_{RIS}\right) \tag{3.13}$$

where γ_{RIS} is the received SNR calculated by (3.5).

For the RIS-assisted scenario, the achievable data rate is maximized by aligning the phases of the reflected signals from the RIS to the phase of the direct path with $\Delta\Phi_i = 0$ for $i = 1, 2, ..., N$ as in (3.6).

In Fig. 3.2, achievable data rates under 3GPP and 5G UMi path loss models are respectively given with respect to varying horizontal distance (d_H) between S and RIS for $d_{SD} = 4d_H$, $d_V = 10$ m, $N_0 = -95$ dBm and $p_t = 5$ W. The results are obtained for an operating frequency of 2.4 GHz for the 3GPP UMi path loss model, while 28 GHz is considered for the 5G UMi-Street Canyon path loss model. Here,

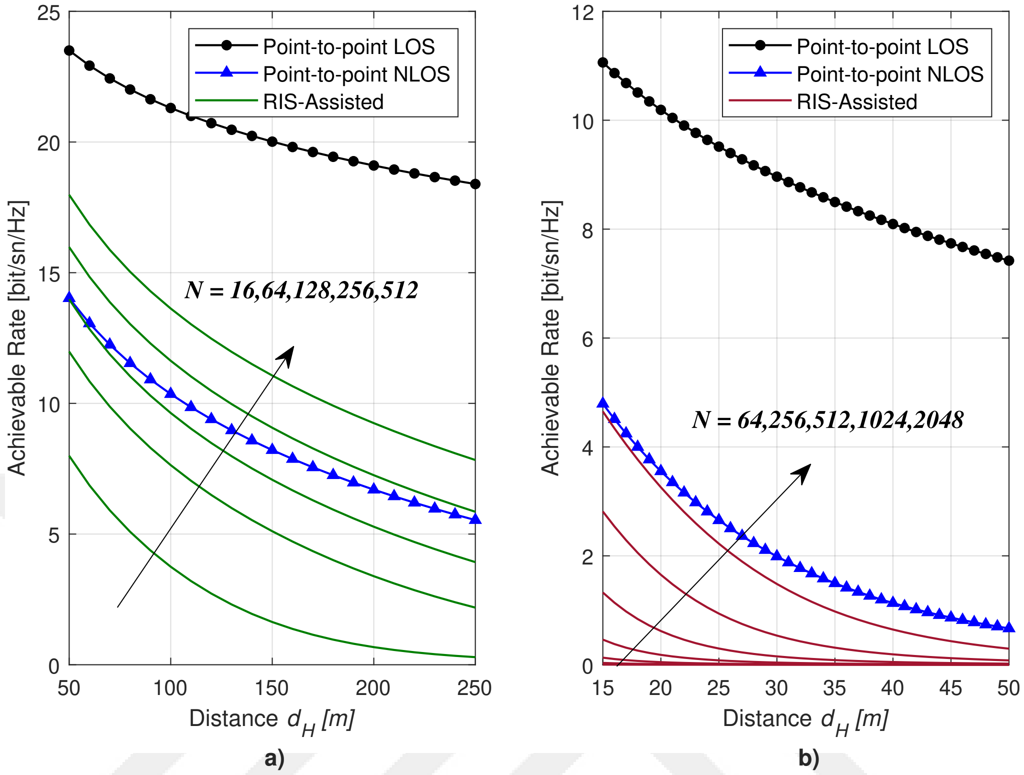

Figure 3.2: The achievable data rate comparison for direct and RIS-assisted transmission under (a) 3GPP UMi path loss model with f_c = 2.4 GHz and (b) 5G UMi-Street Canyon path loss model with f_c = 28 GHz.

the point-to-point physical NLoS link between the S and the D is modeled with Rayleigh distribution and considering the physical NLoS path loss models in (3.11) and (3.12), while the point-to-point LoS link is modeled with Rician distribution and LoS path loss models. In both scenarios, a reliable communication is provided by eliminating the effect of the blocked direct link with increasing N values. It should be also noted that the closer the RIS is placed to the source, the higher the achievable data rate to be reached. Particularly, at high frequencies, in order to transmit at the level of point-to-point LoS scenario, it is necessary to make huge increases in number of reflecting elements, while the same rates can be achieved by using fewer reflectors at 2.4 GHz. Particularly, as shown in Fig. 3.2(b), the achievable rate shows a rapid downfall with increasing distances, since the signals in the mmWave bands are more susceptible to path loss.

3.1.2.2.2 Analysis of Path Loss Exponent Under RISs

Here, we investigate the variation of the average total path loss with respect to distance in an RIS-assisted communication channel and the effect of an RIS on PLE under the log-distance path loss model for different number of reflecting elements for the scenario of Fig.3.1.

3GPP UMi and 5G UMi-Street Canyon path loss models, which are discussed in previous subsection, are utilized to express the path loss of sub-paths, which are defined from S to RIS ($P_L(d_{SR})$) and from RIS to S ($P_L(d_{RD})$). Total received power at the D through the ith RIS element is calculated under the plate scattering paradigm [20] as:

$$p_{r_i} = \frac{p_t G_T |\Gamma_i| G_R}{P_L(d_{SR}) P_L(d_{RD})} \tag{3.14}$$

where G_T and G_R are gains of the transmitter and receiver antennas, respectively. Γ_i is the reflection coefficient of the ith RIS element, which is given by

$$\Gamma_i = e^{-j\varphi_i} G_e^i G_e^r \epsilon_b. \tag{3.15}$$

where φ_i is the phase difference inducted by ith RIS element.

Total received power at the receiver including all RIS elements is expressed as:

$$p_{r_i} = \left(\sum\nolimits_i \sqrt{\frac{p_t G_T |\Gamma_i| G_R}{P_L(d_{SR}) P_L(d_{RD})}} e^{j\phi_i} \right)^2 \tag{3.16}$$

where ϕ_i represents the phase delay of the signal received through ith RIS element.

For simplicity, we assume that RIS-elements reflect signal with unit-gain reflection coefficients ($|\Gamma| = 1$) and in a such way that all the signals coming through different RIS elements are aligned in phase at the receiver ($\varphi_i = \phi_i$). We also assume omni-directional, unit gain antennas in both transmitter receiver. Then (3.16) becomes:

$$p_{r_i} = \left(\sum\nolimits_i \sqrt{\frac{p_t}{P_L(d_{SR}) P_L(d_{RD})}} \right)^2 \tag{3.17}$$

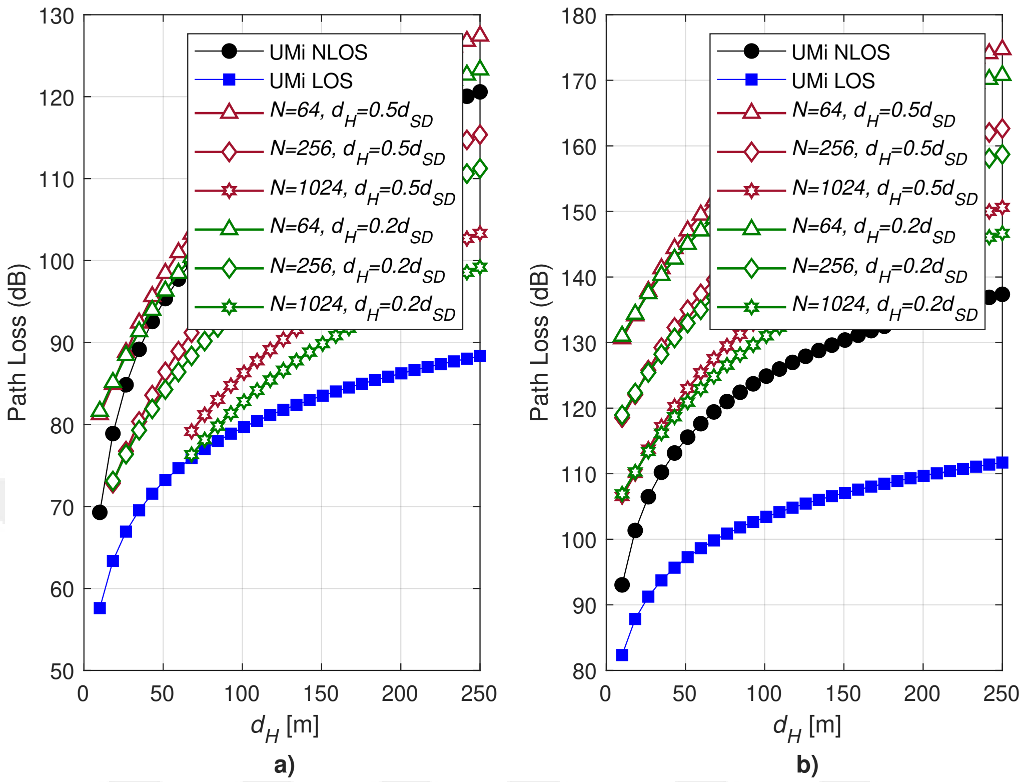

Figure 3.3: Path loss comparison of a single RIS path with varying N and the direct transmission under (a) 3GPP UMi path loss model at 2.4 GHz and (b) 5G UMi-Street Canyon path loss model at 28 GHz.

Therefore the total path loss is given by:

$$P_{L_{TOT}} = \left(\sum\nolimits_i \sqrt{\frac{1}{P_L(d_{SR})P_L(d_{RD})}} \right)^{-2} \tag{3.18}$$

PLE (n) is then calculated by employing log-distance path loss model [85]:

$$P_L(d)\,[\text{dB}] = P_L(d_0) + 10n\log_{10}\left(\frac{d}{d_0}\right) \tag{3.19}$$

where d_0 is the reference distance, which is taken as 10 m.

The effect of an RIS on path loss is investigated for the scenario of Fig. 3.1 for $d_V = 10$ m and d_{SD} from 10 m to 250 m with $N = 64, 256$ and 1024. We consider that the RIS is located both at the midway ($d_H = 0.5d_{SD}$) and closer to D ($d_H = 0.2d_{SD}$). The power received through the NLoS channel is excluded in order

Table 3.1: Path Loss Exponent of RIS Channels

Frequency	RIS Location	PLE (n)
2.4 GHz	No RIS, NLOS	3.67
	No RIS, LOS	2.2
	$d_H = 0.5d_{SD}$	3.08
	$d_H = 0.2d_{SD}$	2.94
28 GHz	No RIS, NLOS	3.17
	No RIS, LOS	2.1
	$d_H = 0.5d_{SD}$	2.94
	$d_H = 0.2d_{SD}$	2.80

to show the RIS effect clearly. The calculated total path loss of the RIS path is shown in Fig. 3.3 with LoS and NLoS UMi path loss models at 2.4 and 28 GHz.

We observe that path loss of the RIS-assisted scenario converges to the system modeled with UMi LoS when number of elements gets higher at lower frequencies. A comparable path loss to the NLoS system is obtained through the RIS path for number of elements greater than 64 at 2.4 GHz, whereas more than 1024 elements are required for NLoS level path loss at 28 GHz. On the other hand, implementation of RISs with higher number of elements is cheaper at high frequencies due to smaller wavelengths. Locating RIS close to one of the terminals yields a minor improvement of 1-2 dB on path loss depending on the distance between terminals over the midway location. Calculated PLEs are listed in Table 3.1. Our results indicate improved PLEs with the RIS paths over the NLoS system model.

Total path loss of RIS assisted channel, including the RIS path and the NLoS path between the terminals from 3GPP UMi and 5G UMi-Street Canyon path loss models is shown in Fig. 3.4 for RISs located at a distance of $0.2d_{SD}$. We observe greater reduction in the path loss at 2.4 GHz in RIS-assisted channel over the NLoS system model when compared to 28 GHz communication channel. Calculated amount of reductions in the RIS-assisted path loss over the NLoS model (ΔP_L) and

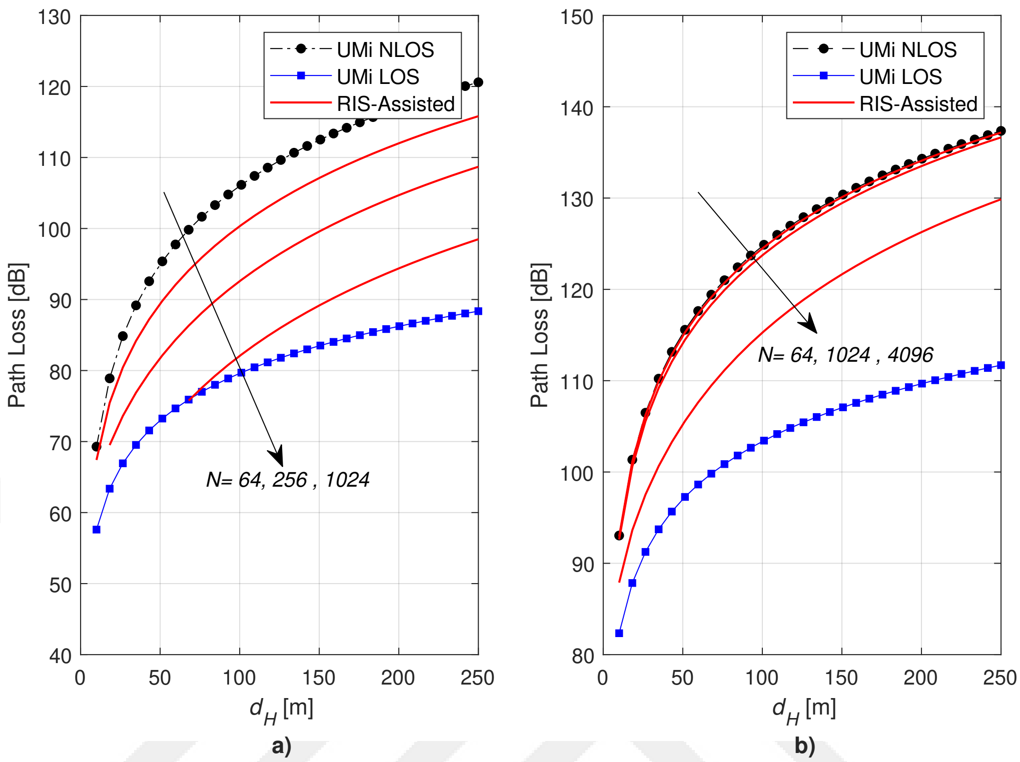

Figure 3.4: Path loss comparison of a single RIS-assisted system with varying N and the direct transmission under (a) 3GPP UMi path loss model at 2.4 GHz and (b) 5G UMi-Street Canyon path loss model at 28 GHz.

the path loss exponents are listed in Table 3.2. 28 GHz channel reduces up to 3.5 dB by use of 1024 RIS elements, whereas 2.4 GHz channel can be improved by an order of 23.8 dB when 1024 RIS elements are in use. RIS assisted channels demonstrate PLEs between NLoS and LoS system models for both frequencies, where as PLE reduces by increasing number of RIS elements. We observe that total path loss reduces inversely by the square of the number of RIS elements when RIS path gets dominant over the NLoS path, which is in agreement with (3.10) and [42] as long as the RIS path is dominant.

Our analysis shows that enhancement and control of path loss and PLE is achievable by use of an RIS in the presence of obstacles blocking the LoS path between the transmitter and the receiver. In other words, an RIS transforms the wireless

Table 3.2: Path Loss Exponent of RIS Assisted Channels

Frequency	N	ΔP_L (dB)	PLE (n)
2.4 GHz	64	5.6	3.373
	256	13.3	3.068
	1024	23.8	2.847
28 GHz	64	0.3	3.159
	256	1	3.130
	1024	3.5	3.038

propagation environment into a controllable entity even by reducing path loss in NLoS propagation environments.

3.1.3 Wireless Communication Through Multiple RISs

In future wireless sytems, the ubiquitous communications of many devices with various sizes are envisaged. However, it may not be reasonable to use multiple antennas or high-power consuming components in those devices to enable reliable and high-speed wireless transmission. Therefore, it becomes necessary to transfer this cost from wireless devices to the available RISs in propagation environments, where we can increase the number of RISs in a more flexible manner. It is worth noting that although many RIS-assisted systems have been investigated in recent times, the communication scenarios with multiple RISs have not been explored in a comprehensive manner so far. Within this perspective, the use of multiple RISs may have the potential to bring more promising advantages in terms of QoS, reliability and flexibility in the system design.

In this section, we conduct performance analysis of multiple RISs under two envisaged scenarios, namely, i) simultaneous transmission over two independent RISs in indoor environments and ii) double-RIS reflected transmission over a single link in outdoor environments. Under these multiple RIS-assisted transmission scenarios, we derive a generalized mathematical framework on the error performance which is

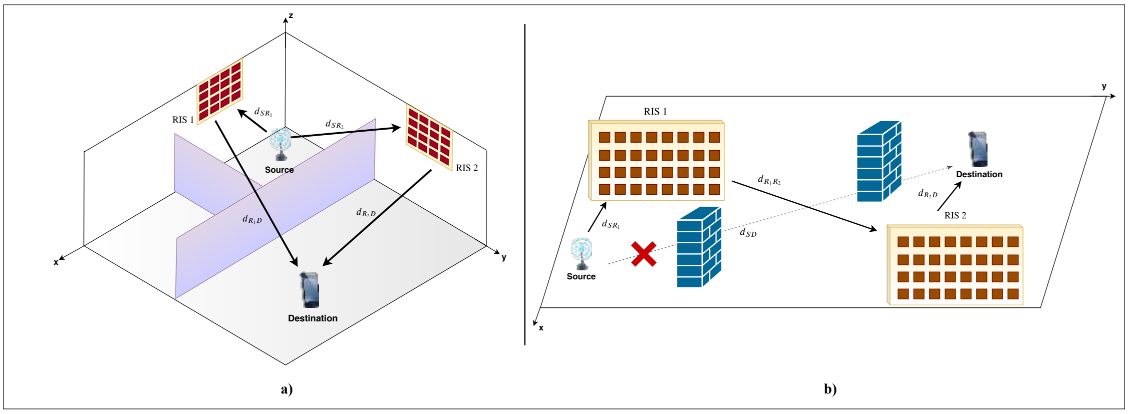

Figure 3.5: Communications over two RISs: (a) Indoor propagation scenario and (b) Outdoor propagation scenario (Each RIS is equipped with N reflecting elements).

valid for various path loss models.

3.1.3.1 Case Study I: Indoor Communications with Multiple RISs

In our first case study, we consider the three dimensional (3D) indoor communications model of Fig. 3.5(a), where the direct path between S and D is blocked owing to the obstacles and the signal transmission is accomplished over two independent paths supported by two different RISs. This indoor scenario, which is given in 3D Cartesian coordinate system, includes typical open and closed large office environments with a maximum S-D separation of 100 m.

In this setup, d_{SR_k} and d_{R_kD} respectively represent the distances of S-to-kth RIS and kth RIS-to-D for $k = 1, 2$. Furthermore, small-scale fading coefficients of the S-to-kth RIS and kth RIS-to-D channels are denoted by $h_i^{SR_k}$ and $h_i^{R_kD}$ for $i = 1, 2, ..., N_k$ and $k = 1, 2$, respectively. In this scenario, RIS 1 is located along the x-z plane and has N_1 reflectors, while RIS 2 is located along the y-z plane with N_2 reflectors.

Under the condition of slow and flat Rician fading channels with Rician factor

K, the baseband signal at D is given by

$$r = \sqrt{p_t}\left[\sqrt{P_L^1}\sum\nolimits_{i=1}^{N_1} h_i^{SR_1} e^{j\phi_i^{(1)}} h_i^{R_1 D} + \sqrt{P_L^2}\sum\nolimits_{j=1}^{N_2} h_j^{SR_2} e^{j\phi_j^{(2)}} h_j^{R_2 D}\right] x + w \tag{3.20}$$

where P_L^k stands for path loss of kth RIS-assisted link and $\phi_i^{(k)}$ denotes the induced phase by ith reflecting element of kth RIS for $k = 1, 2$. The channels can be represented by $h_i^{SR_1} = \alpha_i^{(1)} e^{-j\theta_i^{(1)}}$, $h_i^{R_1 D} = \beta_i^{(1)} e^{-j\varphi_i^{(1)}}$, $h_j^{SR_2} = \alpha_j^{(2)} e^{-j\theta_j^{(2)}}$, and $h_j^{R_2 D} = \beta_j^{(2)} e^{-j\varphi_j^{(2)}}$ in terms of their amplitudes and phases. Therefore, (3.20) can be expressed as

$$r = \sqrt{p_t}\left[\sqrt{P_L^1}\sum\nolimits_{i=1}^{N_1} \alpha_i^{(1)} \beta_i^{(1)} e^{j\Delta\Phi_1} + \sqrt{P_L^2}\sum\nolimits_{j=1}^{N_2} \alpha_j^{(2)} \beta_j^{(2)} e^{j\Delta\Phi_2}\right] x + w \tag{3.21}$$

where $\Delta\Phi_1 = \phi_i^{(1)} - \theta_i^{(1)} - \varphi_i^{(1)}$ and $\Delta\Phi_2 = \phi_j^{(2)} - \theta_j^{(2)} - \varphi_j^{(2)}$ are phase difference terms.

The instantaneous SNR at D can be expressed as

$$\gamma = \frac{\left|\sqrt{P_L^1}\sum_{i=1}^{N} \alpha_i^{(1)} \beta_i^{(1)} e^{j\Delta\Phi_1} + \sqrt{P_L^2}\sum_{j=1}^{N} \alpha_j^{(2)} \beta_j^{(2)} e^{j\Delta\Phi_2}\right|^2 p_t}{N_0}. \tag{3.22}$$

In (3.22), the SNR is maximized with the phase alignment satisfying $\Delta\Phi_1 = \Delta\Phi_2 = 0$, for all $i = 1, 2, ..., N_1$ and $j = 1, 2, ..., N_2$; therefore, the maximized SNR can be obtained as in (3.4):

$$\gamma_{\max} = \frac{\left|\sqrt{P_L^1}\sum_{i=1}^{N_1} \alpha_i^{(1)} \beta_i^{(1)} + \sqrt{P_L^2}\sum_{j=1}^{N_2} \alpha_j^{(2)} \beta_j^{(2)}\right|^2 p_t}{N_0} = \frac{A^2 p_t}{N_0}. \tag{3.23}$$

It should be noted that $\alpha_i^{(k)}$ and $\beta_i^{(k)}$ $(k = 1, 2)$ are independent and follow Rician distribution. In (3.23), the random variable A is the sum of N_1 and N_2 random variables. If $N_1 \gg 1$ and $N_2 \gg 1$, A follows Gaussian distribution, and its mean and variance are respectively given as follows:

$$\begin{aligned} \mathrm{E}[A] &= \frac{\left(N_1\sqrt{P_L^1} + N_2\sqrt{P_L^2}\right)\pi}{4(K+1)} L_{1/2}^2\left(-\frac{K^2}{(K+1)}\right), \\ \mathrm{VAR}[A] &= \left(N_1 P_L^1 + N_2 P_L^2\right)\left(1 - \frac{\pi^2 L_{1/2}^4\left(-\frac{K^2}{(K+1)}\right)}{16(K+1)^2}\right). \end{aligned} \tag{3.24}$$

It is worth noting that γ will have the same distribution regardless of the type of small-scale fading due to the CLT. In order to show effectiveness of our analyses, using the MGF approach and following the same steps as in Section II with (3.8) as well as methodologies in [77] and [12], upper bounded SEP for BPSK can be obtained as

$$P_e \leq \frac{0.5\exp\left(\frac{-\frac{\left(N_1\sqrt{P_L^1}+N_2\sqrt{P_L^2}\right)^2\pi^2 L_{1/2}^4\left(-K^2/(K+1)\right)p_t}{16(K+1)^2N_0}}{1+\frac{\left(N_1P_L^1+N_2P_L^2\right)\left[16(K+1)^2-\pi^2L_{1/2}^4(-K^2/(K+1))\right]p_t}{8(K+1)^2N_0}}\right)}{\sqrt{1+\frac{\left(N_1P_L^1+N_2P_L^2\right)\left[16(K+1)^2-\pi^2L_{1/2}^4(-K^2/(K+1))\right]p_t}{8(K+1)^2N_0}}}. \tag{3.25}$$

We can generalize this simultaneous transmission scenario with two RISs to the general case of N_S independent RISs. If each independent RIS consist of N reflector elements and path losses of all paths are approximately equal with $P_L^i = P_L$ $(i = 1, 2, \ldots, N_S)$, the generalized SEP is expressed as follows for BPSK:

$$P_e \leq \frac{0.5\exp\left(\frac{-\frac{N_S^2N^2P_L\pi^2L_{1/2}^4\left(-K^2/(K+1)\right)p_t}{16(K+1)^2N_0}}{1+\frac{N_SNP_L\left[16(K+1)^2-\pi^2L_{1/2}^4(-K^2/(K+1))\right]p_t}{8(K+1)^2N_0}}\right)}{\sqrt{1+\frac{N_SNP_L\left[16(K+1)^2-\pi^2L_{1/2}^4(-K^2/(K+1))\right]p_t}{8(K+1)^2N_0}}}. \tag{3.26}$$

While the error performance is inversely proportional to $\left(N_1\sqrt{P_L^1}+N_2\sqrt{P_L^2}\right)^2$ in the two RIS-assisted transmission, the simultaneous transmission in the presence of N_S different RISs provides

$$P_e \propto \exp\left(-\frac{N_S^2N^2P_L\pi^2L_{1/2}^4\left(-K^2/(K+1)\right)p_t}{16(K+1)^2N_0}\right) \tag{3.27}$$

where N_SN is the total number of reflectors in the system. In (3.27), it is observed that the error performance is inversely proportional to $(N_SN)^2$, which provides more flexibility in design when the RIS sizes are limited in indoor environments. In other terms, instead of employing a single large RIS, the same performance can be provided by multiple smaller RISs, which is better suited to indoor applications.

3.1.3.2 Case Study II: Outdoor Communications with Multiple RISs

The system model of the double-RIS reflected transmission in outdoor propagation environment is illustrated in Fig. 3.5(b). Here, since the multi-hop RISs-assisted scenarios will deteriorate the received signal power due to the multiplicative path loss, the available RISs have been placed in parallel instead of serial to prevent the loss in the received signal. The outdoor scenario, which is modeled in 2D Cartesian coordinates, includes typical dense urban environments with a minimum S-D separation above 100 m. In this scenario, since the direct path between S and D is blocked, the signal is transmitted via two RISs located near to S and D. This system can be used to alleviate the shortcomings of the use-cases that may arise particularly in outdoor environments in 6G and beyond communications systems, especially in mmWave and THz bands. For instance, if it is desired to convey data in an outdoor environment over a long-distance, at high frequencies, the signal can be attenuated or lost due to many obstacles in between. In this case, the nearest RISs, which are equipped with N reflecting elements, are chosen by S and D for transmission, and communication is carried out by these RISs. We later show that using two RISs, the wireless environment is transformed into a virtual MIMO system.

The double-RIS reflected transmission scenario includes a single path from S to D. The channels between S-to-RIS 1 and RIS 2-to-D can be modeled as deterministic LoS channels while the channel between ith element of RIS 1-to-jth element of RIS 2 $h_{ij}^{R_1R_2}$ is modeled by Rician fading with K factor for $i = 1, 2, ..., N$ and $j = 1, 2, ..., N$. Distance of the S-to-RIS 1, RIS 1-to-RIS 2 and RIS 2-to-D is respectively denoted by d_{SR_1}, $d_{R_1R_2}$ and d_{R_2D}. d_{SR_1} and d_{R_2D} are sufficiently small such that small-scale fading can be ignored. From the standpoint of channel amplitudes and phases, $h_{ij}^{R_1R_2}$ can be expressed as $h_{ij}^{R_1R_2} = \beta_{ij}e^{-j\varphi_{ij}}$.

The baseband signal at D is obtained as follows:

$$r = \sqrt{p_t P_L^R}\left(\sum\nolimits_{i=1}^{N}\sum\nolimits_{j=1}^{N} e^{j\phi_i^{(1)}} h_{ij}^{R_1R_2} e^{j\phi_j^{(2)}}\right) x + w \tag{3.28}$$

where $\phi_i^{(k)}$ is as defined in (3.20). Then, the instantaneous SNR at D can be easily calculated as

$$\gamma = \frac{\left|\sqrt{P_L^R}\sum_{i=1}^{N}\sum_{j=1}^{N}\beta_{ij}e^{j(\phi_i^{(1)}+\phi_j^{(2)}-\varphi_{ij})}\right|^2 p_t}{N_0}. \tag{3.29}$$

SNR at D is maximized with the phase elimination ($\phi_i^{(1)}+\phi_j^{(2)} = \varphi_{ij}$ for $i = 1, 2, ..., N$

and $j = 1, 2, ..., N$). Consequently, the maximized SNR is obtained as

$$\gamma_{\max} = \frac{\left| \sqrt{P_L^R} \sum_{i=1}^{N} \sum_{j=1}^{N} \beta_{ij} \right|^2 p_t}{N_0} = \frac{A^2 p_t}{N_0} \tag{3.30}$$

where A follows Gaussian distribution with $N^2 \sqrt{P_L^R} \sqrt{\pi/(4(K+1))} L_{1/2}\left(-K^2/(K+1)\right)$ mean and $N^2 P_L^R \left(1 - \pi/(4(K+1)) L_{1/2}^2\left(-K^2/(K+1)\right)\right)$ variance due to the CLT for $N \gg 1$. Then, following the same steps as in previous sections, the upper bounded SEP for BPSK can be obtained using (3.8) as

$$P_e \leq \frac{1}{2} \left(\frac{\exp\left(- \frac{\frac{N^4 P_L^R \pi L_{1/2}^2\left(-K^2/(K+1)\right) p_t}{4(K+1)N_0}}{1 + \frac{N^2 P_L^R \left[4(K+1) - \pi L_{1/2}^2\left(-K^2/(K+1)\right)\right] p_t}{2(K+1)N_0}} \right)}{\left(1 + \frac{N^2 P_L^R \left[4(K+1) - \pi L_{1/2}^2(-K^2/(K+1))\right] p_t}{2(K+1)N_0}\right)^{1/2}} \right). \tag{3.31}$$

As can be seen from (3.31), in the low SNR region, the error performance of the double-RIS reflected transmission systems (P_e) can be approximated by

$$P_e \propto \exp\left(- \frac{N^4 P_L^R \pi L_{1/2}^2\left(-K^2/(K+1)\right) p_t}{4(K+1)N_0} \right). \tag{3.32}$$

The term N^4 in (3.32) brings a significant improvement in error performance due to the virtual $N \times N$ MIMO channel created between RIS 1 and RIS 2. It should be also noted that (3.31) can be used with various path loss models directly, while for other small-scale fading models, only slight modifications are required using the MGF approach due to the CLT. While the employing two serial RISs deteriorates the received signal power, it will be possible to maintain a reliable transmission particularly in systems with low power consumption and for cell-edge users by increasing the number of RIS elements and positioning the available RISs appropriately.

3.1.3.3 RIS Selection Strategies

Although it is possible to improve the QoS using multiple RISs in future wireless networks, this will increase the overall complexity and render simultaneous phase adjustment a challenging task. By utilizing RIS selection over multiple RISs, a low-complexity and cost-effective transmission can be provided while many advantages

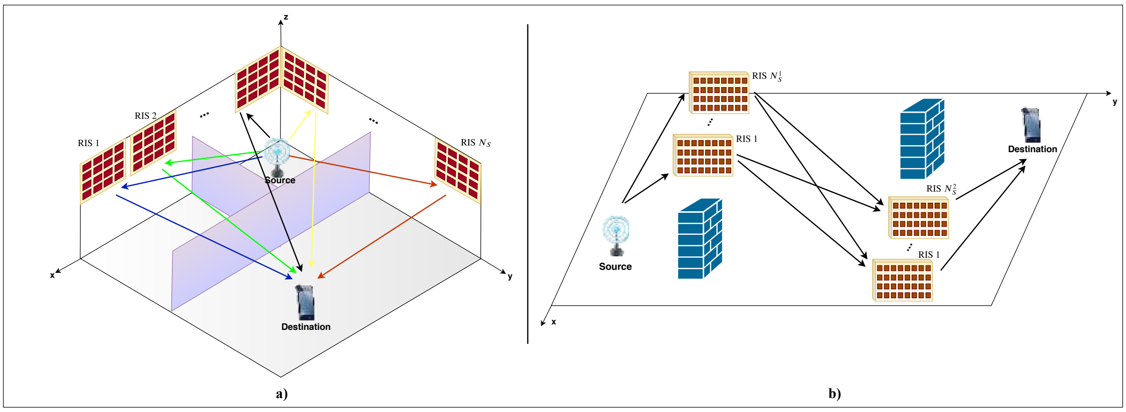

Figure 3.6: RIS-selection based transmission over multiple RISs: (a) Indoor propagation scenario and (b) Outdoor propagation scenario .

of multiple RIS-assisted systems are preserved. For this purpose, we propose the novel concept of RIS selection for the communication scenarios of Fig. 3.6.

As shown in Fig. 3.6(a), N_S RISs are placed in an indoor propagation environment, where each RIS has N reflecting elements. Here, d_{SR_k} and d_{R_kD} respectively represent the distances of S-to-kth RIS and kth RIS-to-D for $k = 1, 2, \ldots, K$. Furthermore, small-scale fading coefficients of the S-to-kth RIS and kth RIS-to-D channels are denoted as in (3.17) by $h_i^{SR_k} = \alpha_i^{(k)} e^{-j\theta_i^{(k)}}$ and $h_i^{R_kD} = \beta_i^{(k)} e^{-j\varphi_i^{(k)}}$ for $i = 1, 2, \ldots, N$ and $k = 1, \ldots, N_S$, respectively. The received SNR of the signal transmitted through only the kth RIS (γ_k) is calculated as

$$\gamma_k = \frac{\left| \sum_{i=1}^{N} \sqrt{P_L^i} \alpha_i^{(k)} \beta_i^{(k)} e^{j\Delta\Phi_i^k} \right|^2 p_t}{N_0}. \tag{3.33}$$

where $\Delta\Phi_k = \phi_i^{(k)} - \theta_i^{(k)} - \varphi_i^{(k)}$ is the phase difference for the kth path. Considering the maximized SNR values as in (3.18), an RIS selection is conducted over N_S RISs to choose the RIS, which has highest SNR, for transmission as

$$\gamma'_{\text{In}} = \max(\gamma_{\max,1}, \gamma_{\max,2}, \ldots, \gamma_{\max,k}) \tag{3.34}$$

where γ'_{In} is the maximized received SNR for RIS selection based system in indoor environment and $\gamma_{\max,k}$ is the maximized SNR of the kth path with proper phase adjustment. Here, we focus on the selection of a single RIS while a generalization might be straightforward.

The generalized system model of the RIS selection based outdoor communication system is illustrated In Fig. 3.6(b). In this model, we assume N_S^1 and N_S^2 RISs, respectively, within the proximity of the transmitter and receiver. Here, the distances of S-to-RIS k, RIS k-to-RIS l and RIS l-to-D are respectively denoted by d_{SR_k}, $d_{R_kR'_l}$ and $d_{R'_lD}$ for $k = 1, \ldots, N_S^1$ and $l = 1, \ldots, N_S^2$ as in (3.28). In this setup, $N_S^1 \times N_S^2$ possible transmission paths are available for communications. By selecting the path that has the highest SNR, the overall cost can be reduced using a single RIS for each terminal. As in (3.30), the maximized SNR is obtained for each path as $\gamma_{\max}^{k,l}$. Therefore, RISs selection for outdoor environment is conducted over $N_S^1 \times N_S^2$ paths as

$$\gamma'_{\text{Out}} = \max_{k,l} \, (\gamma_{\max}^{k,l}) \tag{3.35}$$

where γ'_{Out} is the maximized received SNR for RIS selection based systems in outdoor environment.

3.1.4 Numerical Results

In this section, we used simulation models and studied the effects of various RIS applications taking into account path losses and channel fadings. For all simulations in this section, path loss is modeled as in (3.3), such as $P_L^R \propto (d_{SR}d_{RD})^{-2}$. The common parameters for simulations are set up as follows: $K = 10$ dB, $G_T = 1$, $G_R = 1$, $G_e^i = G_e^r \cong 5$ dBi as in [20].

In Fig. 3.7, we show the bit error rate (BER) of the single-RIS assisted scheme in Fig. 3.1 versus p_t/N_0, where p_t is the power consumed for transmission. Here, the simulations are conducted under $f_c = 2.4$ GHz, $d_{SR} = 25$ m and $d_{RD} = 75$ m. In order to make a fair comparison, we assume that the equal power is consumed for all systems ($p_t = 1$) and BPSK is employed. As clearly seen from Fig. 3.7, the simulation and exact analytical BER results in (3.10) are in close agreement for high N values due to the CLT. By doubling the number of reflectors, approximately a 6

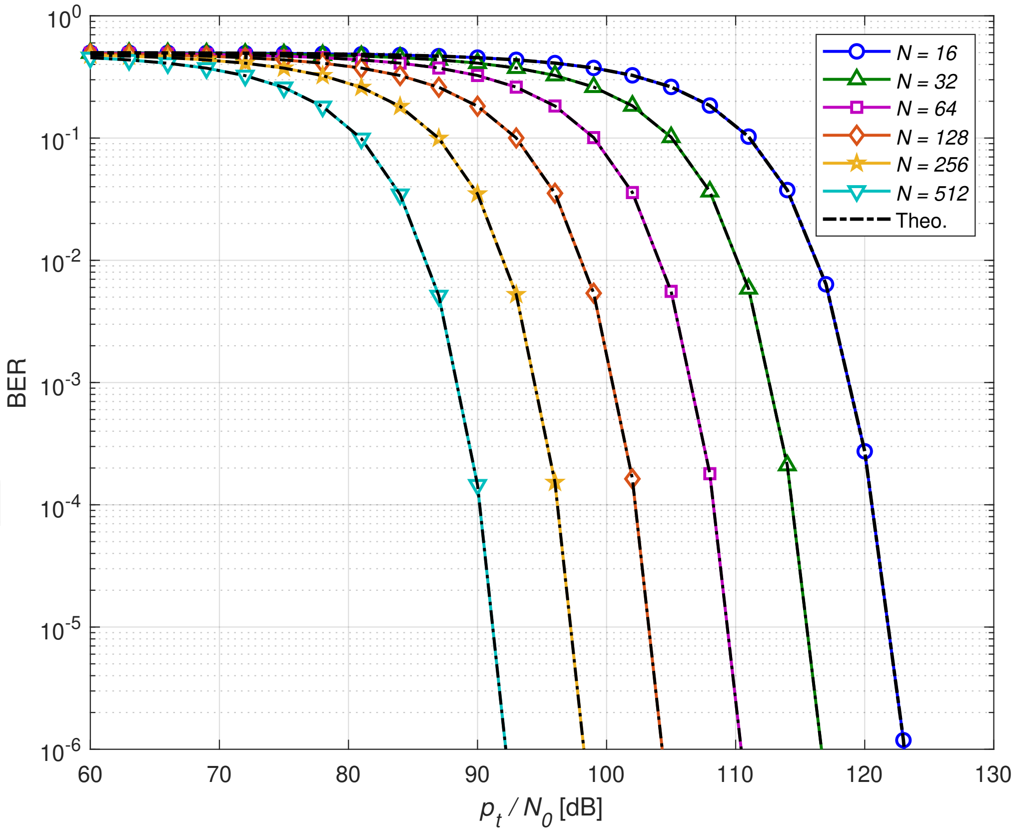

Figure 3.7: BER performance of the single-RIS assisted system for BPSK signaling and varying N values.

dB improvement in the required SNR is achieved, P_e is inversely proportional to N^2 as observed in (3.10).

In Fig. 3.8, the effect of using two simultaneous RISs on the achievable data rate in an indoor office environment with the dimensions of 50 m×50 m×10 m is investigated. In this comparison, achievable data rate analysis of two RISs-assisted and single RIS-assisted systems are performed. Considering the transmission scenario in Fig. 3.5(a), the first RIS with N_1 reflectors is located at $(20, 0, 10)$, while the second RIS with N_2 reflectors is located at $(0, 25, 10)$. Assuming that the source, which is located at $(5, 5, 0)$, transmits information to an user by using RISs-assisted LoS path. The position of the user changes along the x-axis as $(d_x, 40, 0)$. For the single-RISs-assisted scenario, only the first RIS is activated during transmission

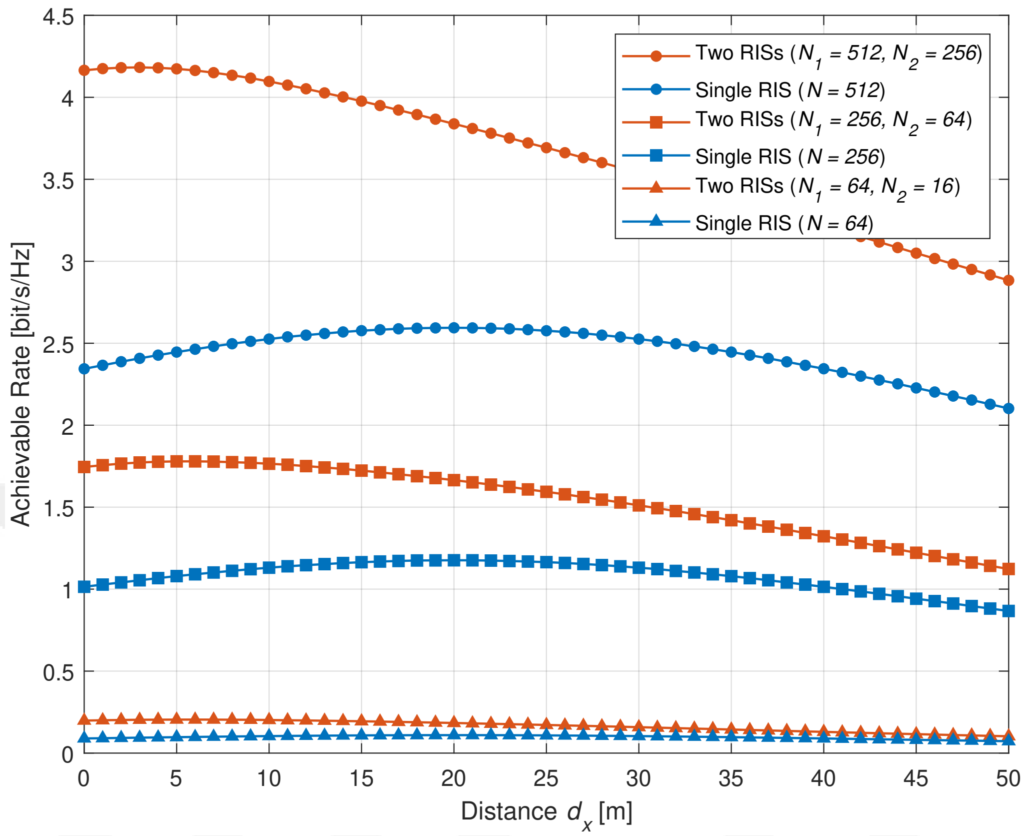

Figure 3.8: Comparison of achievable data rate performance for the two simultaneous RISs assisted system with a single-RIS assisted system in an indoor transmission scenario.

and results are obtained for both systems at 30 GHz operating frequency. Thus, a significant increase in achievable data rate is obtained for changing locations of the user by activating two simultaneous RISs during transmission.

In Fig. 3.9(a), the analytical error performance of systems with single and two RISs in an indoor environment is examined by making comparisons with a reference system utilizing only the direct point-to-point LoS transmission without small-scale fading. The distances are taken as $d_{SD} = 50$ m in the point-to-point LoS system, $d_{SR} = 20$ m, $d_{RD} = 40$ m in the single RIS-assisted system, and $d_{SR_1} = 10$ m, $d_{SR_2} = 15$ m, $d_{R_1D} = 40$ m, $d_{R_2D} = 35$ m in two simultaneous RIS-assisted setup. 30 GHz operating frequency is considered for this comparison. In addition to in-

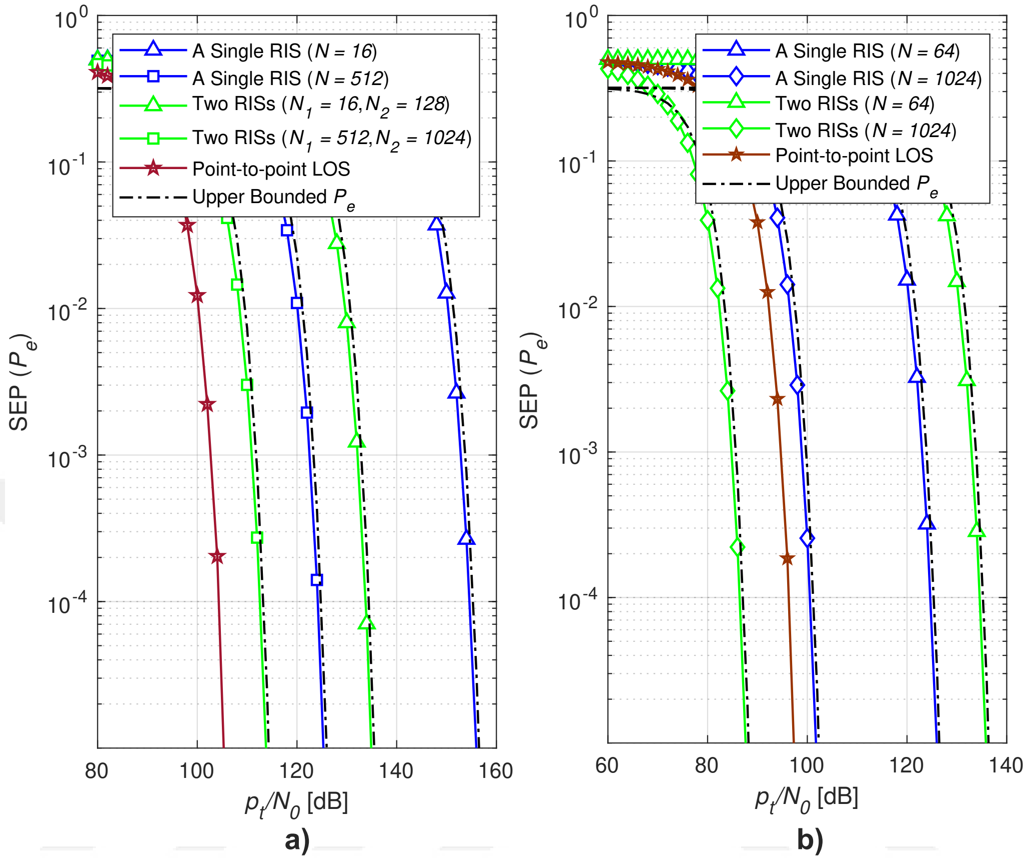

Figure 3.9: Comparison of exact and upper bounded average SEP for the RIS-assisted scenarios in (a) indoor environment and (b) outdoor environment under BPSK.

creasing the data rate, when two RISs are activated simultaneously, it is possible to achieve significant performance increases in the SEP. When N_1 and N_2 are increased sufficiently, it is theoretically possible to achieve the performance of point-to-point LoS communication. In Fig. 3.9(b), we demonstrate the transformative effect of using multiple RISs on the propagation medium. In this comparison, SEP analysis of the double RIS reflected system as illustrated in Fig. 3.5(b) and a single RIS-assisted system in an outdoor environment at 2.4 GHz operating frequency. Here, the point-to-point LoS transmission scenario without fading is considered as a reference. The distances are taken as $d_{SD} = 245$ m in the point-to-point LoS system, $d_{SR} = 75$ m, $d_{RD} = 165$ m in the single RIS-assisted system, and $d_{SR_1} = 20$ m,

$d_{R_1R_2} = 200$ m, $d_{R_2D} = 20$ m in double RIS reflected transmission setup. As clearly seen, even a single RIS with sufficiently large number of reflecting elements RIS can provide an effective solution even if the transmission link is blocked. Furthermore, the double-RIS system provides a better error performance than the other setups when $N = 1024$, since P_e is inversely proportional to the fourth power of the number of reflectors ($P_e \propto N^{-4}$) while we have $P_e \propto (2N)^{-2}$ in simultaneous transmission scenario over two RISs and $P_e \propto N^{-2}$ in a single RIS-assisted system for low p_t/N_0 values. It should be noted that the double-RIS reflected scheme is the most challenging scheme in its design while offering a far better error performance than the others. In other words, it is possible to convert a fading channel to a superior communication channel that acts as a non-fading one by intelligent reflections. It can be also stated that the direct path is transformed into an $N \times N$ virtual MIMO channel with the help of RISs, located close to the transmitter and receiver and each of which contains N reflectors in the double-RIS reflected transmission setup.

In Fig. 3.10, we implement RIS selection strategies for indoor and outdoor scenarios depicted in Fig. 3.6. First, we consider the indoor transmission with three available RISs by selecting the best one from (3.34). Instead of a single RIS-assisted transmission, a best path can be selected among the three possible RIS-assisted paths with the following coordinates of RISs: $(0, 35, 10)$, $(20, 0, 10)$, $(0, 15, 10)$. It is assumed that all RISs are equipped with N reflectors due to the simplicity and $p_t = 5$ W for all systems. The source, which operates at 28 GHz, and user is respectively located at $(5, 5, 0)$ and $(d_x, 40, 0)$. As shown in Fig. 3.10(a), the RIS selection based transmission provides a better data rate performance than single RIS-assisted systems when the direct path is blocked for $N = 64$ and 128. Furthermore, the RIS selection strategy enables a flexible transmission in outdoor propagation environment when the direct path is blocked. When two RISs are available for both the transmitter and the receiver ($N_S^1 = 2$ and $N_S^2 = 2$) as illustrated in Fig. 3.5(b), transmission can be carried out over four possible links ($N_S^1 \times N_S^2 = 4$). In this case, the RIS pairs that provide the highest SNR value are selected by using (3.35) and transmission is provided via a single path. Using the system models in

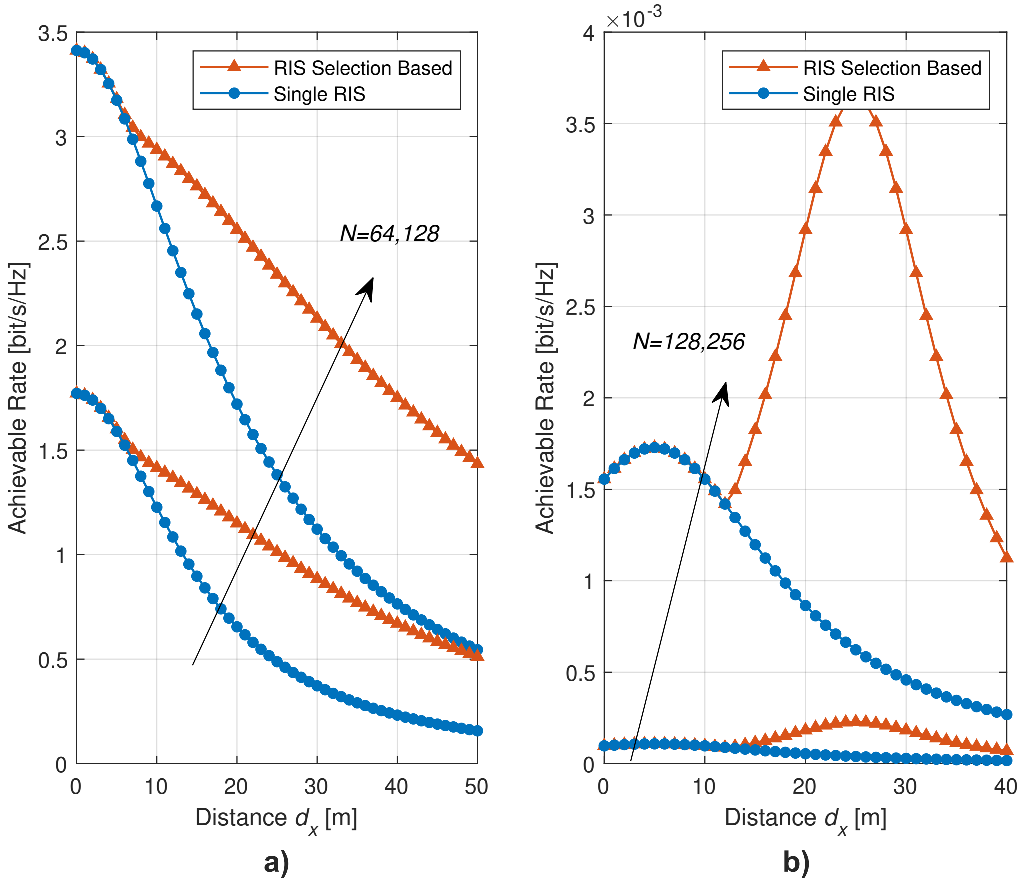

Figure 3.10: Comparison of achievable data rate performance for RIS selection based systems with single and multiple RIS-assisted systems in (a) indoor environment and (b) outdoor environment.

(3.28), the coordinates along the x-y plane for the four RISs are assumed as follows: $(0, 15)$, $(20, 10)$, $(5, 215)$, $(25, 220)$. The source and user are respectively located at $(0, 0)$ and $(d_x, 230)$. The results are obtained by assuming that the user moves along the x-axis. The system which always use a same path for transmission is considered as a reference system for the comparison. As shown in Fig. 3.10(b), an improved achievable data rate performance is obtained under RISs selection with respect to double reflected two-RISs assisted systems without selection while the overall system complexity and phase adjustment costs are decreased. RIS selection based system offers a flexible mechanism by choosing the most reliable path under varying locations and distances. Here, under the changing position of the user on

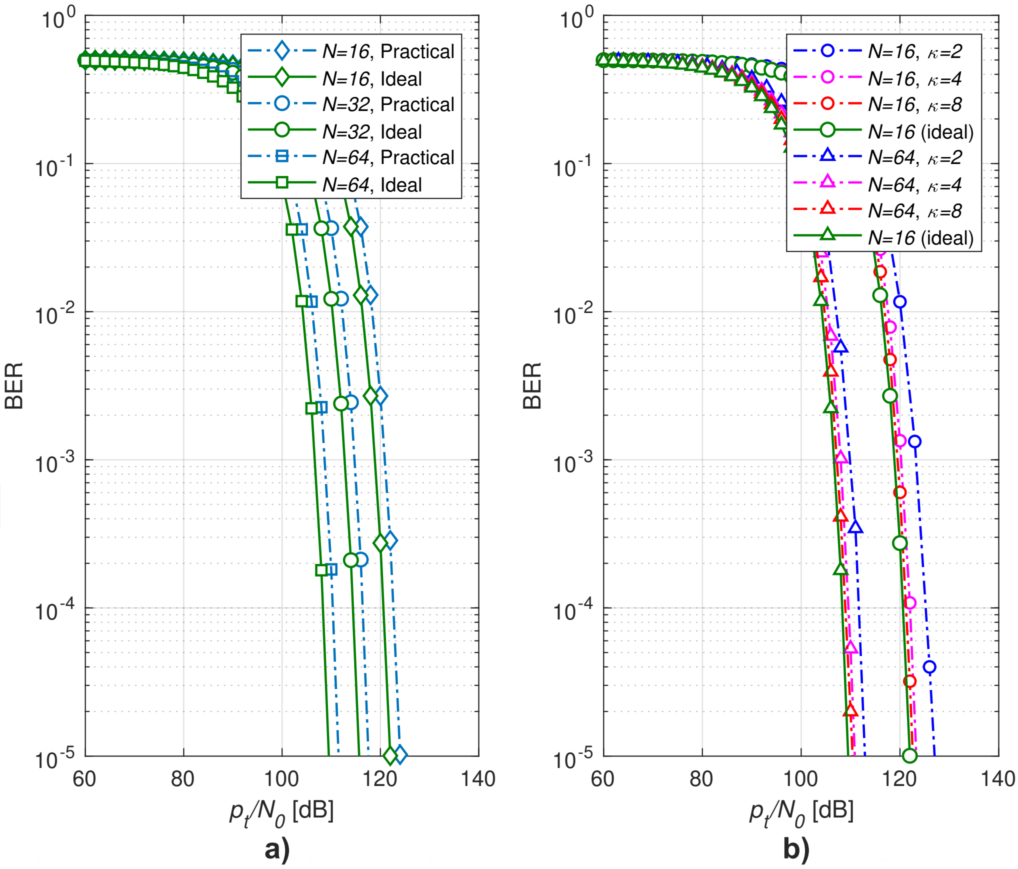

Figure 3.11: BER performance evaluations under the non-ideal conditions: (a) Transmission with practical reconfigurable meta-surface realization and (b) Transmission under imperfect channel phase knowledge.

the x-axis, the best performance is expected to be observed in the regions where the user is close to one of the RISs. Therefore, the highest achievable rate performance is seen where the user is located at 5 and 25 m on the x-axis. Moreover, the most dominant factor in the RIS selection is the path loss rather than small-scale fading. It should be noted that the best way to ensure a reliable transmission is choosing the shortest path for transmission under same fading conditions.

In order to give useful insights into the practical implementation of RISs, we consider the practical reconfigurable metasurface designed in [91]. This metasurface is capable of adjusting reflection phases from $-150°$ to $140°$ for $|\Gamma| = -1$ dB. In Fig. 3.11(a), under a single RIS-assisted scenario, an error performance comparison is given for this RIS and the ideal one, which is capable of reflecting the signal within the $[-180°, 180°]$ phase range for $|\Gamma| = 0$ dB. We observe that even in the case of non-ideal RIS-assisted transmission, there will be no significant changes in error performance. Another problem that may be encountered in real world applications is the imperfect estimation of the channel phase and channel state information. This imperfect phase estimation results in the worsening of the received SNR by preventing the constructive combination of received signals [92]. It is assumed that the phase estimation errors follow a zero-mean von Mises distribution with the concentration parameter κ [93], where κ is a measure of the estimation accuracy. In Fig. 3.11(b), a single RIS-assisted system under imperfect and ideal phase estimation is investigated in terms of the error performance for varying κ and N values. Although small κ values lead to a degradation in error performance, this effect is less noticeable for large N and κ.

3.1.5 Conclusions

In this work, we provide unique RIS-oriented solutions for potential communication scenarios that may emerge in 6G and beyond wireless networks. In this context, we investigate a number of RIS-assisted systems with single or multiple RISs, in terms of error performance, achievable data rate and path loss characteristics in indoor and outdoor environments. To our knowledge, for the first time, our work explores the effect of RISs on the overall path loss under empirical path loss models and the cases of multiple RISs, as well as RIS selection strategies, using a unified error performance framework. Our simulation results indicate that RIS-assisted link acts as an LoS path by suppressing the effect of blocked paths when the number of reflecting elements increases and double-RIS reflected transmission further improves the performance. In other words, one can eliminate the need for LoS transmission utilizing emerging RISs and multiple RIS-assisted systems may be a potential remedy for future dense wireless networks. Since channel estimation and reconfiguration of the phases of the RIS are challenging tasks particularly in multi-RISs and multi-user cases [94], deep learning based solutions can be considered as effective solutions in order to alleviate massive training overhead and complex phase adjustment [95]. We also note that the extension to MIMO and multi-user setups appears as an interesting future research direction. We note that our indoor/outdoor single/multi-RIS communication models can be extended to multi-user system in future studies. To sum up, the communication with real-time controlled RISs can be considered as an exciting technology to meet the demands of 6G and beyond wireless networks.

3.2 Enhanced Coverage through Combined RIS-Aided Reflecting and Decode-and-Forward Relaying Techniques

3.2.1 Introduction

The unprecedented increase in data traffic in recent years has led researchers to explore new horizons beyond the existing paradigms. Although many innovative applications, such as virtual reality, autonomous vehicles, and telemedicine, are being introduced with the fifth-generation (5G) wireless networks, researchers have begun to establish the foundation for 6G wireless networks to fulfill the stringent requirements of the upcoming Internet-of-Everything (IoE) era [4]. In order to accomplish these requirements, reconfigurable intelligent surfaces (RISs) have been regarded as one of the key technologies, owing to their capability to reconfigure the propagation environment with software-controlled reflection [12, 17, 96].

Recently, RIS-aided transmission techniques have recently attracted considerable attention from the research community [39, 63, 97]. In this context, the distinctions between RIS and relaying technologies have been extensively investigated. RISs and relaying technologies are considered as similar technologies to improve the system performance, the received signal is actively processed at the relay, while the RIS only reflects the incident signal without any active transmit module [65]. In [98], the authors compare the energy efficiency of RIS and half-duplex (HD) decode-and-forward (DF) relay-aided transmissions, and they observe that the RIS can achieve the performance of a relaying system by using a large number of reflecting elements. Furthermore, in [99], the authors propose a full-duplex (FD) relay-assisted system incorporating two horn antennas and two RISs near to the relay, and obtain enhancement at an achievable rate even with a small number of reflecting elements. Although rendering end-to-end channel estimation challenging in the case of large numbers of communication nodes and terminals, the using two horn antennas for the FD relay will bring increased hardware costs. A hybrid transmission scenario combining a RIS-aided transmission with a DF relay is introduced in [100] and it is demonstrated that using a single relay for low SNR values surpasses a RIS with a huge number of reflecting elemenets, while for high SNRs, RIS-aided transmission is superior. In [101], the authors recently comnide the RIS and FD relay to enable reliable communication, and a semi-definite relaxation-based approach is also presented to deal with a non-convexity.

As pointed out in the previous discussion, most of the studies related to relaying and RISs consider one of these technologies as an alternative solution to the other. Against this background, in this study, we aim to find the best transmission scenarios where these two exciting technologies efficiently work. In the context of RIS-assisted transmission, the relay serves as an additional component that enhances performance. By engaging the relay, hybrid transmission can effectively counteract rapid variations in channel quality. The primary objective here is to create hybrid systems that incorporate both RIS and relay technologies, optimizing for reduced operational complexity while maintaining their individual benefits. Towards achieving this, the study introduces two distinct, cost-effective approaches aimed at expanding coverage without resorting to multi-hop relaying. Moreover, the study explores optimal placement strategies for both the RIS and relay, particularly in scenarios where the direct link between the Tx and Rx is obstructed.

3.2.2 Signal and Propagation Model

In this section, the hybrid RIS and relay-assisted systems are introduced as well as explaining their working mechanisms. We proposed two novel hybrid transmission concepts, where an RIS and a DF relay are positioned between the source (S) and the destination (D). Here, the relay is assumed to operate as an HD relay and the

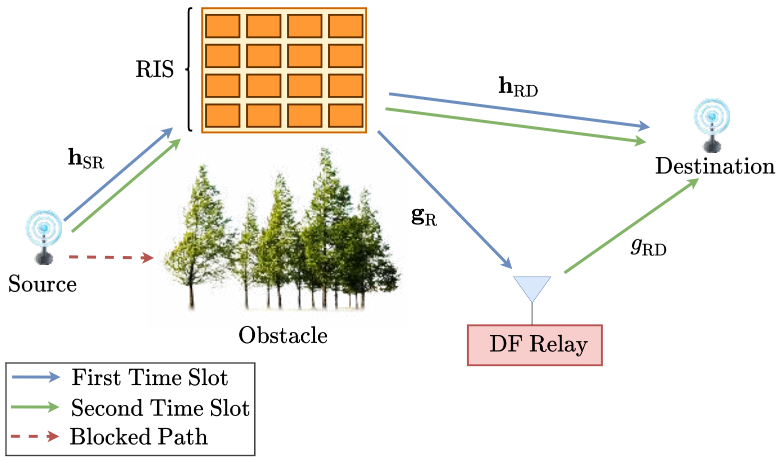

Figure 3.12: The joint transmission scheme integrates the RIS and a relay strategically positioned close to the source (S) and destination (D), respectively, outlining the system model for effective communication.

RIS consists of N reflecting elements by performing the intelligent phase adjustment of the RIS for perfect CSI case. Furthermore, all wireless channels are assumed to exhibit Rician fading with a factor of K.

3.2.2.1 First Scheme for Joint RIS and Relay Transmission

The transmission model of the proposed joint RIS and relay transmission method is shown in Fig. 3.12. As observed from Fig. 3.12, S and D are single antenna terminals, and the S-D and the S-relay channels are obstructed. Due to the sensitivity of the mmWave and THz signals for the blockage, reliable communication for larger distances between the terminals can not be guaranteed. Here, we aim to provide extended coverage for the transmission by positioning an RIS in the proximity of the S.

The received signal in the first time slot at the relay and D are respectively expressed as

$$y_{\mathrm{R}} = \sqrt{P_1}\mathbf{g}_{\mathrm{R}}^T \mathbf{\Phi}_1 \mathbf{h}_{\mathrm{SR}} s + n_{\mathrm{R}}, \tag{3.36}$$

$$y_{\mathrm{D}}^I = \sqrt{P_1}\mathbf{h}_{\mathrm{RD}}^T \mathbf{\Phi}_1 \mathbf{h}_{\mathrm{SR}} s + n_{\mathrm{D}}^I \tag{3.37}$$

where $\mathbf{g}_{\mathrm{R}} \in \mathbb{C}^{N\times 1}$, $\mathbf{h}_{\mathrm{SR}} \in \mathbb{C}^{N\times 1}$, and $\mathbf{h}_{\mathrm{RD}} \in \mathbb{C}^{N\times 1}$ respectively represents the RIS-relay, S-RIS, and RIS-D channels. Here, P_1 stands for the transmission power of S, $\mathbf{\Phi}_1 = \text{diag}\left\{e^{j\phi_1^1}, \ldots, e^{j\phi_1^N}\right\}$, with the phase shift ϕ_1^i for ith reflecting element of the RIS in the first time slot. Moreover, s denotes the transmitted signal with unit-average-power ($\mathbb{E}[|s|^2] = 1$), n_{R} and n_{D}^I stand for the AWGN terms, which are distributed by following $\mathcal{CN}(0, N_0)$.

In the second time slot, considering a perfect decoding capability of the DF relay, the received signal at D is given by

$$y_{\text{D}}^{II} = \sqrt{P_2}\mathbf{h}_{\text{RD}}^T \mathbf{\Phi}_2 \mathbf{h}_{\text{SR}} s + \sqrt{P_3} g_{\text{RD}} s + n_{\text{D}}^{II} \tag{3.38}$$

where $g_{\text{RD}} \in \mathbb{C}$ represents the relay-D channel, P_2 and P_3 respectively denotes the transmit power for S and the relay, $\mathbf{\Phi}_2 = \text{diag}\left\{e^{j\phi_2^1}, \ldots, e^{j\phi_2^N}\right\}$, with the phase shift ϕ_2^i ith reflecting element of the RIS and n_{D}^{II} stands for the AWGN term by following $\mathcal{CN}(0, N_0)$. The first term in (3.38) stands for the RIS-reflected signal, while the transmitted perfectly decoded signal s from the relay is represented by the second term.

By optimizing the phase shifts of the RIS, the maximized received SNR at D in the first time slot is obtaine as

$$\gamma_1 = \max_{\mathbf{\Phi}_1} \frac{P_1 \left|\mathbf{h}_{\text{RD}}^T \mathbf{\Phi}_1 \mathbf{h}_{\text{SR}}\right|^2}{N_0} = \frac{P_1 \left|\sum_{i=1}^{N} |h_{\text{RD,i}}||h_{\text{SR,i}}|\right|^2}{N_0} = \frac{P_1 A^2}{N_0} \tag{3.39}$$

where A has the Gaussian distribution for $N \gg 1$ due to central limit theorem (CLT) with the following mean and variance [39]:

$$\begin{aligned} \mu_A &= \frac{N\sqrt{P_L^{R_1}}\pi}{4(K+1)} L_{1/2}^2(-K), \\ \sigma_A^2 &= NP_L^{R_1} - \frac{NP_L^{R_1}\pi^2}{16(K+1)^2} L_{1/2}^4(-K) \end{aligned} \tag{3.40}$$

where $P_L^{R_1}$ is the path loss for the S-D link and $L_n(x) = \frac{e^x}{n!}\frac{d^n}{dx^n}(e^{-x}x^n)$ is the Laguerre polynomials of degree n. Since γ_1 is a non-central chi-square distributed random variable with one degree of freedom, its moment generating function (MGF) is calculated by

$$\begin{aligned} M_{\gamma_1}(s) = &\left(1 - \frac{sNP_L^{R_1}\left[16(K+1)^2 - \pi^2 L_{1/2}^4(-K)\right]P_1}{8(K+1)^2 N_0}\right)^{-1/2} \\ &\times \exp\left(\frac{\dfrac{sP_L^{R_1}N^2\pi^2 L_{1/2}^4(-K)P_1}{16(K+1)^2 N_0}}{1 - \dfrac{sNP_L^{R_1}\left[16(K+1)^2 - \pi^2 L_{1/2}^4(-K)\right]P_1}{8(K+1)^2 N_0}}\right). \end{aligned} \tag{3.41}$$

By following the similar phase adjustment strategy of the first time slot for $P_2 = P_3$, we obtain the maximized received SNR at the D in the second time slot as

$$\begin{aligned} \gamma_2 =& \max_{\mathbf{\Phi}_2} \frac{P_2 \left|g_{RD} + \mathbf{h}_{\mathrm{RD}}^T \mathbf{\Phi}_2 \mathbf{h}_{\mathrm{SR}}\right|^2}{N_0} \\ =& \frac{P_2 \left||g_{RD}| + \sum_{i=1}^N |h_{\mathrm{RD,i}}||h_{\mathrm{SR,i}}|\right|^2}{N_0} = \frac{P_2 B^2}{N_0}. \end{aligned} \tag{3.42}$$

Here, due to the Lyapunov variant of the CLT [102], B is a Gaussian distributed random variable for $N \gg 1$ with the following mean and variance respectively

$$\begin{aligned} \mu_B =& P_L^D \sqrt{\frac{\pi}{4(K+1)}} L_{1/2}(-K) + \frac{N\sqrt{P_L^{R_1}}\pi}{4(K+1)} L_{1/2}^2(-K), \\ \sigma_B^2 =& P_L^D - \frac{P_L^D \pi L_{1/2}^2(-K)}{(K+1)} + NP_L^{R_1} - \frac{NP_L^{R_1}\pi^2 L_{1/2}^4(-K)}{16(K+1)^2} \end{aligned} \tag{3.43}$$

where P_L^D is the path loss for the relay-D link. Similar to γ_1, γ_2 follows the non-central chi-square distribution with one degree of freedom and its MGF is calculated by

$$M_{\gamma_2}(s) = \left(1 - \frac{2s\sigma_B^2 P_2}{N_0}\right)^{-1/2} \exp\left(\frac{s\mu_B^2 P_2/N_0}{1 - 2s\sigma_B^2 P_2/N_0}\right). \tag{3.44}$$

3.2.2.2 Second Scheme For Integrated RIS and Relay Transmission

In this scheme, we integrate the RIS and the relay in the same device to provide a hybrid transmission as illustrated in Fig. 3.13. Contrary to the combined scenario of joint RIS and relaying, it is proposed that the signal from source S is received by

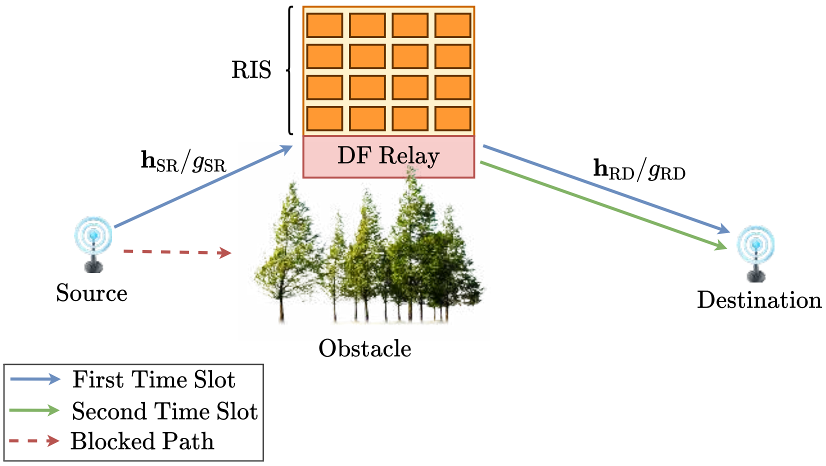

Figure 3.13: The conceptual framework outlining the transmission approach of the integrated RIS and DF relay scheme.

the integrated RIS-relay device, where it undergoes both reflection and DF relaying towards the destination D. In this context, it is further hypothesized that the distance separating S and D is substantially large, leading to the obstruction of the direct communication link between S and D.

By considering this strategy, in the first time-slot the received signal at the relay and D are respectively obtained as

$$y_{\mathrm{R}} = \sqrt{P_1} g_{\mathrm{SR}} s + n_{\mathrm{R}}, \tag{3.45}$$

$$y_{\mathrm{D}}^{I} = \sqrt{P_1} \mathbf{h}_{\mathrm{RD}}^{T} \mathbf{\Phi}_1 \mathbf{h}_{\mathrm{SR}} s + n_{\mathrm{D}}^{I}, \tag{3.46}$$

where $g_{\mathrm{SR}} \in \mathbb{C}$, $\mathbf{h}_{\mathrm{SR}} \in \mathbb{C}^{N\times 1}$ and $\mathbf{h}_{\mathrm{RD}} \in \mathbb{C}^{N\times 1}$ are respectively the the S-relay, S-RIS and RIS-D channels. P_1 stands for the transmission power of S, s represents the transmitted signal from S with the unit-average-power, n_{R} and n_{D}^{I} are the AWGN term at the relay, and D, which follows $\mathcal{CN}(0, N_0)$.

In the second time slot, the received signal transmitted over the ideal DF relay in the is written by

$$y_{\mathrm{D}}^{II} = \sqrt{P_2} g_{\mathrm{RD}} s + n_{\mathrm{D}}^{II}, \tag{3.47}$$

where g_{RD} stands for the relay-D channel, P_2 represents the transmission power of the relay, and n_{D}^{II} is the AWGN term ($n \sim \mathcal{CN}(0, N_0)$).

Following the similar strategy of the joint RIS and relay case, the received SNR in the first time slot is obtained as in (3.39). Therefore, MGF of γ_1 is obtained as in (3.41) for integrated RIS and relay transmission. Furthermore, the received SNR at the D in the second time slot is given by $\gamma_2 = P_2 \left|g_{\mathrm{RD}}\right|^2 / N_0$ where γ_2 has non-central chi-square distribution with two degrees of freedom and its MGF is expressed as

$$M_{\gamma_2}(s) = \left(1 - \frac{P_2 P_L^D}{2(K+1)N_0}\right)^{-1/2} \exp\left(\frac{2sP_2P_L^D K}{2(K+1)N_0 - P_2 P_L^D}\right). \tag{3.48}$$

3.2.3 Performance Analysis and Sequential Optimization

In this section, theoretical average symbol error probability (SEP) and achievable rate expressions of the joint and integrated RIS and relay schemes are evaluated under the ideal DF relay assumption. Further, a sequential optimization algorithm is proposed to maximize the achievable rate of these hybrid schemes under non-ideal relay assumption. By considering the maximum likelihood detection rule, the received signals can be combined by using the maximal ratio combining (MRC) technique for both schemes, and the total SNR at D can be obtained as $\gamma_{\mathrm{tot}} = \gamma_1 + \gamma_2$. Therefore, the MGF of the total SNR is calculated by $M_{\gamma_{\mathrm{tot}}}(s) = M_{\gamma_1}(s) M_{\gamma_2}(s)$. Thus, the average (SEP) of the proposed schemes for M-phase shift keying (PSK) signaling (as a representative example) is obtained as [88]

$$P_e = \frac{1}{\pi} \int_0^{(M-1)\pi/M} M_{\gamma_{\mathrm{tot}}} \left(-\frac{\sin(\pi/M)}{\sin^2 \eta}\right) d\eta. \tag{3.49}$$

For binary PSK (BPSK) case, (3.49) can be easily modified for $M = 2$. Further, under the perfect DF relay assumption, the achievable rate for both transmission scheme is calculated by $R_{\mathrm{Hybrid}} = \log_2 (1 + \gamma_{\mathrm{tot}})$.

On the other hand, we investigate the achievable rate performance of the proposed hybrid RIS and relay transmission schemes and integrate the phase and power optimization algorithm in order to sequentially maximize the achievable rate by assuming the non-ideal DF relays. As the spatial separation between the S and the relay increases, there will be a noticeable deterioration in the decoding efficacy of the transmitted symbol. In these conditions, it becomes essential to modulate the transmission power to ascertain that the performance metrics are optimized. When considering a suboptimal DF relay scenario, the achievable data rate is determined by

$$R^i_{\text{Hybrid}} = 1/2 \log_2 \left(1 + \min\left\{\gamma^i_r, \gamma_{tot}\right\}\right),\ i \in \{1, 2\} \tag{3.50}$$

where γ^1_r and γ^2_r represent the received SNR at the relay for joint ($i = 1$) and integrated ($i = 2$) RIS and relay schemes. To maximize the achievable rate for the hybrid RIS and relay configuration in the joint RIS and relay transmission, we formulate the power optimization problem as

$$\begin{aligned} R^1_{\text{Hybrid}} = \max_{P_1} \quad & \min\left(\frac{P_1|\mathbf{g}^T_{\text{R}}\mathbf{\Phi_1}\mathbf{h}_{\text{SR}}|^2}{N_0}, \frac{P_2\text{A}^2}{N_0} + \frac{P_2\text{B}^2}{N_0}\right) \\ \text{s.t.} \quad & P_2 = (P_{\text{tot}} - P_1)/2, \quad P_1 < P_{\text{tot}} \end{aligned} \tag{3.51}$$

In order to convert this problem to a convex optimization problem, we assume $P_2 = P_3$. In this way, the power constraint in (3.51) is formed by assuming $P_t = P_1 + 2P_2$. The optimization problem for the proposed integrated RIS and relay scheme at D in the second time slot is obtained as

$$\begin{aligned} R^2_{\text{Hybrid}} = \max_{P_1} \quad & \min\left(\frac{P_1|g_{\text{SR}}|^2}{N_0}, \frac{P_2\text{A}^2}{N_0} + \frac{P_2\left|g_{\text{RD}}\right|^2}{N_0}\right) \\ \text{s.t.} \quad & P_2 = P_{\text{tot}} - P_1, \quad P_1 < P_{\text{tot}} \end{aligned} \tag{3.52}$$

Here, we integrated a sequential optimization algorithm given in Algorithm 1 1 to solve (3.51) and (3.52) by considering $P_t = P_1 + P_2$.

3.2.4 Numerical Results

In this section, we analyze the error and achievable rate performances of the proposed hybrid schemes via computer simulations. Throughout the obtained results in this section, we assume Rician factor as $K = 10$ dB, and use the 3GPP Urban Micro (UMi) [89] and 5G UMi-Street Canyon [103] path loss models for 2.4 GHz and 28 GHz, respectively. We also consider a 2D coordinate system that the terminals are located in the xy-plane.

Algorithm 1 Optimization Algorithm for Phase and Power

if Sistem=Joint RIS and relay transmission scheme **then**.
    Given: $N_0, P_t, \mathbf{h}_{\text{SR}}, \mathbf{h}_{\text{RD}}, \mathbf{g}_{\text{R}}, g_{\text{RD}}$.
    Assign $P_2 = (P_t - P_1)/2$.
    Determine $\boldsymbol{\Phi_1}$ and $\boldsymbol{\Phi_2}$ to maximize the outcomes of equations (4) and (7).
    Derive coefficients A and B based on the channel inputs and the phases ($\boldsymbol{\Phi_1}$ and $\boldsymbol{\Phi_2}$).
    Solve for P_1 and P_2 using CVX to obtain the peak value from equation (16)
    return $P_1, \boldsymbol{\Phi_1}, \boldsymbol{\Phi_2}$.
else (Sistem=Integrated RIS and relay transmission scheme)
    Input: $N_0, P_t, \mathbf{h}_{\text{SR}}, \mathbf{h}_{\text{RD}}, g_{\text{SR}}, g_{\text{RD}}$.
    Assign $P_2 = P_t - P_1$.
    Find optimal $\boldsymbol{\Phi_1}$ to maximize the outcomes of (13).
    Acquire parameter A utilizing the given channels and the phase shift $\boldsymbol{\Phi_1}$.
    Seek the best solutions for P_1 and P_2 through CVX to achieve the highest outcome as per equation (17)
    return $P_1, \boldsymbol{\Phi_1}$
end if

Figs. 3.14(a) and (b) demonstrate the theoretical and simulated average bit error rate (BER) performances of the proposed hybrid schemes with respect to SNR, which is defined as P_{tot}/N_0, for BPSK signaling and $P_1 = P_2 = 5$ W at 2.4 GHz under increasing N. In this comparison, a single RIS-assisted transmission scheme is considered as a benchmark system. As clearly seen from Figs. 3.14(a) and (b), the theoretical and simulation results are in perfect agreement for both scenarios. In Fig. 3.14(a), the simulations are conducted for the joint RIS and relay case when coordinates of the S, D, RIS, and the relay in the xy-plane are given as $(5, 0)$, $(5, 10)$, $(0, 15)$, and $(10, 35)$, respectively. Meanwhile, 2D coordinates of the S, D, and the RIS/relay are respectively given as $(40, 0)$, $(40, 75)$, and $(0, 35)$ for the integrated RIS and relay transmission in Fig. 3.14(b). For both scenarios, increasing N pro-

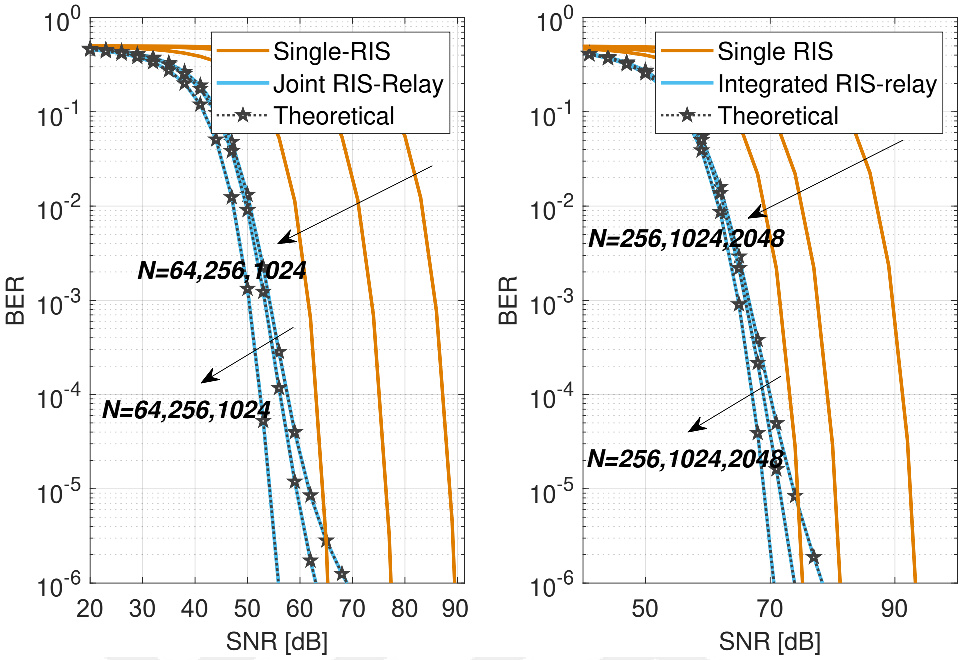

Figure 3.14: BER performance of the (a) joint, and (b) integrated RIS and relay transmission schemes for increasing N values.

vides a significant improvement in BER over a single RIS-assisted transmission, and doubling N leads to about 5 dB gain in SNR for joint RIS and relay case, while it brings approximately 3 dB gain for integrated RIS and relay case. Since the effect of the relay in transmission diminishes for large N values, the BER performances of the single-RIS and hybrid schemes get closer to each other. It demonstrates that joint RIS and relay transmission scheme appears to be more efficient than the integrated RIS and relay scheme in terms of BER performance. Furthermore, the overhead of channel estimation will increase due to the link between RIS and relay in the joint RIS and relay transmission scheme while the integrated RIS and relay scheme leads to a similar overhead of channel estimation as the existing RIS-assisted transmission scenarios in the literature.

In Fig. 3.15, the achievable rate of the integrated RIS and relay transmission scheme is compared to the single-RIS and single-relay assisted transmission scheme under varying N at 2.4 GHz. Here, the S, D, and the RIS/relay are located at $(20, 0)$, $(20, 55)$, and $(0, 20)$, respectively. As shown, increasing N significantly improves the

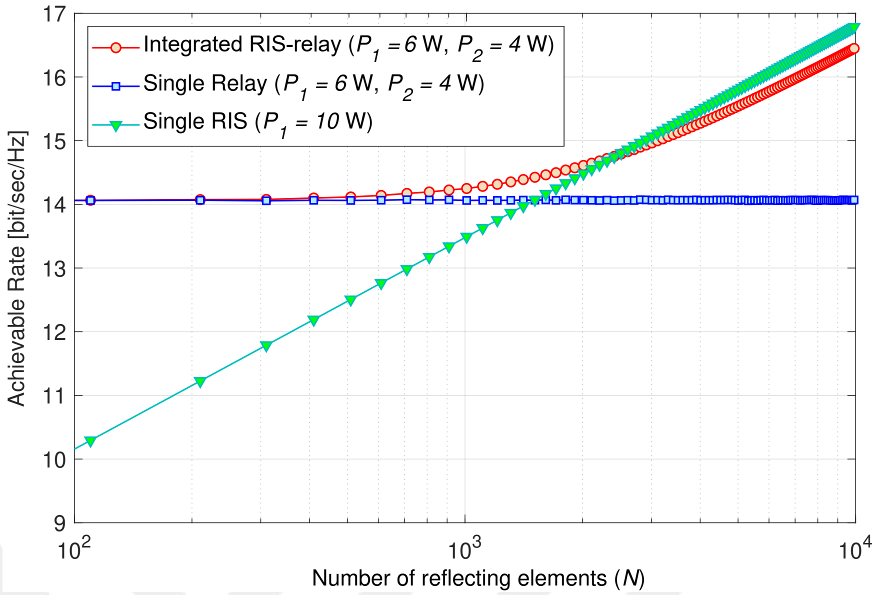

Figure 3.15: Achievable rates with the two proposed RIS and DF relay schemes for varying N values.

effect of the RIS in transmission both in the case of the single-RIS and the integrated RIS and relay scheme. Moreover, for the latter scheme, these three cases can be also considered as three different operating modes, and the activation of the RIS and/or relay for transmission can be dynamically determined according to the requirements. In order to increase energy efficiency, if the number of reflecting elements of RIS is enough for a reliable communication, transmission can be conducted over a single RIS, while the hybrid transmission can be conducted by activating the relay to compensate rapid deterioration in the channel quality.

Figs. 3.16(a) and (b) exhibit the achievable rate comparison of the joint RIS and relay transmission scheme for $P_1 = 5$ W and $P_2 = P_3 = 2.5$ W, and the integrated RIS and relay transmission scheme for $P_1 = P_2 = 5$ W, under changing the RIS position through the y-axis. In order to examine the effect of a finite-level phase adjustment, the case of discrete phase shifts is also considered with two control bits. Here, the S, D, and RIS are respectively located at $(5, 0)$, $(5, 50)$, and $(0, y^{\mathrm{RIS}})$ for both schemes, while the relay is located at $(10, 35)$ for the integrated RIS and relay case. The results shown in Figs. 3.16(a) and (b) indicate that joint RIS and relay

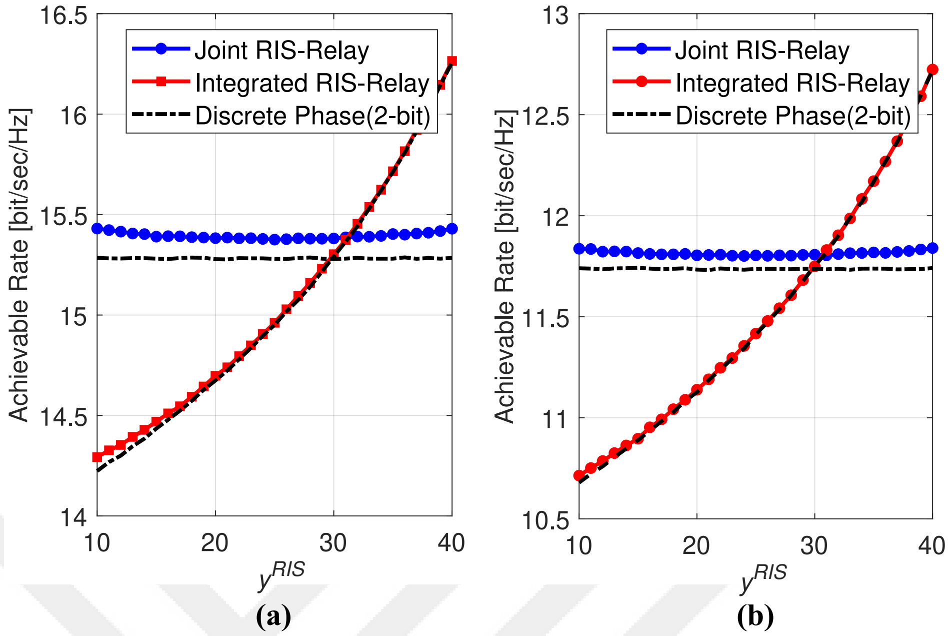

Figure 3.16: Achievable rates of the joint and integrated RIS and relay transmission schemes for (a) $N = 256$ at 2.4 GHz and (b) $N = 2048$ at 28 GHz.

scheme outperforms integrated RIS and relay transmission scheme, although the advantage of the joint RIS and relay case over the integrated RIS and relay case is reduced upon increasing y^{RIS}. More specifically, the best positioning for the RIS is near of the S for the joint RIS and relay transmission, while its proximity to D is the best option for the integrated RIS and relay scheme. Moreover, as clearly seen from Fig. 3.16, both schemes maintain their advantages in the case of discrete phase adjustment.

3.2.5 Conclusions

In our research, we have introduced two novel hybrid transmission frameworks that leverage the key benefits of RIS and relaying technologies to enhance both the achievable rate and error performance. Contrary to the prevailing view in the existing literature that evaluate RISs and relaying as competing technologies, our extensive numerical analyses and theoretical formulations reveal that these two innovative technologies can efficiently operate under well-defined transmission scenarios. Additionally, simulation results have illustrated that in scenarios where there is a rapid variations in channel quality, the relay can serve as a crucial augmentative element to the RIS-aided transmission setup, significantly enhancing performance.

Chapter 4

ADVANCING MASSIVE MIMO WITH RIS-ENHANCED HYBRID BEAMFORMING

This chapter comprehensively reviews RIS-enabled hybrid beamforming designs for massive MIMO systems operating in mmWave and THz frequency bands.

Section 4.1 focuses on RIS-assisted angular-based hybrid beamforming (AB-HBF) design in mmWave massive MIMO systems. This work presents new strategies and methods for maximizing the potential of RIS technology in the mmWave band. RIS technology is of great importance to overcome challenges such as high path loss and signal attenuation at mmWave frequencies. By intelligently manipulating signal reflection, RIS can optimize signal propagation in the mmWave band and thus significantly improve communication quality. By considering the 3D geometry-based mmWave channel model, a three-stage RIS-aided HBF system design is proposed in this work: (i) RF beamformers, (ii) BB precoder/combiner, and (iii) RIS phase shift design. First, the transmit/receive RF beamformers are designed by using the slow time-varying angle-of-departure/angle-of-arrival (AoD/AoA) information of the channel, while the BB precoder and combiner are constructed exploiting the reduced-size effective channel seen from the BB-stage. Then, the RIS phase reflection matrix is designed via particle swarm optimization (PSO) to maximize the achievable rate of massive MIMO systems. Our comprehensive numerical results demonstrate that the RISs significantly enhance the achievable rate performance of the AB-HBF mmWave systems by alleviating the disruptive effects of the wireless propagation environment as well as reducing the CSI overhead.

Section 4.2 discusses multi-RIS-supported THz communication. The THz band opens new horizons in wireless communication with its ultra-high frequencies and wide bandwidths. However, signal attenuation and path loss in the THz band pose major challenges. This study examines in detail how multiple RISs can be used in the THz band and how this technology can improve performance in THz communications. The use of multiple RIS can reduce signal attenuation in the THz band and improve communication reliability, thus making the THz band more usable. This study also presents an innovative approach for THz band communications by leveraging RISs in conjunction with an AB-HBF technique. The study addresses two significant scenarios commonly encountered in THz channels and proposes cost and energy-efficient solutions utilizing RISs to enhance system performance. The first scenario focused on ensuring reliable communication in the presence of obstacles obstructing the direct path between the transmitter and receiver. By utilizing RISs as an alternative transmission path, reliable communication has been maintained. The second scenario explored the utilization of multiple-RIS in LoS dominant or sparse environments to increase the rank of the channel matrix, consequently improving the achievable rate performance. Through the introduction of an innovative HBF design for multiple-RIS-assisted THz massive MIMO systems, enhanced spatial multiplexing gain has been achieved by effectively utilizing NLoS paths and the RIS-assisted path during transmission. This approach has effectively mitigated the disruptive effects of the wireless propagation environment while reducing hardware cost/complexity and power consumption for massive MIMO systems with large antenna arrays. Overall, this research contributes to the advancement of THz band communications, offering efficient and high-performance solutions for overcoming transmission challenges and exploiting the potential of RIS-assisted AB-HBF techniques.

In section 4.3, an innovative system concept called "Spider RIS" is introduced. Spider RIS an innovative system in which the RIS is positioned on a wall-mounted platform and aims to increase the degrees of freedom and performance of the communication system by moving in a limited space. While each antenna element moves independently in the MA systems, in Spider RIS, the entire RIS moves together with the all of its elements. This allows the RIS to be shifted horizontally or vertically within a given spatial region, changing its position to find optimal signal path or channel conditions and thus improve transmission quality. The movement of the Spider RIS can be controlled through motors or other mechanical systems integrated into the platform. This design eliminates the need to control individual antenna elements separately, thereby reducing system complexity and cost while maintaining the ability to reshape the channel matrix flexibly. With these features, Spider RIS has the potential to provide higher efficiency and performance by overcoming the limitations of existing RIS technologies in wireless communication systems. Considering the above advantages of Spider RIS, an AB-HBF system is designed in this study for mmWave massive MIMO systems, which is based on the slowly time-varying angular parameters of the channel and aims to minimize the instantaneous channel estimation overhead. This work also details how Spider RIS can improve wireless network performance and push the boundaries of wireless communications with this innovative system.

Throughout the chapter, in-depth analyses are presented on how RIS technology can be used strategically in massive MIMO systems and how this technology can increase the capacity, coverage, and reliability of wireless networks. This chapter contains innovative ideas and solutions that shape the future of wireless communication technologies, making significant contributions to the development of wireless networks for 6G and beyond.

4.1 *RIS-Aided Angular-Based Hybrid Beamforming Design in mmWave Massive MIMO Systems*

4.1.1 Introduction

In envisioned 6G wireless communication systems, enormously abundant spectrum at high frequencies is needed to be exploited in order to support eccentric applications that impose extreme performance requirements [3]. Although millimeter-wave (mmWave) transmission is one of the cornerstones of fifth-generation (5G) and beyond communication systems, promising technologies such as massive multiple-input multiple-output (MIMO) and reconfigurable intelligent surface (RIS) have been introduced to combat the high path loss and blockage susceptibility at these frequencies [12, 17, 104]. RISs, which are composed of a low-cost and passive reflecting elements, have recently attracted great interest by both academia and industry to improve the capacity and the transmission performance of wireless communication systems [5, 15, 65].

Beamforming (i.e., precoding in transmission and combining in reception) is an essential signal processing technique to ensure reliable communications between the transmitter and receiver. Although the conventional MIMO systems widely considers single-stage fully-digital beamforming, it causes two crucial challenges for the massive MIMO systems: (i) high hardware cost due to a single dedicated power-hungry radio frequency (RF) chain per antenna, (ii) large channel estimation overhead size [105]. Hybrid beamforming (HBF) is introduced as a promising solution, which interconnects analog RF-stage and digital baseband (BB)-stage via employing limited number of RF chains [106]. Furthermore, in [107–109], angular-based HBF (AB-HBF) is developed for also reducing the instantaneous channel estimation overhead size. Particularly, it builds RF-stage via slow time-varying angular information and BB-stage via reduced dimensional channel state information (CSI).

Recently, RIS-assisted HBF studies have been introduced, in which RISs and mmWave massive MIMO systems are combined to achieve the targeted requirements for next-generation communication systems [110–112]. In [110], the authors improved the spectral efficiency performance by jointly optimizing the RIS phase shifts and the hybrid precoder/combiner via a two-stage manifold optimization-based algorithm. While the hardware cost and energy consumption are reduced with the HBF structure proposed in [110], the direct path between the transmitter and the receiver is not taken into account. In [111], the authors considered an RIS-assisted HBF scheme for broadband MIMO system at mmWave frequency by proposing a geometric mean decomposition-based beamforming to avoid the complex bit/power allocation. Moreover, the authors jointly designed the RIS phase shift matrix and hybrid beamformer in [112] for the RIS-assisted hybrid mmWave MIMO systems in the presence of a direct link between the transmitter and the re-

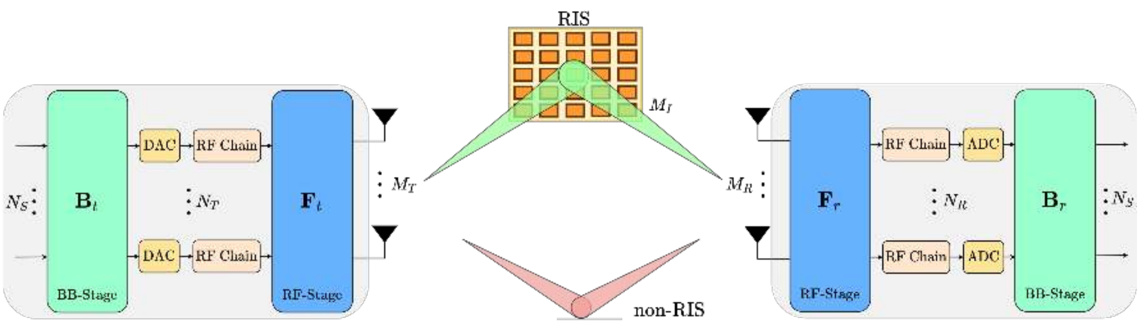

Figure 4.1: RIS-assisted hybrid mmWave massive MIMO system model.

ceiver. Despite improvements in error performance and achievable rate, the existing RIS-assisted HBF studies require full CSI in hybrid beamformer design.

In this work, we introduce an RIS-aided AB-HBF (RIS-AB-HBF) system requiring low CSI overhead for mmWave massive MIMO systems. By considering the 3D geometry-based mmWave channel model, a three-stage RIS-aided HBF system design is proposed: (i) RF beamformers, (ii) BB precoder/combiner, and (iii) RIS phase shift design. First, the transmit/receive RF beamformers are designed by using the slow time-varying angle-of-departure/angle-of-arrival (AoD/AoA) information of the channel, while the BB precoder and combiner are constructed exploiting the reduced-size effective channel seen from the BB-stage. Then, the RIS phase reflection matrix is designed via particle swarm optimization (PSO) to maximize the achievable rate of massive MIMO systems. Our comprehensive numerical results demonstrate that the RISs significantly enhance the achievable rate performance of the AB-HBF mmWave systems by alleviating the disruptive effects of the wireless propagation environment as well as reducing the CSI overhead.

4.1.2 System Model

In this section, we present the system and channel models of the RIS-assisted HBF scheme for mmWave massive MIMO systems as well as provide their working principles.

4.1.2.1 System Model and Problem Formulation

We consider an RIS-assisted hybrid mmWave massive MIMO architecture shown in Fig. 4.1, where there is a single RIS between the transmitter/receiver pair. As shown in Fig. 4.1, the transmission is carried out via an RIS and non-RIS direct link between the transmitter (Tx) and the receiver (Rx). We assume that the Tx, Rx and RIS are in the form of uniform planar array (UPA). Here, the real-time controlled RIS is equipped with $M_I = M_{I_x} \times M_{I_y}$ dynamic reflecting elements that can be adjusted based on channel phases while the Tx and Rx are equipped with $M_T = M_{T_x} \times M_{T_y}$ and $M_R = M_{R_x} \times M_{R_y}$ antennas, respectively. The number of antennas along the x and y-axis of the corresponding UPA are respectively denoted as M_{i_x} and M_{i_y} for $i \in \{I, T, R\}$. N_S data streams are sent from the Tx via digital BB precoder ($\mathbf{B}_t$) and analog RF beamformer ($\mathbf{F}_t$), which are connected with N_T RF chains. At the Rx, the received signal is combined via the analog RF beamformer ($\mathbf{F}_r$) and digital BB combiner ($\mathbf{B}_r$), which are connected with N_R RF chains. Here we assume that the number of data streams is constraint as $N_S \leq \min(N_T, N_R)$ and the number of RF chains are much smaller than both the number of transmit and receive antennas to exploit the benefit of HBF systems (i.e. $N_T \ll M_T$ and $N_R \ll M_R$).

The precoded signal $\mathbf{s} \in \mathbb{C}^{M_T}$ at the Tx is expressed as:

$$\mathbf{s} = \mathbf{F}_t \mathbf{B}_t \mathbf{x}, \tag{4.1}$$

where $\mathbf{F}_t \in \mathbb{C}^{M_T \times N_T}$ represents the transmit RF beamformer, $\mathbf{B}_t \in \mathbb{C}^{N_T \times N_S}$ represents the BB precoder and $\mathbf{x} \in \mathbb{C}^{N_S}$ is the data symbol vector satisfying $\mathbb{E}\left\{\mathbf{x}\mathbf{x}^H\right\} = \mathbf{I}_{N_s}$. The power constraint is also ensured for the transmitted power P_T as $\mathbb{E}\{\|\mathbf{s}\|_2^2\} \leq P_T$.

The direct channel between the Tx and Rx is represented by $\mathbf{H}_{TR} \in \mathbb{C}^{M_R \times M_T}$, while the RIS-assisted link consists of two components: $\mathbf{H}_{TI} \in \mathbb{C}^{M_I \times M_T}$ is the channel from the Tx to RIS and $\mathbf{H}_{IR} \in \mathbb{C}^{M_R \times M_I}$ is the channel from the RIS to Rx. $\mathbf{\Theta} = \text{diag}(e^{j\Omega_1}, \ldots, e^{j\Omega_{M_I}}) \in \mathbb{C}^{M_I \times M_I}$ is the matrix of RIS element response with Ω_i being the phase shift introduced by ith reflecting element of the RIS for

$i = 1, \ldots, M_I$. At the receiver, the signal received from the RIS-assisted and direct link is obtained as:

$$\begin{aligned} \mathbf{y} =& \mathbf{H}\mathbf{s} + \mathbf{v} = (\mathbf{H}_{IR}\boldsymbol{\Theta}\mathbf{H}_{TI} + \mathbf{H}_{TR})\mathbf{s} + \mathbf{v} \\ =& (\mathbf{H}_{IR}\boldsymbol{\Theta}\mathbf{H}_{TI} + \mathbf{H}_{TR})\mathbf{F}_t\mathbf{B}_t\mathbf{x} + \mathbf{v}, \end{aligned} \tag{4.2}$$

where $\mathbf{H} = \mathbf{H}_{IR}\boldsymbol{\Theta}\mathbf{H}_{TI} + \mathbf{H}_{TR} \in \mathbb{C}^{M_R \times M_T}$ stands for the end-to-end channel matrix and $\mathbf{v} \sim \mathcal{CN}(\mathbf{0}, \sigma_v^2 \mathbf{I}_{M_R})$ represents the additive white Gaussian noise. By using (4.1) and (4.2), the received signal after combining is written by:

$$\tilde{\mathbf{y}} = \mathbf{B}_r\mathcal{H}\mathbf{B}_t\mathbf{x} + \mathbf{B}_r\mathbf{F}_r\mathbf{v}, \tag{4.3}$$

where $\mathcal{H} = \mathbf{F}_r(\mathbf{H}_{IR}\boldsymbol{\Theta}\mathbf{H}_{TI} + \mathbf{H}_{TR})\mathbf{F}_t \in \mathbb{C}^{N_r \times N_t}$ is the effective channel matrix seen from the BB-stages, $\mathbf{F}_r \in \mathbb{C}^{N_R \times M_T}$ represents the receive RF beamformer, $\mathbf{B}_r \in \mathbb{C}^{N_S \times N_R}$ denotes the BB combiner.

In this work, our main aim is to efficiently design the transmit RF beamformer and BB precoder at the Tx (i.e., $\mathbf{F}_t$, $\mathbf{B}_t$), the receive RF beamformer and BB combiner at the Rx (i.e., $\mathbf{F}_r$, $\mathbf{B}_r$), and the phase shifts at the RIS (i.e. $\boldsymbol{\Theta}$) to maximize the achievable rate of the system as follows:

$$\max_{\{\mathbf{F}_t, \mathbf{F}_r, \mathbf{B}_t, \mathbf{B}_r, \boldsymbol{\Theta}\}} R = \log_2 \left| \mathbf{I}_{N_s} + \mathbf{R}_w^{-1}\mathbf{B}_r\mathcal{H}\mathbf{B}_t\mathbf{B}_t^H\mathcal{H}^H\mathbf{B}_r^H \right|, \tag{4.4a}$$

$$\text{s.t.} \quad \mathcal{H} = \mathbf{F}_r\mathbf{H}\mathbf{F}_r \in \mathbb{C}^{N_r \times N_t}, \tag{4.4b}$$

$$|\mathbf{F}_t(m,n)| = \frac{1}{\sqrt{M_t}}, |\mathbf{F}_r(m,n)| = \frac{1}{\sqrt{M_r}}, \ \forall (m,n), \tag{4.4c}$$

$$\mathbb{E}\{\|\mathbf{x}\|_2^2\} = \operatorname{tr}\left(\mathbf{B}_t^H\mathbf{F}_t^H\mathbf{F}_t\mathbf{B}_t\right) \le P_T, \tag{4.4d}$$

where $\mathbf{R}_w = \sigma_v^2\mathbf{B}_r\mathbf{F}_r\mathbf{F}_r^H\mathbf{B}_r^H$ is the covariance matrix of the noise $\mathbf{w} = \mathbf{B}_r\mathbf{F}_r\mathbf{v}$. Since phase shifters are used in the implementation of RF beamformer, the constraint of the constant module is ensured as in (4.4c).

4.1.2.2 Channel Model

In mmWave transmission, contrary to the conventional rich-scattering propagation environment, only a few spatial paths are experienced due to scattering limited propagation conditions. Hence, the mmWave channel will be sparse in the angular domain [113]. We assume that $\mathbf{H}_l$ ($l \in \{TR, TI, IR\}$) is a sum of the contributions of C_l scattering clusters, each of which contribute $Z_{l,c}$ ($c = 1, \ldots, C_l$) propagation paths to the corresponding channel matrix. Each sub-channel is assumed to have $Z_l = \sum_{c=1}^{C} Z_{l,c}$ paths in total between the terminals.

By following the UPA structure [107] and the 3D geometry-based mmWave channel model [114], the channel matrix between the terminals is defined as follows:

$$\begin{aligned}\mathbf{H}_l =& \sum_{c=1}^{C_l} \sum_{p=1}^{Z_{l,c}} g_{c_p}^{l} \boldsymbol{\phi}_{l,r}\left(\gamma_{x,r}^{l,c_p}, \gamma_{y,r}^{l,c_p}\right) \boldsymbol{\phi}_{l,t}^{H}\left(\gamma_{x,t}^{l,c_p}, \gamma_{y,t}^{l,c_p}\right) \\ =& \boldsymbol{\Phi}_l^{r} \mathbf{G}_l \boldsymbol{\Phi}_l^{t},\ l \in \{TR, TI, IR\},\end{aligned} \tag{4.5}$$

where $g_{c_p}^{l} \sim \mathcal{CN}\left(0, \frac{\beta^l}{P_l}\right)$ stands for the complex path gain of the p^{th} path within the c^{th} cluster of the corresponding channel with the path index of $c_p = p + \sum_{u=1}^{c-1} Z_{l,u}$, and $\boldsymbol{\phi}_{l,r}\left(\gamma_{x,r}^{l,c_p}, \gamma_{y,r}^{l,c_p}\right)$ is the receive phase response vector while the transmit phase response vector is denoted by $\boldsymbol{\phi}_{l,t}\left(\gamma_{x,t}^{l,c_p}, \gamma_{y,t}^{l,c_p}\right)$. Here, β^l represents the path loss of the corresponding path, which is inversely proportional to the terminal distances (d_l) as $\beta^l \propto d_l^{-\eta}$ with η being path loss exponent for $l \in \{TR, TI, IR\}$. Moreover, $\mathbf{G}_l = \mathrm{diag}\left(g_1^l, \cdots, g_P^l\right) \in \mathbb{C}^{Z_l \times Z_l}$ represents the diagonal matrix including the complex path gains, $\boldsymbol{\Phi}_l^{r}$ and $\boldsymbol{\Phi}_l^{t}$ denote the receive and transmit phase response matrices for the corresponding channel, respectively.

Then, the transmit and receive phase response vectors are defined as:

$$\begin{aligned}\boldsymbol{\phi}_{ij,t}\left(\gamma_x^l, \gamma_y^l\right) =& \left[1, e^{j2\pi d\gamma_x^l}, \cdots, e^{j2\pi d(M_{i_x}-1)\gamma_x^l}\right]^T \\ &\otimes \left[1, e^{j2\pi d\gamma_y^l}, \cdots, e^{j2\pi d\left(M_{i_y}-1\right)\gamma_y^l}\right]^T,\end{aligned} \tag{4.6}$$

$$\begin{aligned}\boldsymbol{\phi}_{ij,r}\left(\gamma_x^l, \gamma_y^l\right) =& \left[1, e^{j2\pi d\gamma_x^l}, \cdots, e^{j2\pi d(M_{j_x}-1)\gamma_x^l}\right]^T \\ &\otimes \left[1, e^{j2\pi d\gamma_y^l}, \cdots, e^{j2\pi d\left(M_{j_y}-1\right)\gamma_y^l}\right]^T,\end{aligned} \tag{4.7}$$

where $(i, j) \in \{(T, R), (T, I), (I, R)\}$ and d denotes the antenna spacing normalized by wavelength. From (4.5), (4.6) and (4.7), the slow time-varying transmit and receive phase response matrices for each sub-channel are respectively written by:

$$\boldsymbol{\Phi}_l^{t} = \begin{bmatrix} \boldsymbol{\phi}_{l,t}^{H}\left(\gamma_{x,r}^{l,1}, \gamma_{y,r}^{l,1}\right) \\ \vdots \\ \boldsymbol{\phi}_{l,t}^{H}\left(\gamma_{x,r}^{l,P_l}, \gamma_{y,r}^{l,P_l}\right) \end{bmatrix},\ \boldsymbol{\Phi}_l^{r} = \begin{bmatrix} \boldsymbol{\phi}_{l,r}^{H}\left(\gamma_{x,r}^{l,1}, \gamma_{y,r}^{l,1}\right) \\ \vdots \\ \boldsymbol{\phi}_{l,r}^{H}\left(\gamma_{x,r}^{l,P_l}, \gamma_{y,r}^{l,P_l}\right) \end{bmatrix}^{H}. \tag{4.8}$$

Table 4.1: AoA and AoD parameters of the l^{th} channel for $l \in \{TR, TI, IR\}$.

$\theta^l_{r,c}$	Mean elevation AoA	$\theta^l_{t,c}$	Mean elevation AoD
$\delta^{l,\theta}_{r,c}$	Elevation AoA spread	$\delta^{l,\theta}_{t,c}$	Elevation AoD spread
$\psi^l_{r,c}$	Mean azimuth AoA	$\psi^l_{t,c}$	Mean azimuth AoD
$\delta^{l,\psi}_{r,c}$	Azimuth AoA spread	$\delta^{l,\psi}_{t,c}$	Azimuth AoD spread

By considering the mean and spread parameters of AoA/AoD in Table 4.1, at the arrival side of each sub-channel l for $l \in \{TR, TI, IR\}$, the coefficients reflecting the elevation AoA and azimuth AoA of the p^{th} path within the c^{th} cluster are respectively defined as $\gamma^{l,c_p}_{x,r} = \sin\left(\theta^l_{r,c_p}\right)\cos\left(\psi^l_{r,c_p}\right)$ and $\gamma^{l,c_p}_{y,r} = \sin\left(\theta^l_{r,c_p}\right)\sin\left(\psi^l_{r,c_p}\right)$, where $\theta^l_{r,c_p} \in \left[\theta^l_{r,c} - \delta^{l,\theta}_{r,c}, \theta^l_{r,c} + \delta^{l,\theta}_{r,c}\right]$ and $\psi^l_{r,c_p} \in \left[\psi^l_{r,c} - \delta^{l,\psi}_{r,c}, \psi^l_{r,c} + \delta^{l,\psi}_{r,c}\right]$. At the departure side of each sub-channel l for $l \in \{TR, TI, IR\}$, the elevation AoD and azimuth AoD of the p^{th} path within the c^{th} cluster are respectively defined as $\gamma^{l,c_p}_{x,t} = \sin\left(\theta^l_{t,c_p}\right)\cos\left(\psi^l_{t,c_p}\right)$ and $\gamma^{l,c_p}_{y,t} = \sin\left(\theta^l_{t,c_p}\right)\sin\left(\psi^l_{t,c_p}\right)$, where $\theta^l_{t,c_p} \in \left[\theta^l_{t,c} - \delta^{l,\theta}_{t,c}, \theta^l_{t,c} + \delta^{l,\theta}_{t,c}\right]$ and $\psi^l_{t,c_p} \in \left[\psi^l_{t,c} - \delta^{l,\psi}_{t,c}, \psi^l_{t,c} + \delta^{l,\psi}_{t,c}\right]$.

4.1.3 RIS-Aided Angular-Based Hybrid Beamforming

In this section, we respectively provide the design of RF beamformers, BB precoder/combiner and phase shift matrix of the RIS for the proposed RIS-aided AB-HBF system. Our primary goal is to maximize the achievable rate of the system as well as reduce the CSI overhead size and the hardware complexity. From this point of view, first, the design procedures of RF beamformers is introduced based on slow-time varying angular parameters. Afterwards, BB precoder/combiner is designed by the singular value decomposition (SVD) and water filling algorithm using effective channel with reduced size. Finally, the phase shifts of the RIS, which enhances the system capacity, is obtained by applying the PSO method.

4.1.3.1 RF Beamformers

In order to design RF-stage efficiently, the range of the azimuth and elevation AoA/AoD angles of the existing paths in the clusters is first required to be appropriately defined as in [108]. Therefore, AoA and AoD angle supports are respectively defined based on (4.5) as:

$$\Upsilon_{\text{AoA}} = \Big\{ [\gamma_x, \gamma_y] = [\sin(\theta)\cos(\psi), \sin(\theta)\sin(\psi)] \Big| \theta \in \boldsymbol{\theta}_r, \psi \in \boldsymbol{\psi}_r \Big\}, \tag{4.9a}$$
$$\Upsilon_{\text{AoD}} = \Big\{ [\gamma_x, \gamma_y] = [\sin(\theta)\cos(\psi), \sin(\theta)\sin(\psi)] \Big| \theta \in \boldsymbol{\theta}_t, \psi \in \boldsymbol{\psi}_t \Big\}, \tag{4.9b}$$

where $\boldsymbol{\theta}_r = \boldsymbol{\theta}_r^{TI} \cup \boldsymbol{\theta}_r^{TR}$, $\boldsymbol{\psi}_r = \boldsymbol{\psi}_r^{TI} \cup \boldsymbol{\psi}_r^{TR}$, $\boldsymbol{\theta}_t = \boldsymbol{\theta}_t^{IR} \cup \boldsymbol{\theta}_t^{TR}$, and $\boldsymbol{\psi}_t = \boldsymbol{\psi}_t^{IR} \cup \boldsymbol{\psi}_t^{TR}$. Here, the elevation and azimuth AoA supports for the corresponding sub-channels are respectively defined as: $\boldsymbol{\theta}_r^l = \cup_{c=1}^{C_l} \left[\theta_{r,c}^l - \delta_{r,c}^{l,\theta}, \theta_{r,c}^l + \delta_{r,c}^{l,\theta}\right]$ and $\boldsymbol{\psi}_r^l = \cup_{c=1}^{C_l} \left[\psi_{r,c}^l - \delta_{r,c}^{l,\psi}, \psi_{r,c}^l + \delta_{r,c}^{l,\psi}\right]$ for $l \in \{IR, TR\}$. Then, the elevation and azimuth AoD supports for the corresponding sub-channels are respectively obtained as: $\boldsymbol{\theta}_t^l = \cup_{c=1}^{C_l} \left[\theta_{t,c}^l - \delta_{t,c}^{l,\theta}, \theta_{t,c}^l + \delta_{t,c}^{l,\theta}\right]$ and $\boldsymbol{\psi}_t^l = \cup_{c=1}^{C_l} \left[\psi_{t,c}^l - \delta_{t,c}^{l,\psi}, \psi_{t,c}^l + \delta_{t,c}^{l,\psi}\right]$ for $l \in \{TI, TR\}$.

By using (4.2) and (4.5), the effective channel seen from the BB-stages can be reorganized as:

$$\begin{aligned} \mathcal{H} =& \mathbf{F}_r \mathbf{H} \mathbf{F}_t, \\ =& \mathbf{F}_r (\boldsymbol{\Phi}_{IR}^r \mathbf{G}_{IR} \boldsymbol{\Phi}_{IR}^t \boldsymbol{\Theta} \boldsymbol{\Phi}_{TI}^r \mathbf{G}_{TI} \boldsymbol{\Phi}_{TI}^t \\ & + \boldsymbol{\Phi}_{TR}^r \mathbf{G}_{TR} \boldsymbol{\Phi}_{TR}^t) \mathbf{F}_t. \end{aligned} \tag{4.10}$$

In order to optimize the receive (transmit) beamforming gain and take advantage of all degrees of freedom enabled by the channel, the subspace spanned by $\boldsymbol{\Phi}_{IR}^r$ and $\boldsymbol{\Phi}_{TR}^r$ ($\boldsymbol{\Phi}_{TI}^t$ and $\boldsymbol{\Phi}_{TR}^t$) should be encompassed in the columns of $\mathbf{F}_r$ ($\mathbf{F}_t$): $\text{Span}(\mathbf{F}_r) \subset (\text{Span}(\boldsymbol{\Phi}_{IR}^r) \cup \text{Span}(\boldsymbol{\Phi}_{TR}^r))$ and $\text{Span}(\mathbf{F}_t) \subset (\text{Span}(\boldsymbol{\Phi}_{TI}^t) \cup \text{Span}(\boldsymbol{\Phi}_{TR}^t))$ should be satisfied. Afterwards, the columns of the RF precoder matrix are created using the transmit steering vector $\mathbf{a}_t(\gamma_x, \gamma_y) = \frac{1}{\sqrt{M_t}} \left[1, e^{j2\pi d \gamma_x}, \cdots, e^{j2\pi d (M_{T_x}-1)\gamma_x}\right]^T \otimes \left[1, e^{j2\pi d \gamma_y}, \cdots, e^{j2\pi d \left(M_{T_y}-1\right)\gamma_y}\right]^T \in \mathbb{C}^{M_T}$. The quantized angle pairs are defined as follows to obtain M_T orthogonal transmit steering vectors as the minimum number of angle pairs spanning the entire elevation and azimuth space [107,108]: $\kappa_{x,t}^m = \frac{2m-1}{M_{T_x}} - 1$ for $m = 1, \cdots, M_{T_x}$ and $\kappa_{y,t}^n = \frac{2n-1}{M_{T_y}} - 1$ for $n = 1, \cdots, M_{T_y}$. Thus, while minimizing the use of the RF chain by covering the entire AoD support, the quantized angle pairs within the AoD support are written as:

$$\left(\kappa_{x,t}^{m}, \kappa_{y,t}^{n}\right) \Bigg| \gamma_x \in \boldsymbol{\kappa}_{x,t}^{m}, \gamma_y \in \boldsymbol{\kappa}_{y,t}^{n}, (\gamma_x, \gamma_y) \in \Upsilon_{\mathrm{AoD}}, \tag{4.11}$$

where $\boldsymbol{\kappa}_{x,t}^{m} = \left[\kappa_{x,t}^{m} - \frac{1}{M_{T_x}}, \kappa_{x,t}^{m} + \frac{1}{M_{T_x}}\right]$ and $\boldsymbol{\kappa}_{y,t}^{n} = \left[\kappa_{y,t}^{n} - \frac{1}{M_{T_y}}, \kappa_{y,t}^{n} + \frac{1}{M_{T_y}}\right]$ respectively represent the boundary of $\kappa_{x,t}^{m}$ and $\kappa_{y,t}^{n}$. Therefore, the RF precoder with N_T quantized angle-pairs is constructed based on (4.9b) as:

$$\mathbf{F}_t = \left[\mathbf{a}_t\left(\kappa_{x,t}^{m_1}, \kappa_{y,t}^{n_1}\right), \cdots, \mathbf{a}_t\left(\kappa_{x,t}^{m_{N_T}}, \kappa_{y,t}^{n_{N_T}}\right)\right] \in \mathbb{C}^{M_T \times N_T}. \tag{4.12}$$

Following the similar procedure for the RF combiner ($\mathbf{F_r}$), the receive steering vector $\mathbf{a}_r\left(\gamma_x, \gamma_y\right) \in \mathbb{C}^{M_R}$ is obtained as:

$$\mathbf{a}_r\left(\gamma_x, \gamma_y\right) = \frac{1}{\sqrt{M_R}}\left[1, e^{j2\pi d\gamma_x}, \cdots, e^{j2\pi d(M_{R_x}-1)\gamma_x}\right]^T \otimes \left[1, e^{j2\pi d\gamma_y}, \cdots, e^{j2\pi d\left(M_{R_y}-1\right)\gamma_y}\right]^T. \tag{4.13}$$

The quantized angle pairs are given by $\kappa_{x,r}^{m} = \frac{2m-1}{M_{R_x}} - 1$ for $m = 1, \cdots, M_{R_x}$ and $\kappa_{y,r}^{n} = \frac{2n-1}{M_{R_y}} - 1$ for $n = 1, \cdots, M_{R_y}$.

In order to minimize the use of the RF chain in the receiver side by covering the entire AoA support, the quantized angle pairs within the AoA support are obtained as:

$$\left(\kappa_{x,r}^{m}, \kappa_{y,r}^{n}\right) \Bigg| \gamma_x \in \boldsymbol{\kappa}_{x,r}^{m}, \gamma_y \in \boldsymbol{\kappa}_{y,r}^{n}, (\gamma_x, \gamma_y) \in \Upsilon_{\mathrm{AoA}}, \tag{4.14}$$

where $\boldsymbol{\kappa}_{x,t}^{m} = \left[\kappa_{x,t}^{m} - \frac{1}{M_{T_x}}, \kappa_{x,t}^{m} + \frac{1}{M_{T_x}}\right]$ and $\boldsymbol{\kappa}_{y,r}^{n} = \left[\kappa_{y,r}^{n} - \frac{1}{M_{R_y}}, \kappa_{y,r}^{n} + \frac{1}{M_{R_y}}\right]$ respectively denote the boundary of $\kappa_{x,r}^{m}$ and $\kappa_{y,r}^{n}$. Finally, the RF combiner with N_R quantized angle-pairs is constructed fulfilling AoA support in (4.9a) as:

$$\mathbf{F}_r = \left[\mathbf{a}_r\left(\kappa_{x,r}^{m_1}, \kappa_{y,r}^{n_1}\right), \cdots, \mathbf{a}_r\left(\kappa_{x,r}^{m_{N_R}}, \kappa_{y,r}^{n_{N_R}}\right)\right] \in \mathbb{C}^{M_R \times N_R}. \tag{4.15}$$

It should be noted that the unitary property for RF beamformers (i.e. $\mathbf{F}_t^H \mathbf{F}_t = \mathbf{I}_{N_T}$, $\mathbf{F}_r \mathbf{F}_r^H = \mathbf{I}_{N_R}$) and the constant modulus condition provided in (4.4c) are satisfied in the RF beamformer design stage.

4.1.3.2 Baseband Precoder/Combiner

After the design of the RF beamformers, this subsection focuses on the BB precoder/combiner design using the low-dimensional effective channel matrix given in (4.10). The singular value decomposition (SVD) of effective channel matrix $\boldsymbol{\mathcal{H}}$ is obtained as $\boldsymbol{\mathcal{H}} = \mathbf{U}\boldsymbol{\Sigma}\mathbf{V}^H$, where $\mathbf{U} \in \mathbb{C}^{N_R \times \text{rank}(\boldsymbol{\mathcal{H}})}$ represents a tall unitary matrix, $\boldsymbol{\Sigma} = \text{diag}\big(\sigma_1^2, \cdots, \sigma^2_{\text{rank}(\boldsymbol{\mathcal{H}})}\big) \in \mathbb{R}^{\text{rank}(\boldsymbol{\mathcal{H}}) \times \text{rank}(\boldsymbol{\mathcal{H}})}$ denotes a diagonal matrix of the singular values in the descending order and $\mathbf{V} \in \mathbb{C}^{N_T \times \text{rank}(\boldsymbol{\mathcal{H}})}$ stands for a tall unitary matrix. Here, $\mathbf{V}$ can be partitioned as $\mathbf{V} = [\mathbf{V}_1, \mathbf{V}_2]$ for $\mathbf{V}_1 \in \mathbb{C}^{N_T \times N_S}$ under $\text{rank}\,(\boldsymbol{\mathcal{H}}) \geq N_S$.

Similar to [108,115], the optimal solution for the BB precoder can be represented as:

$$\mathbf{B}_t = \mathbf{V}_1 \boldsymbol{\Gamma}^{\frac{1}{2}} \in \mathbb{C}^{N_T \times N_T}, \tag{4.16}$$

where $\boldsymbol{\Gamma} = \text{diag}\,(\Gamma_1, \cdots, \Gamma_{N_S}) \in \mathbb{R}^{N_S \times N_S}$ represents a transmit power matrix with $\sum_{n=1}^{N_S} \Gamma_n = P_T$ for meeting the power constraint given in (4.4d). By using the water filling power control solution [116], the powers are allocated as:

$$\Gamma_n = \left(\mu - \frac{\sigma_v^2}{P_T \sigma_n^2}\right)^+, \text{ s.t.} \sum_{n=1}^{N_S} \left(\mu - \frac{\sigma_v^2}{P_T \sigma_n^2}\right)^+ = P_T. \tag{4.17}$$

Then, considering the given RF beamformer ($\mathbf{F}_t/\mathbf{F}_r$), phase response matrix ($\boldsymbol{\Theta}$) and BB precoder ($\mathbf{B}_t$), we strive to design the BB combiner ($\mathbf{B}_r$) that minimize the mean-squared-error (MSE) between the transmitted and processed received signals. Based on (4.3), the MSE expression can therefore be stated as:

$$\begin{aligned} \mathbf{e}_{\text{MSE}} =& \mathbb{E}\big\{\big\|\tilde{\mathbf{y}} - \mathbf{x}\big\|^2\big\} = \text{tr}\big(\mathbb{E}\big\{\tilde{\mathbf{y}}\tilde{\mathbf{y}}^H - \mathbf{x}\tilde{\mathbf{y}}^H - \tilde{\mathbf{y}}\mathbf{x}^H + \mathbf{x}\mathbf{x}^H\big\}\big) \\ =& \text{tr}\Big(\mathbf{B}_\text{r}\boldsymbol{\mathcal{H}}\mathbf{B}_\text{t}\mathbf{B}_\text{t}^\text{H}\boldsymbol{\mathcal{H}}^\text{H}\mathbf{B}_\text{r}^\text{H} + \mathbf{B}_\text{r}\mathbf{R}_{\text{q}_\text{r}}\mathbf{B}_\text{r}^\text{H} - \mathbf{B}_\text{t}^\text{H}\boldsymbol{\mathcal{H}}^\text{H}\mathbf{B}_\text{r}^\text{H} + \mathbf{I}_{\text{N}_\text{s}}\Big). \end{aligned} \tag{4.18}$$

For the purpose of finding the optimal solution for (4.18), the differentiation rules for the complex-valid matrices are applied. Then, the derivative of $\mathbf{e}_{\text{MSE}}$ with respect to BB combiner ($\mathbf{B}_r$) is calculated as:

$$\frac{\partial \mathbf{e}_{\text{MSE}}}{\partial \mathbf{B}_r} = 2\mathbf{B}_r\boldsymbol{\mathcal{H}}\mathbf{B}_t\mathbf{B}_t^H\boldsymbol{\mathcal{H}}^H - 2\mathbf{B}_t^H\boldsymbol{\mathcal{H}}^H. \tag{4.19}$$

Finally, the BB combiner meeting the minimum MSE criterion in (4.18) can be obtained as follows:

$$\mathbf{B}_r = \mathbf{B}_t^H \mathcal{H}^H \left(\mathcal{H}\mathbf{B}_t\mathbf{B}_t^H\mathcal{H}^H\right)^{-1}. \tag{4.20}$$

4.1.3.3 RIS Phase Shift Design

In this subsection, phase shifts of the RIS elements are adjusted by optimizing the achievable rate of the system via the PSO algorithm. In PSO, each particle reconfigures its position at every step by moving through multidimensional space with its own experience and the experience of its peers towards an optimum solution by the whole swarm [117]. Under given RF beamformers ($\mathbf{F}_t, \mathbf{F}_r$) and BB precoder/combiner ($\mathbf{B}_t$, $\mathbf{B}_r$), the optimization problem for maximizing the achievable rate can be formulated as:

$$\begin{aligned}
&\max_{\{\mathbf{\Theta}\}} R\left(\mathbf{F}_t, \mathbf{F}_r, \mathbf{B}_t, \mathbf{B}_r, \mathbf{\Theta}\right) \\
&\text{ s.t. } \mathbf{\Theta} = \operatorname{diag}(e^{j\Omega_1}, \ldots, e^{j\Omega_{M_I}}) \\
&\qquad \mathbb{E}\{\left\|\mathbf{x}\right\|_2^2\} = \operatorname{tr}\left(\mathbf{B}_t^H\mathbf{F}_t^H\mathbf{F}_t\mathbf{B}_t\right) \le P_T \\
&\qquad \Omega_i \in [0, 2\pi], \forall i,
\end{aligned} \tag{4.21}$$

where $R\left(\mathbf{F}_t, \mathbf{F}_r, \mathbf{B}_t, \mathbf{B}_r, \mathbf{\Theta}\right)$ is given in (4.4). In our PSO solution, the phase shifts of the RIS elements (Ω_i, $i \in 1, \ldots, M_I$) are modeled as the positions of the particles, and the objective function in (4.21) is considered as the fitness function of PSO.

N_{par} particles are randomly initialized with position $\mathbf{p} \in \mathbb{C}^{M_I}$ and velocity $\mathbf{v} \in \mathbb{C}^{M_I}$. Each particle has a memory for its local best position ($\mathbf{p}_{\text{best},i}^{(q)}$) and the global best position ($\mathbf{p}_G^{(q)}$), where the superiority of a position is evaluated by the given fitness function. Here, $\mathbf{p}_{\text{best},i}^{(q)}$ is the best position that the i^{th} particle has achieved while $\mathbf{p}_G^{(\text{t})}$ is the best position achieved by any of the particles in the entire swarm in the q^{th} iteration. For each iteration, the velocity and position of each particle are updated according to:

$$\begin{aligned}
\mathbf{v}_i^{(q+1)} &= \zeta\mathbf{v}_i^{(q)} + u_1\rho_1\big(\mathbf{p}_{\text{best},i}^{(q)} - \mathbf{p}_i^{(q)}\big) + u_2\rho_2\big(\mathbf{p}_G^{(q)} - \mathbf{p}_i^{(q)}\big), \\
\mathbf{p}_i^{(q+1)} &= \mathbf{v}_i^{(q+1)} + \mathbf{p}_i^{(q)},
\end{aligned} \tag{4.22}$$

Algorithm 2 Proposed RIS-aided AB-HBF System Design

Input: $\mathcal{H}$, Υ_{AoA}, Υ_{AoD}, P_T, Q, N_{par}, ζ, ρ_1, ρ_2

Output: $\mathbf{F}_t$, $\mathbf{F}_r$, $\mathbf{B}_t$, $\mathbf{B}_r$, $\boldsymbol{\Theta}$

Build $\mathbf{F}_t$ and $\mathbf{F}_r$ via (4.12) and (4.15), respectively.

Initialize N_p particles and their velocities:

for $i = 1 : N_p$ **do**

  Initialize the velocity as $\mathbf{V}_i^{(0)} = \mathbf{0}$.

end for

Find the global best $\hat{\mathbf{P}}_{\text{best}}^{(0)}$.

Perform iterations:

for $q = 1 : Q$ **do**

  Calculate each particle's velocity $\mathbf{v}_i^{(q)}$ and position $\mathbf{p}_i^{(q)}$ via (4.22).

  Calculate each particle's velocity $\mathbf{v}_i^{(q)}$ via (4.22).

  Calculate each particle's position $\mathbf{p}_i^{(q)}$ via (4.22).

  Find each particle's achievable rate via (4.21).

  Update personal best $\mathbf{p}_{\text{best},i}^{(q)}$ and global best $\mathbf{p}_G^{(q)}$.

end for

Set RIS phase-shift matrix as $\boldsymbol{\Theta} = \text{diag}\big(\exp\big(j\mathbf{p}_G^{(Q)}\big)\big)$.

Build $\mathbf{B}_t$ and $\mathbf{B}_r$ via (4.16) and (4.20), respectively.

where ζ is the inertia weight of velocity, ρ_1 and ρ_2 are the acceleration constants, and u_1 and u_2 are uniformly distributed random numbers in $[0, 1]$. Through the iterations, the particles move from $\mathbf{p}_i^{(q)}$ to $\mathbf{p}_i^{(q+1)}$. Finally, after Q iterations, the RIS phase shift matrix is determined at the last iteration as $\boldsymbol{\Theta} = \text{diag}\big(\exp\big(j\mathbf{p}_G^{(Q)}\big)\big)$. The summary of the proposed RIS-aided AB-HBF system design including three stages is precisely explained in Algorithm 2.

4.1.4 Numerical Results

In this section, we provide comprehensive numerical results to investigate the performance of the proposed RIS-aided AB-HBF system. Here, Table 4.2 presents the

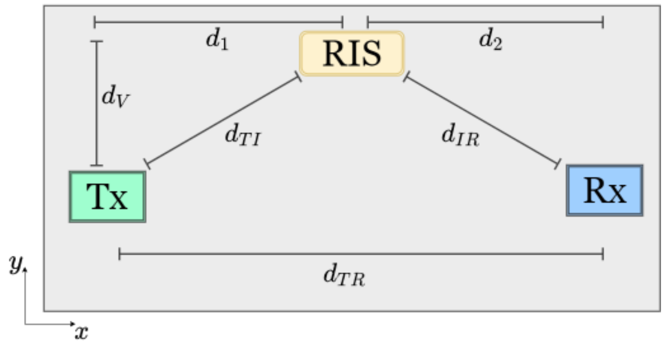

Figure 4.2: Top view of simulation setup for the proposed RIS-aided hybrid MIMO system.

common parameters for all simulations considering the geometry-based mmWave channel given in (4.5). Due to the simplicity, we assume that all subchannels have $Z_{l,c} = 5$ paths within a single cluster $C_l = 1$ for $l \in \{TR, TI, IR\}$ and $c = 1$. Moreover, the azimuth and elevation AoA/AoD spreads for all subchannels are assumed to be the same as $\delta_{i,c}^{l,j} = 10^{\circ}$ for $l \in \{TR, TI, IR\}$, $i =\in \{t, r\}$, $j \in \{\theta, \psi\}$ and $c = 1$. The spacing between two antennas/reflectors is also $d = 0.5$ due to the half-wavelength separation. The top view of the simulation setup, including the terminal distances, is also illustrated in Fig. 4.2. Here, the Tx-Rx channel is assumed to be nearly blocked under non-line-of-sight (NLOS) conditions, while the RIS-assisted cascade channel is assumed to have LoS conditions.

Fig. 4.3 compares the achievable rate performance for the AB-HBF system with or without RIS for varying Tx-RIS separation under fixed Tx and Rx positions. In this comparison, the RIS-assisted AB-HBF schemes with random and constant phase adjustment are also considered as a benchmark system for $d_{TR} = 200$ and $d_V = 5$ m. In this scenario, it is observed that RIS significantly improves system performance when the direct link between the Tx and Rx is nearly blocked. For $d_1 = 100$ m, the PSO-based RIS-assisted AB-HBF system provides 25 dB superiority to the conventional AB-HBF system, while 4.5 dB superiority to the random phase-adjusted RIS-AB-HBF system. Fig. 4.3 also provides practical perspective for the effective positioning of the RIS. For $d_1 = 20$ m, the achievable rate will be measured

Table 4.2: Simulation parameters.

# of transmit antennas	$M_T = 8 \times 8 = 64$
# of receive antennas	$M_R = 4 \times 4 = 16$
# of RIS elements	$M_I = 16 \times 16 = 256$
# of RF Chains	$N_T = 6$, $N_R = 2$
# of data streams	$N_S = 2$
# of clusters for $\mathbf{H}_l$	$C_l = 1$ for $l \in \{TR, TI, IR\}$
# of paths for $\mathbf{H}_l$	$Z_{l,c} = 5$ for $l \in \{TR, TI, IR\}$
Noise PSD	-174 dBm/Hz
Channel Bandwidth	10 kHz
PSO # of iterations	$T = 200$
PSO # of particles	$N_{\text{par}} = 100$
Path loss exponent	$\eta = 2.3$ for LOS, $\eta = 4.5$ for NLoS [118]
Mean elevation AoA/AoD	$\theta_{i,c}^{TR} = 35^\circ$, $\theta_{i,c}^{TI} = 60^\circ$, $\theta_{i,c}^{IR} = 50^\circ$, $i \in \{t, r\}$
Mean azimuth AoA/AoD	$\phi_{i,c}^{TR} = 25^\circ$, $\phi_{i,c}^{TI} = 90^\circ$, $\phi_{i,c}^{IR} = 225^\circ$, $i \in \{t, r\}$

as 10.47 bps/Hz, while it will approximately reduce to one-third, measuring 3.24 bps/Hz for $d_1 = 100$ m. In Fig. 4.4, the achievable rate performance of the AB-HBF system is illustrated depending on the position of Rx changing along the x-axis under the fixed Tx and RIS positions. Here, the fixed distances between the Tx and RIS are given as $d_1 = 10$ m and $d_V = 20$ m. However, doubling the d_{TR} (25 m to 50 m) will result in a performance loss of 22.85% in the PSO-based RIS-AB-HBF system, 28.2% in the random phase RIS AB-HBF, 57.03% in the constant phase RIS-AB-HBF, and 76.53% in the conventional AB-HBF. From the presented results in Figs. 4.3 and 4.4, we conclude that the presence of an RIS in AB-HBF systems alleviates the deteriorated channel conditions by providing an additional reliable transmission link alternative to the blocked Tx-Rx link. Thus, a remarkable increase in achievable rate performance is achieved by effectively positioning the RIS even in the absence of a LoS Tx-Rx channel.

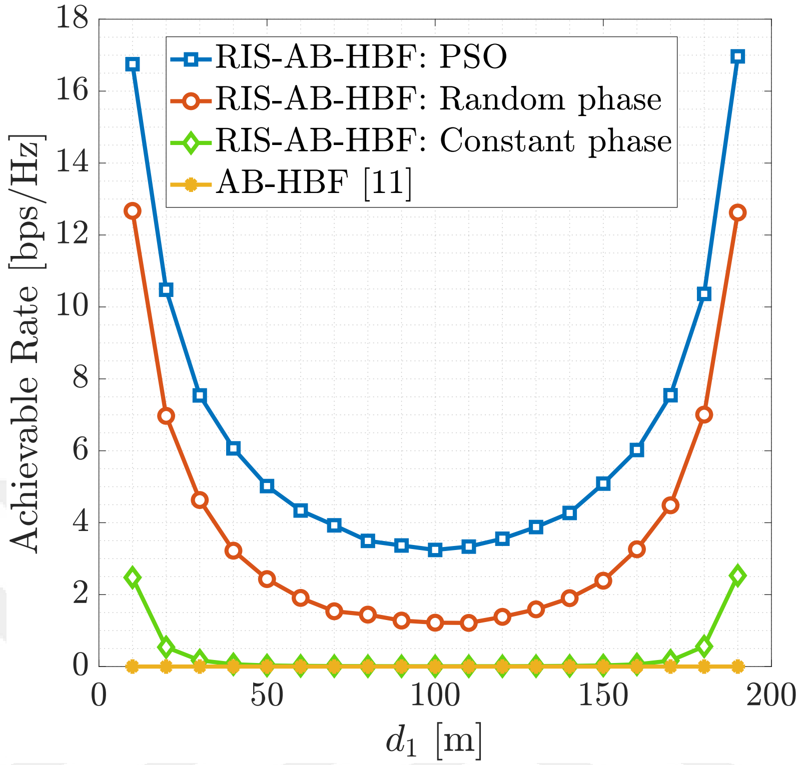

Figure 4.3: Comparison of achievable rate performance for AB-HBF system with or without RIS for varying d_1.

In Fig. 4.5, we present achievable rate comparison results for PSO-based, random and constant phase adjustment for the RIS-aided AB-HBF system at 100 and 400 m d_{TR} values with increasing P_T. Here, the distances for this setup are assumed as $d_V = 5$ and $d_2 = 4d_1$. Fig. 4.5 gives an useful insights for the different operating modes of an RIS. Even if the phase shifts of the RIS are set to a fixed value, a notable increase in the system performance can be achieved by providing an additional LoS path for the transmission. However, when the received signal quality is below a certain threshold value, the transmission performance can be increased by activating the PSO-assisted phase adjustment algorithm. From this point of view, the use of RISs in AB-HBF systems may has the potential to provide more promising advantages in terms of reliability and flexibility in system design.

Finally, Fig. 4.6 demonstrates the achievable rate comparison of the AB-HPC

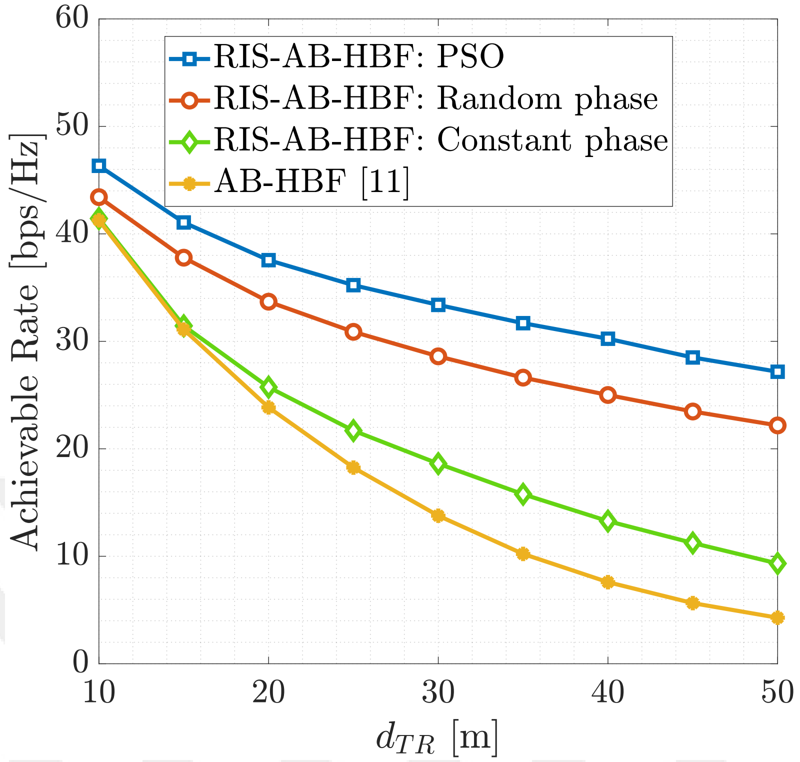

Figure 4.4: Comparison of achievable rate performance for AB-HBF system with or without RIS for varying d_{TR}.

system in the presence of an RIS under varying M_I for $d_{TR} = 100$, $d_1 = 10$, $d_2 = 80$ and $d_V = 10$ m. As observed from Fig. 4.6, increasing M_I significantly enhance the effect of the RIS in transmission both in the case of PSO-based and random phase adjustment. While the constant phase adjustment contributes to the transmission by providing a reliable LoS path, it will become saturated at increasing M_I values. Although the random phase adjustment also leads to an remarkable increase in the system performance, the effect of increasing M_I is more evident for the PSO-based RIS-AB-HBF system. For instance, the PSO-based scenario provides a 3 dB advantage over the random phase adjustment case for $M_I = 10$, while provides 4.5 dB increase for $M_I = 100$.

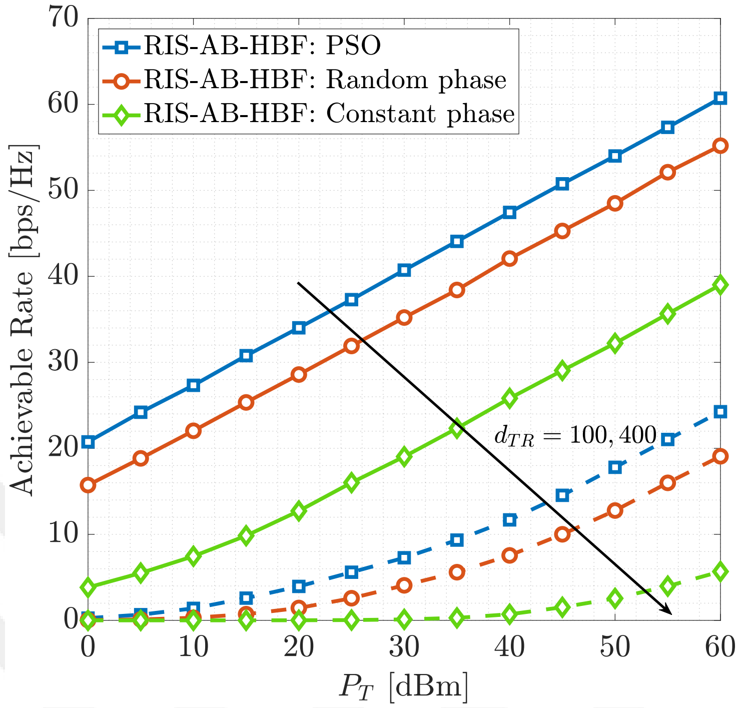

Figure 4.5: Achievable rate comparison of different phase adjustment methods in RIS-aided AB-HPC systems for varying M_I.

4.1.5 Conclusions

In this work, a RIS-aided AB-HBF system has been introduced for the hybrid mmWave massive MIMO system. In this context, we have investigated a number of RIS-aided AB-HBF systems in terms of achievable rate performance to find the most efficient architecture where the RIS and HBF technologies work in harmony with each other. It has been shown via extensive numerical results that a remarkable increase in achievable rate performance is achieved by effectively positioning the RIS even in the absence of a LoS channel between the Tx and Rx. The use of RISs in the AB-HBF systems may have the potential to provide more favorable advantages in terms of reliability and flexibility in system design.

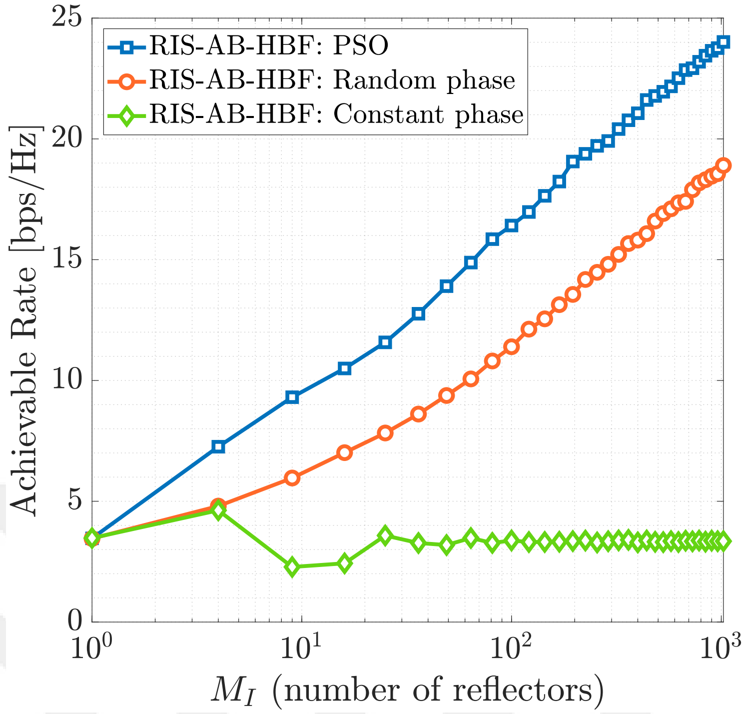

Figure 4.6: Achievable rate performance of the AB-HBF system with and without RIS for varying M_I.

4.2 Multi-RIS Assisted Hybrid Beamforming Design for Terahertz Massive MIMO Systems

In the envisioned future of wireless communication systems, the utilization of a substantially large spectrum at high frequencies is of utmost importance to facilitate the provision of unparalleled performance for unique applications such as holographic teleportation, autonomous systems, extended reality, and digital twins [119]. To meet these demands, it is crucial to enhance the existing wireless spectrum bands below 6 GHz and in the millimeter wave (mmWave) range by migrating towards the higher frequency terahertz (THz) bands, which offer abundant bandwidth [3]. While the mmWave transmission is already established as a fundamental component of fifth-generation (5G) and beyond communication systems, the introduction of promising technologies such as massive multiple-input multiple-output (MIMO) and reconfigurable intelligent surface (RIS) has been undertaken to tackle the challenges arising from high path loss and vulnerability to blockage at the higher frequencies

[12, 15, 17, 104]. RISs, composed of low-cost and passive reflecting elements, have recently garnered significant attention from both academia and industry owing to their capacity-enhancing capabilities and their potential to improve the transmission performance of wireless communication systems.

By leveraging the massive MIMO technique, which employs a large number of antennas at both the transmitter and receiver sides, it becomes possible to exploit the abundant spatial degrees of freedom and achieve substantial capacity enhancements. The high number of antennas allows for increased spatial multiplexing, enabling simultaneous transmission of multiple data streams, thereby significantly boosting the capacity of the system. In THz communications, the integration of massive MIMO systems, which employ beamforming technologies to generate highly directional beams with high gain, offers a practical solution to counteract propagation loss [120]. In terms of cost efficiency, the hybrid beamforming (HBF) architecture has emerged as an appealing choice for massive MIMO systems [116, 121]. By combining the advantages of both analog and digital processing, the HBF architecture achieves a comparable performance to digital beamforming while exhibiting significantly lower hardware cost and power consumption [115, 122]. Moreover, a previous study [107] introduced the angular-based HBF (AB-HBF) technique as a solution that not only minimizes hardware cost and complexity by employing a limited number of radio frequency (RF) chains but also reduces the channel state information (CSI) overhead by designing the RF stage based on slow time-varying CSI, specifically angular information. Consequently, the reduced-size effective CSI is employed in the baseband (BB) stage design. Additionally, AB-HBF also exhibits considerably lower computational complexity compared to conventional single-stage fully digital beamforming approaches.

In traditional HBF systems, designed as a fully-connected HBF (FC-HBF) structure, each RF chain is connected to all antenna elements. Therefore, the FC-HBF systems allow each RF chain to benefit from the complete beamforming capability of all antenna elements within the antenna array. In order to mitigate the cost/complexity associated with the elevated number of RF chains, the sub-connected HBF (SC-HBF) structure has been introduced in [123]. This alternative design enables an arrangement, where a specific RF chain is connected to a carefully chosen subset of antenna elements. Obviously, the SC-HBF structure does not benefit from full beamforming capability for all RF chains, the dynamic selection capability of sub-antenna-arrays provides flexible design opportunities as well as a reduced number of phase shifters [124].

4.2.1 Prior Works

The mmWave/THz channels exhibit sparsity and strong directivity, primarily consisting of a dominant line-of-sight (LoS) cluster and several weaker non-line-of-sight (NLoS) clusters, especially when massive antenna elements are employed [7,17,125]. Furthermore, RISs can also be considered as an efficient tool to enhance the rank of the MIMO channel matrix, mitigate multipath fading, and optimize spatial multiplexing performance by adjusting the RIS-assisted communication channel through the design of the RIS phase shift matrix [5,126,127].

The integration of RIS and massive MIMO hybrid beamforming systems in THz frequencies has emerged as an appealing area of investigation, as evidenced by recent scholarly attention [128–132]. In [128], the authors introduce an HBF technique for multi-hop communication networks assisted by RIS in the THz frequency range, focusing on enhancing coverage range, and employs deep reinforcement learning to jointly optimize the digital beamforming matrix at the base station (BS) and analog beamforming matrices at the RIS to mitigate propagation loss. The study presented in [129] introduces a RIS-based HBF architecture for THz communication, leveraging the energy-efficient properties of the RIS in place of the power-consuming phased array for analog beamforming while also optimizing the hybrid precoding matrix to maximize the sum-rate of the users. In [130], the authors introduce a low-complexity beam training and HBF approach for THz multi-user massive MIMO systems utilizing RIS. Through numerical analysis, they illustrate that integrating RIS results in significant performance improvements compared to systems without RIS. The work [131] presents a comprehensive study on the development of a wideband HBF solution for the joint radar communication architecture in ultra-massive MIMO systems operating in the terahertz (THz) frequency range. They also propose model-based and model-free HBF techniques depending on both CSI and channel covariance matrix.

In summary, to the best of our knowledge, HBF designs in the existing THz communications literature have been mostly made by performing analog beamforming in RIS instead of a transmitter. Moreover, angular-based HBF-based solutions have not yet been considered in RIS-based THz band systems. Consequently, there remains a demand for a power and cost-efficient HBF design that enhances performance and spatial multiplexing gain, effectively exploiting the advantageous features of RIS and massive MIMO systems.

4.2.2 Contributions

In this work, we introduce two innovative angular-based HBF designs for single and multiple-RIS-aided THz massive MIMO systems, employing low CSI overhead. We examine two critical scenarios commonly encountered in THz channels and present cost and energy-efficient solutions utilizing RISs to enhance system performance as well as reduce CSI overhead. Within this context, our major contributions are summarized below:

- First, we focus on a scenario in the presence of obstacles blocking the direct path between the transmitter and receiver, where an RIS offers an alternative transmission path, maintaining reliable communication. At mmWave frequencies, both line-of-sight (LoS) and non-line-of-sight (NLoS) paths play a significant role. However, in the THz band, the NLoS paths have minimal impact on the received power, resulting in a communication scenario characterized by LoS dominance and NLoS assistance at THz frequencies. If the LoS link is blocked, providing the transmission over the weak NLoS channels will threaten reliable communication. In this case, while it is aimed to provide reliable communication by using an LoS RIS-assisted link, NLoS channels efficiently will be used in the transmission to increase the performance of the system by proposing the proper AB-HBF designs.

- Another major challenge in THz channels lies in efficiently transmitting multiple data streams along orthogonal paths, particularly in scenarios where a reliable LoS channel is present between the transmitter and receiver. In this scenario, we explore leveraging multiple-RIS in LoS dominant and sparse environments to transmit multiple data streams over orthogonal links, consequently aiming to improve the achievable rate performance as well as the rank of the channel matrix. Through the introduction of an innovative HBF design for multi-RISs-assisted THz massive MIMO systems, the overarching goal of attaining enhanced spatial multiplexing gain is achieved with the effective utilization of NLoS paths, as well as the RIS-assisted path during the transmission.

- By utilizing a 3D geometry-based THz channel model, we propose a three-stage design for the RIS-aided HBF system: *i)* The transmit and receive RF beamformers, *ii)* the transmit/receive BB precoder/combiner, and *iii)* RIS phase shift matrix design. Here, the transmit and receive RF beamformers are designed based on the slow time-varying angle-of-arrival/angle-of-departure (AoA/AoD) information of the channel, while the BB precoder and combiner exploit the reduced-size effective channel observed at the BB stage. Furthermore, we employ particle swarm optimization (PSO) to design the RIS phase reflection matrix, aiming to maximize the achievable rate of THz massive MIMO systems. Then, we extend this design methodology to multiple-RIS-aided scenarios to optimize the phase shift matrices of each RIS.

- As a natural extension of our proposed system, we extend the traditional FC-HBF-based design to the SC-HBF design for the RIS-enabled THz AB-HBF system. This new approach aims to notably reduce hardware and analog beamforming implementation costs compared to FD-HBF-based THz mMIMO systems. By comparing with FC-HBF systems, we demonstrate the potential for improved adaptability, efficiency, and cost-effectiveness in RIS-enabled THz communication systems, highlighting the advantages of the SC-HBF structure.

- Through extensive numerical experiments, we demonstrate the significant enhancement in achievable rate performance of the THz AB-HBF systems by incorporating RISs, which effectively alleviate the disruptive effects of the wireless propagation environment. The proposed AB-HBF techniques utilize a considerably smaller number of RF chains for connecting the RF-stage and BB-stage compared to the number of antennas. This not only reduces the hardware cost/complexity and power consumption for mMIMO systems with large antenna arrays but also employs reduced-size effective intended channel matrices in the AB-HBF design, replacing the full-size instantaneous CSI. This approach significantly reduces the overhead associated with channel estimation.

4.2.3 System and Channel Model

In this section, we introduce the system and channel models of the single and multiple-RIS-assisted AB-HBF schemes for THz massive MIMO systems, elucidating their underlying operational principles.

4.2.3.1 Single RIS-Aided Transmission

A hybrid THz massive MIMO architecture is considered by incorporating an RIS, as depicted in Fig. 4.7. The system configuration consists of a single RIS positioned between the transmitter (Tx) and receiver (Rx). Both the Tx and Rx, along with the RIS, are equipped with half-wavelength spaced uniform rectangular arrays (URAs). The RIS is equipped with $M_S = M_{S_x} \times M_{S_y}$ dynamically adjustable reflecting elements, while the Tx and Rx possess $M_T = M_{T_x} \times M_{T_y}$ and $M_R = M_{R_x} \times M_{R_y}$ antennas, respectively. The digital BB precoder ($\mathbf{B}_T$) and analog RF beamformer ($\mathbf{A}_T$) are employed at the Tx to transmit N_D data streams, utilizing N_T RF chains. At the Rx, the received signal is processed through the analog RF beamformer

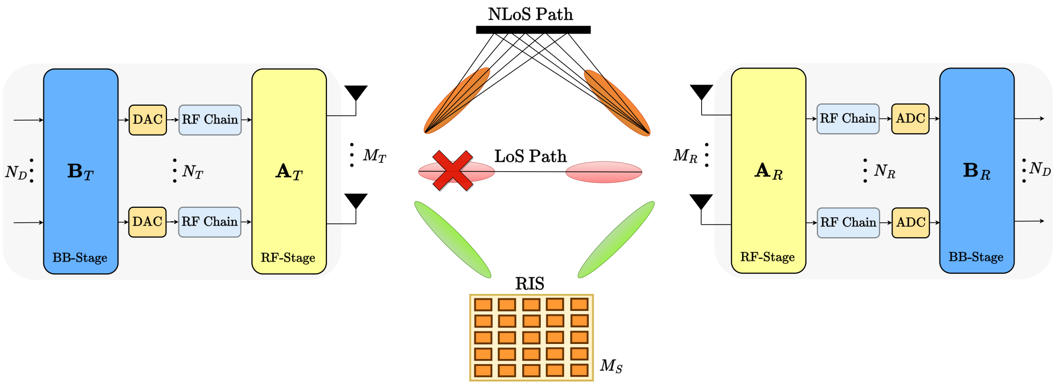

Figure 4.7: RIS-assisted hybrid THz massive MIMO system model.

($\mathbf{A}_R$) and digital baseband combiner ($\mathbf{B}_T$), linked to N_R RF chains. The constraint $N_D \leq \min(N_T, N_R)$ limits the number of data streams, and the number of RF chains is significantly smaller than the count of transmit and receive antennas with $N_T \ll M_T$ and $N_R \ll M_R$ from exploiting the advantages of HBF systems.

The precoded and transmitted signal $\tilde{\mathbf{x}} \in \mathbb{C}^{M_T}$ from the Tx is formulated as:

$$\tilde{\mathbf{x}} = \mathbf{A}_T \mathbf{B}_T \mathbf{x}, \tag{4.23}$$

where $\mathbf{A}_T \in \mathbb{C}^{M_T \times N_T}$ denotes the transmit RF beamformer, $\mathbf{B}_T \in \mathbb{C}^{N_T \times N_D}$ denotes the BB precoder and $\mathbf{x} \in \mathbb{C}^{N_D}$ stands for the data symbol vector, which ensures $\mathbb{E}\left\{\mathbf{x}\mathbf{x}^H\right\} = \mathbf{I}_{N_D}$. Furthermore, the transmitted power P_{T_x} is subject to a power constraint, denoted by $\mathbb{E}\left\{\left\|\tilde{\mathbf{x}}\right\|_2^2\right\} \leq P_{T_x}$.

In the considered communication system, the data can be transmitted over three distinct channels, namely the LoS and NLoS channels between the Tx and Rx, along with the channel assisted by the RIS. Here, the LoS and NLoS channel between the Tx and Rx are respectively denoted by $\mathbf{H}_{\text{LoS}} \in \mathbb{C}^{M_R \times M_T}$ and $\mathbf{H}_{\text{NLoS}} \in \mathbb{C}^{M_R \times M_T}$, while the RIS-assisted link comprises two components: $\mathbf{H}_{\text{Tx-RIS}} \in \mathbb{C}^{M_S \times M_T}$ represents the channel matrix from the Tx to the RIS, and $\mathbf{H}_{\text{Rx-RIS}} \in \mathbb{C}^{M_R \times M_S}$ represents the channel matrix from the RIS to the Rx. Moreover, $\mathbf{\Theta} = \text{diag}(e^{j\Omega_1}, \ldots, e^{j\Omega_{M_S}}) \in \mathbb{C}^{M_S \times M_S}$ corresponds to the phase reflection matrix of the RIS, where Ω_i denotes the phase shift introduced by the ith reflecting element of the RIS for $i = 1, \ldots, M_S$.

Then, the received signal from the LoS, NLoS and RIS-assisted paths at the Rx is expressed as

$$\begin{aligned}\mathbf{r} =&\mathbf{H}\tilde{\mathbf{x}} + \mathbf{n} = (\mathbf{H}_{\text{LoS}} + \mathbf{H}_{\text{NLoS}} + \mathbf{H}_{\text{RIS-Rx}}\boldsymbol{\Theta}\mathbf{H}_{\text{Tx-RIS}})\tilde{\mathbf{x}} + \mathbf{n} \\ =&(\mathbf{H}_{\text{LoS}} + \mathbf{H}_{\text{NLoS}} + \mathbf{H}_{\text{RIS-Rx}}\boldsymbol{\Theta}\mathbf{H}_{\text{Tx-RIS}})\mathbf{A}_T\mathbf{B}_T\mathbf{x} + \mathbf{n},\end{aligned} \tag{4.24}$$

where $\mathbf{H} = \mathbf{H}_{\text{LoS}} + \mathbf{H}_{\text{NLoS}} + \mathbf{H}_{\text{RIS-Rx}}\boldsymbol{\Theta}\mathbf{H}_{\text{Tx-RIS}} \in \mathbb{C}^{M_R \times M_T}$ denotes the end-to-end channel matrix, while $\mathbf{n} \sim \mathcal{CN}(\mathbf{0}, \sigma_n^2 \mathbf{I}_{M_R})$ denotes the complex Gaussian noise vector.

With $\mathcal{H} = \mathbf{A}_R\mathbf{H}\mathbf{A}_T \in \mathbb{C}^{N_R \times N_T}$ being the effective channel matrix seen from the BB stages, the combined signal after the digital BB combiner is expressed as

$$\tilde{\mathbf{r}} = \mathbf{B}_R\mathcal{H}\mathbf{B}_T\mathbf{x} + \mathbf{B}_R\mathbf{A}_R\mathbf{n}, \tag{4.25}$$

where $\mathbf{A}_R \in \mathbb{C}^{N_R \times M_T}$ and $\mathbf{B}_R \in \mathbb{C}^{N_D \times N_R}$ denotes the receive RF beamformer and the BB combiner, respectively.

The primary objective of our study is to effectively design $\mathbf{A}_T$, $\mathbf{B}_T$, $\mathbf{A}_R$, $\mathbf{B}_R$ and $\boldsymbol{\Theta}$. This design aims to maximize the achievable rate of the system, which is represented by

$$\max_{\{\mathbf{A}_T,\mathbf{A}_R,\mathbf{B}_T,\mathbf{B}_R,\boldsymbol{\Theta}\}} \quad R = \log_2 \det\left(\mathbf{I}_{N_D} + \mathbf{R}_v^{-1}\tilde{\mathcal{H}}\tilde{\mathcal{H}}^H\right), \tag{4.26a}$$

$$\text{s.t.} \quad \tilde{\mathcal{H}} = \mathbf{B}_R\mathcal{H}\mathbf{B}_T \in \mathbb{C}^{M_R \times M_T}, \tag{4.26b}$$

$$\mathcal{H} = \mathbf{A}_R\mathbf{H}\mathbf{A}_T \in \mathbb{C}^{N_R \times N_T}, \tag{4.26c}$$

$$|\mathbf{A}_T(i,j)| = \frac{1}{\sqrt{M_T}}, |\mathbf{A}_R(i,j)| = \frac{1}{\sqrt{M_R}}, \ \forall (i,j), \tag{4.26d}$$

$$\mathbb{E}\{\|\mathbf{x}\|_2^2\} = \text{tr}\left(\mathbf{B}_T^H\mathbf{A}_T^H\mathbf{A}_T\mathbf{B}_T\right) \le P_{T_x}, \tag{4.26e}$$

The covariance matrix of the noise $\mathbf{v} = \mathbf{B}_R\mathbf{A}_R\mathbf{n}$ is denoted as $\mathbf{R}_v = \sigma_n^2\mathbf{B}_R\mathbf{A}_R\mathbf{A}_R^H\mathbf{B}_R^H$. In order to satisfy the implementation requirements of the RF beamformer, the constant-modulus constraint in (4.26d) is ensured due to the utilization of phase shifters.

In this section, we also introduce a widely adopted statistical channel model known as the Saleh-Valenzuela (S-V) channel model [133], which finds extensive application in massive MIMO systems. By leveraging the implementation of a large number of antenna elements, sparsity and strong directivity are typically obtained in the THz channel, characterized by a dominant LoS cluster and multiple weaker NLoS clusters [86], [87], [88]. Hence, by considering the URA structure, the channel matrix can be written as

$$
\begin{aligned}
\mathbf{H} = & \underbrace{\frac{z_0}{\sqrt{\alpha \tau_0^{n_0}}} \boldsymbol{a}_R^T(\gamma_{x,R}^{\text{LoS}}, \gamma_{y,R}^{\text{LoS}}) \boldsymbol{a}_T(\gamma_{x,T}^{\text{LoS}}, \gamma_{y,T}^{\text{LoS}})}_{\mathbf{H}_{\text{LoS}}} \\
& + \underbrace{\sum_{q=1}^{Q} \frac{z_q}{\sqrt{\alpha \tau_q^{n}}} \boldsymbol{a}_R^T(\gamma_{x,R}^{\text{NLoS},q}, \gamma_{y,R}^{\text{NLoS,q}}) \boldsymbol{a}_T(\gamma_{x,T}^{\text{NLoS},q}, \gamma_{y,T}^{\text{NLoS},q})}_{\mathbf{H}_{\text{NLoS}}} \\
& + \mathbf{H}_{\text{RIS-Rx}} \boldsymbol{\Theta} \mathbf{H}_{\text{Tx-RIS}}
\end{aligned}
\tag{4.27}
$$

where $z_0 \sim \mathcal{CN}(0,1)$ and $z_q \sim \mathcal{CN}(0, 1/Q)$ respectively stand for the complex path gain of the LoS channel and q^{th} $(q = 1, \ldots, Q)$ path of the NLoS channel with Q being the total number of NLoS paths, the reference path loss is denoted in dB as $\alpha = 32.4 + 20\log_{10}(f_c)$, η_0 and η respectively represents the path loss exponents of LoS and NLoS paths. Moreover, τ_0 and τ_q respectively represent the distance of LoS path and q^{th} NLoS path from the Tx and Rx, where $q = 1, \ldots, Q$. Here, the RIS-assisted sub-channels for the Tx-RIS and RIS-Rx links are respectively defined as

$$
\begin{aligned}
\mathbf{H}_{\text{Tx-RIS}} &= \frac{z_{\text{Tx-RIS}}}{\sqrt{\alpha \tau_{\text{Tx-RIS}}^{n_0}}} \boldsymbol{a}_R^T(\gamma_{x,R}^{\text{Tx-RIS}}, \gamma_{y,R}^{\text{Tx-RIS}}) \boldsymbol{a}_T(\gamma_{x,T}^{\text{Tx-RIS}}, \gamma_{y,T}^{\text{Tx-RIS}}), \\
\mathbf{H}_{\text{RIS-Rx}} &= \frac{z_{\text{RIS-Rx}}}{\sqrt{\alpha \tau_{\text{RIS-Rx}}^{n_0}}} \boldsymbol{a}_R^T(\gamma_{x,R}^{\text{RIS-Rx}}, \gamma_{y,R}^{\text{RIS-Rx}}) \boldsymbol{a}_T(\gamma_{x,T}^{\text{RIS-Rx}}, \gamma_{y,T}^{\text{RIS-Rx}})
\end{aligned}
\tag{4.28}
$$

where $z_i \sim \mathcal{CN}(0,1)$ is the complex path gain, τ_i is the distance of the corresponding path for $i \in \{\text{Tx-RIS}, \text{RIS-Rx}\}$. The Tx/Rx array steering vector for considered URA geometry is obtained as

$$
\begin{aligned}
\boldsymbol{a}_i\left(\gamma_{x,i}^j, \gamma_{y,i}^j\right) = & \left[1, e^{j2\pi d \gamma_{x,i}^j}, \cdots, e^{j2\pi d (M_{k_x}-1)\gamma_{x,i}^j}\right]^T \\
& \otimes \left[1, e^{j2\pi d \gamma_{y,i}^j}, \cdots, e^{j2\pi d \left(M_{k_y}-1\right)\gamma_{y,i}^j}\right]^T,
\end{aligned}
\tag{4.29}
$$

where $i \in \{T, R\}$, $j \in \{\text{LoS}, \text{NLoS}, \text{Tx-RIS}, \text{RIS-Rx}\}$, $k \in \{T, R, S\}$ and d is the inter-element spacing normalized by the wavelength. For the LoS paths, the coefficients reflecting the elevation and azimuth AoA (AoD) can be respectively calculated as $\gamma_{x,R}^j = \sin\left(\theta_R^j\right)\cos\left(\psi_R^j\right)$ $\left(\gamma_{x,T}^j = \sin\left(\theta_T^j\right)\cos\left(\psi_T^j\right)\right)$ and $\gamma_{y,R}^j = \sin\left(\theta_R^j\right)\sin\left(\psi_R^j\right)$

Table 4.3: Angular parameters of q^{th} the NLoS channel for $q = 1, \ldots, Q$.

AoA Parameters		**AoD Parameters**	
$\theta_{R,q}^{\text{NLoS}}$	Mean elevation	$\theta_{T,q}^{\text{NLoS}}$	Mean elevation
$\delta_{R,q}^{\text{NLoS},\theta}$	Elevation spread	$\delta_{T,q}^{\text{NLoS},\theta}$	Elevation spread
$\psi_{R,q}^{\text{NLoS}}$	Mean azimuth	$\psi_{T,q}^{\text{NLoS}}$	Mean azimuth
$\delta_{R,q}^{\text{NLoS},\psi}$	Azimuth spread	$\delta_{T,q}^{\text{NLoS},\psi}$	Azimuth spread

($\gamma_{y,T}^{j} = \sin\left(\theta_T^j\right)\sin\left(\psi_T^j\right)$), where θ_R^j (θ_T^j) and ψ_R^j (ψ_T^j) are respectively elevation and azimuth AoA (AoD) at the receive (transmit) node of each channel with $j \in \{\text{LoS}, \text{Tx-RIS}, \text{RIS-Rx}\}$.

By considering the AoA/AoD mean and spread parameters defined in Table 1, the coefficients reflecting the elevation and azimuth AoA (AoD) for the q^{th} path of the NLoS channel can be respectively calculated as $\gamma_{x,R}^{\text{NLoS},q} = \sin\left(\theta_{R,q}^{\text{NLoS}}\right)\cos\left(\psi_{R,q}^{\text{NLoS}}\right)$ ($\gamma_{x,T}^{\text{NLoS},q} = \sin\left(\theta_{T,q}^{\text{NLoS}}\right)\cos\left(\psi_{T,q}^{\text{NLoS}}\right)$) and $\gamma_{y,R}^{\text{NLoS},q} = \sin\left(\theta_{R,q}^{\text{NLoS}}\right)\sin\left(\psi_{R,q}^{\text{NLoS}}\right)$ ($\gamma_{y,T}^{\text{NLoS},q} = \sin\left(\theta_{T,q}^{\text{NLoS}}\right)\sin\left(\psi_{T,q}^{\text{NLoS}}\right)$), where θ_R^j ($\theta_{T,q}^{\text{NLoS}}$) and $\psi_{R,q}^{\text{NLoS}}$ ($\psi_{T,q}^{\text{NLoS}}$) are respectively elevation and azimuth AoA (AoD) at the receive (transmit) node with $q = 1, \ldots, Q$.

In order to decompose the slow and fast time-varying components of each channel, the end-to-end channel in (4.27) can be rewritten as

$$\mathbf{H} = \underbrace{\mathbf{\Phi}_R \mathbf{G} \mathbf{\Phi}_T}_{\mathbf{H}_{\text{LoS}} + \mathbf{H}_{\text{NLoS}}} + \underbrace{\phi_R^{\text{RIS-Rx}} G_{\text{RIS-Rx}} \phi_T^{\text{RIS-Rx}}}_{\mathbf{H}_{\text{RIS-Rx}}} \mathbf{\Theta} \underbrace{\phi_R^{\text{Tx-RIS}} G_{\text{Tx-RIS}} \phi_T^{\text{Tx-RIS}}}_{\mathbf{H}_{\text{Tx-RIS}}} \tag{4.30}$$

where $\mathbf{\Phi}_R \in \mathbb{C}^{M_R \times (Q+1)}$ and $\mathbf{\Phi}_T \in \mathbb{C}^{(Q+1) \times M_T}$ respectively denote the receive and transmit slow-time varying phase response matrices of LoS and NLoS paths, $\mathbf{G} = \text{diag}\{z_0/\sqrt{\alpha\tau_0^{\eta_0}}, z_1/\sqrt{\alpha\tau_1^{\eta}}, \ldots, z_Q/\sqrt{\alpha\tau_Q^{\eta}}\} \in \mathbb{C}^{(Q+1)\times(Q+1)}$ is the diagonal matrix represents the fast-time varying path gains. Here, the slow-time varying transmit and receive phase response matrices for the LoS and NLoS channels are defined as:

$$\begin{aligned}\mathbf{\Phi}_T &= \begin{bmatrix} \boldsymbol{a}_T^H\left(\gamma_{x,T}^{\text{LoS}}, \gamma_{y,T}^{\text{LoS}}\right) \\ \boldsymbol{a}_T^H\left(\gamma_{x,T}^{\text{NLoS},1}, \gamma_{y,T}^{\text{NLoS},1}\right) \\ \vdots \\ \boldsymbol{a}_T^H\left(\gamma_{x,T}^{\text{NLoS},Q}, \gamma_{y,T}^{\text{NLoS},Q}\right) \end{bmatrix}, \\ \mathbf{\Phi}_R &= \begin{bmatrix} \boldsymbol{a}_R^H\left(\gamma_{x,R}^{\text{LoS}}, \gamma_{y,R}^{\text{LoS}}\right) \\ \boldsymbol{a}_R^H\left(\gamma_{x,R}^{\text{NLoS},1}, \gamma_{y,R}^{\text{NLoS},1}\right) \\ \vdots \\ \boldsymbol{a}_R^H\left(\gamma_{x,R}^{\text{NLoS},Q}, \gamma_{y,R}^{\text{NLoS},Q}\right) \end{bmatrix}^H.\end{aligned} \tag{4.31}$$

Then, the fast and slow-time varying components of the RIS-assisted sub-channels are defined as follows: $G_l = z_l/\sqrt{\alpha\tau_l^{n_0}}$, $\phi_R^l = \boldsymbol{a}_R^T(\gamma_{x,R}^l, \gamma_{y,R}^l)$, $\phi_T^l = \boldsymbol{a}_T^T(\gamma_{x,T}^l, \gamma_{y,T}^l)$ for $l \in \{\text{Tx-RIS}, \text{RIS-Rx}\}$.

4.2.3.2 Multi-RISs-Aided Transmission

The utilization of multiple-RIS holds significant potential in terms of enhancing quality-of-service, improving reliability, and increasing flexibility in system design [5]. Efficiently transmitting multiple data streams along orthogonal paths poses a significant challenge in THz massive MIMO systems, particularly in scenarios where a reliable and dominant LoS channel exists between the Tx and Rx. To address this challenge, we investigate the potential of leveraging multiple-RIS in LoS dominant and sparse environments. By employing multiple-RIS, our objective is to transmit multiple data streams over different RIS-aided orthogonal paths, aiming to improve both the achievable rate performance and spatial multiplexing gain. In order to accomplish that goal, we utilize the multiple-RIS-assisted and NLoS paths during the transmission process by extending the single RIS-aided system model to the multiple-RIS case.

In order to extend the existing single RIS-aided system to a more advanced and versatile transmission scheme, we propose the utilization of multiple-RIS in the target communication system. An advanced hybrid THz massive MIMO architecture

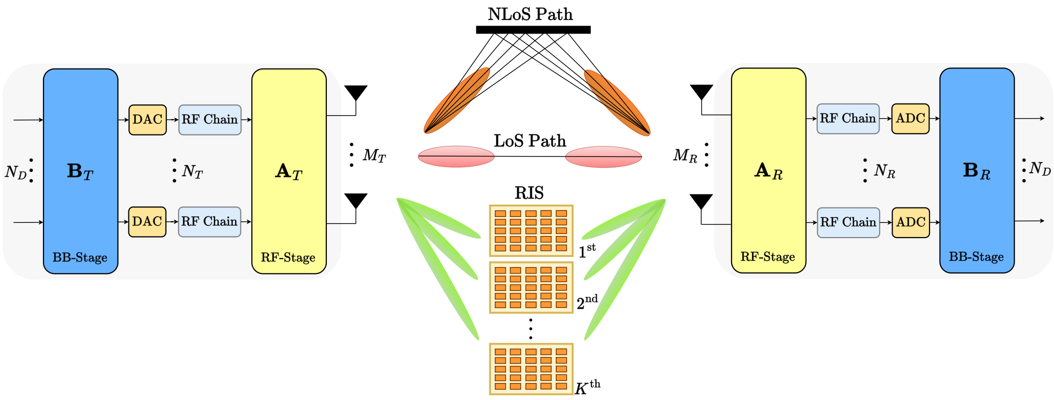

Figure 4.8: RIS-assisted hybrid mmWave massive MIMO system model.

is proposed, leveraging the utilization of multiple-RIS in the transmission, as illustrated in Fig. 4.8. Each RIS consists of M_S reflecting elements, and we consider a total of K RISs in the setup. The system configuration entails K RISs strategically positioned between the Tx and Rx. To facilitate efficient signal propagation, both the Tx and Rx, along with the RISs, are equipped with half-wavelength spaced URA. Similar to the single RIS-aided system, the Tx and Rx are equipped with M_T and M_R antennas, respectively.

At the Tx, a sophisticated combination of the digital BB precoder $\mathbf{B}_T$ and analog RF beamformer $\mathbf{A}_T$ is employed to facilitate the transmission of N_D data streams, effectively utilizing N_T RF chains. On the receiving end, the received signal is skillfully processed through the analog RF beamformer $\mathbf{A}_R$ and digital BB combiner $\mathbf{B}_R$, integrated with N_R RF chains. The presence of a constraint $N_D \leq \min(N_T, N_R)$ regulates the maximum number of data streams, ensuring optimal performance. Notably, the number of RF chains remains considerably smaller than the total number of transmit and receive antennas (i.e., $N_T \ll M_T$ and $N_R \ll M_R$), harnessing the inherent advantages offered by HBF systems. For simplicity, we will consider all parameters and methodologies in Tx and Rx units of the multiple-RIS system model the same as single RIS-aided transmission.

With the integration of multiple RIS, the data can now be transmitted over an expanded set of channels, encompassing the LoS and NLoS channels between the Tx and receiver Rx, as well as the channels assisted by the K RISs. Here, the LoS and NLoS channel between the Tx and Rx are respectively denoted by $\mathbf{H}_{\mathrm{LoS}} \in \mathbb{C}^{M_R \times M_T}$ and $\mathbf{H}_{\mathrm{NLoS}} \in \mathbb{C}^{M_R \times M_T}$, while each RIS-assisted link comprises two components: $\mathbf{H}^k_{\text{Tx-RIS}} \in \mathbb{C}^{M_S \times M_T}$ represents the channel matrix from the Tx to the k^{th} RIS, and $\mathbf{H}^k_{\text{Rx-RIS}} \in \mathbb{C}^{M_R \times M_S}$ represents the channel matrix from the k^{th} RIS to the Rx for $k \in \{1, 2, \ldots, K\}$. It should be noted that each subchannel here is modeled as in (4.27)-(4.29). Moreover, $\boldsymbol{\Theta}_k = \operatorname{diag}(e^{j\Omega^k_1}, \ldots, e^{j\Omega^k_{M_S}}) \in \mathbb{C}^{M_S \times M_S}$ corresponds to the phase reflection matrix of k^{th} RIS, where Ω^k_i denotes the phase shift introduced by the ith reflecting element of the k^{th} RIS for $i = 1, \ldots, M_S$ and $k = 1, \ldots, K$. Consequently, the received signal at the Rx incorporates contributions from the LoS, NLoS, and multiple-RIS-assisted paths. This can be mathematically expressed as

$$\mathbf{r} = \underbrace{\left(\mathbf{H}_{\mathrm{LoS}} + \mathbf{H}_{\mathrm{NLoS}} + \sum_{k=1}^{K} \mathbf{H}^k_{\text{RIS-Rx}} \boldsymbol{\Theta}_k \mathbf{H}^k_{\text{Tx-RIS}}\right)}_{\mathbf{H}_K \in \mathbb{C}^{M_R \times M_T}} \mathbf{A}_T \mathbf{B}_T \mathbf{x} + \mathbf{n}, \tag{4.32}$$

where $\mathbf{H}_K$ stands for the end-to-end channel matrix of the multiple-RIS-aided system, while $\mathbf{n} \sim \mathcal{CN}(\mathbf{0}, \sigma_n^2 \mathbf{I}_{M_R})$ denotes the complex Gaussian noise vector.

By following the similar steps with the single-RIS-aided system, with $\boldsymbol{\mathcal{H}}_K = \mathbf{A}_R \mathbf{H} \mathbf{A}_T \in \mathbb{C}^{N_R \times N_T}$ being the effective channel matrix seen from the BB stages, the combined signal after the digital BB combiner is expressed as

$$\tilde{\mathbf{r}} = \mathbf{B}_R \boldsymbol{\mathcal{H}}_K \mathbf{B}_T \mathbf{x} + \mathbf{B}_R \mathbf{A}_R \mathbf{N}, \tag{4.33}$$

where $\mathbf{A}_R \in \mathbb{C}^{N_R \times M_T}$ and $\mathbf{B}_R \in \mathbb{C}^{N_D \times N_R}$ denotes the receive RF beamformer and the BB combiner, respectively.

Here, we still aim to maximize the achievable rate of the system by carefully designing $\mathbf{A}_T$, $\mathbf{A}_T$, $\mathbf{A}_R$, $\mathbf{B}_R$ and $\{\boldsymbol{\Theta}_1, \ldots, \boldsymbol{\Theta}_K\}$. Then, the multiple-RIS-aided

AB-HBF design can be formulated as the following optimization problem:

$$\max_{\{\mathbf{A}_T,\mathbf{A}_R,\mathbf{B}_T,\mathbf{B}_R,\mathbf{\Theta}_1,\dots,\mathbf{\Theta}_K\}} R = \log_2 \det\Big(\mathbf{I}_{N_D} + \mathbf{R}_v^{-1}\tilde{\mathcal{H}}_K\tilde{\mathcal{H}}_K^H\Big) \tag{4.34a}$$

$$\text{s.t. } \tilde{\mathcal{H}}_K = \mathbf{B}_R\mathcal{H}_K\mathbf{B}_T \in \mathbb{C}^{M_R\times M_T}, \tag{4.34b}$$

$$\mathcal{H}_K = \mathbf{A}_R\mathbf{H}_K\mathbf{A}_T \in \mathbb{C}^{N_R\times N_T}, \tag{4.34c}$$

$$|\mathbf{A}_T(i,j)| = \frac{1}{\sqrt{M_T}}, |\mathbf{A}_R(i,j)| = \frac{1}{\sqrt{M_R}},\ \forall (i,j), \tag{4.34d}$$

$$\mathbb{E}\{\|\mathbf{x}\|_2^2\} = \text{tr}\left(\mathbf{B}_T^H\mathbf{A}_T^H\mathbf{A}_T\mathbf{B}_T\right) \le P_{T_x}, \tag{4.34e}$$

The covariance matrix of the noise $\mathbf{v} = \mathbf{B}_r\mathbf{F}_r\mathbf{n}$ is denoted as $\mathbf{R}_v = \sigma_n^2\mathbf{B}_R\mathbf{A}_R\mathbf{A}_R^H\mathbf{B}_R^H$. Similar to the single RIS-aided case, the constraint of the constant module is ensured as expressed in (4.34d) due to the utilization of phase shifters.

Similar to (4.30), in order to obtain decomposed slow and fast time-varying components of each subchannel, the end-to-end channel $\mathbf{H}_K$ can be rewritten as

$$\mathbf{H}_K = \underbrace{\mathbf{\Phi}_R\mathbf{G}\mathbf{\Phi}_T}_{\mathbf{H}_{\text{LoS}}+\mathbf{H}_{\text{NLoS}}} + \sum_{k=1}^{K} \underbrace{\phi_{R,k}^{\text{RIS-Rx}} G_{\text{RIS-Rx}}^k \phi_{T,k}^{\text{RIS-Rx}}}_{\mathbf{H}_{\text{RIS-Rx}}^k} \mathbf{\Theta}_k \underbrace{\phi_{R,k}^{\text{Tx-RIS}} G_{\text{Tx-RIS}}^k \phi_{T,k}^{\text{Tx-RIS}}}_{\mathbf{H}_{\text{Tx-RIS}}^k} \tag{4.35}$$

where $\mathbf{\Phi}_R \in \mathbb{C}^{M_R\times(Q+1)}$ and $\mathbf{\Phi}_T \in \mathbb{C}^{(Q+1)\times M_T}$ respectively denote the receive and transmit slow-time varying phase response matrices of LoS and NLoS paths defined in (4.31), $\mathbf{G} = \text{diag}\{z_0/\sqrt{\alpha\tau_0^{\eta_0}}, z_1/\sqrt{\alpha\tau_1^{\eta}}, \dots, z_Q/\sqrt{\alpha\tau_Q^{\eta}}\} \in \mathbb{C}^{(Q+1)\times(Q+1)}$ is the diagonal matrix represents the fast-time varying path gains. Here, the fast and slow-time varying components of the sub-channels aided by the kth RIS ($k = 1,\dots,K$) are subsequently defined as $G_l^k = z_l^k/\sqrt{\alpha\tau_{l,k}^{n_0}}$, $\phi_R^{l,k} = \boldsymbol{a}_R^T(\gamma_{x,R}^{l,k}, \gamma_{y,R}^{l,k})$, $\phi_{T,k}^{l} = \boldsymbol{a}_T^T(\gamma_{x,T}^{l,k}, \gamma_{y,T}^{l,k})$ for $l \in \{\text{Tx-RIS}, \text{RIS-Rx}\}$ and $k \in \{1,\dots,K\}$.

4.2.4 Angular-Based Hybrid Beamforming Design For RIS-Aided THz Systems

In this section, we present the design of RF beamformers, BB precoder/combiner, and phase shift matrices of the RISs for the proposed RIS-aided AB-HBF system in the THz band. Our main objective is to maximize the system's achievable rate while simultaneously reducing the size of CSI overhead and hardware complexity.

Considering the extension to multiple-RIS-aided transmission, we provide a generalized approach that is applicable to both single and multiple RIS cases since multiple RIS transmission will be equivalent to single RIS transmission for $K = 1$.

In order to achieve our targets, the design procedures for the RF beamformers are provided based on the slow-time varying angular parameters in the THz band channel conditions. Then, the BB precoder/combiner is designed via the singular value decomposition (SVD) and water filling algorithm using the reduced-size effective channel. Finally, the phase shifts of the RIS are optimized using the PSO method, aiming to maximize the capacity of the system. By integrating these aforementioned design techniques and their benefits, we enhance the achievable rate of the system while alleviating the complexity associated with acquiring and processing CSI. Additionally, the proposed methodology is easily extended to scenarios involving multiple RIS, enabling the optimization of phase shift matrices for each RIS. This comprehensive approach enables the effective utilization of RISs in THz-based AB-HBF systems, leading to improved performance and reduced CSI overhead.

4.2.4.1 RF-Stage Design

The construction of the analog RF beamformer involves the deliberate focusing of signal energy in the desired direction, performed by exploiting the slow-time varying AoA/AoD information. To achieve an efficient design of the RF-stage, it is necessary to accurately define the range of azimuth and elevation AoA/AoD angles for the existing paths within the clusters, as outlined in [108, 125]. Therefore, AoA and AoD supports are obtained using (4.27) as:

$$\Upsilon_{\mathrm{A}} = \Big\{ [\gamma_x, \gamma_y] = \sin(\theta)\left[\cos(\psi), \sin(\psi)\right] \Big| \theta \in \boldsymbol{\theta}_R, \psi \in \boldsymbol{\psi}_R \Big\} \tag{4.36a}$$

$$\Upsilon_{\mathrm{D}} = \Big\{ [\gamma_x, \gamma_y] = \sin(\theta)\left[\cos(\psi), \sin(\psi)\right] \Big| \theta \in \boldsymbol{\theta}_T, \psi \in \boldsymbol{\psi}_T \Big\} \tag{4.36b}$$

where $\boldsymbol{\theta}_R = \boldsymbol{\theta}_R^{\text{Tx-RIS}} \cup \boldsymbol{\theta}_R^{\text{NLoS}} \cup \theta_R^{\text{LoS}}$, $\boldsymbol{\psi}_R = \boldsymbol{\psi}_R^{\text{Tx-RIS}} \cup \boldsymbol{\psi}_R^{\text{NLoS}} \cup \psi_R^{\text{LoS}}$, $\boldsymbol{\theta}_T = \boldsymbol{\theta}_T^{\text{RIS-Rx}} \cup \boldsymbol{\theta}_T^{\text{NLoS}} \cup \theta_T^{\text{LoS}}$, and $\boldsymbol{\psi}_T = \boldsymbol{\psi}_T^{\text{RIS-Rx}} \cup \boldsymbol{\psi}_T^{\text{NLoS}} \cup \theta_T^{\text{LoS}}$. Here, the elevation and azimuth AoA/AoD supports for the NLoS channel are respectively expressed as:

$$\boldsymbol{\theta}_l^{\text{NLoS}} = \cup_{q=1}^{Q} \big[\theta_{l,q}^{\text{NLoS}} - \delta_{l,q}^{\text{NLoS},\theta}, \theta_{l,q}^{\text{NLoS}} + \delta_{l,q}^{\text{NLoS},\theta}\big], \tag{4.37}$$

$$\boldsymbol{\psi}_l^{\text{NLoS}} = \cup_{q=1}^{Q}\left[\psi_{l,q}^{\text{NLoS}} - \delta_{l,q}^{\text{NLoS},\psi}, \psi_{l,q}^{\text{NLoS}} + \delta_{l,q}^{\text{NLoS},\psi}\right] \tag{4.38}$$

for $l \in \{T, R\}$. Furthermore, the elevation and azimuth AoA/AoD supports for the RISs-assisted channels are respectively defined as $\boldsymbol{\theta}_l^j = \cup_{k=1}^{K}\theta_l^j$ and $\boldsymbol{\psi}_l^j = \cup_{k=1}^{K}\psi_l^j$ for $l \in \{T, R\}$ and $j \in \{\text{Tx-RIS}, \text{RIS-Rx}\}$.

By using (4.26c) and (4.35), the effective channel seen from the BB-stages can be rewritten as:

$$\begin{aligned}\mathcal{H}_K &= \mathbf{A}_R\mathbf{H}_K\mathbf{A}_T,\\ &= \mathbf{A}_R\Big(\sum_{k=1}^{K}\phi_{R,k}^{\text{RIS-Rx}}G_{\text{RIS-Rx}}^{k}\phi_{T,k}^{\text{RIS-Rx}}\mathbf{\Theta}_k\phi_{R,k}^{\text{Tx-RIS}}G_{\text{Tx-RIS}}^{k}\phi_{T,k}^{\text{Tx-RIS}} + \mathbf{\Phi}_R\mathbf{G}\mathbf{\Phi}_T\Big)\mathbf{A}_T.\end{aligned} \tag{4.39}$$

To fully leverage the available degrees of freedom offered by the channel and maximize the beamforming gain during transmission (reception), it is necessary for the columns of $\mathbf{A}_T$ ($\mathbf{A}_R$) to reside within the subspace spanned by $\phi_T^{\text{Tx-RIS}}$ and $\mathbf{\Phi}_T$ ($\phi_R^{\text{RIS-Rx}}$ and $\mathbf{\Phi}_R$). Therefore, the conditions as follows should be satisfied:

$$\begin{aligned}&\text{Span}\left(\mathbf{A}_T\right) \subset \left(\text{Span}\left(\phi_T^{\text{Tx-RIS}}\right) \cup \text{Span}\left(\mathbf{\Phi}_T\right)\right)\\ &\text{Span}\left(\mathbf{A}_R\right) \subset \left(\text{Span}\left(\phi_R^{\text{RIS-Rx}}\right) \cup \text{Span}\left(\mathbf{\Phi}_R\right)\right)\end{aligned} \tag{4.40}$$

Then, in order to construct the columns of the transmit RF beamformer matrix, the transmit steering vector is defined as

$$\begin{aligned}\mathbf{e}_T\left(\gamma_x, \gamma_y\right) = &\frac{1}{\sqrt{M_T}}\left[1, e^{j2\pi d\gamma_x}, \cdots, e^{j2\pi d(M_{T_x}-1)\gamma_x}\right]^T\\ &\otimes\left[1, e^{j2\pi d\gamma_y}, \cdots, e^{j2\pi d\left(M_{T_y}-1\right)\gamma_y}\right]^T \in \mathbb{C}^{M_T}.\end{aligned} \tag{4.41}$$

By establishing the quantized angle-pairs as $\Lambda_{x,T}^i = \frac{2i-1}{M_{T_x}} - 1$ for $i = 1, \cdots, M_{T_x}$ and $\Lambda_{y,T}^j = \frac{2j-1}{M_{T_y}} - 1$ for $j = 1, \cdots, M_{T_y}$, we obtain a set of M_T orthogonal transmit steering vectors. These vectors represent the minimum required number of angle-pairs to encompass the entire elevation and azimuth space [107]. Hence, aiming to minimize the utilization of the RF chain while encompassing the complete AoD support, we express the quantized angle pairs within the AoD support as follows:

$$\left(\Lambda_{x,T}^i, \Lambda_{y,T}^j\right) \;\Big|\; \gamma_x \in \mathbf{\Lambda}_{x,T}^i, \gamma_y \in \mathbf{\Lambda}_{y,T}^j, (\gamma_x, \gamma_y) \in \Upsilon_{\text{D}}, \tag{4.42}$$

where the boundary of $\Lambda^{i}_{x,T}$ and $\Lambda^{j}_{y,T}$ are denoted as $\mathbf{\Lambda}^{i}_{x,T} = \left[\Lambda^{i}_{x,T} - \frac{1}{M_{T_x}}, \Lambda^{i}_{x,T} + \frac{1}{M_{T_x}}\right]$ and $\mathbf{\Lambda}^{j}_{y,T} = \left[\Lambda^{j}_{y,T} - \frac{1}{M_{T_y}}, \Lambda^{j}_{y,T} + \frac{1}{M_{T_y}}\right]$, respectively.

Based on (4.36b) and (4.42), the transmit RF beamformer is obtained as:

$$\mathbf{A}_T = \left[\mathbf{e}_T\left(\Lambda^{i_1}_{x,T}, \Lambda^{j_1}_{y,T}\right), \cdots, \mathbf{e}_T\left(\Lambda^{i_{N_T}}_{x,T}, \Lambda^{j_{N_T}}_{y,T}\right)\right] \in \mathbb{C}^{M_T \times N_T}. \tag{4.43}$$

where N_T stands for the number of quantized angle pairs for AoD.

By employing a similar methodology, the receive RF beamformer, $\mathbf{A_R}$, is devised based on the receive steering vector defined as

$$\begin{aligned}\mathbf{e}_R\left(\gamma_x, \gamma_y\right) = \frac{1}{\sqrt{M_R}}&\left[1, e^{j2\pi d\gamma_x}, \cdots, e^{j2\pi d(M_{R_x}-1)\gamma_x}\right]^T \\ &\otimes\left[1, e^{j2\pi d\gamma_y}, \cdots, e^{j2\pi d\left(M_{R_y}-1\right)\gamma_y}\right]^T \in \mathbb{C}^{M_R}.\end{aligned} \tag{4.44}$$

The quantized angle-pairs are defined as $\Lambda^{i}_{x,R} = \frac{2i-1}{M_{R_x}} - 1$ for $i = 1, \cdots, M_{R_x}$ and $\Lambda^{j}_{y,R} = \frac{2j-1}{M_{R_y}} - 1$ for $j = 1, \cdots, M_{R_y}$. Using (4.36a), the quantized angle-pairs encompassing the AoA support can be expressed as

$$\left(\Lambda^{i}_{x,R}, \Lambda^{j}_{y,R}\right) \;\Big|\; \gamma_x \in \mathbf{\Lambda}^{i}_{x,R}, \gamma_y \in \mathbf{\Lambda}^{j}_{y,R}, (\gamma_x, \gamma_y) \in \Upsilon_{\mathrm{A}}, \tag{4.45}$$

where $\mathbf{\Lambda}^{i}_{x,R} = \left[\Lambda^{j}_{x,R} - \frac{1}{M_{R_x}}, \Lambda^{i}_{x,R} + \frac{1}{M_{R_x}}\right]$ and $\mathbf{\Lambda}^{j}_{y,R} = \left[\Lambda^{j}_{y,R} - \frac{1}{M_{R_y}}, \Lambda^{j}_{y,R} + \frac{1}{M_{R_y}}\right]$ respectively denote the boundary of $\Lambda^{i}_{x,R}$ and $\Lambda^{j}_{y,R}$.

Incorporating equations (4.36a) and (4.45), the receive RF beamformer, comprising N_R quantized angle-pairs, is constructed as

$$\mathbf{A}_R = \left[\mathbf{a}_r\left(\Lambda^{m_1}_{x,r}, \Lambda^{n_1}_{y,r}\right), \cdots, \mathbf{e}_T\left(\Lambda^{m_{N_R}}_{x,r}, \Lambda^{n_{N_R}}_{y,r}\right)\right] \in \mathbb{C}^{M_R \times N_R}. \tag{4.46}$$

It is noteworthy to emphasize that both the derived $\mathbf{A}_T$ and $\mathbf{A}_R$ adhere to the constant modulus property, as defined in (4.26d). Furthermore, $\mathbf{A}_T$ and $\mathbf{A}_R^H$ are tall unitary matrices, thereby yielding $\mathbf{A}_T^H\mathbf{A}_T = \mathbf{I}_{N_T}$ and $\mathbf{A}_R\mathbf{A}_R^H = \mathbf{I}_{N_R}$.

4.2.4.2 Baseband Stage Design

Following the RF beamformer design, we provide the design methodology of the BB precoder/combiner in this section, utilizing the low-dimensional effective channel matrix as described in (4.39). The effective channel matrix is subjected to singular value decomposition (SVD), resulting in the expression $\boldsymbol{\mathcal{H}}_K = \mathbf{U}_K\mathbf{\Sigma}_K{\mathbf{V}_K}^H$, where $\mathbf{U}_K \in \mathbb{C}^{N_R \times \text{rank}(\boldsymbol{\mathcal{H}}_K)}$ is a tall unitary matrix, $\boldsymbol{\Sigma}_K = \text{diag}\big(\sigma_1^2, \cdots, \sigma^2_{\text{rank}(\boldsymbol{\mathcal{H}}_K)}\big) \in \mathbb{R}^{\text{rank}(\boldsymbol{\mathcal{H}}_K)\times\text{rank}(\boldsymbol{\mathcal{H}}_K)}$ stands for a diagonal matrix of singular values arranged in descending order, and $\mathbf{V}_K \in \mathbb{C}^{N_T \times \text{rank}(\boldsymbol{\mathcal{H}}_K)}$ denotes another tall unitary matrix. Moreover, it is possible to partition matrix $\mathbf{V}_K$ as $\mathbf{V}_K = [\mathbf{V}_K^1, \mathbf{V}_K^2]$ for $\mathbf{V}_K^1 \in \mathbb{C}^{N_T \times N_D}$ by satisfying $N_D \leq \text{rank}\left(\boldsymbol{\mathcal{H}}_K\right)$.

Following a similar approach as in [108, 115]. The optimal solution for the BB precoder can then be expressed as

$$\mathbf{B}_T = \mathbf{V}_K^1 \boldsymbol{\Pi}^{\frac{1}{2}} \in \mathbb{C}^{N_T \times N_T}, \tag{4.47}$$

where $\boldsymbol{\Pi} = \text{diag}\left(\Pi_1, \cdots, \Pi_{N_D}\right) \in \mathbb{R}^{N_D \times N_D}$ represents a transmit power matrix with $\sum_{n=1}^{N_D} \Pi_n = P_{T_x}$ for meeting the power constraint given in (4.34e). Employing the water-filling power control solution [116], the power allocation is performed as:

$$\Pi_i = \left(\mu - \frac{\sigma_n^2}{P_{T_x}\sigma_i^2}\right)^+, \text{ s.t.} \sum_{i=1}^{N_D} \left(\mu - \frac{\sigma_n^2}{P_{T_x}\sigma_i^2}\right)^+ = P_{T_x}. \tag{4.48}$$

where $\boldsymbol{\Pi} = \text{diag}\left(\Pi_1, \cdots, \Pi_{N_D}\right) \in \mathbb{R}^{N_D \times N_D}$ denotes a transmit power matrix incorporating $\sum_{n=1}^{N_D} \Pi_n = P_{T_x}$ to satisfy the power constraint given in equation (4.34e).

Next, considering the provided RF beamformer ($\mathbf{A}_T/\mathbf{A}_R$), phase response matrix ($\boldsymbol{\Theta}$), and BB precoder ($\mathbf{B}_T$), our objective is to design the BB combiner ($\mathbf{B}_R$) that minimizes the mean-square error (MSE) between the transmitted and processed received signals. Referring to (4.33), the expression for MSE can be formulated as

$$\begin{aligned}\epsilon_{\text{MSE}} &= \mathbb{E}\big\{\left\|\tilde{\mathbf{r}} - \mathbf{x}\right\|^2\big\} = \text{tr}\big(\mathbb{E}\big\{\tilde{\mathbf{r}}\tilde{\mathbf{r}}^H - \mathbf{x}\tilde{\mathbf{r}}^H - \tilde{\mathbf{r}}\mathbf{x}^H + \mathbf{x}\mathbf{x}^H\big\}\big) \\ &= \text{tr}(\mathbf{B}_{\text{R}}\boldsymbol{\mathcal{H}}_{\text{K}}\mathbf{B}_{\text{T}}\mathbf{B}_{\text{T}}^{\text{H}}\boldsymbol{\mathcal{H}}_{\text{K}}^{\text{H}}\mathbf{B}_{\text{R}}^{\text{H}} - \mathbf{B}_{\text{R}}\boldsymbol{\mathcal{H}}_{\text{K}}\mathbf{B}_{\text{T}} - \mathbf{B}_{\text{T}}^{\text{H}}\boldsymbol{\mathcal{H}}_{\text{K}}^{\text{H}}\mathbf{B}_{\text{R}}^{\text{H}} + \mathbf{I}_{\text{N}_\text{D}}).\end{aligned} \tag{4.49}$$

In order to determine the optimal solution for (4.49), the differentiation rules pertaining to complex-valid matrices are applied, resulting in the derivative of ϵ_{MSE} with respect to the BB combiner ($\mathbf{B}_R$) is obtained as

$$\frac{\partial \epsilon_{\text{MSE}}}{\partial \mathbf{B}_R} = 2\mathbf{B}_R\boldsymbol{\mathcal{H}}_K\mathbf{B}_T\mathbf{B}_T^H\boldsymbol{\mathcal{H}}_K^H - 2\mathbf{B}_T^H\boldsymbol{\mathcal{H}}_K^H. \tag{4.50}$$

Ultimately, the BB combiner that satisfies the minimum MSE criterion outlined in equation (4.49) can be obtained according to the following formulation:

$$\mathbf{B}_R = \mathbf{B}_T^H\boldsymbol{\mathcal{H}}_K^H\left(\boldsymbol{\mathcal{H}}_K\mathbf{B}_T\mathbf{B}_T^H\boldsymbol{\mathcal{H}}_K^H\right)^{-1}. \tag{4.51}$$

4.2.4.3 RIS Phase Shift Design

In this subsection, we provide the the adjustment strategy of phase shifts in the RIS elements, aiming to maximize the achievable rate of the system through the utilization of the PSO algorithm. In PSO, each particle undergoes continuous repositioning within a multidimensional space, drawing upon its own experiences as well as the collective knowledge of its peers, all in pursuit of an optimal solution for the entire swarm [117, 125].

After designing the transmit/receive RF beamformers $(\mathbf{A}_T, \mathbf{A}_R)$ and BB precoder/combiner $(\mathbf{B}_T,\ \mathbf{B}_R)$, the optimization problem given in (4.34) can be reformulated as:

$$\begin{aligned} \max_{\{\boldsymbol{\Theta}_1,\dots,\boldsymbol{\Theta}_K\}} \quad & R\left(\mathbf{A}_T, \mathbf{A}_R, \mathbf{B}_T, \mathbf{B}_R, \boldsymbol{\Theta}_G\right) \\ \text{s.t.} \quad & \boldsymbol{\Theta}_G = \operatorname{diag}(e^{j\Omega_1^1}, \dots, e^{j\Omega_{M_S}^1}, e^{j\Omega_1^2}, \dots, e^{j\Omega_{M_S}^K}) \\ & \mathbb{E}\{\left\|\mathbf{x}\right\|_2^2\} = \operatorname{tr}\left(\mathbf{B}_T^H \mathbf{A}_T^H \mathbf{A}_T \mathbf{B}_T\right) \leq P_{T_x} \\ & \Omega_i^k \in [0, 2\pi], \forall i, \forall k \end{aligned} \tag{4.52}$$

where $R\left(\mathbf{A}_T, \mathbf{A}_R, \mathbf{B}_T, \mathbf{B}_R, \boldsymbol{\Theta}_G\right)$ is achievable rate expression defined in (4.34). Here, $\boldsymbol{\Theta}_G$ represents the global phase shift matrix, which captures the phase shifts of all elements across K RISs. It encompasses the collective phase adjustments applied to the elements of the RISs, resulting in a unified representation of the system's phase shift configuration.

In our PSO approach, we model the phase shifts of the RIS elements (Ω_i^k, $i \in \{1, \dots, M_S\}$ and $k \in \{1, \dots, K\}$) as the positions of the particles. The fitness function of the PSO algorithm is defined by the objective function presented in (4.52). Our PSO-based phase adjustment algorithm first initialize N_{P} particles with random positions $\mathbf{p} \in \mathbb{C}^{KM_S}$ and velocities $\mathbf{v} \in \mathbb{C}^{KM_S}$. Then, each particle maintains a record of its local best position ($\mathbf{p}_{\mathrm{best},i}^{(l)}$) and the global best position ($\mathbf{p}_G^{(l)}$), which are determined based on the evaluation of the fitness function. Specifically, $\mathbf{p}_{\mathrm{best},i}^{(l)}$ represents the best position achieved by the i^{th} particle, while $\mathbf{p}_G^{(\mathrm{l})}$ represents the best position achieved by any particle in the entire swarm during the l^{th} iteration.

At each iteration, the velocity and position of each particle are updated using the following equations:

$$\mathbf{v}_i^{(l+1)} = \zeta \mathbf{v}_i^{(l)} + \mu_1 \rho_1 \big(\mathbf{p}_{\text{best},i}^{(l)} - \mathbf{p}_i^{(l)}\big) + \mu_2 \rho_2 \big(\mathbf{p}_G^{(l)} - \mathbf{p}_i^{(l)}\big), \tag{4.53}$$

$$\mathbf{p}_i^{(l+1)} = \mathbf{v}_i^{(l+1)} + \mathbf{p}_i^{(l)}, \tag{4.54}$$

where ζ represents the inertial weight of velocity, ρ_1 and ρ_2 are acceleration constants, and μ_1 and μ_2 are uniformly distributed random numbers within the range $[0, 1]$. As the iterations progress, the particles move from their current positions $\mathbf{p}_i^{(l)}$ to the updated positions $\mathbf{p}_i^{(l+1)}$. By considering the objective function in (4.52), the personal and the global best solutions for i^{th} particle at l^{th} iteration are expressed as:

$$\mathbf{p}_{\text{best},i}^{(l)} = \underset{\mathbf{p}_i^{(l^*)}, \forall l = 0,1,\ldots,l}{\arg\max} \; R\left(\mathbf{A}_T, \mathbf{A}_R, \mathbf{B}_T, \mathbf{B}_R, \mathbf{p}_i^{(l^*)}\right) \tag{4.55}$$

$$\mathbf{p}_{\text{best}}^{(l)} = \underset{\mathbf{p}_{\text{best},i}^{(l^*)}, \forall i = 0,1,\ldots,N_{\text{P}}}{\arg\max} \; R\left(\mathbf{A}_T, \mathbf{A}_R, \mathbf{B}_T, \mathbf{B}_R, \mathbf{p}_{\text{best},i}^{(l)}\right) \tag{4.56}$$

Finally, after L iterations, the RIS phase shift matrix is determined at the last iteration using a diagonal matrix representation: $\mathbf{\Theta}_G = \text{diag}\big(\exp\big(j\mathbf{p}_G^{(L)}\big)\big)$. Algorithm 3 provides a comprehensive summary of the proposed RISs-aided AB-HBF system, which encompasses three stages of design, including our PSO solution for the phase adjustment process.

The proposed RIS-aided AB-HBF technique introduces an efficient approach to construct the transmit and receive RF beamformers by utilizing only the AoD and AoA supports, as defined in (4.36a) and (4.36b), respectively. Subsequently, the BB precoder and combiner are developed according to (4.47) and (4.51), respectively. Furthermore, the phase shift matrices of the RISs are designed to maximize the achievable rate of the system and enhance the spatial multiplexing gain. When compared to the conventional fully digital precoding/combining (FDPC) approach, the proposed AB-HBF technique significantly reduces the required CSI overhead size and RF chain utilization.

In FDPC, the CSI overhead size is determined by a matrix with dimensions M_T by M_R. Thus, the CSI overhead size in FDPC is calculated as the multiplication of

Algorithm 3 Design Steps for the RIS-aided AB-HBF System

Input: $\mathcal{H}_K$, Υ_{A}, Υ_{D}, P_{T_x}, L, N_{P}, ζ, ρ_1, ρ_2

Output: $\mathbf{A}_T$, $\mathbf{A}_R$, $\mathbf{B}_T$, $\mathbf{B}_T$, $\mathbf{\Theta}_1,\ldots,\mathbf{\Theta}_K$

Initiliaze the phase adjustments randomly for each matrix: $\Theta_k = \mathrm{diag}\big(\exp\big(j2\pi(\mathrm{randn}(1, M_S))\big)\big)$, $\forall k$.

Obtain $\mathbf{A}_T$ and $\mathbf{A}_R$ via (4.43) and (4.46), respectively.

Initialize N_{P} particles and their velocities

for $l = 1 : L$ **do**

Velocity of each particle $\mathbf{v}_i^{(l)}$ is obtained as in (4.53).

Position of each particle $\mathbf{p}_i^{(l)}$ is obtained as in (4.54).

Calculate $\mathbf{B}_T$ and $\mathbf{B}_R$ via (4.47) and (4.51), respectively.

Find each particle's achievable rate via (4.52).

Update personal best $\mathbf{p}_{\mathrm{best},i}^{(l)}$ and global best $\mathbf{p}_G^{(l)}$.

end for

Set RIS phase-shift matrix as $\mathbf{\Theta}_G = \mathrm{diag}\big(\exp\big(j\mathbf{p}_G^{(L)}\big)\big)$.

Build $\mathbf{B}_T$ and $\mathbf{B}_R$ as in (4.47) and (4.51) using the optimum phase shift matrix, respectively.

M_T and M_R as $M_T \times M_R$. Conversely, in AB-HBF, a reduced-dimensional representation of CSI is employed, resulting in the CSI overhead size being determined by $N_T \times N_R$.

In terms of the number of RF chains, FDPC requires M_T RF chains for the transmit antennas and M_R RF chains for the receive antennas. Consequently, the total number of RF chains in the FDPC system is obtained by $M_T + M_R$. On the other hand, AB-HBF utilizes N_T RF chains for the transmit antennas and N_R RF chains for the receive antennas, resulting in the total number of RF chains being $N_T + N_R$.

4.2.5 Numerical Results

In this section, we provide a comprehensive analysis of the performance of the proposed RIS-empowered AB-HBF system in the THz massive MIMO system. We conduct extensive numerical simulations to evaluate the efficiency of the proposed system. Our another focus is on optimizing the phase shifts of the RIS using the PSO algorithm. The computer simulations are conducted based on a geometry-based THz channel model, which is described in (4.27). The separation between two antennas and reflectors is set to $d = 0.5$ to ensure a half-wavelength spacing. A schematic top-view representation of the simulation setup, including the distances between the terminals, is illustrated in Fig. 4.9.

4.2.5.1 Fully-Connected AB-HBF

In this subsection, we provide a comprehensive computer simulations by considering the traditional FC structure for RIS-aided AB-HBF system. Table 4.4 provides the common parameters utilized in the simulations. Scenario 1 is considered for the FC-AB-HBF system parameters in this subsection.

In Fig. 4.10, we investigate the achievable rate performance of the AB-HBF systems with or without RIS as a function of the transmit power P_{T_x}. Here, we aim to efficiently use the NLoS and RIS-assisted paths in the environment when the LoS link is blocked. We compare the proposed RIS-aided AB-HBF systems with an AB-HBF system that exclusively transmits data over LoS and NLoS channels. As clearly observed from Fig. 4.10, increasing P_{T_x} value improves the system performance for all schemes notably. Instead of using the NLoS path, only RIS-assisted transmission provides an improvement in achievable rate performance. Furthermore, the RIS and NLoS paths-assisted transmission substantially outperforms the NLoS path-aided transmission by providing additional paths for data transmission. Even if the LoS path does not exist, efficient usage of RIS and NLoS paths in the transmission provides to catch the performance of LoS conditions, especially for higher P_{T_x} values. As we observe, the utilization of the RIS-aided AB-HBF method offers

Table 4.4: System parameters for simulations.

	Scenario 1	Scenario 2
# of Tx antennas	$M_T = 64$	$M_T = 192$
# of Rx antennas	$M_R = 64$	$M_R = 192$
# of RIS elements	$M_S = 1024$	$M_S = 64$
Frequency	100 GHz	
Channel Bandwidth	500 MHz	
Distances [m]	$\tau_0 = 10$, $\tau_1 = 1$, $\tau_2 = 9$, $\tau_\mathrm{q} \in [10, 15]$	
# of paths	$Q = 10$ for $\mathbf{H}_\mathrm{NLoS}$	
Path Loss	$\alpha = 32.4 + 20\log_{10}(f_c) = 72.4$, ($f_c$ [GHz])	
Noise PSD	-174 dBm/Hz	
PSO # of iterations	$L = 30$	
PSO # of particles	$N_\mathrm{P} = 10$	
Path loss exponent	$\eta_0 = 2.1$ for LOS, $\eta = 4.5$ for NLOS	
Elevation AoA/AoD	$\theta_{i,q}^\mathrm{NLoS} = 60°$, $\theta_i^\mathrm{LoS} = 30°$, $i \in \{T, R\}$ $\theta_i^\text{Tx-RIS} = 60°$, $\theta_i^\text{RIS-Rx} = 50°$, $i \in \{T, R\}$	
Azimuth AoA/AoD	$\psi_{i,q}^\mathrm{NLoS} = 120°$, $\psi_i^\mathrm{LoS} = 60°$, $i \in \{T, R\}$ $\psi_i^\text{Tx-RIS} = 90°$, $\psi_i^\text{RIS-Rx} = 225°$, $i \in \{T, R\}$	

the opportunity to convert a non-robust channel characterized by NLoS conditions into an LoS condition. This transformation is achieved by effectively leveraging the NLoS paths and the paths assisted by the RIS. By optimizing the phase shifts of the RIS elements via the proposed PSO-based solution, we are able to enhance the performance of the system and mitigate the disruptive effects of the wireless propagation environment while reducing the CSI overhead.

In Fig. 4.11, we aim to investigate the impact of different propagation environments characterized by varying path loss exponents on the achievable rate performance of the AB-HBF systems. Fig. 4.11(a) presents the achievable rate performance when data is transmitted over the LoS, NLoS, and RIS-aided paths

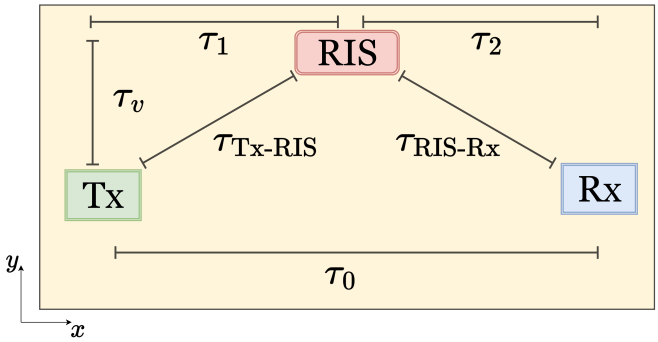

Figure 4.9: Top view of considered scenarios in simulations, illustrating the distances between terminals.

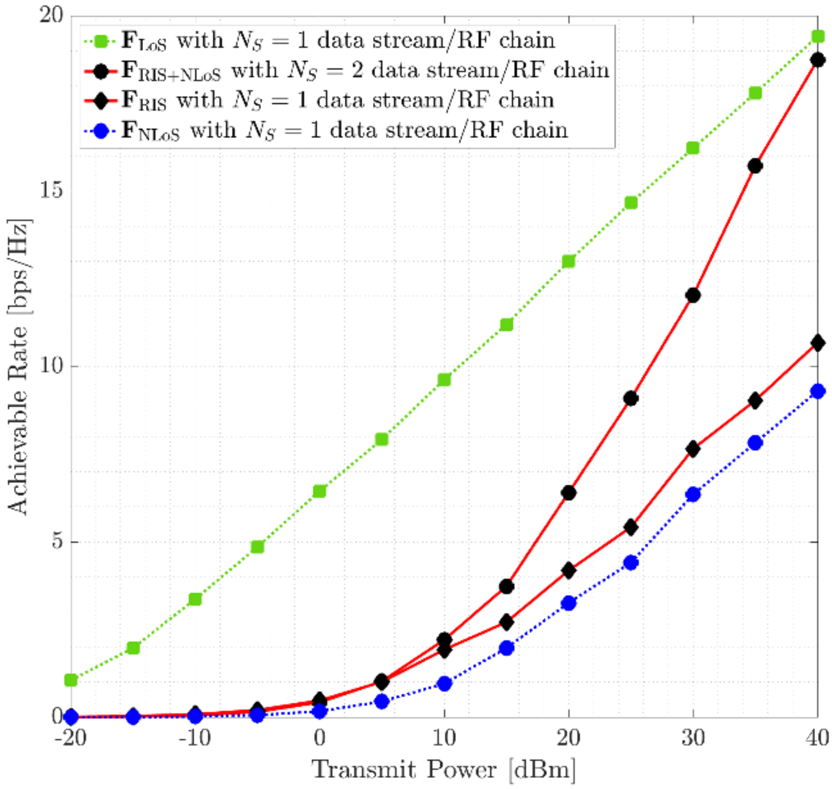

Figure 4.10: Achievable rate comparison for the proposed AB-HBF system with and without the TX-Rx link under changing P_{T_x}.

(R_{ALL}), while Fig. 4.11(b) focuses solely on the achievable rate performance when only LoS channel is available (R_{LoS}). Moreover, Fig. 4.11(c) illustrates the difference in achievable rate performance between the R_{ALL} and the R_{LoS} scenario. This comparison highlights the contribution and effectiveness of incorporating NLoS and

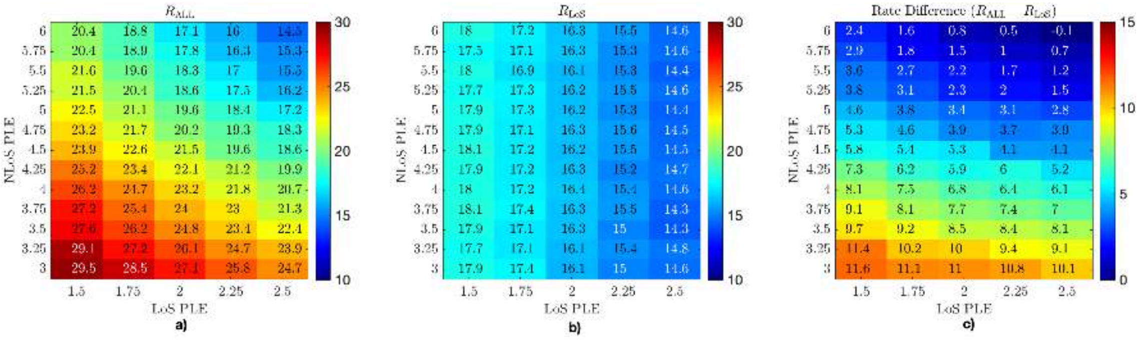

Figure 4.11: Achievable rate performance analysis with varying path loss exponents for a) LOS, NLOS, and RIS-assisted scenario (R_{ALL}), b) considering only LoS path (R_{LoS}), and c) difference in between R_{ALL} and R_{LoS}. The path loss exponent analysis investigates the impact of varying LoS and NLoS path loss exponents on the achievable rate performance of the AB-HBF system.

RIS-assisted paths in enhancing the overall system performance for various propagation characteristics. As seen in Fig. 4.11(c), even in the perfect LoS conditions, the RIS-aided design can provide a significant contribution to the system performance. For a specific scenario where the LoS and NLoS path loss exponents are respectively set to $\eta_0 = 2$ and $\eta = 3$, the achievable rate difference is measured as 11 bps/Hz, which means the 63% performance enhancement is achieved by exploiting the RIS and NLoS paths in the environment. Furthermore, the findings depicted in Fig. 4.11(c) highlight the challenge of improving system performance solely through a single RIS when the LoS channel is highly dominant and the contributions from NLoS channels are comparatively weaker. This observation can be attributed to the predominant influence of LoS propagation in THz channels, which indicates the need to explore the utilization of multiple-RIS to achieve additional performance improvements. Through this analysis, we provide insights into how the AB-HBF systems can effectively utilize and exploit the available LoS and NLoS paths, optimizing their performance based on the specific path loss characteristics of the environment. These results can provide a guideline for designing and optimizing AB-HBF systems to achieve high data rates and reliable communications in various

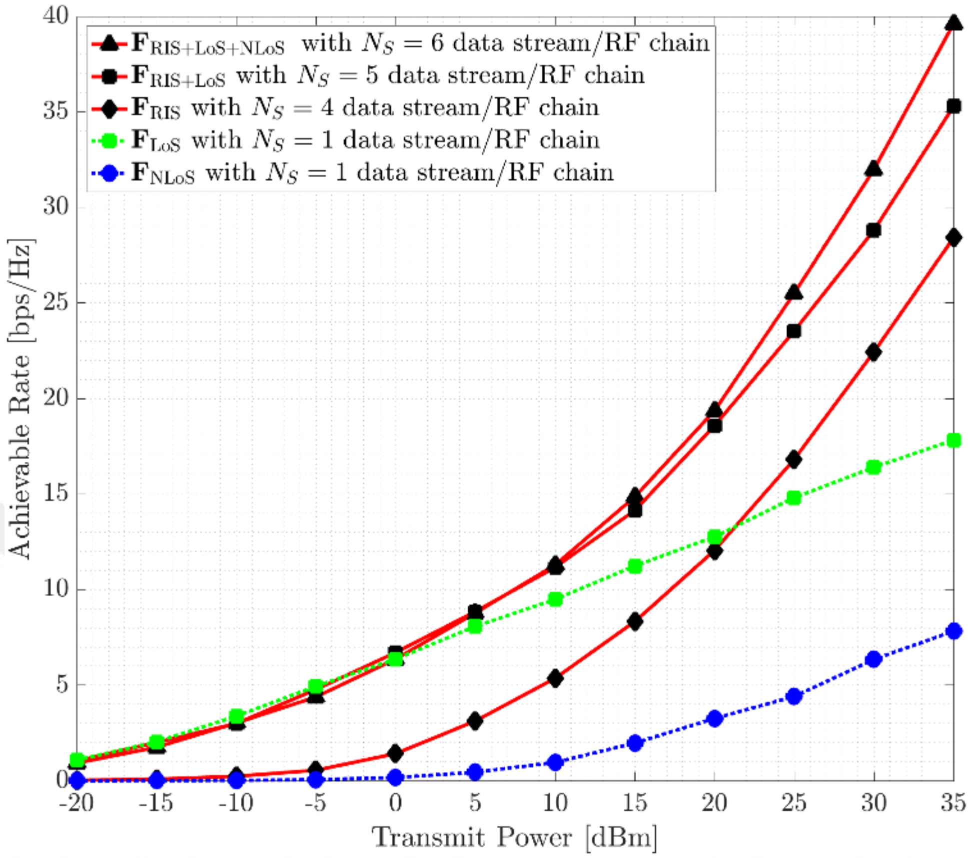

Figure 4.12: Achievable rate comparison for multiple-RIS-aided AB-HBF systems and AB-HBF for $K = 4$ under varying P_{T_x}.

wireless scenarios.

In Fig. 4.12, we investigate the impact of using multiple-RIS on the achievable rate performance of the AB-HBF system in the presence of a LoS link between the Tx and Rx for $K = 4$. Fig. 4.12 demonstrates that the RIS-empowered AB-HBF system offers a significant gain in P_{T_X} as 32 dB compared to the AB-HBF system operating in NLoS conditions. It is also observed that performance superior to LoS conditions is achieved even by using only multiple-RIS-aided channels in the transmission. Furthermore, using multiple-RIS-aided paths as well as LoS path provides 18 dB gain in P_{T_x} compared to AB-HBF systems that transmit only through LoS channels. For higher P_{T_x} values, incorporating NLoS channels in addition to RISs and LoS channels during transmission can effectively enhance the spatial multiplexing gain, resulting in significant increases in the achievable rate performance of the AB-HBF systems.

Fig. 4.13 depicts the effect of increasing the number of RISs (K) on achievable rate performance of the multiple-RIS-empowered AB-HBF systems under varying P_{T_x}. Here, each RIS is vertically stacked with a fixed elevation angle separation of 5°. Each RIS is allocated for an independent data stream transmission, enabling concurrent transmission through multiple-RIS. As depicted in Fig. 4.13, the utilization of a greater number of RISs results in a significant improvement in the achievable rate performance. However, it is observed that the rate of performance enhancement diminishes as the number of RISs increases. The increasing slopes of achievable rate curves for each RIS further validate the spatial multiplexing gain achieved through multiple RIS. The incorporation of multiple-RIS in THz channels with limited scattering effectively enhances the rank of the channel matrix, thereby simulating an artificial rich-scattering environment. The effective utilization of multiple data streams over orthogonal links, which is one of the critical objectives of massive MIMO systems, can be achieved successfully in rich scattering environments. Consequently, the adoption of multiple-RIS emerges as a complementary technology to enhance the effectiveness of massive MIMO systems in THz channels. The use of multiple-RIS enables the exploitation of spatial multiplexing gain and facilitates the realization of the full potential of massive MIMO systems in THz frequency bands.

It should be noted that, in our numerical results, we assume that the LoS channel is blocked in single RIS-assisted transmission, while the LoS channel exists in multiple-RIS-aided transmissions. We can combine and generalize these two scenarios by employing a large and dynamic RIS: If the LoS channel is blocked, the RIS can be activated to maintain the reliability of the transmission. On the other hand, when the LoS channel is not blocked, the large RIS can be partitioned into multiple groups to facilitate the simultaneous transmission of multiple data streams. This flexible and adaptive approach allows for seamless adaptation based on the availability of the LoS channel, maximizing the performance and reliability of the overall system.

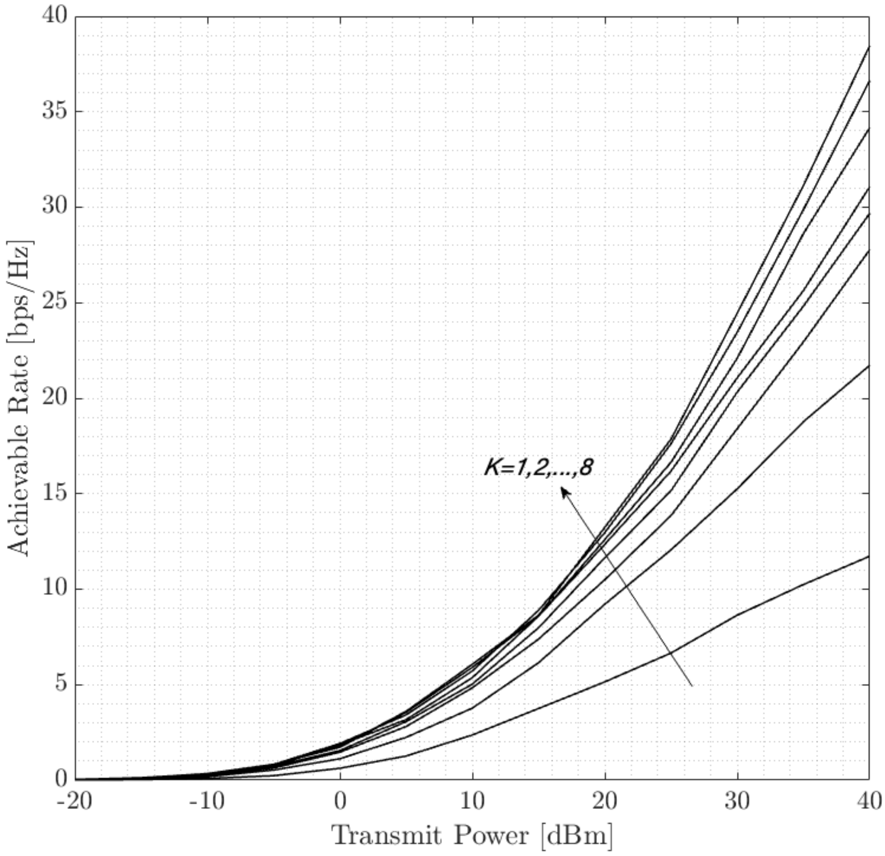

Figure 4.13: Effect of increasing K on achievable rate performance for multiple-RIS-aided AB-HBF systems under varying P_{T_x}.

4.2.5.2 Subarray-Connected AB-HBF

In this subsection, we provide comparisons for the SC-AB-HBF system and FC-AB-HBF system to illustrate the trade-offs between these two use cases. For the numerical simulations in this subsection, we consider Scenario 2 from Table 4.4. Additionally, Fig. 4.9 provides a top view of the considered scenario in these simulations.

Fig. 4.14 illustrates the Tx/Rx antenna subarray configuration for the RIS-aided SC-AB-HBF system that is used for computer simulations. The Tx/Rx antennas are divided into three parts as M_{LoS}, M_{NLoS} and M_{RIS} representing different types of transmission paths associated with LoS, NLoS, and RISs, respectively. Each section specifies the distribution of antenna elements allocated for these specific paths.

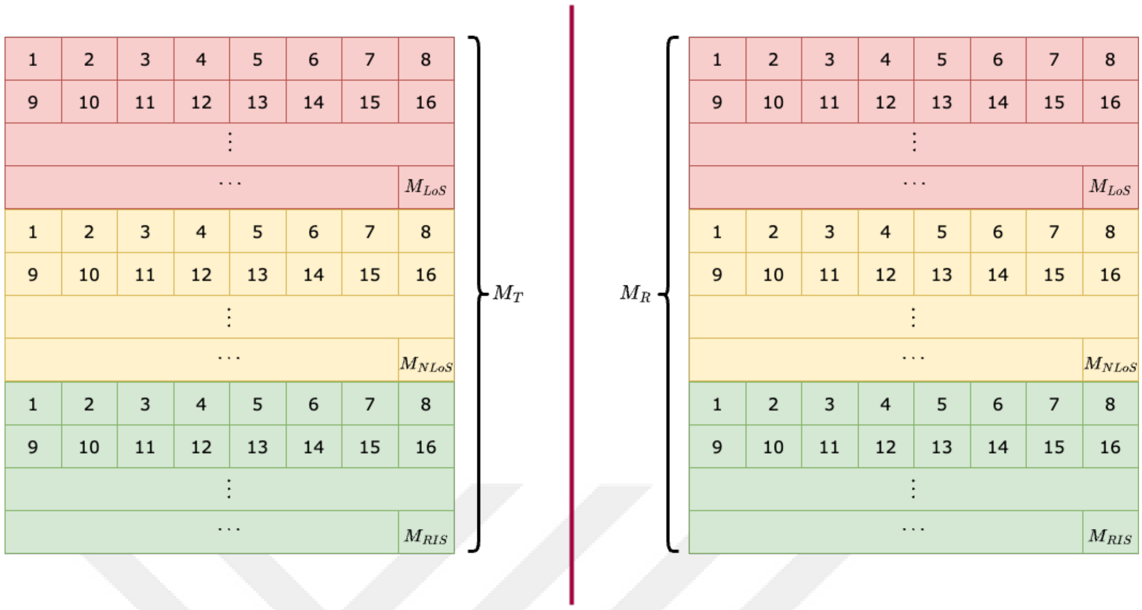

Figure 4.14: Transmit and receive antenna mappings for the SC-HBF structure considered scenarios in simulations.

In Fig. 4.15, we provide a comparative performance analysis of multi-RIS-enabled FC and SC-AB-HBF methods for the THz mMIMO systems under $K = 3$. Fig. 4.15(a) investigates the RIS-assisted FC and SC-AB-HBF systems, encompassing three transmission paths: LoS, NLoS, and RIS-assisted paths while Fig. 4.15(b) compares the performance of the systems in scenarios including only NLoS and RIS-assisted paths. In Fig. 4.15(a), it is observed that if the number of resources allocated to the LoS path is increased for the SC-AB-HBF system, the achievable rate approaches that of the FC-AB-HBF system. In Fig. 4.15(b), it is seen that the performance of the SC-AB-HBF system approaches that of the FC-AB-HBF system by increasing the number of antennas allocated to the RIS-aided path. These observations demonstrate how the adaptive mechanism in the system offers the flexibility needed to improve performance while reducing hardware costs. As a result, the SC-AB-HBF system exhibits a performance close to that of the FC-AB-HBF system, which stands out as a cost-effective solution. The graphs provide valuable information on how RIS-assisted AB-HBF systems can improve wireless communication

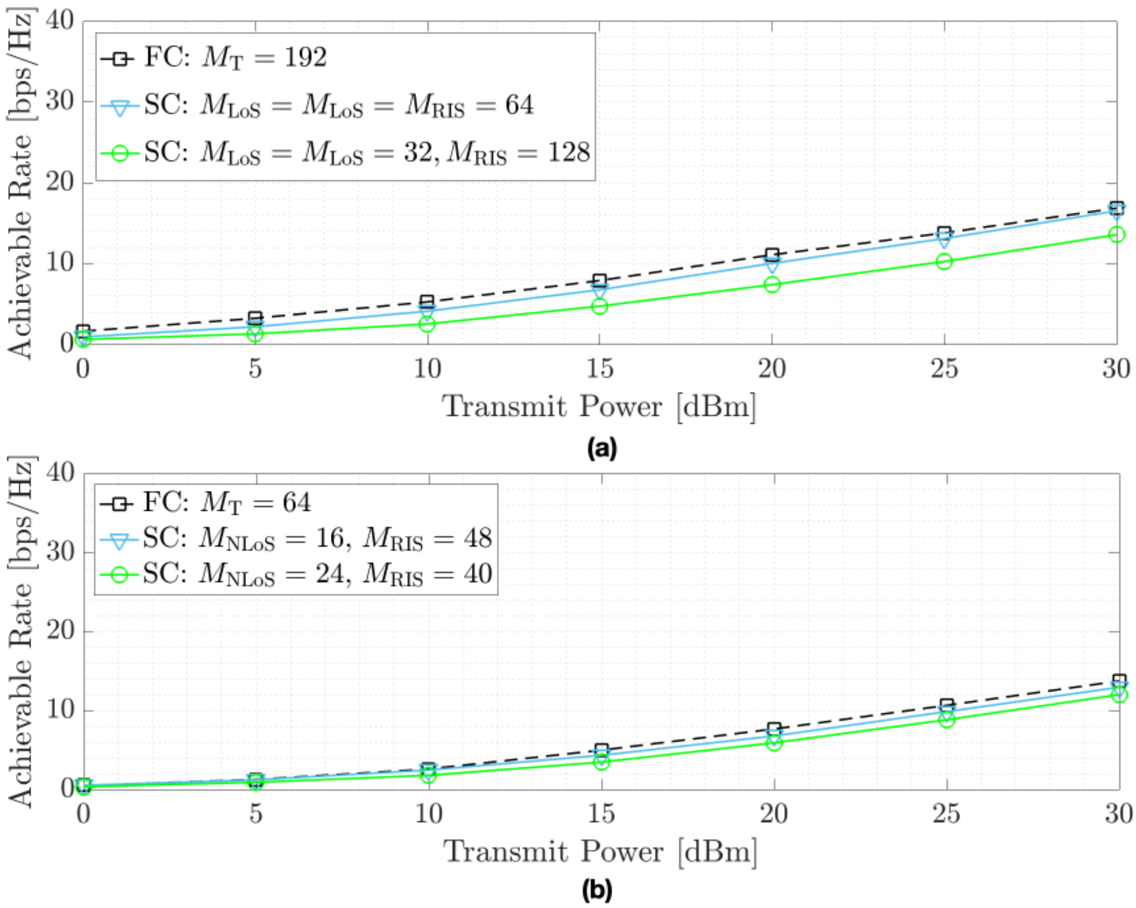

Figure 4.15: Performance comparisons of the FC and SC-AB-HBF Systems under different antenna configurations for (a) LoS, NLoS and RIS-aided, and (b) NloS and RIS-aided transmission.

performance under different antenna configurations and transmission powers.

It is noted that the total number of phase shifters is significantly reduced in the SC-AB-HBF compared to the FC-AB-HBF. For instance, considering $M_T = 192$ for FC-AB-HBF, with the assistance of AB-HBF and the use of $N_T = 14$ RF chains, the total number of phase shifters becomes $M_T \times N_T = 192 \times 14 = 2688$. On the other hand, for SC-AB-HBF, where $M_{LoS} = M_{NLoS} = M_{RIS} = 64$, the total number of phase shifters is reduced to $64 \times 14 = 960$. Thus, despite utilizing approximately one-third of the phase shifters, SC-AB-HBF and FC-AB-HBF exhibit comparable performance.

4.2.6 Conclusions

This work has presented an innovative approach for THz band communications by leveraging RISs in conjunction with an AB-HBF technique. The study has addressed two significant scenarios commonly encountered in THz channels and proposed cost and energy-efficient solutions utilizing RISs to enhance system performance. The first scenario focused on ensuring reliable communication in the presence of obstacles obstructing the direct path between the transmitter and receiver. By utilizing RISs as an alternative transmission path, reliable communication has been maintained. The second scenario explored the utilization of multiple-RIS in LoS dominant or sparse environments to increase the rank of the channel matrix, consequently improving the achievable rate performance. Through the introduction of an innovative HBF design for multiple-RIS-assisted THz massive MIMO systems, enhanced spatial multiplexing gain has been achieved by effectively utilizing NLoS paths and the RIS-assisted path during transmission. We also demonstrate that the SC-AB-HBF configuration offers a remarkable reduction in the total number of phase shifters compared to the FC-AB-HBF. Extensive numerical experiments have demonstrated a significant enhancement in the achievable rate performance of THz AB-HBF systems through the incorporation of RISs. This approach has effectively mitigated the disruptive effects of the wireless propagation environment while reducing hardware cost/complexity and power consumption for massive MIMO systems with large antenna arrays. Overall, this research contributes to the advancement of THz band communications, offering efficient and high-performance solutions for overcoming transmission challenges and exploiting the potential of RIS-assisted AB-HBF techniques.

4.3 Spider RIS: Mobilizing Intelligent Surfaces for Enhanced Wireless Communication

The search for transformative technologies to meet evolving connectivity demands remains paramount in the relentless drive toward the emergence of 6G and the next generation of wireless networks. Key applications of the 6G wireless network include providing users with immersive experiences such as high-definition virtual reality, mobile holography, and digital twins [134]. These applications necessitate exceptionally high data rates and massive connectivity, concurrently requiring high reliability and low latency that promises performance close to wired communication standards [135]. To achieve these goals, 6G is expected to embrace innovative technologies that dynamically program changing wireless signal propagation environments, such as reconfigurable intelligent surfaces (RISs). RISs stand out as a transformative tool for wireless networks to achieve various network goals such as coverage extension, environmental sensing, positioning, and spatiotemporal focusing. Composed of controllable arrays of low-cost passive elements, RISs act as intelligent mediators that modify the reflections of the incoming signals. These intelligent and cost-effective capabilities of the RISs are expected to contribute considerably to realizing the 6G vision by providing a programmable environment to meet the stringent requirements and anticipated use cases of next-generation wireless networks [5, 12, 17, 136].

On the other hand, today's rapidly evolving wireless communications needs shed significant light on the capabilities of unmanned aerial vehicles (UAVs) [137–139]. While UAVs offer 3D mobility, they encounter distinct shortcomings in positioning and energy consumption. High energy consumption is a severe problem in applications requiring long-distance and persistent communication. UAVs require battery replacement or recharging to provide continuous communication services, which limits their flight time and operational range [140]. Additionally, using UAVs in an indoor environment poses severe practical difficulties. Although capable of mobility, UAVs are challenging to maneuver indoors, which can affect the coverage and reliability of transmission. From these perspectives, addressing these battery and maneuver-related challenges is essential for successfully deploying and operating UAV-based communication systems [141].

In current multiple-input multiple-output (MIMO) systems, antennas are deployed in fixed positions, which prevents taking full advantage of the degrees of freedom (DoF) in the continuous spatial domain to optimize spatial multiplexing performance. To overcome this fundamental limitation, the movable antenna (MA) system has been recently proposed as a new solution to fully evaluate wireless channel variations in a continuous spatial domain [142]. Unlike fixed-position antennas, each MA is connected to the radio frequency (RF) chain via a flexible cable, allowing its position to be flexibly adjusted in a given spatial region to achieve more favorable channels to improve communication performance. In MA-supported MIMO systems, channel capacity is maximized by simultaneously adjusting the positions of MAs in the areas where the transmitter and receiver are located [143]. In MA systems, the need for all antenna elements to change position independently and to provide perfect channel state information for each position makes it challenging to use these systems for massive MIMO applications. Optimization of such systems increases algorithmic and computational complexity, making it complicated in terms of cost and practicality to implement for large-scale massive MIMO systems.

In this study, we propose the movable RIS concept, called "Spider RIS", which is an innovative system in which the RIS is positioned on a wall-mounted platform and aims to increase the degrees of freedom and performance of the communication system by moving in a limited space as illustrated in Fig. 4.16. While each antenna element moves independently in the MA systems, in Spider RIS, the entire RIS moves together with the all of its elements. This allows the RIS to be shifted horizontally or vertically within a given spatial region, changing its position to find optimal signal path or channel conditions and thus improve transmission quality. The movement of the Spider RIS can be controlled through motors or other mechanical systems integrated into the platform. This design eliminates the need to control individual antenna elements separately, thereby reducing system complexity and cost while maintaining the ability to reshape the channel matrix flexibly. With these features, Spider RIS has the potential to provide higher efficiency and performance by overcoming the limitations of existing RIS technologies in wireless communication systems. An alternative implementation of the Spider RIS may involve designating the entire movement area on the ceiling or a horizontal wall as the

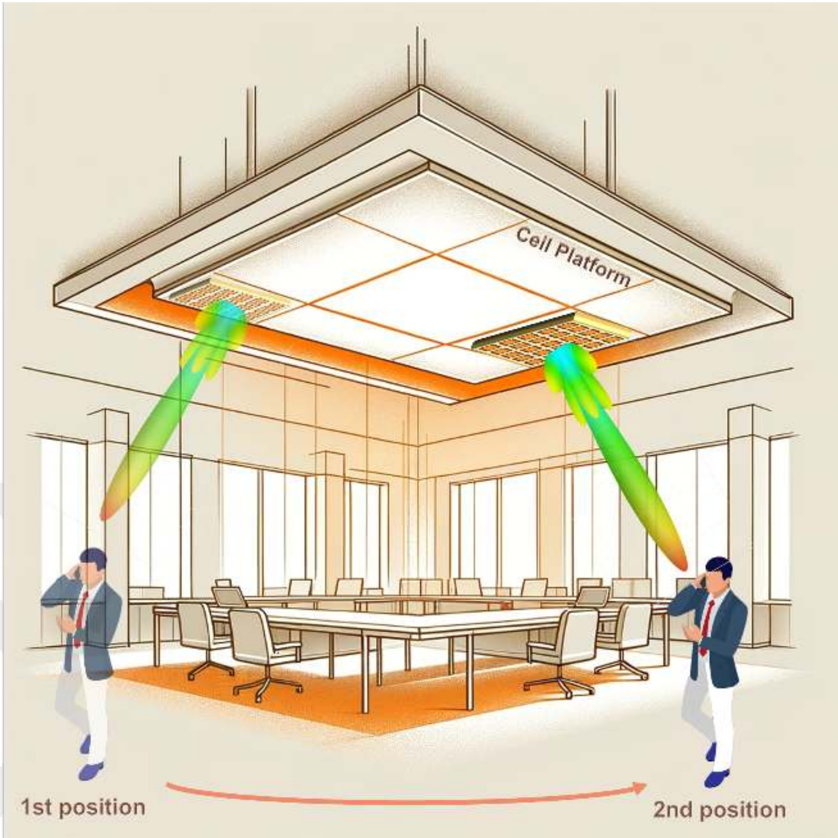

Figure 4.16: Illustration of a moving *Spider RIS* hanging on the ceiling platform in an indoor office environment according to changing positions.

RIS, dynamically activating specific sections for transmission. However, this design becomes impractical in larger indoor or outdoor environments when considering the cost of channel estimation and covering the entire surface with RIS.

Spider RIS is a technology inspired by both MAs and UAVs-supported communication systems while aiming to overcome the challenges brought by these two technologies. Combining the improved spatial DoF capability offered by MAs and the flexible positioning advantages of UAVs, it offers a dynamic and movable RIS capable of dynamically optimizing the physical positions within the movement platform. The motivation of Spider RIS is based on the ability to fully exploit the spatial variability of wireless channels and maximize channel capacity even with a limited number of reflecting elements. This approach aims to overcome the limitations that traditional fixed RIS and energy-intensive UAV systems cannot overcome and to open new horizons in wireless communications.

Considering the above advantages of Spider RIS, an angular-based hybrid beamforming (AB-HBF) system is designed in this study for millimeter wave (mmWave) massive MIMO (mMIMO) systems, which is based on the slowly time-varying angular parameters of the channel and aims to minimize the instantaneous channel estimation overhead [107, 125]. In particular, the RF stage is built on slowly time-varying angular information, and the BB stage is built on reduced-size channel state information (CSI). Considering the mmWave channel model based on 3D geometry, a three-stage HBF design for the Spider RIS-aided mMIMO system is proposed: (i) RF beamformers, (ii) baseband (BB) precoder/combiner, and (iii) joint dynamic RIS Positioning and phase shift design for Spider RIS. First, transmit/receive RF beamformers are designed using the slowly time-varying departure/arrival angle information (AoD/AoA) of the channel, and then the BB precoder and combiner are constructed using the effective channel seen from the BB stage. Then, the RIS phase shift matrix and trajectory of the RIS are designed to maximize the achievable rate of massive MIMO systems through a nature-inspired particle swarm optimization (PSO) algorithm.

4.3.1 System and Channel Model of Spider RIS

In this section, we introduce the system and channel models of the proposed Spider RIS deployment in mMIMO systems.

4.3.1.1 System Model

We consider a point-to-point mmWave mMIMO indoor environment, where the direct line-of-sight (LoS) communication paths between the transmitter (Tx) and receiver (Rx) are frequently obstructed by various obstacles, such as walls, furniture, and other indoor structures. A movable RIS is placed on the ceiling of the floor to address the following challenges: 1) Overcome obstructions; 2) dynamic adoption[1];

[1]The movable RIS can adapt to the ever-changing indoor environment, and it can adjust in real-time to the movements of users.

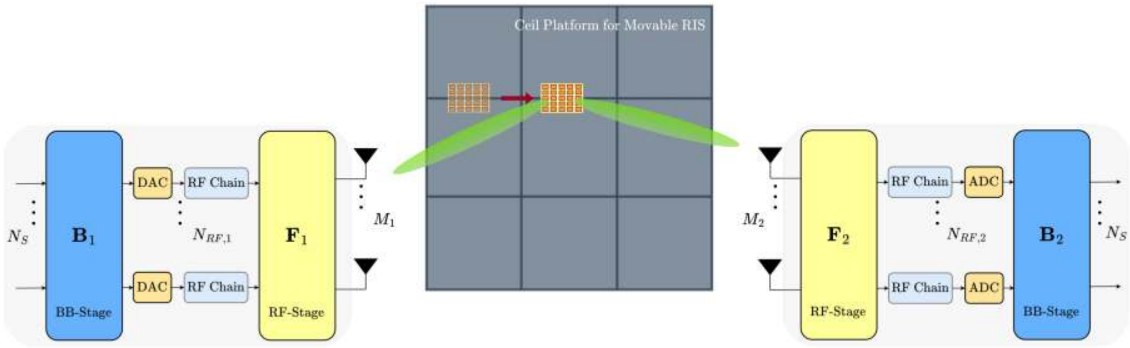

Figure 4.17: Movable RIS-assisted mMIMO HBF system model.

and 3) enhance spectral efficiency. Unlike static RIS, which is deployed at a fixed location, we introduce the Spider RIS to study the performance gains in hybrid mMIMO systems.

As shown in Fig. 4.17, we consider a BS to be equipped with $M_1 = M_{1_x} \times M_{1_y}$ antennas, a Rx with $M_2 = M_{2_x} \times M_{2_y}$ antennas, and a Spider RIS with $M_I = M_{I_x} \times M_{I_y}$ dynamic reflecting elements. The location of Tx, RIS, and Rx is denoted by (x_1, y_1, z_1), (x_r, y_r, z_r) and (x_2, y_2, z_2), respectively. We assume a uniform rectangular array (URA) configuration for the Tx, RIS, and Rx such that M_{i_x} and M_{i_y} represent the number of antenna/reflector elements along x and y-axis, respectively, where $i \in \{1, 2, I\}$. We consider HBF architecture, where the Tx consists of an RF beamforming stage $\mathbf{F}_1 \in \mathbb{C}^{M_1 \times N_{RF_1}}$ and BB stage $\mathbf{B}_1$ $\mathbb{C}^{N_{RF_1} \times N_S}$. Here, N_S represents the data streams from Tx to Rx through channel $\mathbf{H}_1 \in \mathbb{C}^{M_{u,r} \times M_1}$, and N_{RF_1} is the RF chains such that $N_S \leq N_{RF_1} \leq M_1$ to guarantee multi-stream transmission. Considering the transmitted signal is $\mathbf{d} = [d_1, d_2, \ldots, d_{N_S}]^T$ with $\mathbb{E}\{\mathbf{d}\mathbf{d}^H\} = \mathbf{I}_{N_S} \in \mathbb{C}^{N_S \times N_S}$, then the signal transmitted by Tx is given as follows:

$$\mathbf{s} = \mathbf{F}_1 \mathbf{B}_1 \mathbf{d}. \tag{4.57}$$

The power constraint of the beamforming matrices can be expressed as $\|\mathbf{F}_1 \mathbf{B}_1\|_F^2 = P_T$, where P_T denotes the total transmit power. Due to unfavorable propagation conditions (i.e., severe blockage) of the direct link, the transmitted signal arrives at Rx via the Tx-RIS-Rx channel. Let $\mathbf{H}_{TI} \in \mathbb{C}^{M_I \times M_1}$ denote the channel from the Tx to RIS, and $\mathbf{H}_{IR} \in \mathbb{C}^{M_2 \times M_I}$ is the RIS-Rx channel. Then, the received signal at the Rx via Spider RIS is given as follows:

$$\begin{aligned} \mathbf{y} &= \mathbf{H}\mathbf{s} + \mathbf{n} = (\mathbf{H}_{IR}\mathbf{\Phi}\mathbf{H}_{TI})\mathbf{s} + \mathbf{n}, \\ &= (\mathbf{H}_{IR}\mathbf{\Phi}\mathbf{H}_{TI})\mathbf{F}_1\mathbf{B}_1\mathbf{d} + \mathbf{n}, \end{aligned} \tag{4.58}$$

where $\mathbf{n} \sim \mathcal{CN}(\mathbf{0}, \sigma_n^2\mathbf{I}_{M_2})$ represents the additive white Gaussian noise at the Rx and $\mathbf{\Phi} \triangleq \text{diag}(e^{j\phi_1}, \cdots, e^{j\phi_{M_I}}) \in \mathbb{C}^{M_I \times M_I}$ is the RIS phase matrix and $\phi_i \in [0, 2\pi]$ denote the phase shift introduced by the i^{th} element of the RIS. At the Rx, the signal received is processed through RF stage $\mathbf{F}_2 \in \mathbb{C}^{N_{RF_2} \times M_2}$ and BB stage $\mathbf{B}_2 \in \mathbb{C}^{N_S \times N_{RF_2}}$. Then, the received signal at the Rx after combining can be written as:

$$\tilde{\mathbf{y}} = \mathbf{B}_2\mathcal{H}\mathbf{B}_1\mathbf{d} + \mathbf{B}_2\mathbf{F}_2\mathbf{n}. \tag{4.59}$$

For a movable RIS-aided hybrid mMIMO system, where the RIS is positioned at a fixed height z_r (i.e., ceiling), the total achievable rate can be maximized by the joint optimization of RF beamforming/combining and BB stages $\mathbf{F}_1$, $\mathbf{B}_1$, $\mathbf{F}_2$, $\mathbf{B}_2$, the phase shifts at RIS $\mathbf{\Phi}$ as well as the RIS position (x_r, y_r) within a given deployment area. Then, we can formulate the optimization problem as follows:

$$\begin{aligned} \max_{\{\mathbf{F}_1,\mathbf{B}_1,\mathbf{F}_2,\mathbf{B}_2,\mathbf{\Phi},\mathbf{x}_o\}} \quad & \log_2 \left| \mathbf{I}_{N_S} + \mathbf{W}_{\tilde{n}}^{-1}\mathbf{B}_2\mathcal{H}\mathbf{B}_1\mathbf{B}_1^H\mathcal{H}^H\mathbf{B}_2^H \right| \\ \text{s.t.} \quad C_1 : \quad & |\mathbf{F}_1(i,j)| = \frac{1}{\sqrt{M_1}}, |\mathbf{F}_2(i,j)| = \frac{1}{\sqrt{M_2}} \ \forall i, j, \\ C_2 : \quad & \mathbb{E}\{\|\mathbf{s}\|_2^2\} \leq P_T, \\ C_3 : \quad & \mathbf{\Phi} = \text{diag}(e^{j\phi_1}, \cdots, e^{j\phi_{M_I}}), \\ C_4 : \quad & \phi_i \in [0, 2\pi], \ \forall i, \\ C_5 : \quad & x_{\min} \leq \mathbf{x}_o \leq x_{\max}, \end{aligned} \tag{4.60}$$

where $\mathbf{W}_{\tilde{n}} = \sigma_n^2\mathbf{B}_2\mathbf{F}_2\mathbf{F}_2^H\mathbf{B}_2^H$ is the covariance matrix of the noise $\tilde{n} = \mathbf{B}_2\mathbf{F}_2\mathbf{n}$. Here, C_1 refers to the constant-modulus (CM) constraint due to the use of phase shifters at Tx and Rx, C_2 indicates the total transmit power constraint, C_3 specifies the phase matrix design to shape signal propagation, C_4 limits the phase values of RIS elements within [0, 2π], and C_5 establishes the RIS deployment boundary within the indoor environment. The optimization problem defined in (4.60) is challenging due to the non-convexity of the objective function and the CM constraint due to RF beamforming/combining stages. To solve this problem, we first develop HBF stages for the Tx and Rx based on arbitrary RIS location to optimize $\mathbf{x}$. Then, based on the optimal RIS location and phase matrix $\mathbf{\Phi}$, we sequentially update the RF and BB stages.

4.3.1.2 Channel Model

We consider mmWave channels for both Tx-RIS and RIS-Rx links. While LoS channel models can be useful for simple scenarios, they can be limited in their ability to capture the channel complexities (e.g., multi-path fading and shadowing), especially in an indoor environment. Thus, mmWave channel models can provide a more accurate representation of the channel characteristics, including the impact of non-LoS paths and obstacles on the signal propagation in RIS-assisted mMIMO communications. Based on the Saleh-Valenzuela channel model [144], the channel is given as follows:

$$\mathbf{H}_i = \sum\nolimits_{l=1}^{L} \frac{z_{l,i}}{\alpha \tau_i^{\eta}} \mathbf{a}_r\left(\theta_{l,i}^{(r)}, \psi_{l,i}^{(r)}\right) \mathbf{a}_t^T\left(\theta_{l,i}^{(t)}, \psi_{l,i}^{(t)}\right), \tag{4.61}$$

where L is the total number of paths, $\alpha = 32.4 + 20\log_{10}(f_c)$ represents the reference path loss in dB, η is the path loss exponent, and $z_{l,i}$ is the complex gain of l^{th} path in i^{th} channel, where $i \in \{IR, TI\}$, and $\mathbf{a}(.,.)$ is the Tx/Rx array steering vector for URA, which is given as [145]:

$$\begin{aligned} \mathbf{a}_j\left(\theta, \psi\right) = &\left[1, e^{-j2\pi d \sin(\theta)\cos(\psi)}, \cdots, e^{-j2\pi d (M_x - 1)\sin(\theta)\cos(\psi)}\right] \\ &\otimes \left[1, e^{-j2\pi d \sin(\theta)\sin(\psi)}, \cdots, e^{-j2\pi d (M_y - 1)\sin(\theta)\sin(\psi)}\right], \end{aligned} \tag{4.62}$$

where $j = \{t, r\}$, M is the corresponding Tx/Rx antennas, d is the inter-element spacing, and $M_x(M_y)$ is the horizontal (vertical) size of the array. Here, the angles $\theta_{l,i}^{(t)} \in \left[\theta_i^{(t)} - \delta_i^{\theta}, \theta_i^{(t)} + \delta_i^{\theta}\right]$ and $\psi_{l,i}^{(t)} \in \left[\psi_i^{(t)} - \delta_i^{\psi}, \psi_i^{(t)} + \delta_i^{\psi}\right]$ are the elevation AoD (EAoD) and azimuth AoD (AAoD) for l^{th} path in i^{th} channel, respectively. Similarly, the angles $\theta_{l,i}^{(r)} \in \left[\theta_i^{(r)} - \delta_i^{\theta}, \theta_i^{(r)} + \delta_i^{\theta}\right]$ and $\psi_{l,i}^{(r)} \in \left[\psi_i - \delta_i^{\psi}, \psi_i^{(r)} + \delta_i^{\psi}\right]$ are the elevation AoA (EAoA) and azimuth AoA (AAoA). $\theta_i(\psi_i)$ is the mean EAoD(AAoD)/EAoA(AAoA) with angular spread $\delta_i^{\theta}(\delta_i^{\psi})$.

4.3.2 Joint Hybrid Beamforming, RIS Dynamic Positioning and Phase Shift Design

In this section, our objective is to optimize RIS deployment for a dynamic indoor environment jointly with its phase shift design and sequentially construct HBF stages for the Tx and Rx to reduce the CSI overhead size while maximizing the throughput of a movable RIS-assisted mMIMO system. First, we discuss the design of the RF beamformer/combiner and BB stages, which is followed by the PSO-based algorithmic solution to jointly optimize the RIS location and its phase shifts to enhance the capacity.

4.3.2.1 RF Beamforming/Combining Stage Design

The RF beamforming stage for the Tx and Rx are designed as follows:

$$\mathbf{F}_1 = \left[\mathbf{e}_t\left(\lambda_x^{u_1}, \lambda_y^{k_1}\right), \cdots, \mathbf{e}_t\left(\lambda_x^{u_{N_{RF_1}}}, \lambda_y^{k_{N_{RF_1}}}\right)\right] \in \mathbb{C}^{M_1 \times N_{RF_1}}, \tag{4.63}$$

$$\mathbf{F}_2 = \left[\mathbf{e_r}\left(\lambda_x^{u_1}, \lambda_y^{k_1}\right), \cdots, \mathbf{e}_r\left(\lambda_x^{u_{N_{RF,2}}}, \lambda_y^{k_{N_{RF,2}}}\right)\right]^T \in \mathbb{C}^{N_{RF,2} \times M_2}, \tag{4.64}$$

where $\mathbf{e}_j(\cdot,\cdot)$ is the corresponding transmit or receive steering vector, which is defined as:

$$\begin{aligned}\mathbf{e}_j\left(\theta,\psi\right) = &\frac{1}{\mathcal{M}}\left[1, e^{j2\pi d \sin(\theta)\cos(\psi)}, \cdots, e^{j2\pi d(\mathcal{M}_x-1)\sin(\theta)\cos(\psi)}\right]^T \otimes \\ &\left[1, e^{j2\pi d \sin(\theta)\sin(\psi)}, \cdots, e^{j2\pi d(\mathcal{M}_y-1)\sin(\theta)\sin(\psi)}\right]^T,\end{aligned} \tag{4.65}$$

where $\mathcal{M} = \{M_1, M_2\}$ for $j = \{t, r\}$. Here, the RF beamformers are constructed via quantized angle-pairs having a boundary, which are defined as $\lambda_x^u = -1 + \frac{2u-1}{\mathcal{M}_x}$ for $u = 1, \cdots, \mathcal{M}_x$ and $\lambda_y^k = -1 + \frac{2k-1}{\mathcal{M}_y}$ for $k = 1, \cdots, \mathcal{M}_y$. The quantized angle-pairs reduce the number of RF chains while providing complete AoD/AoA support defined as:

$$\text{AoD} = \left\{\sin\left(\theta\right)\left[\cos\left(\psi\right), \sin\left(\psi\right)\right] \middle| \theta \in \boldsymbol{\theta}_t, \psi \in \boldsymbol{\psi}_t\right\}, \tag{4.66}$$

$$\text{AoA} = \left\{\sin\left(\theta\right)\left[\cos\left(\psi\right), \sin\left(\psi\right)\right] \middle| \theta \in \boldsymbol{\theta}_r, \psi \in \boldsymbol{\psi}_r\right\}, \tag{4.67}$$

where $\boldsymbol{\theta}_i = \left[\theta_i - \delta_i^\theta, \theta_i + \delta_i^\theta\right]$ and $\boldsymbol{\psi}_i = \left[\psi_i - \delta_i^\psi, \psi_i + \delta_i^\psi\right]$ denote the azimuth and elevation angle supports.

4.3.2.2 BB Precoder/Combiner Design

After designing the RF stages, the effective channel matrix $\mathcal{H}$ as seen from the BB stage is given as:

$$\mathcal{H} = \mathbf{F_2 H F_1} = \mathbf{U \Sigma V^H}, \tag{4.68}$$

where $\mathbf{U} \in \mathbb{C}^{N_{RF_2} \times \text{rank}(\mathcal{H})}$ and $\mathbf{V} \in \mathbb{C}^{N_{RF_1} \times \text{rank}(\mathcal{H})}$ are tall unitary matrices. Here, $\mathbf{\Sigma}$ is the diagonal matrix with singular values in decreasing order. Assuming $\text{rank}(\mathcal{H}) \geq \mathbf{N_S}$, $\mathbf{V}$ can be partitioned as $\mathbf{V} = [\mathbf{V}_1, \mathbf{V}_2]$ with $\mathbf{V}_1 \in \mathbb{C}^{N_{\mathcal{RF}} \times N_S}$. Then, the optimal $\mathbf{B}_1$ and $\mathbf{B}_2$ can be obtained as [146]:

$$\mathbf{B}_1 = \sqrt{\frac{P_T}{N_S}} \mathbf{V}, \quad \mathbf{B}_2 = \mathbf{U}^H. \tag{4.69}$$

4.3.2.3 Joint Dynamic RIS Positioning & Phase Shift Design

After the design of RF and BB stages for the Tx and Rx, the optimization problem given in (4.60) can be reformulated as:

$$\begin{aligned} \max_{\{\mathbf{\Phi}, \mathbf{x}_o\}} \ & \mathrm{R}_T = \log_2 \left| \mathbf{I}_{N_S} + \mathbf{W}_{\tilde{n}}^{-1} \mathbf{B}_2 \mathcal{H} \mathbf{B}_1 \mathbf{B}_1^H \mathcal{H}^H \mathbf{B}_2^H \right| \\ \text{s.t.} \quad & C_3 - C_5. \end{aligned} \tag{4.70}$$

This resulting problem in (4.70) is intractable due to the joint dependence of both the RIS phase value $\phi_i \in [0, 2\pi]$, $\forall i = \{1, \cdots, M_I\}$ and the RIS deployment $\mathbf{x} = [x_o, y_o]^T$ on the rate expression in (4.60). To overcome this challenge, we propose sequential optimization using swarm intelligence, which employs multiple agents, called particles, to explore the search space of the objective function given in (4.70). First, a total of Z particles are randomly placed in search space such that each particle communicates with one another to share their personal best and update the current global best solution for the objective function. The particles then move iteratively for a total of T iterations to reach the global optimum solution. In particular, each RIS location $\mathbf{x} = [x_r, y_r]^T$ and $\mathbf{\Phi}$ are optimized by using a PSO-based algorithmic solution while maximizing the total achievable rate of RIS-assisted mMIMO system. Particularly, each z^{th} particle at the t^{th} iteration now represents

Algorithm 4 Proposed Joint HBF, RIS Phase Shift and Deployment Algorithm

Input: Z, T, (θ, ψ), (x_1, y_1, z_1), (x_r, y_r, z_r), (x_2, y_2, z_2).

Output: $\mathbf{x}_o, \mathbf{P}_\Phi$, $\mathbf{F}_1, \mathbf{B}_1$, $\mathbf{F}_2, \mathbf{B}_2$.

Formulate RF and BB stages at the Tx using (4.63), (4.69)
Formulate HBF stages at the Rx using (4.64), (4.69)
for $z = 1 : Z$ **do**
  Initialize the velocity as $\mathbf{J}_{v,z}^{(0)} = \mathbf{0}$.
  Each entry of $\mathbf{J}_{p,z}^{(0)}$ is uniformly distributed in $[0, 1]$.
  Set the personal best $\mathbf{J}_{p,\text{best},z}^{(0)} = \mathbf{J}_{p,z}^{(0)}$.
end for
Find the global best $\mathbf{J}_{p,\text{best}}^{(0)}$ as in (4.75).
for $t = 1 : T$ **do**
  for $z = 1 : Z$ **do**
    Update the velocity $\mathbf{J}_{v,z}^{(t)}$ as in (4.73).
    Update the position $\mathbf{J}_{p,z}^{(t)}$ as in (4.72).
    Find the personal best $\mathbf{J}_{p,\text{best},z}^{(t)}$ as in (4.74).
  end for
  Find the global best $\mathbf{J}_{p,\text{best}}^{(t)}$ as in (4.75).
end for
$\mathbf{x}_o = \mathbf{X}_{\text{best}}^{(T)}$, $\mathbf{\Phi} = \text{diag}(e^{(j\mathbf{P}_{\Phi_{\text{best}}})})$
Update $\mathbf{B}_1, \mathbf{B}_2$ for $\mathbf{x}_o$ and $\mathbf{\Phi}$.

an instance of each RIS location and its phase value for a total of M_I RIS elements, which is given as follows:

$$\mathbf{J}_z^{(t)} = [\mathbf{X}_z^{(t)}, \mathbf{P}_{\Phi_z}^{(t)}]^T = [x_z^{(t)}, y_z^{(t)}, p_{\phi_{1,z}}^{(t)}, \cdots, p_{\phi_{M_I,z}}^{(t)}]^T \in \mathbb{R}^{M_I+2}, \tag{4.71}$$

where each z^{th} particle represents the RIS position and its phase value and calculates the objective function as $R_T(\mathbf{F}_1, \mathbf{B}_1, \mathbf{F}_2, \mathbf{B}_2, \mathbf{X}_z^{(t)}, \mathbf{P}_{\Phi_z}^{(t)})$. The position $\mathbf{J}_{p_z}^{(t)}$ and velocity $\mathbf{J}_{v_z}^{(t)}$ for z^{th} particle during t^{th} iteration are updated as follows:

$$\mathbf{J}_{p_z}^{(t+1)} = \mathbf{J}_{p_z}^{(t)} + \mathbf{J}_{v_z}^{(t+1)}, \tag{4.72}$$

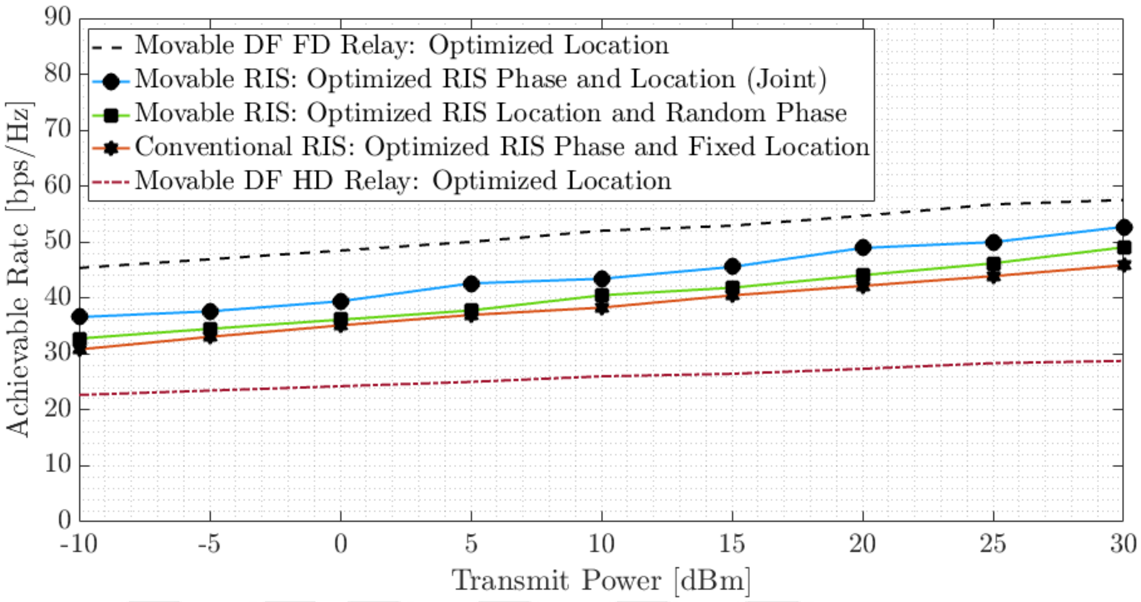

Figure 4.18: Achievable rate comparison of movable RIS and relay-aided AB-HPC systems under increasing P_T.

$$\mathbf{J}_{v_z}^{(t+1)} = \mu_1 \mathbf{Y}_1^{(t)} (\mathbf{J}_{p_{\text{best}}}^{(t)} - \mathbf{J}_{p_z}^{(t)}) + \mu_2 \mathbf{Y}_2^{(t)} (\mathbf{J}_{p_{\text{best}_z}}^{(t)} - \mathbf{J}_{p_z}^{(t)}) + \mu_3^{(t)} \mathbf{J}_{v_z}^{(t)}. \tag{4.73}$$

Finally, the personal and global best solutions for z^{th} particle during t^{th} iteration are obtained as follows:

$$\mathbf{J}_{p_{\text{best}_z}}^{(t)} = \underset{\mathbf{J}_{p_z}^{(t^*)}, \forall t^*=0,1,\cdots,t}{\arg\max} \; R_T(\mathbf{F}_1, \mathbf{B}_1, \mathbf{F}_2, \mathbf{B}_2, \mathbf{X}_z^{(t^*)}, \mathbf{P}_{\Phi_z}^{(t^*)}), \tag{4.74}$$

$$\mathbf{J}_{p_{\text{best}}}^{(t)} = \underset{\mathbf{J}_{p_{\text{best}_z}}^{(t)}, \forall z=0,1,\cdots,Z}{\arg\max} \; R_T(\mathbf{F}_1, \mathbf{B}_1, \mathbf{F}_2, \mathbf{B}_2, \mathbf{X}_{\text{best}_z}^{(t)}, \mathbf{P}_{\Phi_{\text{best}_z}}^{(t)}), \tag{4.75}$$

After T iterations, we update $\mathbf{x}_o = \mathbf{X}_{\text{best}}^{(T)}$ and $\mathbf{\Phi} = \text{diag}(e^{(j\mathbf{P}_{\Phi_{\text{best}}})})$. Algorithm 4.3.2.3 summarizes the proposed joint HBF, RIS phase shift, and deployment scheme.

4.3.3 Numerical Results

In this section, we have analyzed the achievable rate performances of the proposed Spider RIS systems through computer simulations. For performance comparison,

Table 4.5: Simulation parameters.

# of transmit antennas	$M_T = 8 \times 8 = 64$
# of receive antennas	$M_R = 8 \times 8 = 64$
Operating frequency	28 GHz
# of data streams	$N_S = 2$
Tx position	$(0, 0, 2)$ m
User position	$(100, 100, 2)$ m
Ceiling platform x-axis Range	$[40, 70]$ m
Ceiling platform y-axis Range	$[40, 70]$ m
# of paths for $\mathbf{H}_l$	$L = 10$ for $l \in \{TI, IR\}$
Noise PSD	-174 dBm/Hz
Channel bandwidth	10 kHz
PSO # of iterations	$T = 30$
PSO # of particles	$N_{\text{par}} = 10$
Path loss exponent	$\eta = 3.6$
Mean elevation AoA/AoD	$\theta_i^t = \theta_i^r = 60°$,
Mean azimuth AoA/AoD	$\psi_i^t = \psi_i^r = 120°$
Angular spread	$\delta i^\theta = \delta i^\psi = 10°$,

analyses have been conducted taking the traditional fixed RIS, FD relay, and HD relay-aided systems as references. The common system parameters for the provided simulations are presented in Table 4.5.

In Fig. 4.18, we investigate the effect of increasing P_T on the achievable rate performances for the proposed Spider RIS architecture. To establish a benchmark, we consider movable FD and HD relay-aided scenarios, serving as the upper and lower bounds to gauge the performance limits of our proposed system, respectively. According to the obtained results, it is observed that joint optimization of RIS phase and position enhances the performance of RIS-aided communication systems with fixed location or random phase cases. Furthermore, even in the absence of phase optimization, Spider RIS systems outperform fixed-position RIS systems with optimized phase adjustment. This result indicates that mobility is an essential factor in improving the performance of RIS systems. Although the achievable rates of all systems increase as the transmission power increases, the system that reaches the performance of the movable FD relay-aided system is the Spider RIS system, where position and phase optimization are performed together.

It is observed in Fig. 4.19 that the increasing number of reflectors progressively enhances the performance of Spider RIS with that of movable FD relay-aided systems for $P_T = 30$ dBm. The increasing number of reflectors narrows the performance gap, bringing Spider RIS-aided systems in proximity to the achievable rate levels demonstrated by mobile FD relaying. This proximity is pivotal, particularly concerning cost and energy efficiency, exploiting the inherently passive nature of RIS elements. In contrast to relays equipped with active elements, Spider RIS-aided systems provide comparable performance metrics at a notably lower cost and energy consumption. This emphasizes that RIS technology stands as a cost-effective and energy-efficient alternative within wireless communication systems through the strategic augmentation of reflector numbers. Especially when the reflector costs are minimal, the cost and energy efficiency advantages of Spider RIS can potentially replace existing power-hungry solutions and significantly contribute to the future development of wireless networks.

Fig. 4.20 compares the performances of fixed-position RIS and mobile Spider RIS for three different locations of user equipment (UE). Fig. 4.20(a) shows the achievable rates provided by the fixed-position RIS according to UE locations, while Fig. 4.20(b) demonstrates the achievable rates obtained by Spider RIS after phase and position optimization according to three different locations of the UE. In Fig. 4.20(a), with the fixed RIS position, the achievable rates for different UE locations vary between 20.48 and 23.09 bps/Hz, while in Fig. 4.20(b), it is observed that achievable rates improved between 24.58 and 25.68 bps/Hz with Spider RIS. This enhancement reflects that Spider RIS provides superior performance for each user location compared to fixed RIS with optimized phase adjustment. The observed re-

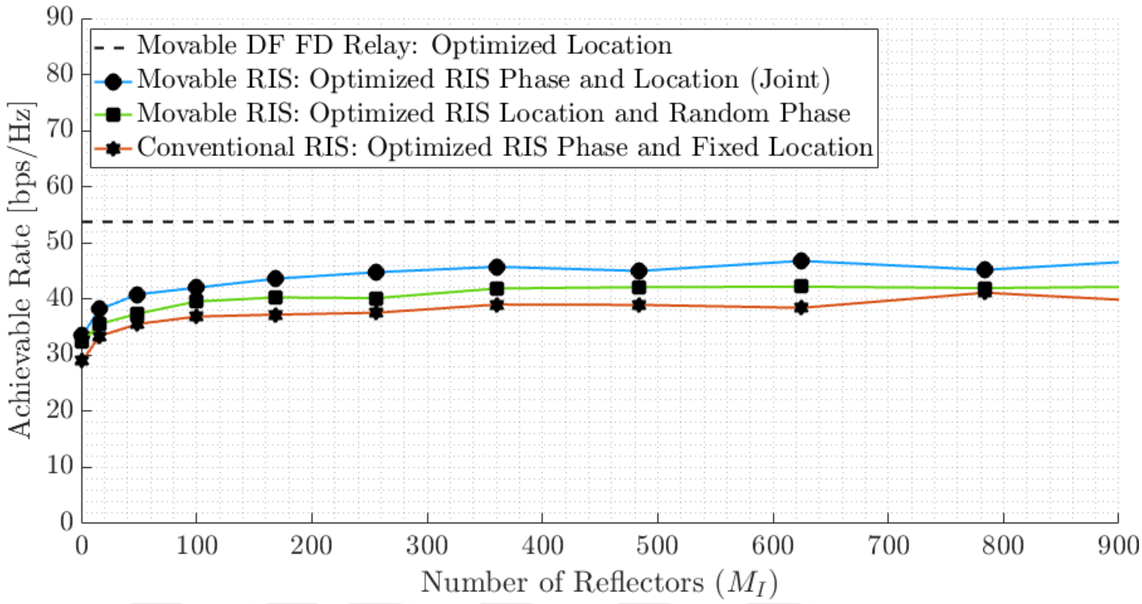

Figure 4.19: Achievable rate comparison of different phase adjustment methods in RIS-aided AB-HPC systems for varying M_I.

sults underline the superior performance of the Spider RIS in various user positions compared to the fixed RIS with optimized phase adjustment. The visual representation further illustrates Spider RIS's capability to dynamically transition from its initial position to optimal locations, all within a designated "Ceiling Platform". This not only exemplifies the inherent mobility of Spider RIS but also highlights its adaptability as it dynamically responds to various user locations. The overall implication of these findings is the transformative potential of mobile RIS technology, significantly raising the efficiency and adaptability benchmarks for wireless networks. This type of dynamic adaptability positions Spider RIS at the forefront of innovations that can seamlessly meet the diverse and evolving needs of wireless communications.

4.3.4 Conclusions

In this study, we have focused on the inherent benefits of Spider RIS, emphasizing its remarkable performance bolstered by strategic mobility and optimization capabilities. Spider RIS offers superior performance than fixed RIS, providing more effective

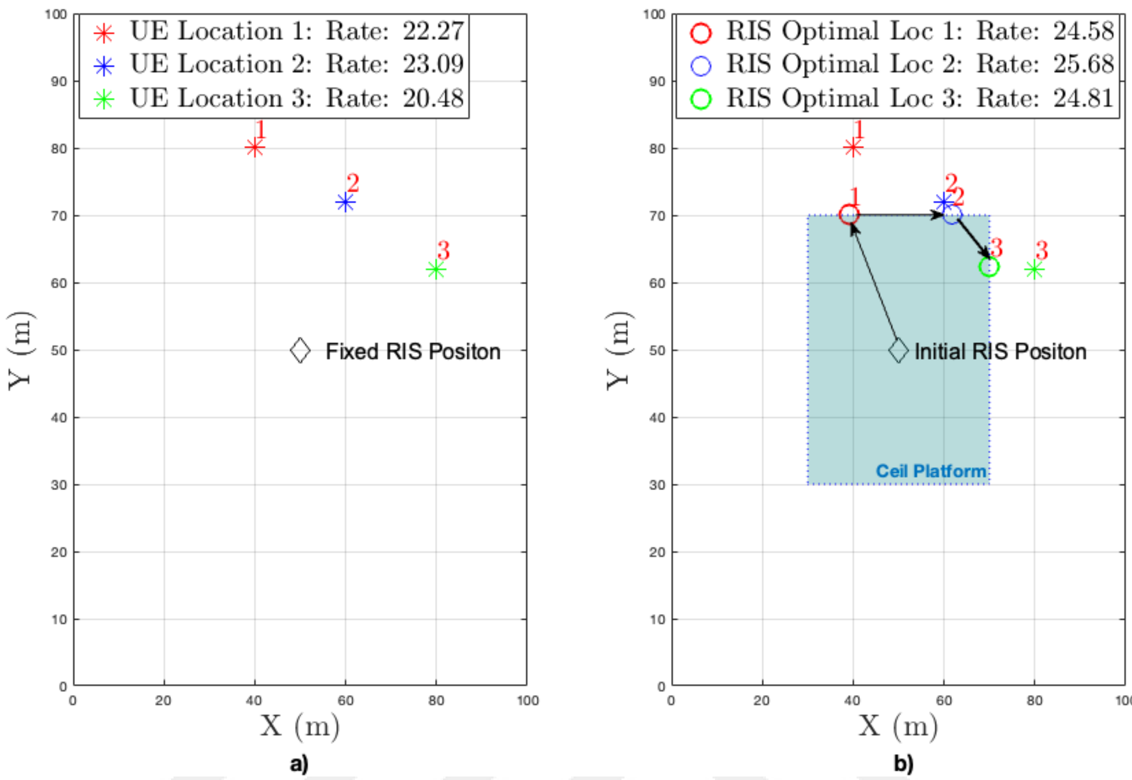

Figure 4.20: Achievable rate comparison of different phase adjustment methods in RIS-aided AB-HPC systems for varying M_I.

and dynamic transmission in changing user locations. The mobility and optimization strategy also allows Spider RIS to improve communication performance by increasing achievable rates. These findings highlight not only Spider RIS's adaptability but also its ability to react efficiently and dynamically to different user locations. The overall results of this study highlight the potential of Spider RIS to become a groundbreaking technology in wireless communications, indicating its potential to take a significant step toward increasing efficiency and adaptability in indoor and outdoor communication systems. The mechanical movement of the Spider RIS is one of the current drawbacks, and movement algorithms that will work more efficiently in the future need to be studied. Further research should also focus on the development of more sophisticated algorithms to jointly increase the efficiency of this mechanical movement and phase adjustment and further expand the potential of Spider RIS.

Chapter 5

CONCLUSION

It is worth noting that communication through intelligent surfaces is different compared with other related technologies currently employed in wireless networks, such as relaying, MIMO beamforming, passive reflect-arrays, and backscatter communications. This can be attributed to the unique features of RISs such as their nearly passive structure without requiring any RF signal processing, up/down-conversion, power amplification or filtering, inherently full-duplex nature, low cost, and more importantly, real-time reconfigurability. These distinctive characteristics make RIS-assisted communication a unique technology and introduce important design challenges that need to be tackled under the rich applications and use-cases. It is inevitable that 6G networking will necessitate radically new concepts for the PHY design of next-generation radios. Within this context, this thesis has discussed the potential of intelligent surfaces-empowered communication by following a bottom-up approach from its main methodology and use-cases to its open problems and potential future directions. This thesis has also extended the potential of RIS technology in wireless communication systems and demonstrated how it can be an effective solution in areas such as extending the coverage of wireless networks, improving communication quality, and optimizing network performance. It plays an important role in shaping future wireless communication networks by providing valuable information on how RIS can play a strategic role in wireless networks and direct the development of 6G and later wireless network technologies. This comprehensive thesis has made significant contributions to the development of wireless networks for 6G and beyond, by containing innovative ideas and solutions that shape the future of wireless communication technologies.

Chapter 2 has discussed in detail the revolutionary potential offered by RIS technology in wireless communication networks. This chapter has mainly aimed to shed light on the potential use-cases of RISs in future wireless systems by means of a novel channel modeling methodology as well as a new software tool for RIS-empowered millimeter-wave communication systems. It is shown by the open-source, user-friendly, and widely applicable *SimRIS Channel Simulator* that RISs will work under certain use-cases and communication environments. Potential future research directions are also discussed to bridge the gap between the theory and practice of RIS-empowered systems toward their standardization for 6G wireless networks.

In Chapter 3, unique RIS-oriented solutions have been proposed for potential communication scenarios that may emerge in 6G and beyond wireless networks. In this context, a number of RIS-assisted systems with single or multiple RISs have been investigated in terms of error performance, achievable data rate and path loss characteristics in indoor and outdoor environments. To our knowledge, for the first time, the studies produced within this thesis has explored the effect of RISs on the overall path loss under empirical path loss models and the cases of multiple RISs, as well as RIS selection strategies, using a unified error performance framework. Chapter 3 has also focused on the combination of RIS-aided reflection and decode-and-forward transmission techniques, highlighting the potential of wireless networks to expand the coverage area. This chapter has taken an important step in expanding the coverage of wireless networks by demonstrating how the integrated use of RIS and relaying technologies can optimize network performance, especially in challenging communication environments.

Chapter 4 discussed RIS-enhanced hybrid beamforming in massive MIMO systems and presented innovative solutions for systems operating in mmWave and THz frequency bands. Through the introduction of an innovative HBF design for single and multiple-RIS-assisted massive MIMO systems, enhanced spatial multiplexing gain has been achieved by effectively utilizing NLoS paths and the RIS-assisted path during transmission. This approach has effectively mitigated the disruptive effects of the wireless propagation environment while reducing hardware cost/complexity and power consumption for massive MIMO systems with large antenna arrays. Overall, these research findings have contributed to the advancement of mmWave and THz band communications, offering efficient and high-performance solutions for overcoming transmission. It has been also introduced an innovative system concept called "Spider RIS", revealing how this technology can be used strategically in wireless networks and push the boundaries of wireless communications. The inherent benefits of Spider RIS have been discussed, emphasizing its remarkable performance bolstered by strategic mobility and optimization capabilities. Spider RIS has offered superior performance than fixed RIS, providing more effective and dynamic transmission in changing user locations. The mobility and optimization strategy has also allowed Spider RIS to improve communication performance by increasing achievable rates. These findings have highlighted not only Spider RIS's adaptability but also its ability to react efficiently and dynamically to different user locations. This chapter has made significant contributions to the development of wireless networks by examining the applications and effects of RIS technology in wireless communication systems in detail.

Within the scope of this thesis, numerous significant studies have been conducted, each pioneering its own field within the RIS literature. All of these studies aim to address practical challenges in future-generation wireless communication systems and generate innovative solutions. Every proposed work in this thesis aspires to contribute to the perspective of intelligent radio environments, putting efforts into laying the groundwork for technologies that will shape the future. With the insights gained from this thesis, endeavors will be made to delve deeper into the practical applications of RIS, striving to understand this technology with a more profound insight. The goal is to become an integral part of the effort to transform RIS into real-world applications.

BIBLIOGRAPHY

[1] K. B. Letaief, W. Chen, Y. Shi, J. Zhang, and Y.-J. A. Zhang, "The roadmap to 6G: AI empowered wireless networks," *IEEE communications magazine*, vol. 57, no. 8, pp. 84–90, 2019.

[2] R. Gupta, D. Reebadiya, and S. Tanwar, "6G-enabled edge intelligence for ultra-reliable low latency applications: Vision and mission," *Computer Standards & Interfaces*, vol. 77, p. 103521, 2021.

[3] W. Jiang, B. Han, M. A. Habibi, and H. D. Schotten, "The road towards 6G: A comprehensive survey," *IEEE Open J. Commun. Soc.*, vol. 2, pp. 334–366, 2021.

[4] K. B. Letaief *et al.*, "The roadmap to 6G: AI empowered wireless networks," *IEEE Commun. Mag.*, vol. 57, pp. 84–90, Aug. 2019.

[5] I. Yildirim, A. Uyrus, and E. Basar, "Modeling and analysis of reconfigurable intelligent surfaces for indoor and outdoor applications in future wireless networks," *IEEE Trans. Commun.*, vol. 69, no. 2, pp. 1290–1301, 2021.

[6] Y. Liu, X. Liu, X. Mu, T. Hou, J. Xu, M. Di Renzo, and N. Al-Dhahir, "Reconfigurable intelligent surfaces: Principles and opportunities," *IEEE Commun. Surveys & Tuts.*, vol. 23, pp. 1546–1577, May 2021.

[7] E. Basar, I. Yildirim, and F. Kilinc, "Indoor and outdoor physical channel modeling and efficient positioning for reconfigurable intelligent surfaces in mmWave bands," *IEEE Trans. Commun.*, vol. 69, no. 12, pp. 8600–8611, 2021.

[8] E. Basar, "Reconfigurable intelligent surface-based index modulation: A new beyond MIMO paradigm for 6G," *IEEE Trans. Commun.*, vol. 68, pp. 3187–3196, Feb. 2020.

[9] I. Yildirim, A. Koc, E. Basar, and T. Le-Ngoc, "RIS-aided angular-based hybrid beamforming design in mmWave massive MIMO systems," in *GLOBECOM 2022-2022 IEEE Global Communications Conference*, pp. 5267–5272, IEEE, 2022.

[10] Samsung, "Samsung's 6G white paper lays out the company's vision for the next generation of communications technology." `https://research.samsung.com/next-generation-communications`, July 2020.

[11] N. Rajatheva, I. Atzeni, E. Bjornson, A. Bourdoux, S. Buzzi, J.-B. Dore, S. Erkucuk, M. Fuentes, K. Guan, Y. Hu, *et al.*, "White paper on broadband connectivity in 6G," Apr. 2020.

[12] E. Basar, M. Di Renzo, J. De Rosny, M. Debbah, M.-S. Alouini, and R. Zhang, "Wireless communications through reconfigurable intelligent surfaces," *IEEE Access*, pp. 116753–116773, Sep. 2019.

[13] Q. Wu, S. Zhang, B. Zheng, C. You, and R. Zhang, "Intelligent reflecting surface aided wireless communications: A tutorial," *IEEE Trans. Commun.*, vol. 69, no. 5, pp. 3313–3351, 2021.

[14] E. Basar, "Reconfigurable intelligent surface-based index modulation: A new beyond MIMO paradigm for 6G," Apr. 2019.

[15] I. Yildirim, F. Kilinc, E. Basar, and G. C. Alexandropoulos, "Hybrid RIS-empowered reflection and decode-and-forward relaying for coverage extension," *IEEE Commun. Lett.*, vol. 25, no. 5, pp. 1692–1696, 2021.

[16] E. Arslan, I. Yildirim, F. Kilinc, and E. Basar, "Over-the-air equalization with reconfigurable intelligent surfaces," June 2021.

[17] E. Basar and I. Yildirim, "Reconfigurable intelligent surfaces for future wireless networks: A channel modeling perspective," *IEEE Wireless Commun.*, vol. 28, no. 3, pp. 108–114, 2021.

[18] M. Di Renzo, F. H. Danufane, X. Xi, J. De Rosny, and S. Tretyakov, "Analytical modeling of the path-loss for reconfigurable intelligent surfaces – Anomalous mirror or scatterer?," in *IEEE Int. Workshop Signal Process. Adv. Wireless Commun. (SPAWC)*, pp. 1–5, 2020.

[19] J. B. Garcia, A. Sibille, and M. Kamoun, "Reconfigurable intelligent surfaces: Bridging the gap between scattering and reflection," *IEEE J. Sel. Areas Commun*, vol. 38, pp. 2538–2547, Nov. 2020.

[20] S. Ellingson, "Path loss in reconfigurable intelligent surface-enabled channels," Nov. 2021.

[21] O. Ozdogan, E. Bjornson, and E. G. Larsson, "Intelligent reflecting surfaces: Physics, propagation, and pathloss modeling," *IEEE Wireless Commun. Lett.*, vol. 9, pp. 581–585, May 2020.

[22] W. Tang, M. Z. Chen, X. Chen, J. Y. Dai, Y. Han, M. Di Renzo, Y. Zeng, S. Jin, Q. Cheng, and T. J. Cui, "Wireless communications with reconfigurable intelligent surface: Path loss modeling and experimental measurement," *IEEE Trans. Wireless Commun.*, vol. 20, no. 1, pp. 421–439, 2021.

[23] F. H. Danufane, M. D. Renzo, J. de Rosny, and S. Tretyakov, "On the path-loss of reconfigurable intelligent surfaces: An approach based on green's theorem applied to vector fields," *IEEE Trans. Commun.*, vol. 69, no. 8, pp. 5573–5592, 2021.

[24] E. Björnson and L. Sanguinetti, "Power scaling laws and near-field behaviors of massive MIMO and intelligent reflecting surfaces," *IEEE Open J. Commun. Soc*, vol. 1, pp. 1306–1324, 2020.

[25] M. Najafi, V. Jamali, R. Schober, and H. V. Poor, "Physics-based modeling and scalable optimization of large intelligent reflecting surfaces," *IEEE Trans. Commun.*, vol. 69, no. 4, pp. 2673–2691, 2021.

[26] G. Gradoni and M. Di Renzo, "End-to-end mutual coupling aware communication model for reconfigurable intelligent surfaces: An electromagnetic-compliant approach based on mutual impedances," *IEEE Wireless Commun. Lett.*, vol. 10, no. 5, pp. 938–942, 2021.

[27] X. Qian and M. D. Renzo, "Mutual coupling and unit cell aware optimization for reconfigurable intelligent surfaces," *IEEE Wireless Commun. Lett.*, vol. 10, no. 6, pp. 1183–1187, 2021.

[28] A. Abrardo, D. Dardari, M. D. Renzo, and X. Qian, "MIMO interference channels assisted by reconfigurable intelligent surfaces: Mutual coupling aware sum-rate optimization based on a mutual impedance channel model," Feb. 2021.

[29] Y. Sun, C.-X. Wang, J. Huang, and J. Wang, "A 3D non-stationary channel model for 6G wireless systems employing intelligent reflecting surface," in *Int. Conf. Wireless Commun. Signal Process. (WCSP)*, (Nanjing, China), pp. 19–25, Oct. 2020.

[30] Y. Sun, C.-X. Wang, J. Huang, and J. Wang, "A 3D non-stationary channel model for 6G wireless systems employing intelligent reflecting surfaces with practical phase shifts," *IEEE Trans. Cogn. Commun.*, vol. 7, no. 2, pp. 496–510, 2021.

[31] G. Sun, R. He, Z. Ma, B. Ai, and Z. Zhong, "A 3D geometry-based non-stationary MIMO channel model for RIS-assisted communications," in *IEEE Veh. Technol. Conf (VTC2021-Fall)*, (Norman, OK, USA), pp. 1–5, 2021.

[32] H. Jiang, C. Ruan, Z. Zhang, J. Dang, L. Wu, M. Mukherjee, and D. B. da Costa, "A general wideband non-stationary stochastic channel model for intelligent reflecting surface-assisted MIMO communications," *IEEE Trans. Wireless Commun.*, vol. 20, no. 8, pp. 5314–5328, 2021.

[33] B. Xiong, Z. Zhang, H. Jiang, H. Zhang, J. Zhang, L. Wu, and J. Dang, "A statistical MIMO channel model for reconfigurable intelligent surface assisted wireless communications," *IEEE Trans. Commun. (Earl Access)*, pp. 1–1, 2021.

[34] E. Basar and I. Yildirim, "SimRIS channel simulator for reconfigurable intelligent surface-empowered mmWave communication systems," in *Proc. IEEE Latin-American Conf. Commun. (LATINCOM 2020)*, pp. 1–6, Nov. 2020.

[35] F. Kilinc, I. Yildirim, and E. Basar, "Physical channel modeling for RIS-empowered wireless networks in sub-6 GHz bands," Nov. 2021.

[36] W. Saad, M. Bennis, and M. Chen, "A vision of 6G wireless systems: Applications, trends, technologies, and open research problems," *IEEE Netw. (to appear)*, Feb. 2019.

[37] Q. Wu and R. Zhang, "Towards smart and reconfigurable environment: Intelligent reflecting surface aided wireless network," *IEEE Commun. Mag.*, pp. 106–112, Jan. 2019.

[38] E. Basar and I. F. Akyildiz, "Reconfigurable intelligent surfaces for Doppler effect and multipath fading mitigation," Dec. 2019.

[39] I. Yildirim, A. Uyrus, and E. Basar, "Modeling and analysis of reconfigurable intelligent surfaces for indoor and outdoor applications in future wireless networks," *IEEE Trans. Commun. (Early access)*, Nov. 2020.

[40] D. Dardari, "Communicating with large intelligent surfaces: Fundamental limits and models," *IEEE J. Sel. Areas Commun.*, vol. 38, no. 11, pp. 2526–2537, 2020.

[41] M. Di Renzo *et al.*, "Smart radio environments empowered by reconfigurable intelligent surfaces: How it works, state of research, and the road ahead," *IEEE J. Sel. Areas Commun.*, vol. 38, no. 11, pp. 2450–2525, 2020.

[42] E. Basar, "Transmission through large intelligent surfaces: A new frontier in wireless communications," in *Proc. European Conf. Netw. Commun. (EuCNC 2019)*, (Valencia, Spain), June 2019.

[43] W. Tang, J. Y. Dai, M. Chen, X. Li, Q. Cheng, S. Jin, K. Wong, and T. J. Cui, "Programmable metasurface-based RF chain-free 8PSK wireless transmitter," *Elect. Lett.*, vol. 55, pp. 417–420, Apr. 2019.

[44] V. Jamali, A. M. Tulino, G. Fischer, R. Müller, and R. Schober, "Intelligent reflecting and transmitting surface aided millimeter wave massive MIMO," Sep. 2019.

[45] J. Hey, H. Wymeersch, T. Sanguanpuaky, O. Silvenz, and M. Juntti, "Adaptive beamforming design for mmWave RIS-aided joint localization and communication," Nov. 2019.

[46] X. Yang, C.-K. Wen, and S. Jin, "MIMO detection for reconfigurable intelligent surface-assisted millimeter wave systems," Apr. 2020.

[47] M. Najafi *et al.*, "Physics-based modeling and scalable optimization of large intelligent reflecting surfaces," Sep. 2020.

[48] K. Ntontin *et al.*, "Reconfigurable intelligent surface optimal placement in millimeter-wave networks," Nov. 2020.

[49] W. L. Stutzman and P. G. A. Thiele, *Antenna Theory and Design.* USA: Wiley, 2012.

[50] “3GPP TR 38.901 V16.1.0 - Study on channel model for frequencies from 0.5 to 100 GHz,” Dec. 2019.

[51] I. A. Hemadeh, K. Satyanarayana, M. El-Hajjar, and L. Hanzo, “Millimeter-wave communications: Physical channel models, design considerations, antenna constructions, and link-budget,” *IEEE Commun. Surveys Tuts.*, vol. 20, pp. 870–913, 2nd Quart. 2018.

[52] P. Nayeri, F. Yang, and A. Z. Elsherbeni, *Reflectarray Antennas: Theory, Designs, and Applications.* USA: Wiley, 2018.

[53] C. A. Balanis, *Antenna Theory Analysis and Design.* USA: Wiley, 2016.

[54] S. Buzzi and C. D’Andrea, “On clustered statistical MIMO millimeter wave channel simulation,” Apr. 2016.

[55] M. K. Samimi and T. S. Rappaport, “Statistical channel model with multi-frequency and arbitrary antenna beamwidth for millimeter-wave outdoor communications,” in *2015 IEEE Globecom Workshops (GC Wkshps)*, pp. 1–7, 2015.

[56] O. E. Ayach, S. Rajagopal, S. Abu-Surra, Z. Pi, and R. W. Heath, “Spatially sparse precoding in millimeter wave mimo systems,” *IEEE Tran. Wireless Commun.*, vol. 13, pp. 1499–1513, Mar. 2014.

[57] NTT Docomo, “5G channel model for bands up to 100 GHz.” `http://http://www.5gworkshops.com/2016/5G_Channel_Model_for_bands_up_to100_GHz(2015-12-6).pdf`, Oct. 2016.

[58] T. S. Rappaport, G. R. MacCartney, M. K. Samimi, and S. Sun, "Wideband millimeter-wave propagation measurements and channel models for future wireless communication system design," *IEEE Trans. Commun.*, vol. 63, pp. 3029–3056, Sep. 2015.

[59] M. Alonzo, S. Buzzi, A. Zappone, and C. D'Elia, "Energy-efficient power control in cell-free and user-centric massive MIMO at millimeter wave," *IEEE Trans. Green Commun. Netw.*, vol. 3, pp. 651–663, Sep. 2019.

[60] K. Haneda *et al.*, "5G 3GPP-like channel models for outdoor urban microcellular and macrocellular environments," in *Proc. 2016 IEEE 83rd Veh. Technol.Conf. (VTC Spring)*, pp. 1–7, 2016.

[61] E. Björnson and L. Sanguinetti, "Power scaling laws and near-field behaviors of massive MIMO and intelligent reflecting surfaces," *IEEE OJ-COMS*, vol. 1, pp. 1306–1324, 2020.

[62] C. Liaskos *et al.*, "A new wireless communication paradigm through software-controlled metasurfaces," *IEEE Commun. Mag.*, vol. 56, pp. 162–169, Sep. 2018.

[63] E. Basar and I. Yildirim, "Indoor and outdoor physical channel modeling and efficient positioning for reconfigurable intelligent surfaces in mmWave bands," May 2020.

[64] Q. Wu and R. Zhang, "Intelligent reflecting surface enhanced wireless network via joint active and passive beamforming," *IEEE Trans. Wireless Commun.*, pp. 5394–5409, Nov. 2019.

[65] C. Huang *et al.*, "Reconfigurable intelligent surfaces for energy efficiency in wireless communication," *IEEE Trans. Wireless Commun.*, Aug. 2019.

[66] T. Hou, Y. Liu, Z. Song, X. Sun, Y. Chen, and L. Hanzo, "MIMO assisted networks relying on large intelligent surfaces: A stochastic geometry model," Oct. 2019.

[67] M. Dunna *et al.*, "ScatterMIMO: Enabling virtual MIMO with smart surfaces," in *Proc. ACM Annu. Int. Conf. Mobile Comput. Netw.*, pp. 1–14, 2020.

[68] Ericsson, "World's first 5G NR radio." https://www.ericsson.com/en/networks/offerings/5g/nr-radio, 2018.

[69] T. S. Rappaport *et al.*, "Wireless communications and applications above 100 GHz: Opportunities and challenges for 6G and beyond," *IEEE Access*, vol. 7, pp. 78729–78757, June 2019.

[70] E. Basar, "Index modulation techniques for 5G wireless networks," *IEEE Commun. Mag.*, vol. 54, pp. 168–175, June 2016.

[71] L. Dai, B. Wang, Y. Yuan, S. Han, C. l. I, and Z. Wang, "Non-orthogonal multiple access for 5G: Solutions, challenges, opportunities, and future research trends," *IEEE Commun. Magç*, vol. 53, pp. 74–81, Sept. 2015.

[72] P. Banelli *et al.*, "Modulation formats and waveforms for 5G networks: Who will be the heir of OFDM?: An overview of alternative modulation schemes for improved spectral efficiency," *IEEE Signal Process. Mag.*, vol. 31, pp. 80–93, Nov 2014.

[73] X. Tan, Z. Sun, J. M. Jornet, and D. Pados, "Increasing indoor spectrum sharing capacity using smart reflect-array," in *Proc. 2016 IEEE Int. Conf. Commun. (ICC)*, (Kuala Lumpur, Malaysia), pp. 1–6, May 2016.

[74] X. Tan, Z. Sun, D. Koutsonikolas, and J. M. Jornet, "Enabling indoor mobile millimeter-wave networks based on smart reflect-arrays," in *Proc. IEEE Conf. Comput. Commun.*, pp. 270–278, Apr. 2018.

[75] C. Huang *et al.*, "Holographic MIMO surfaces for 6G wireless networks: Opportunities, challenges, and trends," *IEEE Wireless Commun.*, pp. 1–8, 2020.

[76] M. Di Renzo *et al.*, "Smart radio environments empowered by reconfigurable AI meta-surfaces: An idea whose time has come," *EURASIP J. Wireless Commun. Net.*, vol. 2019, p. 129, May 2019.

[77] E. Basar, "Reconfigurable intelligent surface-based index modulation: A new beyond MIMO paradigm for 6G," *IEEE Trans. Commun.*, vol. 68, no. 5, pp. 3187–3196, 2020.

[78] M. Di Renzo *et al.*, "Reconfigurable intelligent surfaces vs. relaying: Differences, similarities, and performance comparison," *IEEE Open Journal of the Communications Society*, vol. 1, pp. 798–807, 2020.

[79] Q. Wu and R. Zhang, "Intelligent reflecting surface enhanced wireless network: Joint active and passive beamforming design," in *Proc. IEEE Global Commun. Conf.*, (Abu Dhabi, UAE), Dec. 2018.

[80] Q. Wu and R. Zhang, "Beamforming optimization for intelligent reflecting surface with discrete phase shifts," in *Proc. 2019 IEEE Int. Conf. Acoust. Speech Signal Process. (ICASSP)*, (Brighton, UK), May 2019.

[81] C. Huang, G. C. Alexandropoulos, A. Zappone, M. Debbah, and C. Yuen, "Energy efficient multi-user MISO communication using low resolution large intelligent surfaces," in *Proc. IEEE Global Commun. Conf.*, (Abu Dhabi, UAE), Dec. 2018.

[82] M. Cui, G. Zhang, and R. Zhang, "Secure wireless communication via intelligent reflecting surface," May 2019.

[83] X. Yu, D. Xu, and R. Schober, "Enabling secure wireless communications via intelligent reflecting surfaces," in *Proc. IEEE Global Commun. Conf. (GLOBECOM)*, (Waikoloa, HI, USA), Apr. 2019.

[84] H. Shen *et al.*, "Secrecy rate maximization for intelligent reflecting surface assisted multi-antenna communications," *IEEE Commun. Lett.*, vol. 23, pp. 1488–1492, Sep. 2019.

[85] T. S. Rappaport, *Wireless Communications: Principles and Practice, 2. Ed.* Upper Saddle River, NJ: Prentice Hall, Inc., 2002.

[86] F. P. Fontán and P. M. Espiñeira, *Modelling the wireless propagation channel: A simulation approach with MATLAB.* John Wiley & Sons, 2008.

[87] J. G. Proakis, *Digital Communications.* New York: McGraw-Hill, 5 ed., 2008.

[88] M. Simon and M. S. Alouini, *Digital Communications over Fading Channels.* New Jersey: John Wiley & Sons, 2 ed., 2005.

[89] 3GPP-TR-36.814, *Evolved Universal Terrestrial Radio Access (E-UTRA);Further Advancements for E-UTRA Physical Layer Aspects*, 2010.

[90] T. S. Rappaport *et al.*, "Overview of millimeter wave communications for fifth-generation (5G) wireless networks—with a focus on propagation models," *IEEE Trans. Antennas Propag.*, vol. 65, pp. 6213–6230, Dec. 2017.

[91] F. Liu, O. Tsilipakos, A. Pitilakis, A. C. Tasolamprou, M. S. Mirmoosa, N. V. Kantartzis, D.-H. Kwon, M. Kafesaki, C. M. Soukoulis, and S. A. Tretyakov, "Intelligent metasurfaces with continuously tunable local surface impedance for multiple reconfigurable functions," *Phys. Rev. Applied*, vol. 11, p. 044024, Apr. 2019.

[92] X. Hu *et al.*, "Location information aided multiple intelligent reflecting surface systems," *IEEE Trans. Commun.*, pp. 1–1, 2020.

[93] M. Badiu and J. P. Coon, "Communication through a large reflecting surface with phase errors," *IEEE Wireless Commun. Lett.*, vol. 9, no. 2, pp. 184–188, 2020.

[94] L. Wei *et al.*, "Parallel factor decomposition channel estimation in RIS-assisted multi-user MISO communication," in *2020 IEEE 11th Sensor Array and Multichannel Signal Processing Workshop (SAM)*, pp. 1–5, 2020.

[95] C. Huang, R. Mo, and C. Yuen, "Reconfigurable intelligent surface assisted multiuser MISO systems exploiting deep reinforcement learning," *IEEE J. Sel. Areas Commun.*, vol. 38, pp. 1839–1850, Aug. 2020.

[96] C. Huang *et al.*, "Holographic MIMO surfaces for 6G wireless networks: Opportunities, challenges, and trends," *IEEE Wireless Commun.*, vol. 27, no. 5, pp. 118–125, 2020.

[97] M. Di Renzo *et al.*, "Smart radio environments empowered by reconfigurable ai meta-surfaces: An idea whose time has come," *EURASIP J. Wireless Commun. and Netw.*, vol. 2019, pp. 1–20, May 2019.

[98] E. Björnson, O. Ozdogan, and E. G. Larsson, "Intelligent reflecting surface versus decode-and-forward: How large surfaces are needed to beat relaying?," *IEEE Wireless Commun. Lett.*, vol. 9, pp. 244–248, Feb. 2020.

[99] X. Ying, U. Demirhan, and A. Alkhateeb, "Relay aided intelligent reconfigurable surfaces: Achieving the potential without so many antennas," 2020.

[100] Z. Abdullah *et al.*, "A hybrid relay and intelligent reflecting surface network and its ergodic performance analysis," *IEEE Wireless Commun. Lett.*, vol. 9, pp. 1653–1657, Oct. 2020.

[101] Z. Abdullah *et al.*, "Optimization of intelligent reflecting surface assisted full-duplex relay networks," *IEEE Wireless Commun. Lett. (Early Access)*, Oct. 2020.

[102] P. Billingsley, *Probability and Measure.* New York: John Wiley & Sons, 2 ed., 1995.

[103] S. Sun *et al.*, "Propagation path loss models for 5G urban micro- and macro-cellular scenarios," in *Proc. 2016 IEEE 83rd Veh. Technol. Conf. (VTC Spring)*, pp. 1–6, 2016.

[104] E. G. Larsson, O. Edfors, F. Tufvesson, and T. L. Marzetta, "Massive MIMO for next generation wireless systems," *IEEE Commun. Mag.*, vol. 52, pp. 186–195, Feb. 2014.

[105] N. Fatema, G. Hua, Y. Xiang, D. Peng, and I. Natgunanathan, "Massive MIMO linear precoding: A survey," *IEEE Syst. J.*, vol. 12, no. 4, pp. 3920–3931, Dec. 2017.

[106] I. Ahmed, H. Khammari, A. Shahid, A. Musa, K. S. Kim, E. De Poorter, and I. Moerman, "A survey on hybrid beamforming techniques in 5G: Architecture and system model perspectives," *IEEE Commun. Surveys Tuts.*, vol. 20, pp. 3060–3097, 4th Quart. 2018.

[107] A. Koc, A. Masmoudi, and T. Le-Ngoc, "3D angular-based hybrid precoding and user grouping for uniform rectangular arrays in massive MU-MIMO systems," *IEEE Access*, vol. 8, pp. 84689–84712, May 2020.

[108] A. Koc and T. Le-Ngoc, "Hybrid millimeter-wave massive MIMO systems with low CSI overhead and few-bit DACs/ADCs," in *2020 IEEE 92nd Veh. Technol. Conf. (VTC2020-Fall)*, pp. 1–5, Dec. 2020.

[109] A. Koc and T. Le-Ngoc, "Swarm intelligence based power allocation in hybrid massive MIMO systems," in *2021 IEEE Wireless Commun. and Netw. Conf. (WCNC)*, pp. 1–7, Mar. 2021.

[110] P. Wang *et al.*, "Joint transceiver and large intelligent surface design for massive MIMO mmWave systems," *IEEE Trans. Wireless Commun.*, vol. 20, no. 2, pp. 1052–1064, 2021.

[111] K. Ying *et al.*, "GMD-based hybrid beamforming for large reconfigurable intelligent surface assisted millimeter-wave massive MIMO," *IEEE Access*, vol. 8, pp. 19530–19539, 2020.

[112] S. H. Hong *et al.*, "Hybrid beamforming for intelligent reflecting surface aided millimeter wave MIMO systems," *IEEE Trans. Wireless Commun (Early Access)*, 2022.

[113] A. Alkhateeb, J. Mo, N. Gonzalez-Prelcic, and R. W. Heath, "MIMO precoding and combining solutions for millimeter-Wave systems," *IEEE Commun. Mag.*, vol. 52, pp. 122–131, Dec. 2014.

[114] X. Cheng, B. Yu, L. Yang, J. Zhang, G. Liu, Y. Wu, and L. Wan, "Communicating in the real world: 3D MIMO," *IEEE Wireless Commun.*, vol. 21, pp. 136–144, Aug. 2014.

[115] S. Park, A. Alkhateeb, and R. W. Heath, "Dynamic subarrays for hybrid precoding in wideband mmWave MIMO systems," *IEEE Trans. Wireless Commun.*, vol. 16, pp. 2907–2920, Mar. 2017.

[116] F. Sohrabi and W. Yu, "Hybrid analog and digital beamforming for mmWave OFDM large-scale antenna arrays," *IEEE J. Sel. Areas Commun.*, vol. 35, pp. 1432–1443, July 2017.

[117] W. Tong, A. Hussain, W. X. Bo, and S. Maharjan, "Artificial intelligence for vehicle-to-everything: A survey," *IEEE Access*, vol. 7, pp. 10823–10843, 2019.

[118] A. I. Sulyman *et al.*, "Directional radio propagation path loss models for millimeter-wave wireless networks in the 28-, 60-, and 73-GHz bands," *IEEE Trans. Wireless Commun.*, vol. 15, no. 10, pp. 6939–6947, 2016.

[119] C. Chaccour, M. N. Soorki, W. Saad, M. Bennis, P. Popovski, and M. Debbah, "Seven defining features of terahertz (THz) wireless systems: A fellowship of communication and sensing," *IEEE Commun. Surveys Tuts.*, vol. 24, no. 2, pp. 967–993, 2022.

[120] E. G. Larsson, O. Edfors, F. Tufvesson, and T. L. Marzetta, "Massive MIMO for next generation wireless systems," *IEEE Commun. Mag.*, vol. 52, pp. 186–195, Feb. 2014.

[121] A. F. Molisch, V. V. Ratnam, S. Han, Z. Li, S. L. H. Nguyen, L. Li, and K. Haneda, "Hybrid beamforming for massive MIMO: A survey," *IEEE Commun. Mag.*, vol. 55, pp. 134–141, Sept. 2017.

[122] X. Yu, J.-C. Shen, J. Zhang, and K. B. Letaief, "Alternating minimization algorithms for hybrid precoding in millimeter wave mimo systems," *IEEE J. Sel. Topics Signal Process*, vol. 10, pp. 485–500, Apr. 2016.

[123] S. Park, A. Alkhateeb, and R. W. Heath, "Dynamic subarrays for hybrid precoding in wideband mmwave MIMO systems," *IEEE Trans. Wireless Commun.*, vol. 16, no. 5, pp. 2907–2920, 2017.

[124] W. Zheng, A. Koc, and T. Le-Ngoc, "Sub-connected hybrid precoding architectures in massive MIMO systems," in *Proc. IEEE Global Commun. Conf. (GLOBECOM)*, (Taipei, Taiwan), pp. 1–6, Dec. 2020.

[125] I. Yildirim, A. Koc, E. Basar, and T. Le-Ngoc, "RIS-aided angular-based hybrid beamforming design in mmWave massive MIMO systems," in *Proc. IEEE Global Commun. Conf. (GLOBECOM)*, (Rio de Janeiro, Brazil), pp. 5267–5272, Dec. 2022.

[126] M. Jian, R. Liu, and Y. Zhao, "Spatial multiplexing optimization for ris-assisted wireless communication using practical models," in *in Proc. IEEE*

Global Commun. Conf. (GLOBECOM), (Rio de Janeiro, Brazil), pp. 656–661, Dec. 2022.

[127] O. Ozdogan, E. Björnson, and E. G. Larsson, "Using intelligent reflecting surfaces for rank improvement in MIMO communications," in *Proc. IEEE ICASSP*, pp. 9160–9164, May. 2020.

[128] C. Huang, Z. Yang, G. C. Alexandropoulos, K. Xiong, L. Wei, C. Yuen, and Z. Zhang, "Hybrid beamforming for RIS-empowered multi-hop terahertz communications: A DRL-based method," in *Proc. IEEE GLOBECOM Workshops (GC Wkshps*, pp. 1–6, 2020.

[129] Y. Lu, M. Hao, and R. Mackenzie, "Reconfigurable intelligent surface based hybrid precoding for THz communications," *Intelligent and Converged Networks*, vol. 3, pp. 103–118, Mar. 2022.

[130] B. Ning, Z. Chen, W. Chen, Y. Du, and J. Fang, "Terahertz multi-user massive MIMO with intelligent reflecting surface: Beam training and hybrid beamforming," *IEEE Trans. Veh. Technol.*, vol. 70, no. 2, pp. 1376–1393, 2021.

[131] A. M. Elbir, K. V. Mishra, and S. Chatzinotas, "Terahertz-band joint ultra-massive MIMO radar-communications: Model-based and model-free hybrid beamforming," *IEEE J. Sel. Topics Signal Process*, vol. 15, pp. 1468–1483, Nov. 2021.

[132] E. K. Agbogla, I. Trigui, K. Humadi, W. Ajib, and W.-P. Zhu, "Adaptive coordinated direct and multi-RIS transmissions for ultrareliable terahertz systems," *IEEE Trans. Veh. Technol. (Early Access)*, pp. 1–6, 2023.

[133] A. Saleh and R. Valenzuela, "A statistical model for indoor multipath propagation," *IEEE J. Sel. Areas Commun.*, vol. 5, pp. 128–137, Feb. 1987.

[134] G. Gui, M. Liu, F. Tang, N. Kato, and F. Adachi, "6G: Opening new horizons for integration of comfort, security, and intelligence," *IEEE Wireless Commun.*, vol. 27, no. 5, pp. 126–132, 2020.

[135] S. Dang, O. Amin, B. Shihada, and M. Alouini, "What should 6G be?," *Nat. Electron.*, vol. 3, pp. 20–29, Jan. 2020.

[136] M. Jian, G. C. Alexandropoulos, E. Basar, C. Huang, R. Liu, Y. Liu, and C. Yuen, "Reconfigurable intelligent surfaces for wireless communications: Overview of hardware designs, channel models, and estimation techniques," *Intelligent and Converged Networks*, vol. 3, no. 1, pp. 1–32, 2022.

[137] B. Li, Z. Fei, and Y. Zhang, "UAV communications for 5G and beyond: Recent advances and future trends," *IEEE Internet Things J.*, vol. 6, no. 2, pp. 2241–2263, 2019.

[138] X. Liu, Y. Liu, and Y. Chen, "Machine learning empowered trajectory and passive beamforming design in UAV-RIS wireless networks," *IEEE J. Sel. Areas Commun.*, vol. 39, no. 7, pp. 2042–2055, 2021.

[139] A. C. Pogaku, D.-T. Do, B. M. Lee, and N. D. Nguyen, "UAV-assisted RIS for future wireless communications: A survey on optimization and performance analysis," *IEEE Access*, vol. 10, pp. 16320–16336, 2022.

[140] F. Zhou, Y. Wu, H. Sun, and Z. Chu, "UAV-enabled mobile edge computing: Offloading optimization and trajectory design," in *IEEE Int. Conf. on Commun. (ICC)*, (Kansas City, MO, USA), pp. 1–6, May 2018.

[141] L. Li, X. Wen, Z. Lu, Q. Pan, W. Jing, and Z. Hu, "Energy-efficient UAV-enabled MEC system: Bits allocation optimization and trajectory design," *Sensors*, vol. 19, no. 20, 2019.

[142] L. Zhu, W. Ma, and R. Zhang, "Movable antennas for wireless communication: Opportunities and challenges," June 2023.

[143] W. Ma, L. Zhu, and R. Zhang, "Mimo capacity characterization for movable antenna systems," *IEEE Transactions on Wireless Communications (Early Access)*, pp. 1–16, Sep. 2023.

[144] S. Ju, Y. Xing, O. Kanhere, and T. S. Rappaport, "Millimeter wave and sub-terahertz spatial statistical channel model for an indoor office building," *IEEE J. Sel. Areas Commun.*, vol. 39, no. 6, pp. 1561–1575, 2021.

[145] M. Mahmood, M. Ghadaksaz, A. Koc, and T. Le-Ngoc, "Deep learning meets swarm intelligence for UAV-assisted IoT coverage in massive MIMO," *IEEE Internet Things J.*, pp. 1–1, 2023.

[146] M. Mahmood, A. Koc, and T. Le-Ngoc, "Spherical array-based joint beam-forming and UAV positioning in massive MIMO systems," in *Proc. IEEE 97th Veh. Technol. Conf. (VTC-Spring)*, pp. 1–5, 2023.